UNIVERSIDADE ESTADUAL PAULISTA
"JÚLIO DE MESQUITA FILHO"
Faculdade de Ciências Farmacêuticas
Campus Araraquara
Programa de Pós-Graduação em Ciências Farmacêuticas

Development of iron- and zinc-based quantum dots for fluorescence and magnetic resonance bioimaging applications

Desenvolvimento de pontos quânticos à base de ferro e zinco para aplicações de bioimagem por fluorescência e ressonância magnética

Thúlio Wliandon Lemos Barbosa

Orientadora (UNESP): Prof. Dra. Leila Aparecida Chiavacci Favorin
Supervisor (Université d'Angers): Dr. Laurent Lemaire

Araraquara - SP
2024

UNIVERSIDADE ESTADUAL PAULISTA
"JÚLIO DE MESQUITA FILHO"
Faculdade de Ciências Farmacêuticas
Campus Araraquara
Programa de Pós-Graduação em Ciências Farmacêuticas

Development of iron- and zinc-based quantum dots for fluorescence and magnetic resonance bioimaging applications

Desenvolvimento de pontos quânticos à base de ferro e zinco para aplicações de bioimagem por fluorescência e ressonância magnética

Thúlio Wliandon Lemos Barbosa

Tese apresentada ao Programa de Pós-graduação em Ciências Farmacêuticas (Unesp) para obtenção do título de Doutor em Ciências, área: Pesquisa e desenvolvimento de Fármacos e medicamentos.

Orientadora (UNESP): Prof Dra. Leila Aparecida Chiavacci Favorin
Supervisor (Université d'Angers): Dr. Laurent Lemaire

Araraquara - SP
2024

Barbosa, Thúlio Wliandon Lemos.
B238d Development of iron- and zinc-based quantum dots for fluorescence and magnetic resonance bioimaging applications = Desenvolvimento de pontos quânticos à base de ferro e zinco para aplicações de bioimagem por fluorescência e ressonância magnética / Thúlio Wliandon Lemos Barbosa. – Araraquara, 2024.
194 f. : il.

Orientadora: Leila Aparecida Chiavacci Favorin.
Coorientador: Laurent Lemaire.

Tese (Doutorado) – Universidade Estadual Paulista. "Júlio de Mesquita Filho". Faculdade de Ciências Farmacêuticas. Programa de Pós-Graduação em Ciências Farmacêuticas. Área de Pesquisa e Desenvolvimento de Fármacos e Medicamentos.

1. Zinco. 2. Ferro. 3. Luminescência. 4. Ressonância magnética. 5. Imagem biológica. I. Favorin, Leila Aparecida Chiavacci, orient. II. Lemaire, Laurent, coorient. III. Título.

Diretoria do Serviço Técnico de Biblioteca e Documentação - Faculdade de Ciências Farmacêuticas
UNESP - Campus de Araraquara

CAPES: 33004030078P6
Esta ficha não pode ser modificada

UNIVERSIDADE ESTADUAL PAULISTA

Câmpus de Araraquara

CERTIFICADO DE APROVAÇÃO

TÍTULO DA TESE: Desenvolvimento de pontos quânticos à base de ferro e zinco para aplicações de bioimagem por fluorescência e ressonância magnética

AUTOR: THÚLIO WLIANDON LEMOS BARBOSA
ORIENTADORA: LEILA APARECIDA CHIAVACCI FAVORIN

Aprovado como parte das exigências para obtenção do Título de Doutor em Ciências, área: Pesquisa e Desenvolvimento de Fármacos e Medicamentos pela Comissão Examinadora:

Profa. Dra. LEILA APARECIDA CHIAVACCI FAVORIN (Participaçao Presencial)
Departamento de Farmacos e Medicamentos / Faculdade de Ciencias Farmaceuticas do Campus de Araraquara da Unesp

Prof. Dr. ARNÓBIO ANTONIO DA SILVA JUNIOR (Participaçao Virtual)
Departamento de Farmácia / Universidade Federal do Rio Grande do Norte (UFRN)

Profa.Dra. SANDRA HELENA PULCINELLI (Participaçao Presencial)
Departamento de Química Analítica, Físico-Química e Inorgânica / Instituto de Química do Campus de Araraquara da Unesp

Prof. Dr. FERNANDO LUCAS PRIMO (Participaçao Presencial)
Departamento de Engenharia de Bioprocessos e Biotecnologia / Faculdade de Ciencias Farmaceuticas do Campus de Araraquara da Unesp

Prof. Dr. LUCAS AMARAL MACHADO (Participaçao Presencial)
Departamento de Fármacos e Medicamentos / Faculdade de Ciências Farmacêuticas do Campus de Araraquara da Unesp

Araraquara, 29 de maio de 2024

Dedico este trabalho à minha mãe, Cleide, um exemplo de força e resiliência, que sempre me apoiou nos momentos mais difíceis e a quem amo muito.

Acknowledgements

I would like to thank everyone who has contributed in any way to the completion of this thesis. As you know, it has been a very difficult time, not only for me, but for everyone, as we have lived through a pandemic that has greatly affected my efforts to complete this thesis. However, I followed my dream of getting a Ph.D. from a prestigious university, and I had the cooperation of many people who helped me complete this journey with good results. As well as the opportunity to study abroad and improve my professional performance.

I would like to thank my family, my parents Cleide and Wliandon and my siblings Natália, Najara and Thiago, for their support and understanding that at this stage of my life I had to make many choices and miss important moments that would be fundamental for my professional life.

I would like to thank those who have become my family in Araraquara and who have given me the strength to carry on and never give up. To my friends Marina, Natália, Rafael, Péricles, Mariana and Bruna for their partnership. To the students I had the honor of helping Mariah, Bruno and Larissa.

A special thanks to two important friends I made during my doctorate, Guillherme Esquibola and Ewerton Mima, who have always supported me and whose friendship I would like to carry with me for the rest of my life.

To the friends I made in Angers, Shayan, Melina, Oksana, Cecile, Sebastian and Jaspe, who received me and helped me in some way to complete my thesis.

I would like to thank my professional colleagues, especially my supervisors, Leila Aparecida Chiavacci and Laurent Lemaire, who gave me a broad view of what it means to be a trained professional in the field I love to work. A thank to Isabelle for her support in the biological analyses, to Olivier for his teaching on nanomaterials and the use of the Liophilizer, and to Patrick for welcoming me to the INSERM laboratory.

I am grateful to the UNESP-Araraquara and University of Angers for their hospitality and support during my sandwich Ph.D. period. The experience and resources provided by both institutions were fundamental to the development of this work.

I also thank the CAPES PrInt Program (CAPES/PRINT - Edital nº 41/2017) for the financial support through the scholarship grant, which made my stay and research abroad possible. Without this support, the realization of this thesis would not have been possible.

This study was financed in part by the Coordenação de Aperfeiçoamento de Pessoal de Nível Superior - Brasil (CAPES) - Finance Code 001.

RESUMO

Devido à toxicidade associada a compostos inorgânicos como cádmio e gadolínio, a seleção de agentes de contraste para diagnóstico é crucial. Compostos à base de zinco e ferro surgiram como alternativas potenciais devido à sua abundância, baixo custo e baixa toxicidade. O óxido de zinco (ZnO) oferece alta luminescência devido ao seu alto rendimento quântico, enquanto o óxido de ferro (IO) exibe propriedades de relaxividade adequadas para ressonância magnética. Este projeto visa sintetizar e explorar as propriedades luminescentes e magnéticas de agentes de contraste à base de ferro e zinco para aplicações potenciais de imagem diagnóstica. Compostos incluindo ZnO, IO, cobre-índio-zinco-enxofre/sulfeto de zinco (CIS/ZnS) e óxido de zinco dopado com ferro (FeZnO) foram obtidos e incorporados em um copolímero de ácido poliláctico-glicólico (PLGA) visando aumentar a sua estabilidade em meios biológicos. A caracterização dos sistemas poliméricos foi realizada usando espalhamento dinâmico de luz (DLS) e microscopia eletrônica de transmissão (TEM). As propriedades ópticas foram examinadas por meio de espectros de absorção e fluorescência, enquanto as propriedades magnéticas foram quantificadas por meio de medidas de tempo de relaxação transversal e longitudinal. O primeiro sistema foi avaliado baseado em nanopartículas de PLGA, contendo ZnO e IO. Em uma proporção de PLGA:ZnO:IO de 10:6:1 foi possível obter um agente de contraste duplo com emissão em 540 nm ao ser excitado em 343 nm e um forte efeito T2 com uma relaxividade r2 de 171 mmol L^{-1} s^{-1} a 7 teslas. O tamanho das nanopartículas determinado por DLS foi de aproximadamente 200 nm com um PDI abaixo de 0,3, enquanto as partículas de ZnO e IO incorporadas tinham cerca de 4 nm e 8 nm, respectivamente. A investigação de um segundo agente de contraste envolvendo a dopagem das nanopartículas de ZnO com ferro revelou que uma concentração molar de Fe entre 0,1 e 1,0% e um tempo de adição de dopante de 30 minutos produziram material luminescente com emissão em 540 nm quando excitado a 343 nm, com tamanhos de nanopartículas de aproximadamente 4 nm. As propriedades magnéticas exibiram propriedades de relaxação T1 e T2, com uma relaxividade de r2 = 18,47 mmol L^{-1} s^{-1} e r1 = 1,79 mmol L^{-1} s^{-1} a 7T para a amostra FeZnO0.1. A investigação de um terceiro agente de contraste baseado em compostos de cobre-índio-zinco-enxofre revelou que as nanopartículas dopadas com Fe e sistemas núcleo-casca perderam suas propriedades de luminescência. No entanto, a coencapsulação de agentes

de contraste à base de cobre-índio-zinco-enxofre e óxido de ferro dentro do polímero PLGA resultou na produção de um sistema caracterizado por uma forte emissão a 650 nm ao ser excitado a 365 nm e 525 nm, bem como propriedades magnéticas exibindo um efeito T2 a 7T. No geral, este estudo destaca o potencial de agentes de contraste à base de ferro e zinco para aplicações de imagem diagnóstica.

Palavras-chave: zinco; ferro; luminescência; ressonância magnética; imagem biológica.

ABSTRACT

Due to the toxicity associated with inorganic compounds like cadmium and gadolinium, selecting contrast agents for diagnostics is crucial. Zinc- and iron-based compounds have emerged as potential alternatives due to their abundance, low cost, and low toxicity. Zinc oxide (ZnO) offers high luminescence due to its high quantum yield, while iron oxide (IO) exhibits relaxivity properties suitable for magnetic resonance imaging (MRI). This thesis aims to synthesize and explore the luminescent and magnetic properties of iron- and zinc-based contrast agents for potential diagnostic imaging applications. Compounds including ZnO, IO, copper-indium-zinc-sulfide/zinc sulfide (CIS/ZnS), and iron-doped zinc oxide (FeZnO) were obtained and incorporated into a poly(lactic-co-glycolic acid) (PLGA) copolymer to increase their stability in biological environments. The characterization of the polymer systems was carried out using dynamic light scattering (DLS) and transmission electron microscopy (TEM). Optical properties were examined through absorption and fluorescence spectra, while magnetic properties were quantified using transverse and longitudinal relaxation time measurements. The first system was evaluated based on PLGA nanoparticles containing ZnO and IO. With a PLGA:ZnO:IO ratio of 10:6:1, a dual contrast agent was obtained with emission at 540 nm when excited at 343 nm and a strong T2 effect with an r2 relaxivity of 171 mmol L^{-1} s^{-1} at 7 teslas. The size of the nanoparticles determined by DLS was approximately 200 nm with a PDI below 0.3, while the incorporated ZnO and IO particles were around 4 nm and 8 nm, respectively. Investigation of a second contrast agent involving doping ZnO nanoparticles with iron revealed that an iron molar concentration between 0.1% and 1.0%, and a dopant addition time of 30 minutes, produced luminescent material with emission at 540 nm when excited at 343 nm, with nanoparticle sizes of approximately 4 nm. The magnetic properties displayed both T1 and T2 relaxation characteristics, with r2 = 18.47 mmol L^{-1} s^{-1} and r1 = 1.79 mmol L^{-1} s^{-1} at 7T for the FeZnO0.1 sample. The investigation of a third contrast agent based on copper-indium-zinc-sulfide compounds revealed that Fe-doped nanoparticles and core-shell systems lost their luminescence properties. However, co-encapsulation of copper-indium-zinc-sulfide-based contrast agents and iron oxide within the PLGA polymer resulted in a system characterized by strong emission at 650 nm when excited at 365 nm and 525 nm, along with magnetic properties exhibiting a T2 effect at 7T. Overall, this

study highlights the potential of iron- and zinc-based contrast agents for diagnostic imaging applications.

Keywords: zinc; iron; luminescence; magnetic resonance imaging; biological imaging.

List of Figures

List of Tables

List of abbreviations

AE	-	Adverse Effects
CA	-	Contrast Agents
CNS	-	Central Nervous System
CT	-	Computed tomography
DDT	-	1-dodecanotiol
DCM	-	Dicloromethane
GI	-	Gastrointestinal
GPTMS	-	3-glycidoxypropyl)trimethoxysilane
IO	-	Iron Oxide
FeZnO	-	Iron-doped Zinc Oxide
Mf	-	Magnetic Field
Mm	-	Magnetic Moment
Mp	-	Magnetic Properties
Mr	-	Magnetic ressonance
MRI	-	Magnetic ressonance Imaging
NP	-	Nanoparticle
PLGA	-	Poly(lactic-co-glycolic acid)
PLGA:IO	-	PLGA + iron oxide NP
PLGA:ZnO	-	PLGA + zinc oxide NP
PLGA:FeZnO	-	PLGA + iron-doped Zinc Oxide NP
PLGA:ZnO:IO	-	PLGA + zinc oxide + iron oxide NP
QD	-	Quantum Dot
RT	-	Repetition time
RE	-	Echo time
SPION	-	Superparamagnetic Iron Oxide Nanoparticle
TEM	-	Transmission electron microscopy
T1	-	Spin-lattice relaxation
T2	-	Spin-spin relaxation

ZnO - Zinc oxide

Summary

INTRODUCTION

INTRODUCTION

Cancer represents a significant challenge to global public health. In 2022, approximately 20 million new cases of cancer were reported worldwide, with 9.7 million cancer-related deaths (BRAY BSC et al., 2024). Efforts in cancer prevention are essential for reducing the overall disease burden. Additionally, early detection holds critical importance in improving treatment efficacy and bolstering survival rates (SRINIVASA; SRINIVASA, 2023; VITORINO et al., 2023).

Diagnosing cancer in its early stages plays a fundamental role in effective treatment, allowing for a more favourable prognosis of the disease (PULUMATI et al., 2023). When cancer is identified early stages, treatment options are broader and less invasive, preventing it from spreading to other parts of the body, thereby increasing the chances of cure, and reducing the morbidity associated with treatment (PRIYADHARSHINI et al., 2023; TOBORE, 2020). Additionally, early cancer diagnosis enhances patients' quality of life. By being diagnosed and treated early, patients have access to appropriate medical and supportive interventions from the outset, which can help mitigate the side effects of treatment (WHITAKER, 2020).

Imaging techniques play an important role in cancer diagnosis, allowing for a detailed assessment of the body's internal structures. Among these techniques, we can mention radiography, computed tomography (CT), magnetic resonance imaging (MRI), and ultrasonography (BARENTSZ et al., 2016). X-rays are widely used due to their availability and speed, although they have limitations in detecting certain types of cancer and may involve exposure to ionizing radiation (FASS, 2008). On the other hand, CT provides detailed images and is effective in detecting tumors and metastases, but repeated use may pose risks due to radiation exposure (POWER et al., 2016). Meanwhile, ultrasound imaging, although safe and widely available, has limitations in visualizing deep structures (TENAJAS et al., 2023). On the other hand, MRI provides excellent soft tissue details with high resolution without using ionizing radiation, although they are more expensive and less accessible (ARNOLD et al., 2023). Additionally, MRI can be used to assess tumor response to treatment and monitor patient progress over time (LAU; CORRIE; GALLAGHER, 2022).

The fluorescence technique is another option that can be used as an imaging method for cancer diagnosis. Fluorescence is often employed in conjunction with contrast agents (CAs) that emit light when excited by a specific energy source. These CAs can be targeted to specific cancer cells or biological markers, allowing direct visualization of the tumor during surgical procedures or imaging exams (HELLEBUST; RICHARDS-KORTUM, 2012). Fluorescence offers high sensitivity and specificity, as well as real-time imaging, which can facilitate early detection of cancerous lesions and guidance during tumor removal surgery (MONDAL et al., 2014).

CAs are widely employed in medical imaging exams to enhance the visibility of anatomical structures and physiological processes. Among the most used are iodinated CAs and barium CAs, often utilized in CT to highlight vascular and abdominal structures, respectively (LUSIC; GRINSTAFF, 2013). They offer rapid availability and the ability to provide high-resolution images in a short amount of time. However, they carry the risk of allergic reactions, especially in patients sensitive to iodine, and the potential for adverse effects (AE) on the kidneys, particularly in patients with renal dysfunction (CHIU; CHU, 2022; “HEALTH EFFECTS - Toxicological Profile for Barium and Barium Compounds - NCBI Bookshelf”, [s.d.]; “Intravenous Radiocontrast Media: A Review of Allergic Reactions”, [s.d.]). Paramagnetic CAs, such as gadolinium-based CAs (GBCAs), are widely used in MRI to enhance images of organs and soft tissues, providing greater contrast in areas where they accumulate, however, the potential risk of gadolinium toxicity is a disadvantage in the use of this CA (IYAD et al., 2023).

The combination of two imaging diagnostic techniques using CAs offers significant advantages. Integrating different imaging modalities, such as fluorescence imaging and MRI, can provide complementary information about a particular pathology, allowing for a more comprehensive and accurate assessment (LI et al., 2019; MULDER et al., 2007). While fluorescence imaging is excellent for visualizing cellular and molecular structures based on light emission (ACUÑA-RODRIGUEZ; MENA-VEGA; ARGÜELLO-MIRANDA, 2022), MRI is a technique more effective, radiation-free, non-invasive imaging that provides three-dimensional (3D) visualization of tissues (FLORKOW et al., 2022). Additionally, the combination of imaging techniques can increase the sensitivity and specificity of diagnosis, enabling early

detection of lesions and abnormalities that may not be identified by a single imaging modality (MORATO et al., 2021).

Quantum dots (QDs) are semiconductor nanomaterials that exhibit unique optical properties, making them promising CAs in medical imaging (MATEA et al., 2017). Among the most used semiconductor QDs are cadmium sulfide (CdS) (GHASEMPOUR et al., 2023), cadmium selenide (CdSe) (HSU et al., 2023), and indium arsenide (InAs) (BAHMANI JALALI et al., 2022). These materials offer high quantum efficiency and light emission across a broad spectral range, making them ideal for biomedical imaging applications.

Although quantum dots (QDs) present promising properties in medical imaging, their application also poses significant challenges. For example, studies have shown that certain cadmium QDs may exhibit toxicity, raising concerns about their biological safety, and health risks due to potential cadmium ion release in biological environments (HU; ZHONG; HE, 2021). Furthermore, the persistence of these QDs in the body has also been documented, with studies demonstrating their accumulation in tissues over time, as observed in experiments with mice (LIU et al., 2011; LU et al., 2016; TANG et al., 2013). Another concern is the potential interaction of QDs with biological components such as proteins and enzymes, which may affect normal cellular function and compromise the validity of biological experiments. For example, cellular imaging studies have revealed that certain QDs can induce oxidative stress and DNA damage in human cells, emphasizing the need for careful assessment of their biocompatibility (FANG; TANG, 2024; ZHANG et al., 2015).

Zinc oxide (ZnO) and iron oxide (IO) emerge as highly promising compounds in the field of diagnostic imaging. With their distinct luminescent and magnetic properties (MP), respectively, these compounds offer significant potential to enhance medical imaging techniques. For example, ZnO can be used as a CA in fluorescence-based imaging, standing out for its high colloidal stability and strong luminescent emission (ZHANG; XIONG, 2015).

On the other hand, IO is widely employed in MRI due to its ability to alter tissue relaxation times, providing high-resolution and high-contrast images (RAHMAN, 2023). Iron oxide nanoparticles induce magnetic effects when an external magnetic field is applied. Due to their superparamagnetic properties, these nanoparticles predominantly

exhibit spin-spin (T2) magnetic relaxation. This results in enhanced T2 contrast in magnetic resonance imaging (MRI). The superparamagnetism of the iron oxide nanoparticles allows for better image resolution and contrast in T2-weighted MRI scans, making them highly effective as contrast agents.

Incorporating iron (Fe) and zinc (Zn)-based polymeric systems opens a vast field of possibilities in the development of CAs for diagnostic imaging. The combination of these elements in polymeric systems offers several advantages, such as enhanced colloidal stability, biocompatibility, and vectorization capability. For example, the use of polymers like poly(lactide-co-glycolide) (PLGA) as a matrix for nanoparticles (NPs) allows for the controlled delivery and increasing their efficacy and minimizing toxicity. Additionally, the presence of the polymer can improve the dispersion of NP in the biological medium, facilitating their interaction with target cells.

PLGA facilitates dispersion in biological media due to its biocompatibility and biodegradability, which enhance its interaction with biological tissues. Its hydrophilic and hydrophobic balance allows for better solubility and stability in aqueous environments. Moreover, PLGA nanoparticles can be engineered to have surface modifications that improve their dispersibility and reduce aggregation. This results in more uniform distribution and controlled release of encapsulated drugs or agents, making PLGA an ideal material for biomedical applications (DING; ZHU, 2018).

The CIS/ZnS compound, a combination of copper, indium, sulfur, and zinc sulfide, emerges as effective option for fluorescence imaging applications (CHOI et al., 2015; DENG et al., 2012; LV et al., 2016). Its optical properties, such as high luminescence and colloidal stability, can be notice it as a promising alternative to traditional CAs. When excited by an appropriate energy source, CIS/ZnS emits visible light and near-red wavelength, offering a valuable tool for studies in cell biology and medical diagnosis (LV et al., 2016).

The objective of this study was to synthetize iron and zinc based NPs exhibiting robust visible emission and enhanced MPs, while ensuring stability in biological environments. This was achieved through surface modification techniques or integration into polymeric nanosystems, aimed at enhancing their suitability for bioimaging applications. This thesis has been divided into 4 important chapters.

The first part (Chapter III) discussed the incorporation of ZnO and IO nanosystem coated with oleic acid for incorporation into a polymeric system. The NPs were coated with oleic acid for possible dispersion in an organic solvent, and it was possible to proceed with the synthesis of polymers containing both particles using a simple emulsion and solvent evaporation method. At this stage, the appropriate proportions for suitable luminescence and MRI between the QDs were studied. Infrared, absorbance, fluorescence (excitation and emission), MRI, and transmission electron microscopy (TEM) techniques were used to characterize the samples.

In Chapter IV, the combination of both elements in the same compound was investigated. A doping method was used in which ZnO NPs were doped with iron ions and the luminescent and MPs of this material were verified. Previously, the ZnO materials studied were evaluated by modifying them with a silane-based compound, GPTMS, which ensured suitable dispersion in water. The same material was used to modify the surface of the iron-doped zinc oxide NPs (FeZnO NPs). These NPs were also modified with oleic acid for incorporation into polymeric particles.

It is known that ZnO produced with a size of 4 nm has a suitable luminescence at a wavelength of 540 nm and that the excitation range of this compound is up to 350 nm, which can pose some risks for diagnostic imaging. Therefore, in Chapter V, another component based on CIS/ZnS was studied, which has a suitable emission in the orange region, around 630 nm, and an excitation wavelength in the region of 525 nm. This compound and the IO were incorporated into polymer particles for possible use in bimodal imaging.

The Chapter VI closes with preliminary studies of cytotoxicity assays and cellular uptake using THP-1 cells, phagocytes with efficient uptake capacity, which were investigated with molecules discussed in previous chapters.

REFERENCES

ACUÑA-RODRIGUEZ, J. P.; MENA-VEGA, J. P.; ARGÜELLO-MIRANDA, O. Live-cell fluorescence spectral imaging as a data science challenge. **Biophysical Reviews**, v. 14, n. 2, p. 579, 2022.

ARNOLD, T. C. et al. Low-field MRI: Clinical promise and challenges. **Journal of Magnetic Resonance Imaging**, v. 57, n. 1, p. 25, 2023.

BAHMANI JALALI, H. et al. Indium arsenide quantum dots: an alternative to lead-based infrared emitting nanomaterials. **Chemical Society Reviews**, v. 51, n. 24, p. 9861–9881, 2022.

BARENTSZ, J. et al. Commonly Used Imaging Techniques for Diagnosis and Staging, v. 24, n. 20, p. 3234–3244, 2016.

BRAY BSC, F. et al. Global cancer statistics 2022: GLOBOCAN estimates of incidence and mortality worldwide for 36 cancers in 185 countries. CA: A Cancer Journal for Clinicians, 2024.

CHIU, T. M.; CHU, S. Y. Hypersensitivity Reactions to Iodinated Contrast Media. **Biomedicines**, v. 10, n. 5, 2022.

CHOI, H. S. et al. Highly luminescent, off-stoichiometric Cu x In y S 2 /ZnS quantum dots for near-infrared fluorescence bio-imaging. **RSC Advances**, v. 5, n. 54, p. 43449–43455, 2015.

DING, D.; ZHU, Q. Recent advances of PLGA micro/nanoparticles for the delivery of biomacromolecular therapeutics. **Materials Science and Engineering: C**, v. 92, p. 1041–1060, 2018.

DENG, D. et al. High-quality CuInS 2/ZnS quantum dots for in vitro and in vivo bioimaging. **Chemistry of Materials**, v. 24, n. 15, p. 3029–3037, 2012.

FANG, Q.; TANG, M. Oxidative stress-induced neurotoxicity of quantum dots and influencing factors, 2024.

FASS, L. Imaging and cancer: A review. **Molecular Oncology**, v. 2, n. 2, p. 115, 2008.

FLORKOW, M. C. et al. Magnetic Resonance Imaging Versus Computed Tomography for Three-Dimensional Bone Imaging of Musculoskeletal Pathologies: A Review. **Journal of Magnetic Resonance Imaging**, v. 56, n. 1, p. 11, 2022.

GHASEMPOUR, A. et al. Cadmium Sulfide Nanoparticles: Preparation, Characterization, and Biomedical Applications. **Molecules**, v. 28, n. 9, 2023.

HEALTH EFFECTS - Toxicological Profile for Barium and Barium Compounds - NCBI Bookshelf. Available in: <https://www.ncbi.nlm.nih.gov/books/NBK598777/>. Acess in: 15 abr. 2024.

HELLEBUST, A.; RICHARDS-KORTUM, R. Advances in molecular imaging: targeted optical contrast agents for cancer diagnostics. v. 7, n. 3, p. 429–445, 2012.

HSU, J. C. et al. Nanomaterial-based contrast agents. **Nature Reviews Methods Primers 2023** 3:1, v. 3, n. 1, p. 1–21, 2023.

HU, L.; ZHONG, H.; HE, Z. Toxicity evaluation of cadmium-containing quantum dots: A review of optimizing physicochemical properties to diminish toxicity. **Colloids and Surfaces B: Biointerfaces**, v. 200, p. 111609, 2021.

Intravenous Radiocontrast Media: A Review of Allergic Reactions. Available in: <https://www.uspharmacist.com/article/intravenous-radiocontrast-media-a-review-of-allergic-reactions>. Acess in: 15 abr. 2024.

IYAD, N. et al. Gadolinium contrast agents- challenges and opportunities of a multidisciplinary approach: Literature review. **European Journal of Radiology Open**, v. 11, p. 100503, 2023.

LAU, D.; CORRIE, P. G.; GALLAGHER, F. A. MRI techniques for immunotherapy monitoring. **Journal for ImmunoTherapy of Cancer**, v. 10, n. 9, p. e004708, 2022.

LI, H. et al. Bimodal Fluorescence-Magnetic Resonance Contrast Agent for Apoptosis Imaging. **Journal of the American Chemical Society**, v. 141, n. 15, p. 6224–6233, 2019.

LIU, W. et al. CdSe Quantum Dot (QD)-Induced Morphological and Functional Impairments to Liver in Mice. **PLOS ONE**, v. 6, n. 9, p. e24406, 2011.

LU, Y. et al. CdSe/ZnS quantum dots induce hepatocyte pyroptosis and liver inflammation via NLRP3 inflammasome activation. **Biomaterials**, v. 90, p. 27–39, 2016.

LUSIC, H.; GRINSTAFF, M. W. X-Ray Computed Tomography Contrast Agents. **Chemical reviews**, v. 113, n. 3, p. 1641–1666, 2013.

LV, G. et al. Near-Infrared Emission CuInS/ZnS Quantum Dots: All-in-One Theranostic Nanomedicines with Intrinsic Fluorescence/Photoacoustic Imaging for Tumor Phototherapy. **ACS Nano**, v. 10, n. 10, p. 9637–9645, 2016.

MATEA, C. T. et al. Quantum dots in imaging, drug delivery and sensor applications. **International Journal of Nanomedicine**, v. 12, p. 5421, 2017.

MONDAL, S. B. et al. Real-Time Fluorescence Image-Guided Oncologic Surgery. **Advances in Cancer Research**, v. 124, p. 171–211, 2014.

MORATO, Y. L. et al. Recent Advances in Multimodal Molecular Imaging of Cancer Mediated by Hybrid Magnetic Nanoparticles. **Polymers**, v. 13, n. 17, 2021.

MULDER, W. J. M. et al. Magnetic and fluorescent nanoparticles for multimodality imaging, v. 2, n. 3, p. 307–324, 2007.

POWER, S. P. et al. Computed tomography and patient risk: Facts, perceptions and uncertainties. **World Journal of Radiology**, v. 8, n. 12, p. 902, 2016.

PRIYADHARSHINI, N. et al. A novel hybrid Extreme Learning Machine and Teaching–Learning-Based Optimization algorithm for skin cancer detection. **Healthcare Analytics**, v. 3, p. 100161, 2023.

PULUMATI, A. et al. Technological advancements in cancer diagnostics: Improvements and limitations. **Cancer Reports**, v. 6, n. 2, 2023.

RAHMAN, M. Magnetic Resonance Imaging and Iron-oxide Nanoparticles in the era of Personalized Medicine. **Nanotheranostics**, v. 7, n. 4, p. 424, 2023.

SRINIVASA, J.; SRINIVASA, F. K. Emerging Strategies in Cancer Prevention: Focus on Targeted Interventions and Lifestyle Modifications. **Journal of Oncology Research**, v. 5, n. 2, 2023.

TANG, Y. et al. The role of surface chemistry in determining in vivo biodistribution and toxicity of CdSe/ZnS core–shell quantum dots. **Biomaterials**, v. 34, n. 34, p. 8741–8755, 2013.

TENAJAS, R. et al. Recent Advances in Artificial Intelligence-Assisted Ultrasound Scanning. **Applied Sciences 2023**, v. 13, n. 6, p. 3693, 2023.

TOBORE, T. O. On the need for the development of a cancer early detection, diagnostic, prognosis, and treatment response system. **Future Science OA**, v. 6, n. 2, 2020.

VITORINO, R. et al. Diagnostic and monitoring applications using near infrared (NIR) spectroscopy in cancer and other diseases. **Photodiagnosis and Photodynamic Therapy**, v. 42, p. 103633, 2023.

WHITAKER, K. Earlier diagnosis: the importance of cancer symptoms. **The Lancet Oncology**, v. 21, n. 1, p. 6–8, 2020.

ZHANG, T. et al. Threshold Dose of Three Types of Quantum Dots (QDs) Induces Oxidative Stress Triggers DNA Damage and Apoptosis in Mouse Fibroblast L929 Cells. **International Journal of Environmental Research and Public Health 2015**, v. 12, n. 10, p. 13435–13454, 2015.

ZHANG, Z. Y.; XIONG, H. M. Photoluminescent ZnO Nanoparticles and Their Biological Applications. **Materials**, v. 8, n. 6, p. 3101, 2015.

OBJECTIVE

The objective of this thesis was to develop bimodal contrast agents based on iron and zinc quantum dots for simultaneous use in magnetic resonance imaging (MRI) and luminescence imaging techniques. To achieve this, the contrast agents needed to be incorporated into a polymeric system designed to optimize performance under biological conditions.

CHAPTER I

LITERATURE REVIEW

CHAPTER I. LITERATURE REVIEW

The development of research on contrast agents (CA) for medical diagnostics are discussed, with a focus on the relevance of zinc and iron-based compounds as promising alternatives to traditional inorganic CA.

1.1 CONTRAST AGENTS: BIOAVAILABILITY AND TOXICITY

CAs are chemical substances used in medical imaging procedures to enhance the visualization of tissues, organs, and internal structures of the human body. They play an important role in diagnosis by providing information to identify diseases, injuries, and anomalies with greater accuracy (Wallyn et al., 2019).

The main function of CAs is to enhance the differences in density, chemical composition, or physical characteristics among different tissues or bodily fluids. This is achieved because these agents have properties that make them visible in certain imaging modalities, such as magnetic resonance imaging (MRI) (Caspani et al., 2020), X-ray computed tomography (CT) (Aslan et al., 2020), fluorescence optical imaging (Huang et al., 2020), and radiography (De La Vega & Häfeli, 2015).

MRI is a widely used imaging technique due to its excellent soft tissue contrast and high spatial resolution, without exposure to ionizing radiation (Mukhatov et al., 2023). However, inorganic CAs, primarily gadolinium chelates, have limitations such as short circulation in the body and relatively low proton relaxation efficiency. Administration of these agents at high doses can be harmful, leading to potential AE, such as nephrogenic systemic fibrosis syndrome (Ni et al., 2017).

Although widely used in various clinical applications, such as imaging of lesions in the central nervous system (CNS), breast, and abdomen, gadolinium-based agents represent most commercially available products. However, the limited availability of CA options for specific areas, such as angiographic or liver imaging, underscores the ongoing need for the development and enhancement of safe and effective CAs (Wahsner et al., 2019).

The most common CAs in MRI are small molecule gadolinium (Gd(III)) complexes. Some examples include agents intended for imaging lesions in the central

nervous system (CNS), such as Gd-EOB-DTPA, and agents for liver imaging, like the Mn(II) complex (Mn-DPDP). Other options include agents for angiography (blood vessels), such as the Gd(III) complex MS-325, a superparamagnetic iron oxide nanoparticle (SPION) formulation for liver imaging (ferumoxide), and an oral SPION formulation for gastrointestinal (GI) imaging (ferumoxsil) (Wahsner et al., 2019).

Similarly, inorganic CAs used in CT can enhance the visibility of certain structures or processes within the body, making them more distinguishable from surrounding areas in imaging studies (Attia et al., 2018). Several metallic NPs are used as CAs in CT, including bismuth, tungsten, tantalum, yttrium, and gadolinium NPs. These NPs can be coated with organic molecules or functionalized with antibodies to improve their effectiveness. Additionally, alternative metallic NP like silver, iron, platinum, lead, and copper are also employed in studies of CT Imaging (Aslan et al., 2020b).

Suspensions of barium sulphate and water-soluble aromatic iodinated compounds are the most used CAs in CT. However, due to the inherent toxicity of Ba^{2+} ions, the use of barium sulphate is restricted to GI imaging. Additionally, while iodinated agents are generally considered safe, severe AE sometimes occur due to their high osmolarity and viscosity (Lee et al., 2013). This potential toxicity highlights the importance of developing new and safer CAs.

Fluorescence imaging offers high resolution and sensitivity, but its application *in vivo* imaging has been limited by the limited penetration of light into tissues and the reduction in spatial resolution due to light scattering (Musnier et al., 2021; Wegner & Hildebrandt, 2015). Recent advances have shown promise in generating emission light with shorter wavelengths, thereby improving tissue penetration depth (Fan et al., 2023). Multicolor absorption based on inorganic NP such as semiconductor quantum dots (QDs) offers enhanced resistance to photobleaching, high brightness and allows for tuning of the emission spectra (Rizvi et al., 2010; Wagner et al., 2019).

However, concerns about the toxicity of cadmium-containing QDs have led to the exploration of cadmium-free alternatives. The release of Cd2+ and the formation of reactive oxygen species (ROS) are generally recognized as the primary causes of cytotoxicity (Mo et al., 2017). New NPs demonstrate low toxicity and improved tissue

penetration, making them promising candidates for safer and more efficient bioimaging, such as InP/ZnS and CuInS2/ZnS NPs.

I.2 NANOMATERIALS: LUMINESCENCE AND MAGNETIC PROPERTIES

The physicochemical properties of semiconductor materials are size-dependent. In addition, the shape and the interactions and arrangement of atoms between the nanomaterials can also promote the physicochemical properties of the material (KHAN, SAEED, KHAN, 2019). Two main properties are studied in this work: a) the luminescence properties of semiconductor materials described in section I.2.1; and b) the paramagnetic properties of metallic materials described in section I.2.2.

I.2.1 Luminescence Proprieties

Certain materials, when excited by an external source like electrons or light, can emit light in a specific wavelength and this phenomenon is known as luminescence (“Fundamentals of luminescence”, 2022). Luminescence includes two distinct processes: fluorescence and phosphorescence, which differ in their emission timescales. Fluorescence occurs when light is emitted almost immediately after excitation, typically within nanoseconds to microseconds, while phosphorescence involves a delayed emission due to a change in the electron's spin state, leading to longer emission timescales ranging from milliseconds to minutes (MCGOWN; NITHIPAHKOM, 2000). Some materials become luminescent when they are in the form of nanomaterials (WOLFBEIS, 2015). Luminescence is useful for studying the electronic structure of a material. It gives information not only about the conduction and valence band transitions, but also about the localised state due to impurities or dopants (CAPELLETTI, 2005).

The luminescence of the material can be explained by the Jablonski diagram (**Figure I.3**) (SO; DONG, 2002). The electron orbitals are represented by electronic energy levels (S0, S1, S2), also called vibrational levels. For an electron to move between energy levels, the energy of light is used via the photon energy. The electron moves from the ground state S0 to the vibrational levels (S1, S2...) when it is excited. There is an energy level absorption when the electron is excited. Then there is an internal conversion of energy levels, where the electron goes from the S2 state to S1,

and finally the electron stops from the vibrational state S1 to the ground state S0, releasing energy in the form of 1 photon, thus creating the fluorescence effect. This process takes place in milliseconds. The absorption energy when the electron is excited is much higher than the fluorescence emission energy. Therefore, the excitation wavelength (higher energy) is much shorter than the emission wavelength (lower energy).

Figure I. 1 Jablonsk diagram.

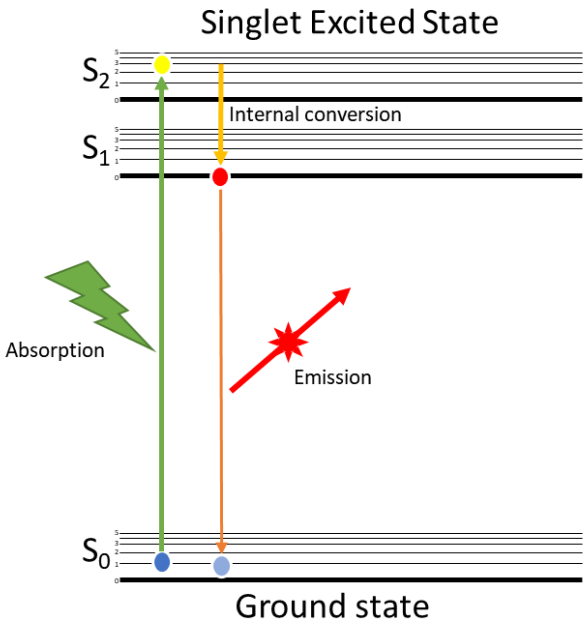

Source: Adapted from ISLER et al. (2018).

In semiconductor materials, when the electron in the valence band is excited, it moves to the conduction band, leaving behind a hole. The resulting electron-hole pair can be considered a quasi-NP, also known as an exciton (SMITH, NIE, 2010). The number of excitons formed affects the intensity of emitted light. The more excitons are formed, the higher the intensity of the light that can be emitted (KOCH et al., 2006). An energy diagram (**Figure I.4**) is used to visualize the different energy bands in a material, such as the valence and conduction bands in a semiconductor, and the gap between them, known as the "band gap" (ABDELHAMID, O'MULLANE, SNOOK, 2015).

Figure I. 2 Energy level diagram.

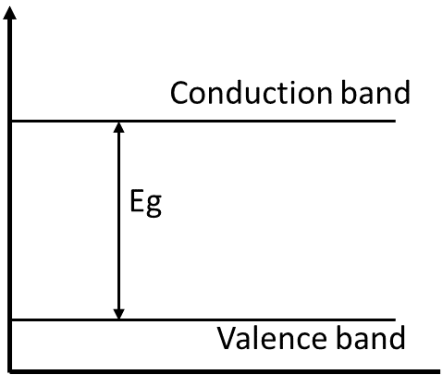

Source: Adapted from Abdelhamid et al. (2015)

The energy gap (Eg) can be defined as the energy required to create a free electron and a free hole. The size of the exciton is often comparable to the size of a NP. The size of the exciton can be calculated, depending on factors such as the electron and hole masses, the dielectric constant of the semiconductor material (E) and the energy gap Eg itself (BRUS, 1984). This allows a correlation to explain the dependence of the particle size on the variation of the gap energy (**Figure I.3**).

Figure I.3. Variation of the gap energy as a function of particle size.

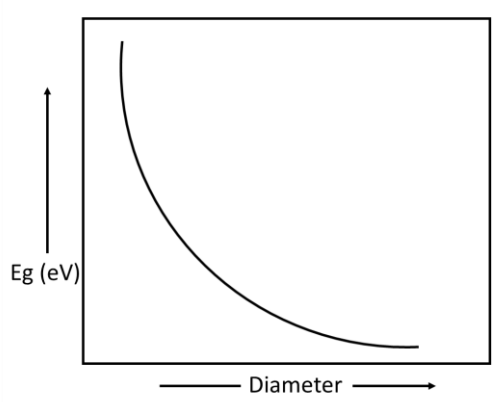

Source: Adapted from Brus (1984).

I.2.2 Magnetic Properties of Superparamagnetic Materials

Every metallic particle has a specific magnetic moment (Mm). The Mm is created by the magnetic field (Mf) around a moving charge. The application of a Mf changes the spin and orbital motion of the electrons (KRISHNAN, 2016; MORTON,

2012). This will be explained in more detail in Session I.4.2. Depending on the material, the response to external Mf can vary, creating different types of magnetic materials, classified as diamagnetic, paramagnetic, ferromagnetic, antiferromagnetic and ferrimagnetic.

Ferromagnetic and paramagnetic materials are highlighted in this context because IO, a superparamagnetic substance, is used in MRI and relates to these terms. Paramagnetic materials possess random Mm, resulting in zero magnetism in the absence of an applied Mf. However, when an external Mf is introduced, the Mm align with the field's direction, thereby exhibiting magnetic susceptibility (MORTON, 2012; KRISHNAN, 2016).

Ferromagnetic materials, on the other hand, have regions of many atoms, ions or molecules with permanent Mm, in which their Mm is oriented in the same direction. They are materials that exhibit spontaneous magnetisation and hysteresis loop behaviour when a Mf is applied (MORTON, 2012; KRISHNAN, 2016).

Ferromagnetic materials have domains of magnetisation, which can be single domain or multiple domains. In a single domain, all the spins of the atom are aligned in the same direction, as in paramagnetic materials (STEWART, 1954).

Magnetic NPs exhibit the preferential formation of single domains (DÍEZ et al., 2022). These materials do not exhibit coercivity and hysteresis loops like ferromagnetic materials. Because they exhibit a Mm in a single direction when a Mf is applied, like paramagnetic materials, they are classified as superparamagnetic materials.

I.3 IMAGING DIAGNOSTICS: FLUORESCENCE AND MAGNETIC RESONANCE IMAGING

The imaging of tissues or organs is based on the physicochemical properties of matter, and that the use of specific compounds can significantly enhance image resolution. In the medical field, improved image resolution can facilitate diagnosis and thereby contribute to the treatment of specific diseases (AVASTHI et al., 2020).

The field of pharmaceutical sciences also encompasses the study of particles with significant properties that aid in visualizing the diagnosis of diseases, such as

cancer. To support the advancement of this field, several reviews have been conducted to explore and develop new CAs (CHINEN et al., 2015; ESTELRICH, SÁNCHEZ-MARTÍN, BUSQUETS, 2015; JENKINS, BURDETTE, FOULGER, 2016; AVASTHI et al., 2020).

There are various types of diagnostic imaging, and this thesis will focus on two specific techniques that employ NP. The techniques in question are Fluorescent Imaging and MRI.

I.3.1 Fluorescence Imaging System

Fluorescence refers to the emission of light by a molecule in all directions (LICHTMAN, CONCHELLO, 2005). However, the fluorescence characteristics of a molecule can be influenced by various factors, including the surrounding environment, particularly by the polarity, viscosity, pH, and temperature (QIN et al., 2021). These environmental factors determine the intensity and wavelength of the emitted light, with certain conditions potentially enhancing or diminishing the fluorescence (SCHULMAN; DI; JUCHUM, 1999).

The maximum emission wavelength is usually longer than the maximum excitation wavelength in fluorescent materials. This difference between the emission and excitation wavelengths is called Stoke's shift (ZHU et al., 2017). The range of wavelengths that can excite a molecule is known as the absorption spectrum, while the range of wavelengths emitted is referred to as the emission spectrum (BERLMAN,1971). These spectra are essential for choosing the appropriate excitation and emission filters in a fluorescence instrument. By narrowing the excitation and emission wavelengths, image quality can be improved, which is particularly beneficial for diagnostic purposes (SANDERSON et al., 2014).

Due to exceptional properties of QDs such as high luminescence, resistance to photodegradation, high quantum yield and size-dependent tunability of the emission wavelength, have been widely used for a variety of applications in the last decades (BAILEY, SMITH, NIE, 2004; DEL ROSAL et al., 2017; REN et al., 2022). QDs have already been successfully used as luminescent CAs in vivo, demonstrating their ability to monitor various processes at the cellular level (ZDOBNOVA, LEBEDENKO, DEYEV, 2011; DEL ROSAL et al., 2017).

I.3.2 Magnetic Resonance Imaging (MRI)

One of the techniques used in this thesis is MRI, which promotes topographic images with deep penetration, suitable resolution and high contrast of soft tissues (PINHO et al., 2019). It is a safe diagnostic imaging modality that does not involve ionising radiation and is based on the hydrogens of water molecules (DILL, 2008).

MRI combines the Mf of a machine with the hydrogen protons in human tissue to create a modified radio frequency that can be captured and converted into an image (MAZZOLA, 2009). The phenomenon of Mr is due to an interaction between the atom and an external Mf, in which the particles have a Mm that exhibits a moment of precession under a Mf (MAZZOLA, 2009; CHIZHIK et al., 2014).

A spherical particle, such as a proton, has a movement around its axis called spin. This spin can rotate in two different directions, called +1/2 and -1/2. The same particle has a charge which, when it moves, creates a Mf. This Mf is usually represented by a vector. The human body, at a temperature of 36.5°C, without the action of a Mf, presents random Mf vectors of its atoms. In a Mf of 1.5 T, for example, these vectors point in the same direction, but in the case of the atom, they can point parallel or anti-parallel to the Mf, depending on the energy state of these spins (parallel for higher energy, anti-parallel for lower energy) (MAZZOLA, 2009). Another important movement to study is precession, which depends on the frequency of the applied Mf. When a field is applied, the sum of the parallel and anti-parallel spins is important for vectorisation in a single direction, creating the conditions for image intensity.

In relation to radio frequency (RF) fields, an electric current is applied by a short duration RF pulse, creating a Mf with a direction of 90° or 180° relative to the source Mf. The amplitude of the signal increases due to the distortion of the resulting Mm. When the RF field is removed, the signal amplitude decreases for a period of time, also known as the relaxation process, and the Mm tends to return to its equilibrium (MAZZOLA, 2009; LEE et al., 2021). The return of the Mm of the spins to the same direction for a relaxation time is called free induction decay (FID) (MAZZOLA, 2009; PAI et al., 2023).

The relaxation of the spins that generates FID is formed by the exchange of energy through two relaxation processes, called longitudinal and transverse relaxation,

which describe the time constants T1 and T2, respectively. The longitudinal relaxation process (T1), which refers to the reduction of magnetisation in the longitudinal plane, is given by the interaction of the spins with the lattice, while the transverse relaxation process, which refers to the reduction of magnetisation in the transverse plane, is given by the spin-spin interaction (MAZZOLA, 2009; PAI et al., 2023).

Another important phenomenon of MRI is the spin echo. Where a first RF pulse is emitted with the appearance of the first FID signal. A second RF pulse is sent after time t, a second signal appears at time 2 t. This means that the echo time can be controlled for signal analysis. The echo time (TE) is the time from the first signal to the echo signal (2 t) and the repetition time (TR) is the time between two RF pulses. TE determines how much relaxation is present in the echo in the longitudinal plane, and TR determines how much magnetisation has recovered between successive pulses (MAZZOLA, 2009; LUGAUER, WETZL, 2018).

The Mf used for diagnosis has a strength of 0.5, 1.5 and 3 Tesla (T), which can affect image contrast. A strong Mf improves image resolution and reduces acquisition time. On the other hand, a strong Mf is also more prone to the appearance of artefacts in the image (GROVER et al., 2015).

This can be used to calculate the T_1 or T_2 relaxation time, which provides contrast images of human tissue. For compounds used in diagnostic imaging, the quality of CAs is characterised by their relaxivity. Relaxivity is the degree to which the CA can enhance the relaxation rate of water and is expressed as a longitudinal relaxation rate constant, represented by $R_1 = 1/T_1$ in seconds^{-1}, and a transverse relaxation rate constant, represented by $R_2 = 1/T_2$ in seconds^{-1}. This is used to calculate the longitudinal (r_1) and transverse (r_2) relaxivity as a function of concentration in mmoL. If a CA has a higher relaxivity, the higher the contrast will be at low concentrations, which can offer lower toxicity impact on the human body (JACQUES et al., 2010).

I.4 NANOPARTICLES OF IRON AND ZINC

The NPs chosen for this work have been designed based on results previously presented by the research group. They are inorganic compounds with high fluorescence emission capacity and low toxicity. Iron is introduced to exploit the Mp of the material. The compounds used were ZnO, IO, a study of FeZnO and a study of CIS/ZnS QDs.

I.4.1 Zinc oxide quantum dots

ZnO is commonly found in the form of a white crystalline solid and most often exhibits a wurtzite crystal structure. In its wurtzite structure, characterized by a hexagonal arrangement of atoms, each zinc atom is surrounded by four oxygen atoms, forming a tetrahedral configuration, while each oxygen atom is similarly surrounded by four zinc atoms. Apart from the wurtzite structure, ZnO can also exist in other crystalline forms, such as sphalerite (or cubic zinc blende) and rock salt structures, though these are less common (RAHA, AHMARUZZAMAN, 2022).

The crystal configuration of ZnO imparts unique properties, such as semiconductor material, piezoelectricity, and luminescence, making it valuable for a range of industrial, electronic, optical, and biomedical applications (BORYSIEWICZ, 2019). It is commonly used in sunscreens and correlated products (GUEDENS et al., 2014; KIM et al., 2017), and electronic components like light-emitting diodes (LEDs) (RAHMAN, 2019). Additionally, ZnO has been investigated for its potential in CAs and bioimaging due to its luminescent properties, compatibility with living organisms, and additional benefits such as anticancer and antibacterial activity (JIANG, PI, CAI, 2018).

Intrinsic luminescence in ZnO refers to the emission of light resulting from processes directly related to the fundamental properties of the material, without the need for doping or external additives. This type of luminescence occurs due to electronic transitions between the conduction band and the valence band, or from intrinsic defects within the crystal structure (LIMA et al., 2001).

Band-to-band luminescence occurs when an electron in the conduction band returns to the valence band, releasing energy in the form of ultraviolet (UV) light. This direct transition typically leads to the emission of light at around 380 nm, which is characteristic of ZnO due to its wide band-gap of approximately 3.37 eV (RAJI, GOPCHANDRAN, 2017).

In addition to band-to-band transitions, luminescence can also occur due to structural defects or impurities in the ZnO crystal. Defects such as oxygen vacancies (Vo) and zinc interstitials (Zn_i) can create intermediate energy levels within the bandgap, leading to visible light emission at various wavelengths (CAMARDA et al., 2016; GURYLEV, PERNG, 2021). The luminescence resulting from these defects can occur in yellow/orange range, depending on the type and concentration of the defects (LV, LI, CHAI, 2019).

The size of NP plays a significant role in determining the luminescent properties of materials, particularly in nanomaterials like ZnO (KUMAR JANGIR et al., 2017). This size-dependent behavior in ZnO is driven by quantum confinement, which can alter electronic states, leading to shifts in luminescent wavelengths (blue shift or red shift). Additionally, smaller particles tend to have a higher proportion of surface defects, which can introduce new pathways for luminescence. These effects, combined with increased interactions with the surrounding environment, contribute to the complex luminescent behavior observed in ZnO NP (REPP, ERDEM, 2016; LV, LI, CHAI, 2019).

Reduced particle size also increases their susceptibility to interactions with the surrounding environment. These interactions can impact luminescence, such as through the adsorption of molecules or ions onto the particle surface, which can affect both the intensity and the spectrum of the luminescence. Coating NP is a potential method to modify or protect their luminescent properties against adverse environmental effects (ZHENG et al., 2018).

The broad-band emission of ZnO is typically linked to structural defects, such as oxygen and zinc vacancies or interstitials, resulting in non-excitonic recombination, or impurities within the ZnO, leading to an emission range between 400 and 600 nm. Additionally, a high concentration of surface defects can lead to greater variability and intensity in the emission (WILLANDER et al., 2010).

1.4.1.1 Enhancing ZnO Luminescence: The Role of Doping

To enhance the luminescence of ZnO, various approaches can be taken to increase the intensity of emitted light, adjust the emission wavelength, and improve the stability and durability of the luminescent properties.

By introducing specific atoms or ions into the crystal structure of ZnO, it is possible to modify its optical, electronic, and structural characteristics (LV, LI, CHAI, 2019). Doping is used to Alter Emission Color by introducing rare-earth ions, such as europium (Eu) (DASH, PANDA, SAHU, 2019), terbium (Tb) (KUMAR et al., 2020), or gadolinium (Gd) (THANGEESWARI et al., 2021), or transition metals like manganese (Mn) (WU, LI, LI, 2019), cobalt (Co) (CHANDA et al., 2017), or nickel (Ni) (MA et al., 2020). These dopants can be incorporated into ZnO to change the color

of luminescence, with each ion having unique emission characteristics that can be used to create a range of colors in the visible spectrum (DERRI et al., 2023).

Doping can also be used to control emission intensity, either by reducing the presence of intrinsic defects or by enhancing photoluminescence (TARASENKA et al., 2022). Some ions, when introduced into ZnO, can increase photoluminescence intensity through mechanisms such as energy transfer or the creation of more effective trap states (XIAO et al., 2012).

By customizing the luminescent properties of ZnO through doping, more effective CAs for bioimaging can be created (LIU et al., 2011; SYAMCHAND, APARNA, SONY, 2017). Doping with non-toxic or biocompatible ions, such as magnesium (MANAIA et al., 2015), calcium (SAEEDI et al., 2023), or iron (CAROFIGLIO et al., 2021), can be used for this purpose.

Doping is typically conducted during the synthesis process of ZnO, where the dopant element is incorporated into the crystalline structure (SINGH, KUMAR, SINGH, 2019). The distribution, concentration, and insertion location of the dopant in the ZnO structure are factors determining the final luminescence outcome (DAS; BASAK, 2021; MESAROS et al., 2015). Regarding the dopant concentration, the amount introduced into ZnO must be carefully controlled, as excessive doping can lead to AEs such as quenching or loss of structural properties (KUMAWAT, CHATTOPADHYAY, MISRA, 2023; MAHESHA et al., 2023).

I.4.2 Superparamagnetic iron oxide nanoparticles (SPIONs)

IO are NP with Mp and mainly provides T2 contrast in MRI (BABES et al., 1999). Numerous IO NP synthesis methods have been proposed (“US4329241A - Magnetic fluids and process for obtaining them - Google Patents”, 1979) among which the co-precipitation of iron salts in an aqueous solution and a tetramethylammonium hydroxide solution (TMAOH). In this work, we will not only discuss the formation of the IO, but also the main methods for the coating before embedding into polymers such as PLGA.

IO represents a family of compounds characterized by a diverse range of Mp and is utilized in various applications, including biomedical fields (SANGAIYA & JAYAPRAKASH, 2018). A range of IO NPs are used in treatments and diagnostic techniques of MRI for infectious diseases, cardiovascular diseases, pulmonary diseases,

autoimmune diseases, neurodegenerative disorders, and cancer (RAHMAN, 2023). In the brain, for example, they can be employed to identify tumors, and regions of inflammation (ISRAEL et al., 2020).

The mainly types of IO include Fe_3O_4 (Magnetite), Fe_2O_3 (Hematite), and γ-Fe_2O_3 (Maghemite) (HUSSEN et al., 2020). Magnetite is among the most recognized IOs, noted for its strong Mp (WALLYN, ANTON, & VANDAMME, 2019). It exhibits ferrimagnetism, characterized by high spontaneous magnetization, which makes it a material for various biomedical applications, including MRI CAs, magnetic hyperthermia and targeted drug delivery (WALLYN, ANTON, & VANDAMME, 2019; ANDRADE et al., 2020).

IO NPs are widely used due to their reduced size and enhanced Mp. The Mp of NPs can be influenced by size, morphology, and composition (NGOI et al., 2021). For instance, smaller NPs tend to exhibit superparamagnetism, which means they don't retain residual magnetization once the external Mf is removed (GOODRIDGE et al., 2023).

To improve the biocompatibility and stability of IO NPs, specific coatings are applied (SHATERABADI et al., 2017). Organic coatings, such as polymers and surfactants (MUTHIAH et al., 2013; SHATERABADI et al., 2017), as well as inorganic coatings, like silica (MALVINDI et al., 2014), provide stability to the NPs by preventing their aggregation and helping to avoid undesirable interactions with the immune system (SHAH & DOBROVOLSKAIA, 2018).

IO NPs are important CAs in MRI (SHEN et al., 2017; FERNÁNDEZ-BARAHONA et al., 2020; CHEN et al., 2022). Thanks to their superparamagnetic properties and strong response to Mf, these NPs significantly enhance the quality of MRI images, facilitating more precise identification of anatomical structures and pathologies.

IO CAs in MRI, such as SPION, can alter the relaxivity of their surrounding environment, thereby enhancing the visibility of the regions where they are in MRI images (CASPANI et al., 2020b). This effect occurs because the NPs influence how hydrogen protons behave under Mf, leading to increased image contrast (HUANG et al., 2012).

I.4.3 Iron doped ZnO NPs

Fe-doped ZnO NPs (FeZnO) have suitable photocatalytic activity. That is, by light excitation, FeZnO molecules can produce free radicals such as °OH, which have high oxidative capacity (BA-ABBAD et al., 2013; GHALAJKHANI; HAGHIGHI; SHABANI, 2018). In order to obtain iron-based NPs, it should be known that the critical size of the particles induces the property of superparamagnetism (SHIN et al., 2020). The application of ZnO is limited due to the rapid recombination of photon-generated electron-hole pairs (BA-ABBAD et al., 2013; GHALAJKHANI; HAGHIGHI; SHABANI, 2018), as ZnO has a wide band gap (3.37 eV) and can only be used at ultraviolet wavelengths.

A small particle size means a small radioactive lifetime (ZHANG et al., 2010). In solution, there is a need for improvement of luminescence and separation of exciton from surface defects (ZHANG et al., 2010). In the solid state, ZnO QDs are very stable as their growth is stopped. Even after one month, their emission colour and intensity remain the same.

Conjugation with type II-IV heteroconjunction metals, such as iron doping, can be an excellent strategy to decrease the bandgap of ZnO and cause a shift to longer wavelengths in the visible light region at the edge of the ZnO absorbance spectrum (BA-ABBAD et al., 2013; GHALAJKHANI, HAGHIGHI, SHABANI, 2018). The use of Fe as a dopant for ZnO NPs not only improves the optical properties by enhancing the electron-hole pair separation and reducing the band gap, but also contributes to reducing the particle size with increased surface area, reduced toxicity, and better dissolution (BA-ABBAD et al., 2013; MUTHUKUMAR, 2018).

Fe^{3+} can enter the crystal lattice of ZnO through a doping process by filling Zn^{2+} vacancies and because the ionic radius of Fe^{3+} (0.076 nm) is smaller than the ionic radius of Zn^{2+} (0.083 nm) (BA-ABBAD et al., 2013).

Red shift in absorbance spectra was observed for FeZnO QDs. However, ZnO QDs with a small size and many defects show strong emission in the visible region. On the other hand, QDs with a larger size and a perfect crystalline structure show a strong emission in the ultraviolet region (ZHANG et al., 2010).

A sol-gel method for producing visible light-activated FeZnO has been described (BA-ABBAD et al., 2013). Producing FeZnO using this route offers several advantages over other NP production techniques, such as ease of processing, compositional control, purity, and homogeneity of the produced material (BA-ABBAD et al., 2013).

I.4.4 CIS/ZnS quantum dots

Cu-In-S (CIS) QDs are the most promising of the I-III-VI QDs. They are composed of inexpensive and earth-abundant elements and exhibit a wide tunable range, low toxicity and a small band gap (SADEGHIMAKKI et al., 2017; WANG et al., 2018). The CIS QD has a unique ternary structure that allows great structural and compositional flexibility, as it is composed of multiple cations with different ratios of Cu, In and S precursors, allowing control of the growth rate, structural arrangement and optical properties (SADEGHIMAKKI et al., 2017).

Cu deficiency preferentially generates Cu vacancies and In interstitials, creating radiative recombination pathways and improving QD optical quality. In addition, increasing the Zn precursors can also improve the optical behaviour (SADEGHIMAKKI et al., 2017).

GCIS/ZnS QDs with suitable fluorescence properties in the near-infrared region, high longitudinal relativity in water and suitable colloidal stability were obtained by Yang et al. (2015). The band gap is an important factor in the evaluation of QDs to determine the optical properties of the compounds used, and their broad absorption spectrum allows simultaneous excitation in multiple fluorescent colours (MIR et al., 2018).

CIS/ZnS core/shell QDs exhibit suitable properties such as size-dependent emission, high photoluminescence quantum yield (PLQY) and have been investigated as alternatives for applications as biodiagnostic tools because QDs have higher brightness and are considered more resistant to photobleaching compared to fluorescent organic dyes and fluorescent proteins (MIR et al., 2018; WANG et al., 2018). Furthermore, the luminescence properties of CIS/ZnS QDs can be manipulated by varying the reaction conditions such as temperature, reaction time and ZnS shell formation (WANG et al., 2018).

CIS/ZnS core/shell QDs using 1-dodecanotial as the ligand not only enhance the colloidal stability by avoiding proton transfer between the ligands, but also improve the electronic property. By controlling the molar ratio between the cations, the photoluminescence emission peak of CIS/ZnS QDs can be shifted from 530 to 710 nm (WANG et al., 2018).

I.5 SURFACE MODIFICATION OF QDs

Coating and encapsulation are fundamental techniques for enhancing the luminescent stability of ZnO (GALDÁMEZ-MARTÍNEZ et al., 2023). Both methods help protect ZnO from environmental factors that could degrade its luminescent properties. Additionally, coating and encapsulation can improve ZnO's biocompatibility, making it safer for biomedical applications (MOHAMMAD et al., 2023).

Surface modification of quantum dots is used to enable the inorganic NPs to be dispersed and stabilized in hydrophilic or hydrophobic media. In the present work, the surface modification of ZnO allowed the quantum dots to be dispersed in water without changing the particle size or luminescence when modified with GPTMS. The oleic acid was used for the dispersion in organic solvents such as dichloromethane, hexane, and toluene.

The QD stability of ZnO is dramatically reduced by heat treatment. It is necessary to increase the stability and photoluminescence emission of ZnO NPs for practical applications. This can be achieved by modifying their surface (SHI et al., 2011). Most of the modifiers presented the problem of red-shifted particle growth and insolubility issues or could not be purified or redispersed in other polymer matrices for future applications (SHI et al., 2011).

The surface modification such as cationic and anionic surface binding sites can affect the luminescence of ZnO QDs (ZHANG, XIONG, 2015). Most of the defects are expected to be on the surface of ZnO QDs and, relative to the particle, the closer to the surface, the higher the concentration of these defects and thus the higher the number of exciton recombination centres near the NP surface (ZHANG, XIONG, 2015).

GPTMS (3-glycidoxypropyl)trimethoxysilane) is a silane-based compound that has a molecular formula described according to **Figure I.4**.

Figure I.4. Molecular structure of GPTMS.

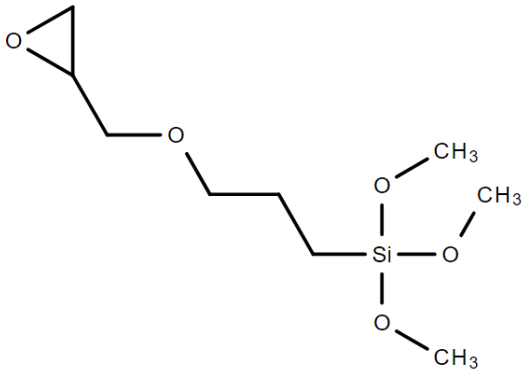

Source: Adapted by the author.

GPTMS is an amphiphilic compound. It has a polar layer and an apolar layer which may have an affinity for the aqueous medium. Modifying ZnO NPs with GPTMS was shown to induce long-term stability in organic media by modifying surface hydrophilicity and reducing NP agglomeration (BAGHDADI et al., 2020).

Oleic acid (**Figure I.5**) is a long carbon chain component that has an apolar character. It is widely used for surface modification of inorganic compounds and has considerable biocompatibility. Pharmaceutical systems have an apolar character at their core and this would help to carry inorganic drugs to their target site. Organic acid has been used to modify the compounds used in this work (ZnO, IO and CIS/ZnS).

Figure I.5. Molecular structure of Oleic acid.

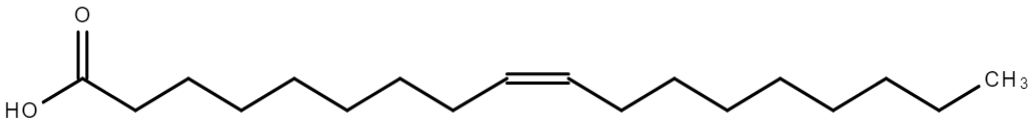

Source: Adapted by the author.

I.6 POLYMERIC NANOPARTICLES

The approach of embedding the CAs in polymers is an efficient way to entrap two types of CAs into a single nanosystem. However, the main limitation lies in the fact that as the nanosystem degrades, the two types of CAs separate. For this purpose,

PLGA-based copolymer was chosen, which is currently under investigation; however, and to the best of our knowledge, there are no reports on the co-encapsulation of zinc- and iron-based CAs into this type of polymer.

I.6.1 PLGA particles and their relationship to ZnO, SPIONS and CIS/ZnS

NPs based on biodegradable poly(lactic-co-glycolic acid) (PLGA) polymers have attracted much interest in developing nanosystem for drug delivery (ALSAAB et al., 2022; LUQUE-MICHEL et al., 2019). Indeed, PLGA NPs exhibit selective cytotoxicity towards cancer cells (CHIU et al., 2021b).

PLGA is a biodegradable particle that is used in the treatment of cancer. It is a hydrophobic copolymer which has two major monomers: lactic acid and glycolic acid (**Figure I.6**). It can encapsulate hydrophobic and hydrophilic drugs and is used for its biocompatibility and biodegradability (KIM et al., 2019; REZVANTALAB, KESHAVARZ, MORAVEJI, 2019). In cancer, PLGA NPs show high permeability, adequate drug release and high accumulation in the tumour vasculature, as well as the ability to conjugate with ligands on the copolymer surface (KIM et al., 2019).

Figure I.6. Molecular structure of PLGA.

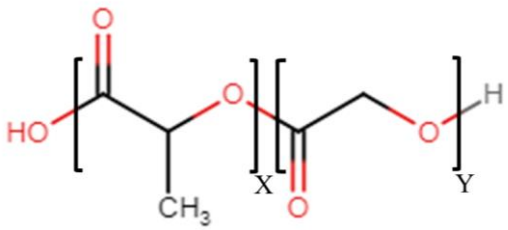

Source: Adapted by the author.

Some properties of PLGA copolymers should be preserved for suitable use in biological conditions, such as the size of PLGA NPs, which are usually synthesised with an average size of 200 nm. Higher cytotoxicity and inefficient loading of the drug into the polymer may occur with a PLGA size smaller than 100 nm. On the other hand, PLGA NPs larger than 300 nm may not be able to be uptake by cancer cells.

PLGA has been used as a nanocarrier for CAs in MRI and anticancer agents using SPIONS and docetaxel. The PLGA improved cellular uptake and was tested in FR-positive KB cancer cells (SHANAVAS et al., 2017). Another study shows PLGA

particles with SPIONs and docetaxel for use in prostate cancer PC3 cells (LING et al., 2011). Luque-Michel (2021) used PLGA NPs as theranostics against gioblastoma cells. They created SPIONS-doxirrubcin PLGA NPs and verified the effect by magnetic targeting and MRI in vivo studies (LUQUE-MICHEL et al., 2019).

On the other hand, there are some studies on PLGA:ZnO in the literature. These studies use PLGA:ZnO NPs in microbial activity (LI, YIN, XU, 2022; STANKOVIĆ et al., 2016). Stankovic et al. (2016) tested the antimicrobial activity of these NPs on several gram-positive and gram-negative bacteria. Despite the use of ZnO NPs, this is different from the work in this paper as the particle size used for ZnO was 100 nm and the luminescence properties of this material were not investigated. Another study shows PLGA:ZnO NPs with a size of 40-70 nm and a ZnO concentration of 0.001, 0.01 and 0.1%. The results show that as the percentage of ZnO increases, the bacteriostatic properties increase, but the cytotoxicity remains low (LI, YIN, XU, 2022). A study by Mozaffari et al (2023) used PLGA:ZnO NPs to evaluate the cytotoxicity of human gingival fibroblast (HGF) cells, and the strategy of incorporating ZnO into the PLGA copolymer reduced the cytotoxicity to the tested cells (MOZAFFARI et al., 2023). Until now, there is no study about the concomitant use of PLGA, ZnO and IO for diagnostic imaging.

Up to now, no study was reported on PLGA particles encapsulating CIS/ZnS or concomitantly, CIS/ZnS and IO.

REFERENCES

ABDELHAMID, M. E.; O'MULLANE, A. P.; SNOOK, G. A. Storing energy in plastics: a review on conducting polymers & their role in electrochemical energy storage. **RSC Advances**, v. 5, n. 15, p. 11611–11626, 2015.

ALSAAB, H. O. et al. PLGA-Based Nanomedicine: History of Advancement and Development in Clinical Applications of Multiple Diseases. **Pharmaceutics**, v. 14, n. 12, 2022.

ASLAN, N. et al. Metallic nanoparticles as X-Ray computed tomography (CT) contrast agents: A review. **Journal of Molecular Structure**, v. 1219, p. 128599, 2020.

ATTIA, M. F. et al. Inorganic Nanoparticles for X-Ray Computed Tomography Imaging. Critical Reviews™ in **Therapeutic Drug Carrier Systems**, v. 35, n. 5, p. 391–432, 2018.

AVASTHI, A. et al. Magnetic Nanoparticles as MRI Contrast Agents. **Topics in current chemistry (Cham)**, v. 378, n. 3, 2020.

BABES, L. et al. Synthesis of Iron Oxide Nanoparticles Used as MRI Contrast Agents: A Parametric Study. **Journal of Colloid and Interface Science**, v. 212, n. 2, p. 474–482, 1999.

BAGHDADI, Y. N. et al. The effects of modified zinc oxide nanoparticles on the mechanical/thermal properties of epoxy resin. **Journal of Applied Polymer Science**, v. 137, n. 43, p. 49330, 2020.

BAILEY, R. E.; SMITH, A. M.; NIE, S. Quantum dots in biology and medicine. **Physica E: Low-dimensional Systems and Nanostructures**, v. 25, n. 1, p. 1–12, 2004.

BORYSIEWICZ, M. A. ZnO as a Functional Material, a Review. **Crystals 2019**, v. 9, n. 10, p. 505, 2019.

BRUS, L. E. Electron–electron and electron-hole interactions in small semiconductor crystallites: The size dependence of the lowest excited electronic state. **The Journal of Chemical Physics**, v. 80, n. 9, p. 4403–4409, 1984.

CAMARDA, P. et al. Luminescence mechanisms of defective ZnO nanoparticles. Phys. Chem. Chem. Phys, v. 18, p. 16237, 2016.

CAPELLETTI, R. Luminescence. Encyclopedia of Condensed Matter Physics, p. 178–189, 2005.

CAROFIGLIO, M. et al. Iron-doped zno nanoparticles as multifunctional nanoplatforms for theranostics. **Nanomaterials**, v. 11, n. 10, p. 2628, 2021.

CASPANI, S. et al. Magnetic Nanomaterials as Contrast Agents for MRI. **Materials 2020**, v. 13, n. 11, p. 2586, 2020.

CHANDA, A. et al. Study of structural, optical and magnetic properties of cobalt doped ZnO nanorods. **RSC Advances**, v. 7, n. 80, p. 50527–50536, 2017.

CHINEN, A. B. et al. Nanoparticle Probes for the Detection of Cancer Biomarkers, Cells, and Tissues by Fluorescence. **Chemical reviews**, v. 115, n. 19, p. 10530, 2015.

CHIU, H. I. et al. Cytotoxicity of targeted PLGA nanoparticles: a systematic review. **RSC Advances**, v. 11, n. 16, p. 9433, 2021.

CHIZHIK, V. I. et al. Magnetic resonance and its applications. **Magnetic Resonance and Its Applications**, v. 9, p. 1–782, 2014.

DAS, A.; BASAK, D. Efficacy of Ion Implantation in Zinc Oxide for Optoelectronic Applications: A Review. **ACS Applied Electronic Materials**, v. 3, n. 9, p. 3693–3714, 2021.

DASH, D.; PANDA, N. R.; SAHU, D. Photoluminescence and photocatalytic properties of europium doped ZnO nanoparticles. **Applied Surface Science**, v. 494, p. 666–674, 2019.

DEL ROSAL, B. et al. In Vivo Luminescence Nanothermometry: from Materials to Applications. **Advanced Optical Materials**, v. 5, n. 1, p. 1600508, 2017.

DERRI, A. et al. Insight into the photoluminescence and morphological characteristics of transition metals (TM = Mn, Ni, Co, Cu)-doped ZnO semiconductor: a comparative study. **Optical Materials**, v. 145, p. 114467, 2023.

DÍEZ, A. G. et al. Multicomponent magnetic nanoparticle engineering: the role of structure-property relationship in advanced applications. **Materials Today Chemistry**, v. 26, p. 101220, 2022.

DILL, T. Contraindications to magnetic resonance imaging: non-invasive imaging. **Heart (British Cardiac Society)**, v. 94, n. 7, p. 943–948, 2008.

ESTELRICH, J.; SÁNCHEZ-MARTÍN, M. J.; BUSQUETS, M. A. Nanoparticles in magnetic resonance imaging: from simple to dual contrast agents. **International Journal of Nanomedicine**, v. 10, p. 1727, 2015.

FAN, Q. et al. Recent advances of lanthanide nanomaterials in Tumor NIR fluorescence detection and treatment. **Materials Today Bio**, v. 20, p. 100646, 2023.

Fundamentals of luminescence. **Phosphor Handbook: Fundamentals of Luminescence**, p. 17–88, 2022.

GALDÁMEZ-MARTÍNEZ, A. et al. Controlling Green-to-Blue Luminescence in Multidimensional ZnO Interfaces: Mechanistic Insights. **ACS Applied Optical Materials**, v. 1, n. 8, p. 1414–1426, 2023.

GROVER, V. P. B. et al. Magnetic Resonance Imaging: Principles and Techniques: Lessons for Clinicians. **Journal of clinical and experimental hepatology**, v. 5, n. 3, p. 246–255, 2015.

GUEDENS, W. J. et al. ZnO-based sunscreen: The perfect example to introduce nanoparticles in an undergraduate or high school chemistry lab. **Journal of Chemical Education**, v. 91, n. 2, p. 259–263, 2014.

GURYLEV, V.; PERNG, T. P. Defect engineering of ZnO: Review on oxygen and zinc vacancies. **Journal of the European Ceramic Society**, v. 41, n. 10, p. 4977–4996, 2021.

BERLMAN, I.B. **Handbook of florescence spectra of Aromatic Molecules**, 1971.

ISLER, E. et al. Trapeamento de LNAPL observado por meio da técnica de fluorescência induzida por laser (LIF). **Águas Subterrâneas**, v. 32, n. 3, p. 315–324, 2018.

JACQUES, V. et al. High relaxivity MRI contrast agents part 2: Optimization of inner- and second-sphere relaxivity. **Investigative radiology**, v. 45, n. 10, p. 613, 2010.

JENKINS, R.; BURDETTE, M. K.; FOULGER, S. H. Mini-review: fluorescence imaging in cancer cells using dye-doped nanoparticles. **RSC Advances**, v. 6, n. 70, p. 65459–65474, 2016.

JIANG, J.; PI, J.; CAI, J. The Advancing of Zinc Oxide Nanoparticles for Biomedical Applications. **Bioinorganic Chemistry and Applications**, v. 2018, 2018.

KHAN, I.; SAEED, K.; KHAN, I. Nanoparticles: Properties, applications and toxicities. **Arabian Journal of Chemistry**, v. 12, n. 7, p. 908–931, 2019.

KIM, K. B. et al. Risk assessment of zinc oxide, a cosmetic ingredient used as a UV filter of sunscreens. **Journal of Toxicology and Environmental Health, Part B**, v. 20, n. 3, p. 155–182, 2017.

KIM, K. T. et al. Recent Progress in the Development of Poly(lactic- co-glycolic acid)-Based Nanostructures for Cancer Imaging and Therapy. **Pharmaceutics**, v. 11, n. 6, 2019.

KOCH, S. W. et al. Semiconductor excitons in new light. **Nature Materials,** v. 5, n. 7, p. 523–531, 2006.

KRISHNAN, K. M. Fundamentals and applications of magnetic materials. **Oxford**, p. 794, 2016.

KUMAR JANGIR, L. et al. Investigation of luminescence and structural properties of ZnO nanoparticles, synthesized with different precursors. **Materials Chemistry Frontiers**, v. 1, n. 7, p. 1413–1421, 2017.

KUMAR, P. et al. Optical and magnetic properties of terbium doped zinc oxide nanoparticles with lithium as charge compensator. **Optik**, v. 216, p. 164839, 2020.

KUMAWAT, A.; CHATTOPADHYAY, S.; MISRA, K. P. Significant impact of co-doping Eu-doped ZnO nanoparticles with Li on structural–optical properties relationship. **Materials Technology**, v. 38, n. 1, 2023.

LEE, N. et al. Nano-Sized CT Contrast Agents. **Advanced Materials**, v. 25, n. 19, p. 2641–2660, 2013.

LEE, S. K. et al. Radio-Frequency Vector Magnetic Field Mapping in Magnetic Resonance Imaging. **IEEE Transactions on Medical Imaging**, v. 40, n. 3, p. 963–973, 2021.

LI, S.; YIN, J.; XU, L. Batch Fabrication and Characterization of ZnO/PLGA/PCL Nanofiber Membranes for Antibacterial Materials. **Fibers and Polymers**, v. 23, n. 5, p. 1225–1234, 2022.

LICHTMAN, J. W.; CONCHELLO, J. A. Fluorescence microscopy. **Nature Methods** 2:12, v. 2, n. 12, p. 910–919, 2005.

LIMA, S. A. M. et al. Luminescent properties and lattice defects correlation on zinc oxide. **International Journal of Inorganic Materials**, v. 3, n. 7, p. 749–754, 2001.

LING, Y. et al. Dual docetaxel/superparamagnetic iron oxide loaded nanoparticles for both targeting magnetic resonance imaging and cancer therapy. **Biomaterials**, v. 32, n. 29, p. 7139–7150, 2011.

LIU, Y. et al. Fluorescence-enhanced gadolinium-doped zinc oxide quantum dots for magnetic resonance and fluorescence imaging. **Biomaterials,** v. 32, n. 4, p. 1185–1192, 2011.

LUGAUER, F.; WETZL, J. Magnetic Resonance Imaging. **Lecture Notes in Computer Science** (including subseries Lecture Notes in Artificial Intelligence and Lecture Notes in Bioinformatics), v. 11111 LNCS, p. 91–118, 2018.

LUQUE-MICHEL, E. et al. Co-encapsulation of superparamagnetic nanoparticles and doxorubicin in PLGA nanocarriers: Development, characterization and in vitro antitumor efficacy in glioma cells. **European Journal of Pharmaceutics and Biopharmaceutics**, v. 145, p. 65–75, 2019.

LV, J.; LI, C.; CHAI, Z. Defect luminescence and its mediated physical properties in ZnO. **Journal of Luminescence**, v. 208, p. 225–237, 2019.

MA, Z. et al. Structural, electrochemical and optical properties of Ni doped ZnO: Experimental and theoretical investigation. **Optik**, v. 219, p. 165204, 2020.

MAHESHA, A. et al. Chromium-doped ZnO nanoparticles synthesized via auto-combustion: Evaluation of concentration-dependent structural, band gap-narrowing effect, luminescence properties and photocatalytic activity. **Ceramics International**, v. 49, n. 14, p. 22890–22901, 2023.

MANAIA, E. B. et al. Surface modified Mg-doped ZnO QDs for biological imaging. **European Journal of Nanomedicine**, v. 7, n. 2, p. 109–120, 2015.

MAZZOLA, A. A. Ressonância magnética: princípios de formação da imagem e aplicações em imagem funcional. **Revista Brasileira de Física Médica**, v. 3, n. 1, p. 117–129, 2009.

MCGOWN, L. B.; NITHIPAHKOM, K. Molecular fluorescence and phosphorescence. **Applied Spectroscopy Reviews**, v. 35, n. 4, p. 353–393, 2000.

MESAROS, A. et al. A valence states approach for luminescence enhancement by low dopant concentration in Eu-doped ZnO nanoparticles. **Journal of Materials Science**, v. 50, n. 18, p. 6075–6086, 2015.

MIR, I. A. et al. Eco-friendly synthesis of CuInS2 and CuInS2@ZnS quantum dots and their effect on enzyme activity of lysozyme. **RSC Advances**, v. 8, n. 53, p. 30589–30599, 2018.

MO, D. et al. Cadmium-containing quantum dots: properties, applications, and toxicity. Applied Microbiology and Biotechnology 2017 101:7, v. 101, n. 7, p. 2713–2733, 2017.

MOHAMMAD, F. et al. Influence of Surface Coating towards the Controlled Toxicity of ZnO Nanoparticles In Vitro. **Coatings**, v. 13, n. 1, p. 172, 2023.

MORTON, J. J. Magnetic properties of materials Part 2. Types of magnetism (or $-1 \leq \chi < \text{inf}$). **Trinity**, p. 23, 2012.

MOZAFFARI, A. et al. Cytotoxicity of PLGA-zinc oxide nanocomposite on human gingival fibroblasts. Journal of Advanced Periodontology & **Implant Dentistry**, v. 15, n. 1, p. 27–33, 2023.

MUKHATOV, A. et al. A comprehensive review on magnetic imaging techniques for biomedical applications. **Nano Select**, v. 4, n. 3, p. 213–230, 2023.

MUSNIER, B. et al. Optimization of spatial resolution and scattering effects for biomedical fluorescence imaging by using sub-regions of the shortwave infrared spectrum. **Journal of Biophotonics**, v. 14, n. 2, p. e202000345, 2021.

NI, D. et al. Engineering of inorganic nanoparticles as magnetic resonance imaging contrast agents. **Chemical Society Reviews**, v. 46, n. 23, p. 7438–7468, 2017.

PAI, A. et al. Magnetic Resonance Imaging Physics. **Textbook of Radiology for CT and MRI Technicians with MCQs**, p. 109–109, 2023.

PINHO, S. L. C. et al. Gd- and Eu-Loaded Iron Oxide@Silica Core-Shell Nanocomposites as Trimodal Contrast Agents for Magnetic Resonance Imaging and Optical Imaging. **Inorganic chemistry**, v. 58, n. 24, p. 16618–16628, 2019.

QIN, X. et al. Polarity-based fluorescence probes: properties and applications. **RSC Medicinal Chemistry**, v. 12, n. 11, p. 1826, 2021.

RAHA, S.; AHMARUZZAMAN, M. ZnO nanostructured materials and their potential applications: progress, challenges and perspectives. **Nanoscale Advances**, v. 4, n. 8, p. 1868–1925, 2022.

RAHMAN, F. Zinc oxide light-emitting diodes: a review. **Optical Engineering**, v. 58, n. 1, p. 010901, 2019.

RAJI, R.; GOPCHANDRAN, K. G. ZnO nanostructures with tunable visible luminescence: Effects of kinetics of chemical reduction and annealing. **Journal of Science: Advanced Materials and Devices**, v. 2, n. 1, p. 51–58, 2017.

REN, X. et al. Perovskite Quantum Dots for Emerging Displays: Recent Progress and Perspectives. **Nanomaterials**, v. 12, n. 13, p. 2243, 2022.

REPP, S.; ERDEM, E. Controlling the exciton energy of zinc oxide (ZnO) quantum dots by changing the confinement conditions. **Spectrochimica Acta Part A: Molecular and Biomolecular Spectroscopy**, v. 152, p. 637–644, 2016.

REZVANTALAB, S.; KESHAVARZ MORAVEJI, M. Microfluidic assisted synthesis of PLGA drug delivery systems. **RSC Advances**, v. 9, n. 4, p. 2055–2072, 2019.

RIZVI, S. B. et al. Semiconductor quantum dots as fluorescent probes for in vitro and in vivo bio-molecular and cellular imaging. **Nano Reviews**, v. 1, n. 1, p. 5161, 2010.

SADEGHIMAKKI, B. et al. Synthesis of CIS Quantum Dots in Low-Temperature Regime: Effects of Precursor Composition and Temperature Ramps. **IEEE Transactions on Nanotechnology**, v. 16, n. 4, p. 659–666, 2017.

SAEEDI, A. M. et al. Antimicrobial Agent Based on Ca-Doped ZnO Nanopowders. **Physica status solidi (a)**, v. 220, n. 18, p. 2300162, 2023.

SANDERSON, M. J. et al. Fluorescence Microscopy. Cold Spring Harbor protocols, v. 2014, n. 10, p. pdb.top071795, 2014.

SCHULMAN, S. G.; DI, Q. Q.; JUCHUM, J. Organic Chemistry Applications of Fluorescence Spectroscopy. **Encyclopedia of Spectroscopy and Spectrometry**, p. 1718–1725, 1999.

SHANAVAS, A. et al. Magnetic core-shell hybrid nanoparticles for receptor targeted anti-cancer therapy and magnetic resonance imaging. **Journal of colloid and interface science**, v. 486, p. 112–120, 2017.

SHI, H. Y. et al. Synthesis of zinc oxide nanoparticles with strong, tunable and stable visible light emission by solid-state transformation of Zn(II)–organic coordination polymers. **Journal of Materials Chemistry**, v. 21, n. 33, p. 12309–12315, 2011.

SINGH, P.; KUMAR, R.; SINGH, R. K. Progress on Transition Metal-Doped ZnO Nanoparticles and Its Application. **Industrial and Engineering Chemistry Research**, v. 58, n. 37, p. 17130–17163, 2019.

SMITH, A. M.; NIE, S. Semiconductor nanocrystals: Structure, properties, and band gap engineering. **Accounts of Chemical Research**, v. 43, n. 2, p. 190–200, 2010.

SO, P. T.; DONG, C. Y. Fluorescence Spectrophotometry. **Encyclopedia of Life Sciences**, 2002.

STANKOVIĆ, A. et al. PLGA/Nano-ZnO Composite Particles for Use in Biomedical Applications: Preparation, Characterization, and Antimicrobial Activity. **Journal of Nanomaterials**, v. 2016, 2016.

STEWART, K. H. Ferromagnetic domains. **Cambridge University Press**, p. 176, 1954.

SYAMCHAND, S. S.; APARNA, R. S.; SONY, G. Plasmonic enhancement of the upconversion luminescence in a Yb3+ and Ho3+ co-doped gold-ZnO nanocomposite for use in multimodal imaging. **Microchimica Acta**, v. 184, n. 7, p. 2255–2264, 2017.

TARASENKA, N. et al. Photoluminescent neodymium-doped ZnO nanocrystals prepared by laser ablation in solution for NIR-II fluorescence bioimaging. **Heliyon**, v. 8, n. 6, p. e09554, 2022.

THANGEESWARI, T. et al. Synthesize of gadolinium-doped ZnO nano particles for energy applications by enhance its optoelectronic properties. **Materials Today: Proceedings**, v. 34, p. 448–452, 2021.

US4329241A - Magnetic fluids and process for obtaining them - Google Patents. Disponível em: <https://patents.google.com/patent/US4329241A/en>. Acess in: 11 set. 2023.

WAGNER, A. M. et al. Quantum Dots in Biomedical Applications. **Acta biomaterialia**, v. 94, p. 44, 2019.

WAHSNER, J. et al. Chemistry of MRI contrast agents: Current challenges and new frontiers. **Chemical Reviews**, v. 119, n. 2, p. 957–1057, 2019.

WALLYN, J. et al. Biomedical Imaging: Principles, Technologies, Clinical Aspects, Contrast Agents, Limitations and Future Trends in Nanomedicines. **Pharmaceutical Research,** v. 36, n. 6, p. 1–31, 2019.

WANG, Z. et al. Facile Synthesis of Cu-In-S/ZnS Core/Shell Quantum Dots in 1-Dodecanethiol for Efficient Light-Emitting Diodes with an External Quantum Efficiency of 7.8%. **Chemistry of Materials**, v. 30, n. 24, p. 8939–8947, 2018.

WEGNER, K. D.; HILDEBRANDT, N. Quantum dots: bright and versatile in vitro and in vivo fluorescence imaging biosensors. **Chemical Society Reviews**, v. 44, n. 14, p. 4792–4834, 2015.

WILLANDER, M. et al. Luminescence from Zinc Oxide Nanostructures and Polymers and their Hybrid Devices. **Materials**, v. 3, n. 4, p. 2643, 2010.

WOLFBEIS, O. S. An overview of nanoparticles commonly used in fluorescent bioimaging. **Chemical Society Reviews**, v. 44, n. 14, p. 4743–4768, 2015.

WU, B.; LI, J.; LI, Q. Preparation and photoluminescence behavior of Mn-doped nano-ZnO. **Optik**, v. 188, p. 205–211, 2019.

XIAO, F. et al. Efficient energy transfer and enhanced infrared emission in Er-oped ZnO-SiO 2 omposites. **Journal of Physical Chemistry C**, v. 116, n. 24, p. 13458–13462, 2012.

ZDOBNOVA, T. A.; LEBEDENKO, E. N.; DEYEV, S. M. Quantum Dots for Molecular Diagnostics of Tumors. **Acta Naturae**, v. 3, n. 1, p. 29, 2011.

ZHANG, Z. Y.; XIONG, H. M. Photoluminescent ZnO Nanoparticles and Their Biological Applications. **Materials**, v. 8, n. 6, p. 3101, 2015.

ZHENG, Z. et al. Luminescent zinc oxide nanoparticles: from stabilization to slow digestion depending on the nature of polymer coating. **Polymer Chemistry**, v. 10, n. 1, p. 145–154, 18 dez. 2018.

ZHU, X. et al. Anti-Stokes shift luminescent materials for bio-applications. **Chemical Society Reviews**, v. 46, n. 4, p. 1025–1039, 20 fev. 2017.

CHAPTER II

Materials and methods

CHAPTER II MATERIALS AND METHODS

II.1 Materials

The materials used for the fabrication of the quantum dots, the modification of the surface and the preparation of the polymer system are described below:

a) ZnO and FeZnO QDs:

Zinc acetate dihydrate $C_4H_6O_4Zn.2H_2O$ Sigma-aldrick® (Índia), Lithium hydroxide monohydrate $LiOH.H_2O$ Chemicals™ (Ribeirão Preto, Brazil); Iron (III) chloride hexahydrate 97% Sigma-Aldrich™ (Germany); Iron (II) acetate 95% Thermo Scientific™ (Armenia); Iron (III) nitrate nonahydrate 98% Sigma-Aldrich (USA); Ethanol (Qhemis, 99.5%); Heptane 99.5% Sigma-Aldrich™ (Germany); (3-Glycidyloxypropyl)-trimethoxysilane (GPTMS) 98% Sigma-Aldrich™ (USA);

b) Iron oxide NPs:

Iron (II) chloride hexahydrate 98% Sigma-Aldrich™ (Germany); Iron (III) chloride hexahydrate 97% Sigma-Aldrich™ (Germany); Tetramethylammonium hydroxide pentahydrate 97% Sigma-Aldrich™ (USA); Oleic acid 90% Sigma-Aldrich (USA); Perchloric acid Sigma-Aldrich™ (USA);

c) CIS/ZnS QDs and FeCIS/ZnS QDs:

Copper (II) acetylacetonate 99% Sigma-Aldrich™ (United Kingdom); Indium (III) acetylacetonate 99% Sigma-Aldrich™ (USA); 1-Dodecanothiol (DDT) $C_{12}H_{26}S$ Sigma-Aldrich (USA); Oleylamine 70% Sigma-Aldrich™ (Belgium);

d) PLGA samples:

Poly(lactic-co-glycolic acid) polymer (Resomer RG 503H, PLGA 50:50) Sigma-Aldrich™ (Germany); Tween 80 (Polysorbate 80) Sigma-Aldrich™ (Germany); triethylamine Sigma-Aldrich™ (Germany); Ethyl acetate 99.8% Fisher Chemical™ (United Kingdom); Dichloromethane (DCM) Sigma-Aldrich™ (Germany); Polyvinylalkohol 20-98 Sigma-Aldrich™ (Germany). The water Milli-Q was obtained by ultrapurification process in Merck™ Millipore (France).

II.2 SYNTHESIS

II.2.1 ZnO QDs synthesis

The ZnO was obtained by a modified sol-gel method according to Spanhel & Anderson (1991). It consists of 2 main stages:

1) Formation of acetyl zinc acetate precursor: 1.487g of zinc acetate hexahydrate and 50ml of ethyl alcohol PA were added in a heating and condensation system at 98°C for 2 hours, obtaining a solution of 0.1 mol L^{-1}. The powder dissolves completely and the solution is transparent. Subsequently, the solution is cooled at RT and diluted to a total of 100 mL. The final concentration is 0.05 mol L^{-1}. The solution was stored for 30 minutes at ~4°C;

2) Formation of the ZnO colloidal suspension: the colloidal suspension of ZnO was carried out by a hydrolysis and condensation reaction, in high power ultrasound (frequency 37, power 60 W), at 60°C, for 60 minutes, using lithium hydroxide (LiOH) as hydrolysis agent. The 1:1 molar ratio of Zn:OH was used to calculate the LiOH mass. The suspension was cooled and stored for surface modification. The production flowchart of ZnO NPs is described in **Figure II.1a**.

II.2.2 Fe-doped ZnO QDs synthesis

The method used to synthesize Fe-doped ZnO QDs was adapted and modified from that developed by Spanhel & Anderson (1991) to produce zinc precursor solution and Manaia et al. (2015) for the doping process. The production flowchart of FeZnO NPs is described in **Figure II.1b**.

Initially, acetyl zinc acetate precursor is prepared: 1.487g of zinc acetate hexahydrate and 50ml of ethyl alcohol PA were added in a heating and condensation system at 98°C for 2 hours, obtaining a solution of 0.1 mol L^{-1}. The powder dissolves completely and the solution showed transparent. After this step, the solution is cooled at RT and diluted to a total of 100 mL. The final concentration is 0.05 mol L^{-1}. The solution was stored for 30 minutes at ~4°C;

In parallel, iron solutions - in ethanol - were prepared either with iron chloride ($FeCl_3$), iron nitrate ($Fe(NO_3)_3$) or iron acetate ($Fe(C_2H_3O_2)_2$). for the latest, the same process as the one performed to produce the zinc acetate precursor was carried out.

Fe-doped NPs were prepared by adding iron solution within zinc acetate precursor. The molar concentration [Fe+Zn] was kept constant relative to LiOH, Fe:Zn (mol:mol) ratios was set at 0.01, 0.05, 0.1, 0.3, 0.5, 10, 15, 20 were tested. To assess the influence of the timing of the addition of the iron solution, the iron solution was added concomitantly, 15 min or 30 min after the beginning of start of the reaction. The reactions conditions were high power ultrasound (frequency 37, power 60 W at 60°C) for a total time of 60 minutes. **Table II.1** describes the volume of precursors added in the reaction. **Table II.1** describes the volume of precursors added.

Table II.1. Amount of the Zn precursor and Fe precursor

Samples	**Zn (precursor) 0.05 mol L^{-1} (mL)**	**Fe (precursor) 0.1 mol L^{-1} (mL)**	**EtOH (mL)**	**Final volume (mL)**
pristine ZnO	10	-	-	10
FeZnO 0.1	9.99	0.005	0.005	10
FeZnO 0.5	9.95	0.025	0.025	10
FeZnO 1	9.9	0.05	0.05	10
FeZnO 3	9.7	0.15	0.15	10
FeZnO 5	9.5	0.25	0.25	10
FeZnO 10	9	0.5	0.5	10
FeZnO 15	8.5	0.75	0.75	10
FeZnO 20	8	1	1	10

The tested conditions for the preparation of FeZnO NPs were carried out according to 1) choosing the doping iron precursor: between the salts of iron chloride, iron acetate and iron nitrate; 2) choosing the appropriate concentration of iron used between 0 and 20 % of Fe; and 3) choosing the doping time: the time of addition of iron source between the start of the reaction (0 min), after 15 min, and after 30 min of reaction.

II.2.3 ZnO and FeZnO Surface modification with GPTMS

The modification of ZnO and FeZnO QDs with GPTMS was carried out by a hydrolysis and condensation reaction from the synthesis proposed by Lallo Da Silva et al. (2019). Initially, 225 µL GPTMS and 84 mg LiOH were added to 10 mL ethanolic

colloidal suspension of the above QDs at 0.05 mol L^{-1}. The final concentrations of GPTMS and LiOH were 0.2 mol L^{-1} and 0.1 mol L^{-1}, respectively. The suspension was subjected to ultrasonic treatment (frequency 37, power 60 W) at a temperature of 35 °C for 30 minutes. The suspension was centrifuged at 6000 rpm for 15 minutes at room temperature (25°C). The precipitate was dried overnight, weighed, and dispersed in water to the appropriate concentration. The surface modification flowchart of QDs with GPTMS is described in **Figure II.1c**.

II.2.4 ZnO and FeZnO surface modification with Oleic Acid

The ZnO and FeZnO coating steps were prepared by a simple stirred reaction at 60°C for 1 h with stirring at 400 rpm. Oleic acid was initially added according to the method described by Manaia et al. (2015). The oleic acid was preheated to 60 °C. Hence, 75 µL of oleic acid was added to 10 mL of the pre-prepared QDs ethanolic suspension. The final concentration of oleic acid was 18.57 mmol L^{-1}. The suspension was stored overnight. The washing step was performed the following day. The magnetic stirrer was removed, and the solution was transferred to a 25 mL glass tube. The suspension was centrifuged and washed 3 times with 10 mL ethanol-PA at 2000 rpm at room temperature to remove the reagents excess such as oleic acid and excess ZnO that was not coated. The tubes were weighed, dried for 3 hours at Room temperature, and weighed again. The centrifuged sample was diluted in DCM to a final concentration of 40 mg mL^{-1}. The surface modification flowchart of QDs with oleic acid is described in **Figure II.1c**.

II.2.5 Powder obtainment

The as-synthesised colloidal suspensions (ZnO and FeZnO) were precipitated according to the method described by Meulenkamp (1998). The QDs were mixed with heptane in a 1:4 (v:v) ratio to induce precipitation. The suspension was transferred to a Falcon tube and centrifuged at 6000 rpm for 15 min at room temperature. The supernatant was removed, and the powders dried overnight at room temperature for analysis.

Figure II.1. Flowchart of ZnO QDs (a) and FeZnO QDs (b) production, along with their surface modification (c) using GPTMS and oleic acid. *Iron source: iron chloride, iron acetate, or iron nitrate.

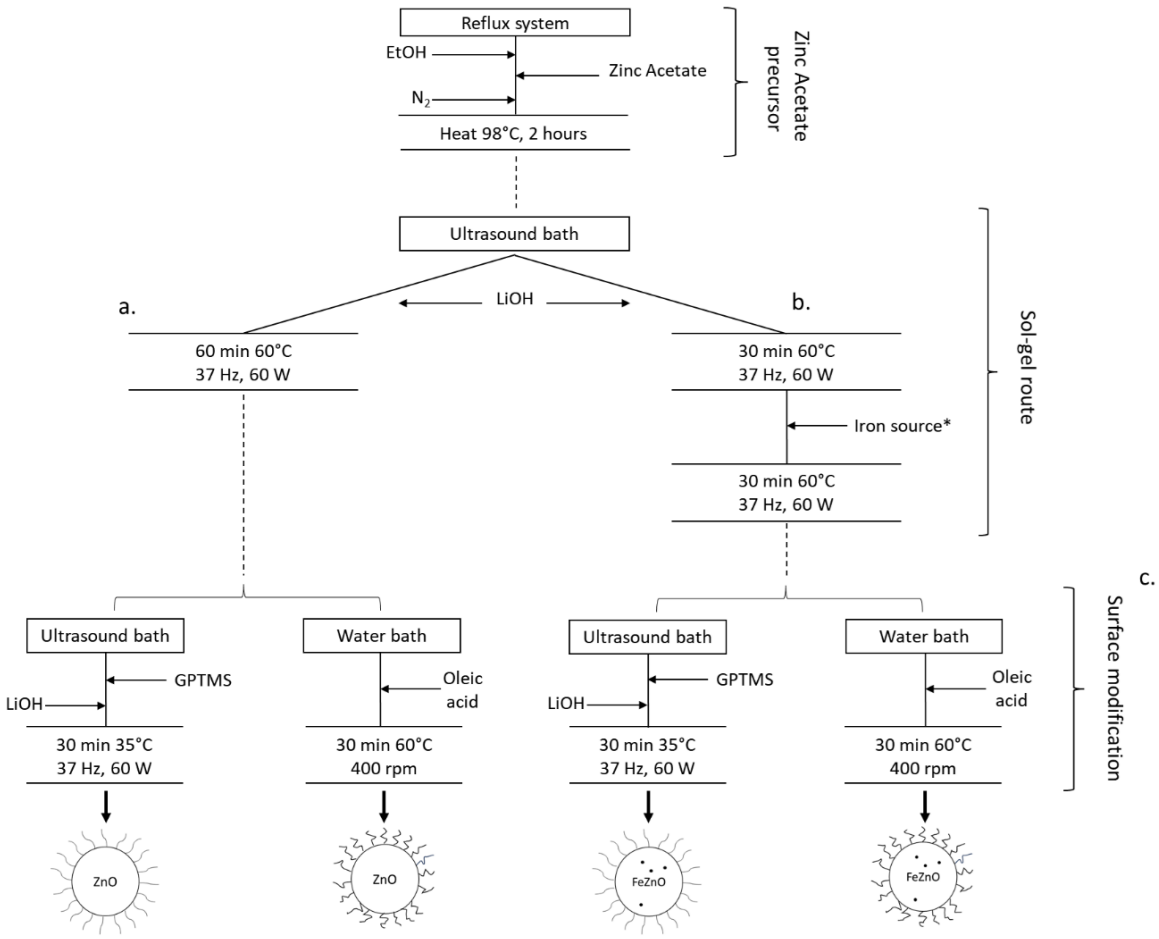

Source: by the author.

II.2.6 Iron Oxide NPs

The synthesis of IO was prepared according to Babes et al. (1999), and it is presented in **Figure II.2**. To produce the IO, it needs four solutions prepared: s1) TMAOH solution: 362.72 mg in 2 mL of distilled water; s2) $FeCl_2$ solution 0.314 mol L^{-1}: 6.62 mg of $FeCl_2.4H_2O$ in 100 µL of distilled water; s3) $FeCl_3$ solution 0.666 mol L^{-1}: 18 mg in 100 µL of distilled water; and s4) wash solution $HClO_4$ 20 %: 2 mL $HClO_4$ PA and 8 mL of distilled water.

The reaction was performed by three steps: a) IO reaction: the mix solution of $FeCl_2$ (s2) and FeCl3 (s3) (200 µL) was added dropwise at 2 mL TMAOH solution. The

solution was magnetically stirred at RT for 5 minutes; b) IO coated by oleic acid: The reaction was transferred to a 75°C water bath. After 3 minutes of thermal equilibration, 75 µL of oleic acid at 75°C was added in one shot. The solution was stirred for 15 minutes in a water bath and, after, stirred for 15 minutes at room temperature; and c) Wash step: the final solution was washed with 2 mL of wash solution pre prepared (s4), a brownish precipitate was formed, and 10 times with 10 mL of distilled water. In each wash, the IO coated by oleic acid were separated using a strong magnetic. Finally, a drop of oil containing the IO was formed. The drop was washed with ethanol 3x and dry for 1 hour, weighed and dissolved in DCM with adequate concentration (40 mg mL^{-1}). A homogeneous black solution was formed. The solution was stored in room temperature.

Figure II.2. Flowchart of Fe_3O_4 NPs production with their surface modification using oleic acid.

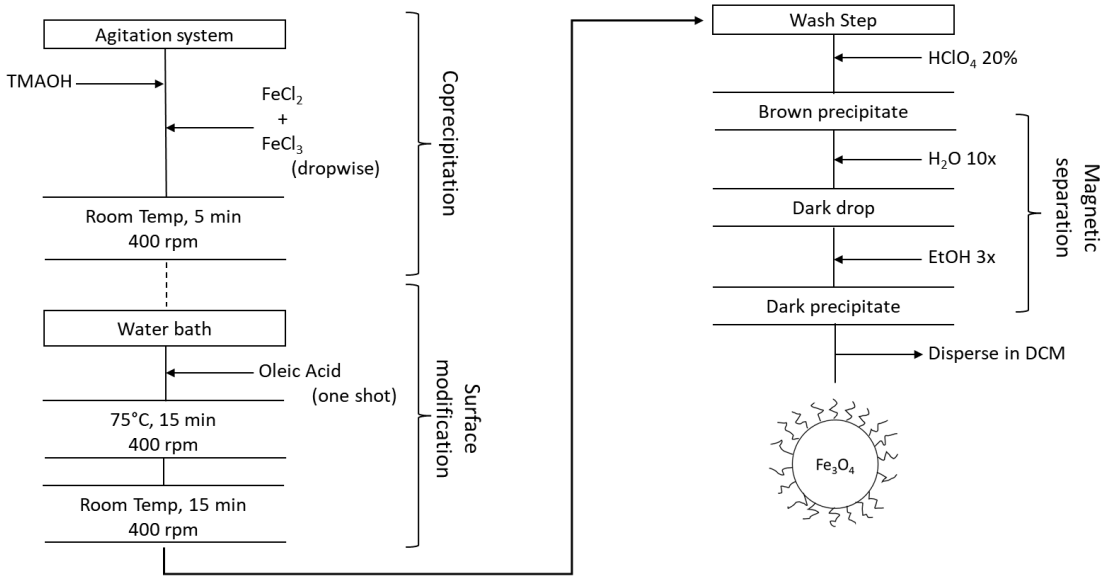

Source: by the author.

II.2.7 Synthesis of CIS/ZnS quantum dots

Synthesis of CIS QDs: The synthesis of copper, indium, and sulfur/zinc sulfide (CIS/ZnS) QDs was performed following a previously reported procedure (WANG et al., 2015; YI et al., 2015) with some modifications. 1-Dodecanethiol (1-DDT) was used as the surface ligand, the sulfur source, and the solvent for the reaction. Typically,

$Cu(acac)_2$ (0.2 mmol), $In(acac)_3$ (0.2 mmol) and 15 mL DDT were mixed in a three-necked flask under magnetic stirring. The mixture was degassed under nitrogen atmosphere at 110°C for 30 min to remove all oxygen atmosphere from the flask. The mixture was then heated to a temperature of 245 °C. At this stage of nucleation and CIS core formation, the nucleation seed growth time was tested in 120 minutes of reaction. Following, the heat source was removed, and the samples were cooled and stored for further ZnS shell formation step.

Synthesis of CIS/ZnS core-shell QDs: The CIS solution was heated to a temperature of 220°C, then a Zn stock solution (110 mg zinc acetate in 8 mL DDT, 1 mL OLA and 1 mL OA) was slowly added to the hot mixture 4 times at 20 min intervals. Finally, the sample was cooled, and an excess of ethanol was added. The solution was centrifuged at 4000 rpm for 30 minutes. After centrifugation, the samples are obtained by drying the centrifugate as a colloidal system. The resulting precipitate was dispersed in a suitable organic solvent (DMC or toluene) of appropriate concentration and stored at 4°C for future use.

Synthesis of FeCIS core QDs: Iron, copper, indium, and sulfur/zinc sulfide (FeCIS/ZnS) QDs are synthesized according to the previously reported method (WANG et al., 2015; YI et al., 2015) with some modifications. 1-Dodecanethiol was used as the surface ligand, sulfur source, and reaction solvent. $Cu(acac)_2$ (0.2 mmol), $In(acac)_3$ (0.2 mmol), $Fe(acac)_3$ (0.1 mmol) and 15 mL DDT are mixed in a three-necked round-bottomed flask under magnetic stirring. The mixture was degassed under a nitrogen atmosphere at 110 °C for 30 min to remove all the oxidative atmosphere from the flask. The mixture was then heated to a temperature of 245°C. In this step of nucleation and core formation of FeCIS, three different growth times of the nucleation seeds (30, 60, and 90 minutes) are tested. Soon after, the heat source was removed, and the samples are cooled down and stored for the next step of the ZnS shell formation process.

Synthesis of FeCIS/ZnS core-shell QDs: FeCIS solution was heated to the temperature of 220°C, then a solution of Zn (110 mg zinc acetate in 8 mL DDT, 1 mL OLA and 1 mL OA) was slowly added to the hot mixture in 4 times at each interval of 20 minutes. Finally, the solution was cooled, an excess of ethanol was added, and the solution was centrifuged at 4000 rpm for 30 minutes. After centrifugation, the samples are obtained in the form of a colloidal system. The precipitate formed was dispersed in an appropriate organic solvent and concentration.

The production of CIS/ZnS core-shell QDs and FeCIS/ZnS core-shell particles was illustrated in **Figure II.3**.

Figure II.3. Flowchart of CIS/ZnS NPs (a) and FeZIS/ZnS NPs (b) production with their surface modification using oleic acid and oleylamine.

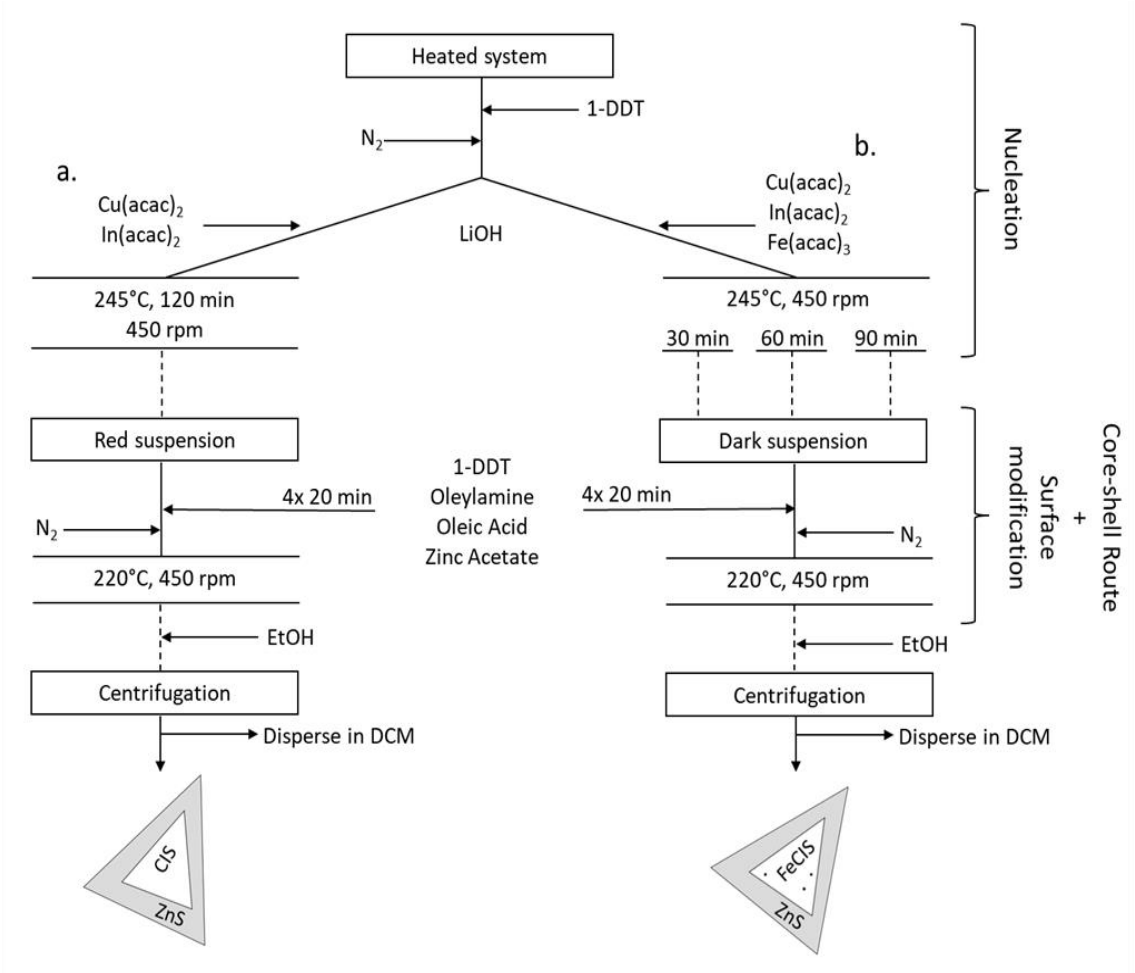

Source: by the author.

II.2.8 Synthesis and coupling of CIS/ZnS NPs with FeZnO NPs

The coupling of CIS/ZnS and FeZnO NPs was carried out following the methodology of Donat et al. (2017), with some modifications. The coupling was performed by heating the NPs in a muffle furnace under a self-assembly process. The coupling was achieved by heating in a muffle furnace at a temperature of 260°C for 5 minutes. The calculated powders were dispersed in chloroform, and after complete solvent evaporation, the resulting mixtures were placed in the muffle furnace. The

proportions used are described in **Table II.2**. The proportions were calculated based on the nominal mass.

Table II.2. Nominal mass proportion of FeZnO@CIS/ZnS samples

Samples	Proportion (w:w)
ZnO@CIS/ZnS 80:20	80% ZnO + 20% CIS/ZnS
ZnO@CIS/ZnS 60:20	60% ZnO + 40% CIS/ZnS
ZnO@CIS/ZnS 40:60	40% ZnO + 60% CIS/ZnS
0.1FeZnO@CIS/ZnS 80:20	80% 0.1FeZnO + 20% CIS/ZnS
0.1FeZnO@CIS/ZnS 60:40	60% 0.1FeZnO + 40% CIS/ZnS
0.1FeZnO@CIS/ZnS 40:60	40% 0.1FeZnO + 60% CIS/ZnS
0.5FeZnO@CIS/ZnS 80:20	80% 0.5FeZnO + 20% CIS/ZnS
0.5FeZnO@CIS/ZnS 60:40	60% 0.5FeZnO + 40% CIS/ZnS
0.5FeZnO@CIS/ZnS 40:60	40% 0.5FeZnO + 60% CIS/ZnS
1.0FeZnO@CIS/ZnS 80:20	80% 1.0FeZnO + 20% CIS/ZnS
1.0FeZnO@CIS/ZnS 60:40	60% 1.0FeZnO + 40% CIS/ZnS
1.0FeZnO@CIS/ZnS 40:60	40% 1.0FeZnO + 60% CIS/ZnS

II.2.9 Synthesis of PLGA-QDs particles

The synthesis of the PLGA polymer system dispersed in water was carried out as described by Luque-Michel, Lemaire & Blanco-Prieto (2021), with a few modifications. The synthesis was performed using 10 mg of PLGA as the starting material.

First, three solutions are prepared:

a) PLGA and QDs solution: in a 5 mL glass tube, 10 mg of poly(lactic-co-glycolic acid) (PLGA) polymer (Resomer RG 503H, PLGA 50:50) was dissolved in 0.8 mL of a mixture of triethylamine and acetyl acetate solution (1:1000), and then 0.2 mL of CA to be encapsulated dispersed in DCM was added at the appropriate concentration; b) 1% T80 solution: In a 5 mL glass tube, 20 mg of T80 are added in 2 mL of pure water; and c) 0.3% T80 and 0.4% PVA solution: 40 mg of PVA and 5 mL of pure water were added to a glass vial. The solution must be stirred and heated to dissolve the PVA. In another glass vial, add 30 mg of T80 and 5 mL of pure water, stock. Mix the two solutions.

The reaction was performed in two steps.

Step 1: Using a glass syringe, add solution (a) dropwise into the glass tube containing solution (b) at 700 rpm and room temperature. A two-phase solution was

observed. Remove the magnetic stirrer and place the ultrasonic probe under an ice bath at 20 W for 20 seconds. A uniform emulsion was formed.

Step 2: Stir solution 3 (400 rpm) at room temperature in a hood with airflow. Slowly add the emulsion from step 1 dropwise using a glass syringe. At the end, a slightly cloudy but stable solution was observed with no formation of visible particles. The solution was kept under magnetic stirring for 1.5 hours with the flask uncapped. The organic solvent was completely removed by evaporation.

The solution was washed 3 times with pure water and centrifuged. The centrifugation step was performed at 12800 rpm, 4°C for 15 minutes in MIKTO 200R centrifuges. The lyophilization step was performed by adding 500 µL of Trehalose 37% (amount based on Trehalose:PLGA, w:w).

The production flowchart of PLGA NPs is described in **Figure II.4**.

Figure II.4. Flowchart of PLGA NPs production containing QDs incorporated.

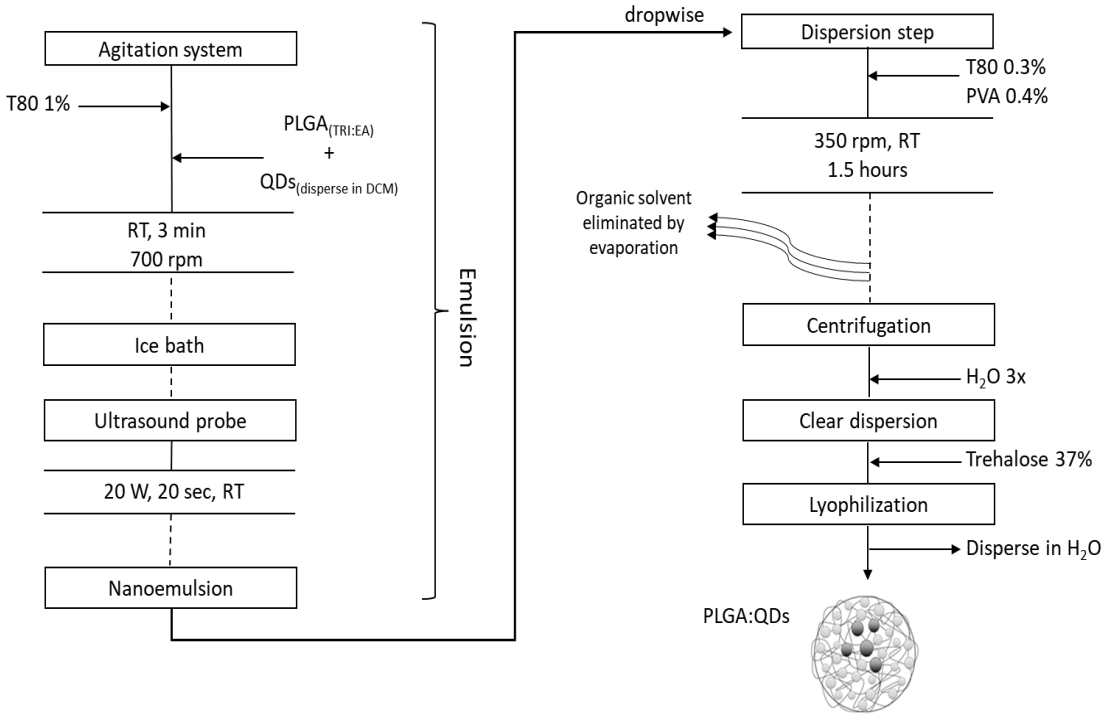

Source: by the author.

II.3 CHARACTETIZARION

II.3.1 Evaluation of luminescent Properties

The absorption spectra were measured using a Cary Win 4000 UV-vis spectrophotometer with a bucket of 1 mm optical path. The spectra of the QD colloidal suspensions were recorded between 200 and 400 nm, with a wavelength step of 1 nm, and an average counting time of 0.2 s per point.

Particles luminescence were evaluated by measuring the spectra of emission (PL) and excitation spectra (PLE). Spectra were recorded in the visible range on a spectrophotometer Fluorolog 3 at room temperature, equipped with a double excitation monochromator, and a Hamamatsu R928 photomultiplier with a Xe lamp (450W). The wavelength of emission and excitation was based in previously wavelength test.

II.3.2 Fourier Transform Infrared Spectroscopy (FTIR)

FTIR-ATR spectra were obtained using a Shimadzu™ Fourier transform infrared spectrophotometer model Affinity-1 (Tokyo, Japan). Spectra were recorded at 25C in the 4000-600 cm^{-1} range in the transmittance mode, with a resolution of 4 cm^{-1} and 32 scans for each sample.

II.3.3 X-Ray Diffraction

The X-ray diffraction (XRD) analyses were performed on a Siemens D5000 diffractometer using Cu-Kalfa with a wavelength in 1.5418 A. The diffraction intensity data were measured in the 2θ range 5 - 80 ° by the step counting method (0.1 deg. step and 3 s counting time).

II.3.4 Transmission Electron Microscopy (TEM)

TEM images were obtained with a JEOL Electron Microscope (model JEM-1400; SUPER TWIN) operated at 600 kV of magnitude. The samples dispersed in water were deposited on carbon grids (100 mesh). Image analysis was performed by ImageJ software (National Institute of Health, Bethesda, MD, USA) in 200, 100, 50 and 20 nm scale bar. More time exposition to see inside. No contrast was used in the analysis.

II.3.5 Inductively Coupled Plasma Mass Spectrometry (ICP-MS)

Iron and zinc concentrations were determined using inductively coupled plasma mass spectrometry (ICP-MS) according to the protocol adopted in partnership with the Institute of Chemical Sciences of the University of Rennes (ISCR).

II.3.6 Evaluation of particle size distribution and zeta potential

Particle size distribution and zeta potential measurements were performed on Malvern Dynamic Light Scattering equipment (Malvern, UK). The samples were diluted adequately in distilled water, and the measurements were made at 25 °C in count rate above 300 kcpt and attn between 6 and 9. Results were collected in triplicate.

II.3.7 Magnetic Resonance Imaging

The MRI was carried out using a 7T scanner (Biospec 70/20 Avance III, Bruker Wissembourg, France) equipped with BGA12S gradient system (675 mT/m). Emission and reception were ensured by a 72 mm diameter resonator. Sets of spin echo sequence weighted in T1 or T2 images were acquired using respectively variable repetitions times (from 200 to 10000ms) with a fixed echo time of 8ms and a fixed repetition time of 2000ms for variable echo time (ranging from 8 to 200ms). In both cases, images were acquired with a field of view = 6 cm x 4 cm, a matrix = 256 x 192, and a slice thickness of 2 mm.

II.3.8 X-ray absorption spectroscopy (XAS)

The X-Ray Absorption near Edge Structure (XANES) and Extended X-Ray Absorption Fine Structure (EXAFS) data were collected at the Synchrontron Soleil (France) wiggler beam line Rock, at a storage ring energy of 2.75 GeV and a nominal current of 500 mA. Reference samples were measured as pellets in boron nitride (15-20% wt. for Zn-based species and 3-4% wt. for Fe-based species. The data were performed with Athena graphical interface software (RAVEL; NEWVILLE, 2005). All spectra were collected using the fluorescence yield mode at room temperature.

II.4 BIOLOGICAL ANALYZES

II.4.1 Cytotoxicity Assay using Resazurin Test

The cytotoxicity assay examines the efficacy of NP treatment under cell culture. The test was performed using resazurin as a dye for dead cells. Phagocytes (TPH-1) were seeded into a 96-well plate 8.5 x 10^3 cells by well. After 24 hours, PLGA NPs were added at a concentration range from 0.078 to 128 ug mL^{-1} for a 4-h and 24-h incubation period. Cells were then washed and allowed to grow for a further 24 h before the addition of 20 µL of resazurin solution 25 µg mL^{-1} in phosphate-buffered saline (PBS). After 4 hours, wells analyses were carried out in the microplate reader EnSpire® (PerkinElmer, Waltham, MA, USA) at 570 nm and the basal absorbance was corrected at 590 nm. The percentage of viable cells was calculated following Equation (1):

$$\text{Viable cells (\%)} = (\text{DO sample} - \text{DO media})/(\text{DO cells} - \text{DO media})/100 \quad (1)$$

where, Viable cells (%) is the percentage of viable cells in the sample, DO sample is the optical density (or absorbance) measured from the sample containing the cells, DO media is the optical density (or absorbance) measured from the cell-free culture medium, and DO cells is the optical density (or absorbance) measured from a sample with a known quantity of viable cells. The analyses were performed in triplicate.

II.4.2 Uptake and fluorescence teste

The cell uptake assay was performed using TPH1 cell line. Cells were seeded onto 24 wells. Increasing concentrations were tested according to cytotoxicity assay for the different CAs. Incubation times were fixed at 4 and 24 hours. After the incubation, the cells were washed to remove the NPs no captured by the cells. The fluorescence analyses were carried out in microplate reader (MA, USA). The excitation in 343 nm and emission in 540 nm was used for PLGA:ZnO:IO.

REFERENCES

BABES, L. et al. Synthesis of Iron Oxide Nanoparticles Used as MRI Contrast Agents: A Parametric Study. **Journal of Colloid and Interface Science**, v. 212, n. 2, p. 474–482, 15 abr. 1999.

DONAT, F. et al. ZnO nanoparticles sensitized by CuInZn x S2+x quantum dots as highly efficient solar light driven photocatalysts. **Beilstein journal of nanotechnology**, v. 8, n. 1, p. 1080–1093, 2017.

LALLO DA SILVA, B. et al. Increased antibacterial activity of ZnO nanoparticles: Influence of size and surface modification. **Colloids and Surfaces B: Biointerfaces**, v. 177, p. 440–447, 1 maio 2019.

LUQUE-MICHEL, E.; LEMAIRE, L.; BLANCO-PRIETO, M. J. SPION and doxorubicin-loaded polymeric nanocarriers for glioblastoma theranostics. **Drug Delivery and Translational Research**, v. 11, n. 2, p. 515–523, 1 abr. 2021.

MANAIA, E. B. et al. Surface modified Mg-doped ZnO QDs for biological imaging. **European Journal of Nanomedicine**, v. 7, n. 2, p. 109–120, 1 abr. 2015.

MANAIA, E. B. et al. Physicochemical characterization of drug nanocarriers. **International Journal of Nanomedicine**, v. 12, p. 4991–5011, 13 jul. 2017.

MEULENKAMP, E. A. Synthesis and Growth of ZnO Nanoparticles. **Journal of Physical Chemistry B**, v. 102, n. 29, p. 5566–5572, 16 jul. 1998.

RAVEL, B.; NEWVILLE, M. ATHENA, ARTEMIS, HEPHAESTUS: data analysis for X-ray absorption spectroscopy using IFEFFIT. urn:issn:0909-0495, v. 12, n. 4, p. 537–541, 15 jun. 2005.

SPANHEL, L.; ANDERSON, M. A. Semiconductor Clusters in the Sol-Gel Process: Quantized Aggregation, Gelation, and Crystal Growth in Concentrated ZnO Colloids. **Journal of the American Chemical Society**, v. 113, n. 8, p. 2826–2833, 1991.

WANG, X. et al. A high efficient photoluminescence Zn-Cu-In-S/ZnS quantum dots with long lifetime. **Journal of Alloys and Compounds**, v. 640, p. 134–140, 15 ago. 2015.

YI, C. et al. Synthesis, characterization and biomedical application of multifunctional luminomagnetic core-shell nanoparticles. **Materials Science and Engineering C**, v. 46, p. 32–40, 1 jan. 2015.

CHAPTER III

Study of PLGA particles containing NPs of ZnO and IO for bimodal image

CHAPTER III. Study of PLGA particles containing NPs of ZnO and IO for bimodal image

III.1 INTRODUCTION

PLGA NPs were chosen to incorporate the studied CAs. PLGA is a biodegradable copolymer that can be easily formed into NPs by a simple emulsion method and used as a drug delivery system. The synthesized nanosystem were characterized using dynamic light scattering for size and zeta potential, MRI for Mp and fluorescence spectroscopy for luminescence. TEM was also performed to assess the morphology. PLGA particles, PLGA containing ZnO, PLGA containing IO, and PLGA containing both ZnO and IO were evaluated.

III.2 RESULTS AND DISCUSSION

III.2.1 Synthesis of ZnO NPs coated with Oleic Acid

The synthesis of ZnO NPs was performed as described by Spanhel & Anderson (1991). The results are shown in **Figure III.1**.

Figure III.1 Pictures of a) System of zinc acetate precursor preparation; b) colloidal suspension of ZnO at day light; c) colloidal suspension of ZnO in a UV chamber when excited in a 365 nm lamp.

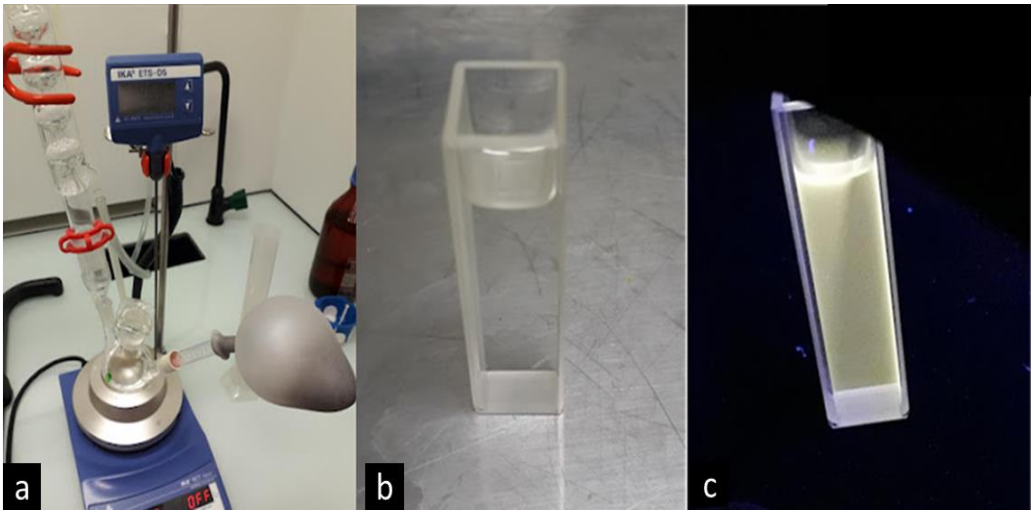

Source: by the author.

The zinc acetate precursor (**Figure III.1a**) was transparent and the ZnO suspension showed luminescence when excited in the UV-Vis chamber at a wavelength of 365 nm (**Figure III.1c**). To ensure luminescence stability against aggregation and pH degradation, the surface of the ZnO particle must be modified. Coating with oleic acid was shown to be efficient to fulfil this goal with Mg-doped ZnO (MANAIA et al., 2015) and NP coated, or at least IO coated with oleic acid have been shown to help for the embedding within PLGA particle (LUQUE-MICHEL, LEMAIRE, BLANCO-PRIETO, 2021). This molecule was then tested.

First, the amount of oleic acid required for the coating was evaluated. Different volumes ranging from 50 and 125 µL of oleic acid were tested for 10 mL of ZnO suspension at the theoretical concentration of 0.05 mol L^{-1} (**Figure III.2**).

Figure III.2. Picture of ZnO ethanolic suspensions coated with different concentrations of oleic acid and observed by UV chamber at 365 nm: a) 50 µL OA (14 mmol L^{-1}), b) 60 µL OA (17 mmol L^{-1}), c) 75 µL OA (21 mmol L^{-1}), d) 100 µL OA (28 mmol L^{-1}), and e) 125 µL OA (35 mmol L^{-1}). Luminescence was observed by UV chamber when excited in a 365 nm lamp.

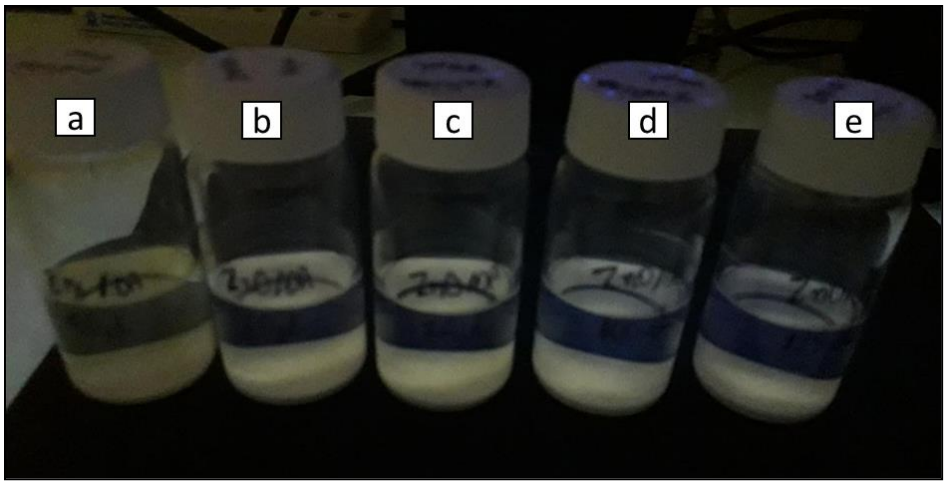

Source: by the author.

Figure III.2. shows that with 50 µL of oleic acid (14 mmol L^{-1}) the supernatant remains yellow when excited at 254 nm. This suggests that at this concentration there are uncoated ZnO NPs. This solution was ignored. For the other solutions, the luminescence was observed in the precipitate formed, the solution obtained with 75 µL of oleic acid (21 mmol L^{-1}) looking the most intense. The samples were kept refrigerated overnight. The samples are shown in **Figure III.3**.

Figure III.3. Pictures of ZnO NPs coated by a) 60 µL (17 mmol L^{-1}), b) 75 µL (21 mmol L^{-1}), c) 100 µL (28 mmol L^{-1}) and d) 125 µL (35 mmol L^{-1}) of oleic acid and dispersed in ethanol.

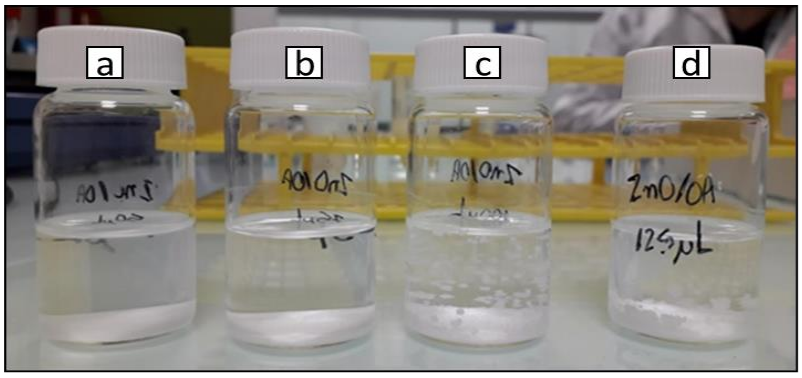

Source: by the author.

According to **Figure III.3**, some deposits of oleic acid are observed on the glass vials wall for the ZnO coated with OA by 100 µL (28 mmol L^{-1}) and 125 µL (35 mmol L^{-1}) samples. This suggests that oleic acid was in excess ion. The samples were centrifuged at 2000 rpm for 10 min and washed 3 times with 10 mL of ethanol each time. The samples were kept drying by 1-2 hours in the hood to study the coating using infrared technique. The results are shown in **Figure III.4**.

Figure III.4. Infrared spectra of uncoated ZnO NP compared to ZnO samples coated with 60 µL (17 mmol L^{-1}), 75 µL (21 mmol L^{-1}), 100 µL (28 mmol L^{-1}) and 125 µL (28 mmol L^{-1}) of oleic acid.

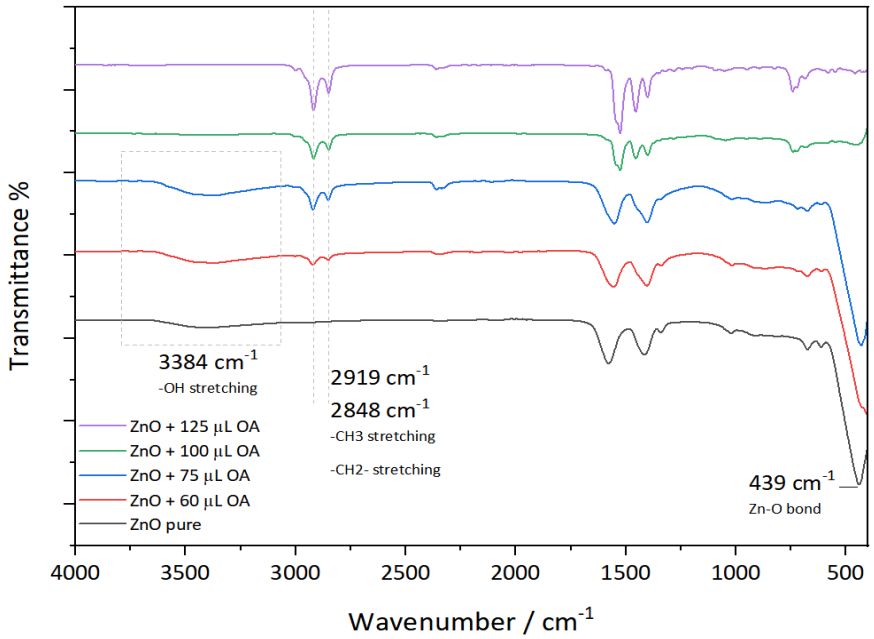

Source: by the author.

Based on the results shown in **Figure III.4**, the stretching bands at 2919 cm^{-1} and 2848 cm^{-1} are attributed to the stretching of $-CH_3$ and $-CH_2$, respectively, indicating the presence of oleic acid as observed by Yang et al. (2016). Additionally, the absorption band at 439 cm^{-1} is attributed to the Zn-O bond in ZnO NPs (Chakraborty et al., 2019). The -OH stretch at 3384 cm^{-1}, attributed to OH clusters on the surface of the ZnO NPs, disappears with increasing amounts of oleic acid in the synthesis.

This suggests that the structure of the ZnO is maintained when the solution is synthesized with 60 µL (17 mmol L^{-1}) and 75 µL (21 mmol L^{-1}) of oleic acid. However, with 100 µL of oleic acid, the ZnO bands disappear completely, indicating that the ZnO NPs are no longer present or are significantly covered by oleic acid. This disappearance might also be influenced by the decrease in solution pH, which could affect the stability of the ZnO NPs.

The next step corresponds to the evaluation of the fluorescence properties of the different preparation when redispersed in DCM (the solvent used for the PLGA based NP synthesis). The results are presented in **Figure III.5.**

Figure III.5. Pictures of ZnO samples coated with 60 µL (17 mmol L^{-1}), 75 µL (21 mmol L^{-1}), 100 µL (28 mmol L^{-1}) and 125 µL (28 mmol L^{-1}) of oleic acid dispersed in DCM.

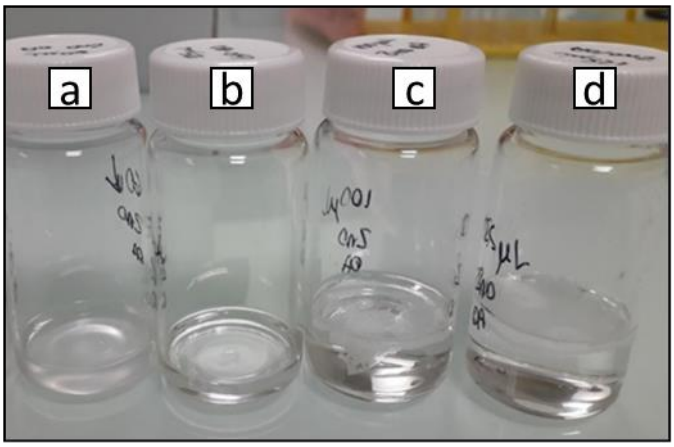

Source: by the author.

According to the results presented in **Figure III.5**, all samples were dispersed in sufficient volumes of DCM to obtain a final concentration of 40 mg mL^{-1}. It was observed that the solution synthesised from 60 µL of oleic acid showed turbidity with

the presence of precipitates. It can be assumed that the amount of oleic acid was not sufficient to completely coat and disperse the ZnO in the medium. The sample was discarded. In the solutions synthesised from 100 µL and 125 µL oleic acid, part of the oleic acid did not dissolve in the DCM and formed a drop on the surface. ZnO/OA with 75 µL oleic acid (21 mmol L^{-1}) was the only sample that gave a clear solution. The solutions remained luminescent when excited under a lamp at 365 nm. The samples synthesised from 75 µL, 100 µL and 125 µL of oleic acid were evaluated by emission spectrum when excited at 343nm. The results are shown in **Figure III.6**.

Figure III.6. Emission spectra of ZnO NPs coated with different concentrations of 75 µL (21 mmol L^{-1}), 100 µL (28 mmol L^{-1}) and 125 µL (35 mmol L^{-1}) of oleic acid dispersed in DCM with a final concentration of 40 mg mL^{-1}. Excitation wavelength in 343 nm.

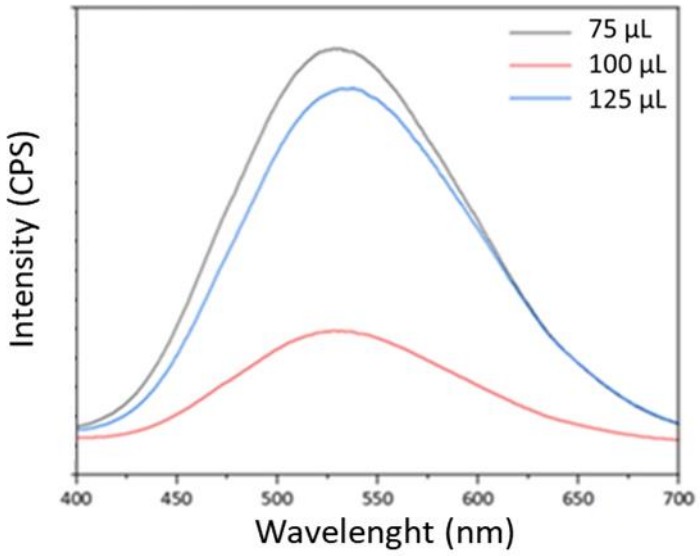

Source: by the author.

Figure III.6 shows that the amount of oleic acid used can interfere with the ZnO luminescence. The results are shown for the excitation wavelength of 343 nm. All samples were prepared under the same synthesis conditions. The concentration of 100 µL oleic acid shows lower luminescence. For all the tested conditions, the concentration of 75 µL (21 mmol L^{-1}) of oleic acid for 10 mL of suspension ethanolic of ZnO NP at a theoretical concentration of 0.05 mol L^{-1} gives the best results. Hence, 75 µL of oleic acid has been selected as the permanent amount for use in assays with PLGA NPs.

III.2.2 Synthesis of IO NPs coated with Oleic Acid

The synthesis method was based on the procedure described by Babes et al. (1999). However, the amount of IO recovered after dispersion in DCM is not specified in the report. To optimize this process, a method was developed to wash and purify the IO using only ethanol, avoiding any aggregation.

After synthesis and drop formation in water, the IO NPs were washed with 5 mL of ethanol in a glass vial. The NPs were dried for 2 h and dispersed in DCM. The results are shown in **Figure III.7**.

Figure III.7. Pictures of a) IO/OA coated in ethanol separated by magnet; and b) IO/OA coated dispersed in DCM at the concentration of 40 mg mL^{-1}.

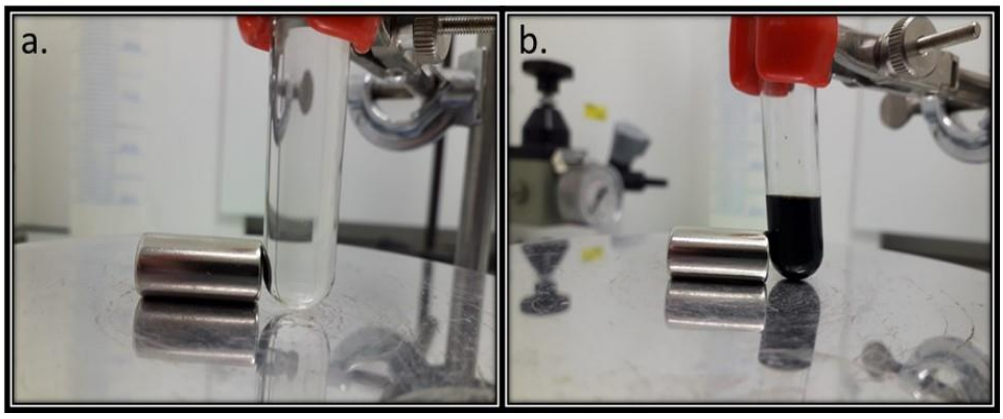

Source: by the author.

As shown in **Figure III.7**, NPs IO/OA are easily separated in ethanol when a Mf was applied. The ethanol washing process, using only the Mf, allowed the elimination of excess oleic acid that did not react with the IO particles. The oleic acid is soluble in ethanol and serves both to remove excess oleic acid and to evaporate residual water. When dispersed in DCM (**Figure III.7b**), NPs easily disperse. However, separation was difficult. As observed when dispersed in ethanol, a Mf is present, but it is not completely separated within minutes. It is possible that it has a colloidal stability in the DCM. After 24 hours of storage, the solution was subject to analysis. The results are shown in **Figure III.8**.

Figure III.8. Pictures of IO/OA coated dispersed in DCM after 24 hours of synthesis and storage at RT and with Mf applied (right image).

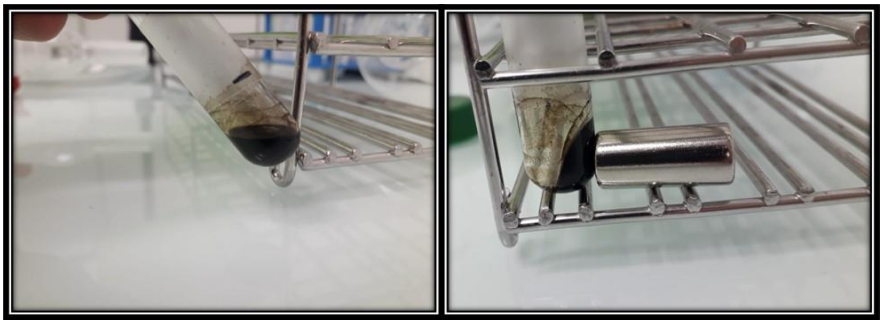

Source: by the author.

According to **Figure III.8**, some of the solvent has evaporated. The Mf remains, but as the solvent evaporated, some larger particles appeared, showing the aggregation process and the loss of the initial concentration. Therefore, the oleic acid-coated IO can be stored in ethanol before use, or the suspension can be used on the same day of preparation to obtain a suspension with suitable stability.

III.2.3 PLGA:ZnO:IO particles

The synthesis of PLGA particles was performed by a simple solvent evaporation emulsion reaction described by Luque-Michel, Lemaire & Blanco-Prieto (2021). Some parameters of the synthesis were modified so that the product formed has suitable luminescence results.

The synthesis of PLGA NPs containing ZnO and IO was determined by the nominal ratio of each component in the formulation. For instance, in a sample of PLGA:ZnO:IO 10:1:1 (w:w:w, mg), the initial ratio of components used is 10 mg of PLGA, 1 mg of ZnO, and 1 mg of IO. Preliminary results can be observed by looking at the luminescence results of each sample.

III.2.3.1 PLGA:IO

The first step was to test different ratios between each of the components and their responses as a function of size, zeta potential, absorbance, and luminescence (excitation and emission). The ratio of the NPs containing the IO was the first one to be

tested. Amounts of IO/AO were tested in the range of 1 to 4 mg. **Table III.1** describes the ratio of each formulation to mass.

Table III.1. Nominal ratio of the IO to PLGA used in the experiments.

Sample	Proportion
PLGA:IO 10:1 (w:w, mg)	10 mg of PLGA + 1 mg IO/AO
PLGA:IO 10:2 (w:w, mg)	10 mg of PLGA + 2 mg IO/AO
PLGA:IO 10:3 (w:w, mg)	10 mg of PLGA + 3 mg IO/AO
PLGA:IO 10:4 (w:w, mg)	10 mg of PLGA + 4 mg IO/AO

The results of the particle size distribution are described in **Table III.2**.

Table III.2. Size of PLGA:IO particles in DLS analyses.

PLGA:IO	Synthesis		15 days	
(w:w, mg)	Size (nm)	PDI	Size (nm)	PDI
10:1	152.1 ± 0.9	0.099 ± 0.026	149.5 ± 0.4	0.120 ± 0.015
10:2	146.8 ± 0.8	0.128 ± 0.013	144.9 ± 3.1	0.174 ± 0.024
10:3	148.7 ± 1.5	0.106 ± 0.007	148.1 ± 0.8	0.136 ± 0.014
10:4	147.8 ± 0.6	0.184 ± 0.017	145.4 ± 2.9	0.164 ± 0.010

The size of PLGA:IO NPs with varying IO ratios remained largely unchanged after 15 days in PVA solution, as indicated in **Table III.2**. Furthermore, the size of PLGA:IO particles appeared consistent across different IO ratios. The uniformity in size is evidenced by the PDI values after 15 days, indicating suspension stability. The particle size falls within the range of 100 to 300 nm, conducive to effective incorporation (CHIU et al., 2021a). Luminescence parameters of the samples are analysed. PLGA:IO and PLGA NPs are tested. The results are shown in **Figure III.9**.

Figure III.9. Representation of PLGA:IO particles solutions, arranged from left to right: PLGA:IO 10:1, 10:2, 10:3, and 10:4 (a). Excitation spectra with emission at 540 nm (b), emission spectra with excitation at 343 nm (c), and emission spectra with excitation at 350 nm (d).

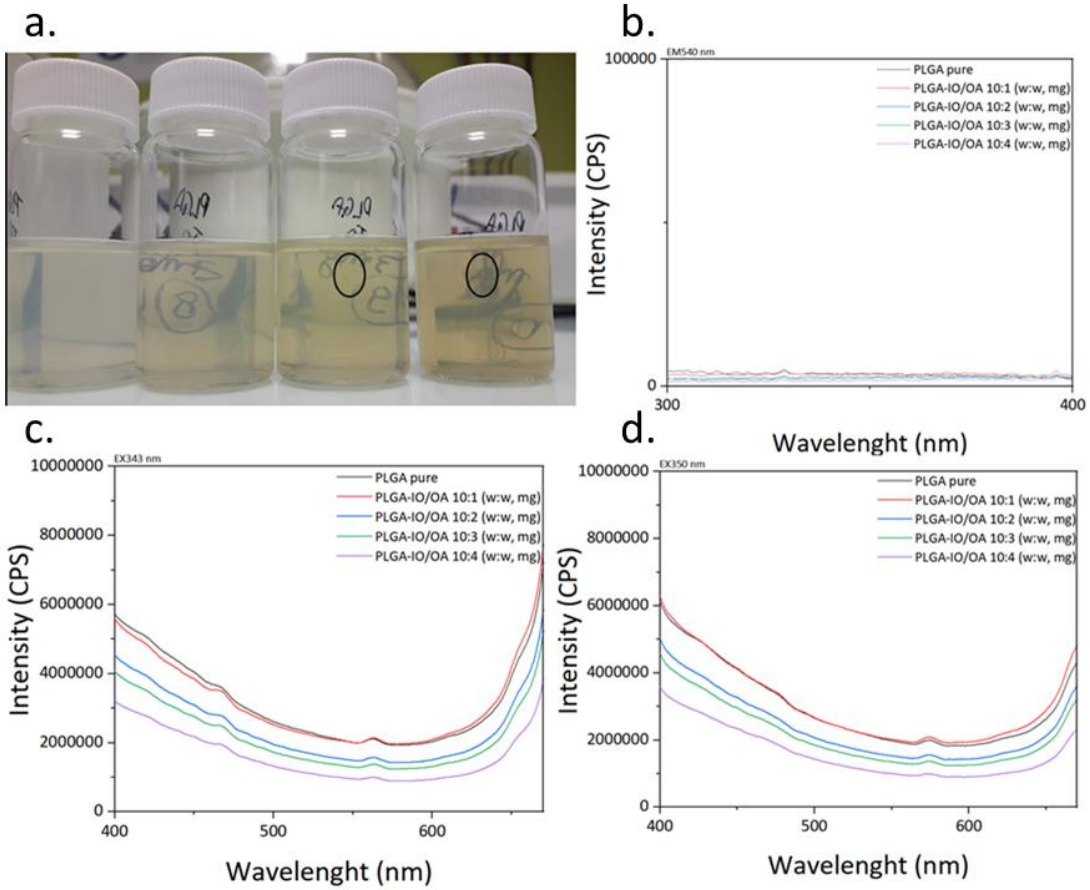

Source: by the author.

According to **Figure III.9**, Analysis was conducted on the emission spectra resulting from sample excitation at 343 nm and 350 nm, along with the excitation spectra corresponding to emission at 540 nm. These wavelengths align with those commonly employed for both excitation and emission of pristine ZnO. As anticipated, PLGA:IO NPs exhibited no excitation bands within the ZnO excitation range, reflecting the absence of ZnO in their composition (**Figure III.9b**). Moreover, an inverse relationship was observed between the luminescence intensity at 540 nm and the iron content used for NP formation, with higher iron amounts correlating with decreased intensity of luminescence (**Figure III.9c**). Additionally, PLGA exhibited no discernible emission or excitation intensity at these wavelengths.

III.2.3.2 PLGA:ZnO

NPs with different ratios of PLGA and ZnO are also investigated. The nominal proportion of PLGA and ZnO studied are shown in **Table III.3**.

Table III.3. Nominal ratio of the ZnO to PLGA used in the experiments.

Sample	Proportion
PLGA:ZnO 10:2 (w:w, mg)	10 mg of PLGA + 2 mg ZnO/AO
PLGA:ZnO 10:4 (w:w, mg)	10 mg of PLGA + 4 mg ZnO/AO
PLGA:ZnO 10:6 (w:w, mg)	10 mg of PLGA + 6 mg ZnO/AO
PLGA:ZnO 10:8 (w:w, mg)	10 mg of PLGA + 8 mg ZnO/AO

The amount of ZnO coated with oleic acid was dispersed in DCM at a concentration of 40 mg mL^{-1}. The amount in volume was added in the proportions described in **Table III.3** and dissolved in DCM to a final volume of 0.2 mL. The results are shown in **Figure III.10**.

Figure III.10. Pictures of samples after synthesis and excited by the 245 nm lamp of PLGA:ZnO proportion of a) 10:2, b) 10:4, c) 10:6, and d) 10:8.

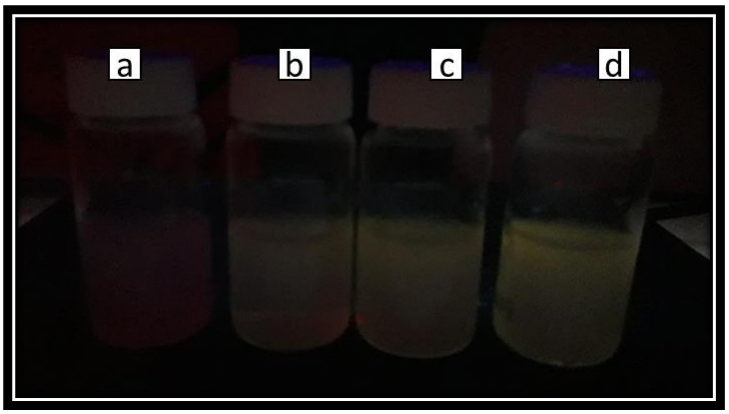

Source: by the author.

According to **Figure III.10**, the PLGA:ZnO 10:4, 10:6, and 10:8 samples remained luminescent when excited in a 254 nm lamp. This indicates that the ZnO properties remained unchanged after incorporation into the PLGA particle. Particle sizes were evaluated in PVA and T80 solution and the results are shown in **Table III.4**.

Table III.4. DLS analysis of PLGA:ZnO NPs for size determination.

PLGA:ZnO	Synthesis		15 days	
(w:w, mg)	Size (nm)	PDI	Size (nm)	PDI
10:2	251.5 ± 1.5	0.118 ± 0.016	243.0 ± 1.1	0.096 ± 0.022
10:4	211.4 ± 10.9	0.205 ± 0.014	254.2 ± 1.9	0.189 ± 0.023
10:6	224.6 ± 2.9	0.078 ± 0.040	226.3 ± 1.9	0.069 ± 0.025
10:8	219.4 ± 1.3	0.093 ± 0.016	214.8 ± 1.5	0.095 ± 0.002

According to the results in **Table III.4**, the size of the PLGA:ZnO NPs is about 220 nm. The size is larger compared to the size of PLGA:IO NPs (~150nm), indicating that the loading of ZnO NPs has a different interaction behaviour with PLGA. The size of the particles did not change after 15 days of storage in PVA solution. Samples were analysed using luminescence techniques. The samples were diluted at a ratio of 2:1000 (v:v) sample:water. The results are presented in **Figure III.11**.

Figure III.11. Spectroscopic analysis of PLGA:ZnO (w:w, mg) in proportion 10:2, 10:4, 10:6, and 10:8. a) Absorbance spectra between 200 to 400 nm; b) Excitation spectra, emission in 540 nm; c) Emission spectra, excitation in 343 nm; and d) Emission spectra, excitation in 350 nm.

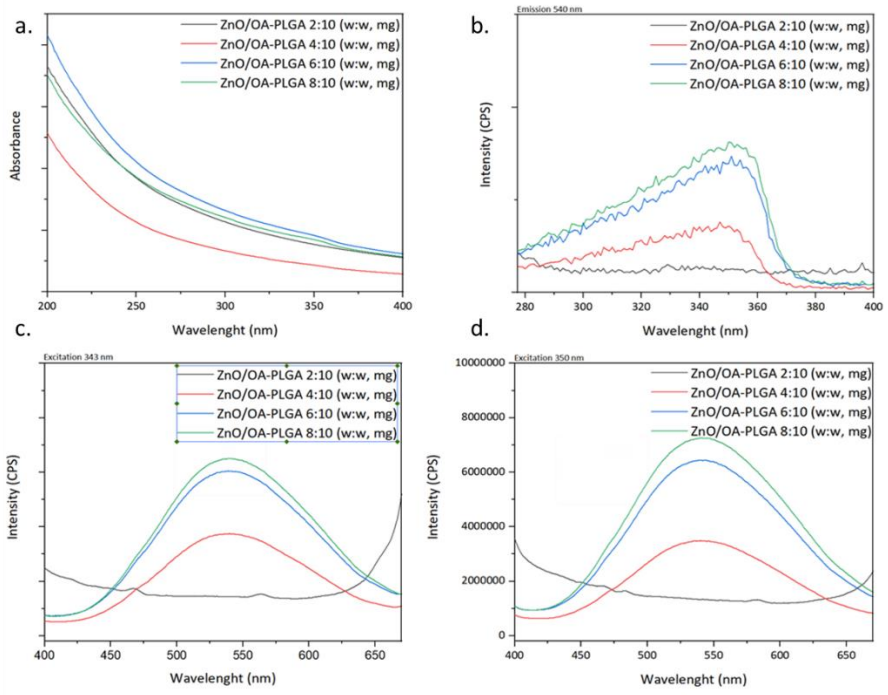

Source: by the author.

The absorbance plots of the samples incorporated into the PLGA polymer system do not clearly display the ZnO band at ~350 nm, as showed in **Figure III.11a**. This is primarily due to the overlapping absorbance of the polymer and the absence ZnO band being analysed. Consequently, confirming the presence of ZnO in the NPs solely based on absorbance spectra is challenging. However, examination of the excitation spectrum (**Figure III.11b**) clearly indicates the presence of ZnO. Additionally, a distinct excitation region peaking between 340 and 360 nm is observed in the PLGA:ZnO excitation spectrum, characteristic of ZnO. Notably, within this excitation range, the nanosystem exhibits strong emission. The behaviour of the excitation spectrum varies depending on the concentration of ZnO in the PLGA polymer system, with a decrease in intensity observed above 365 nm. Consequently, two emission spectra were constructed: one based on excitation at 343 nm, consistent with previous tests, and the other at 350 nm, close to the excitation wavelength limit. The choice of 343 nm excitation is preferred, as it minimizes excitation losses dependent on ZnO NP size, ensuring accurate intensity measurement. The intensity of luminescence increases with the ZnO concentration in the polymer system, with PLGA:ZnO 10:8 displaying the highest luminescence intensity observed. Interestingly, the emission intensity of PLGA:ZnO 10:6 is comparable to that of PLGA:ZnO 10:8. Notably, at an excitation wavelength of 350 nm, the luminescence intensity is higher compared to 343 nm excitation, without any observed shift in the emission peak, which remains around 540 nm. However, despite multiple attempts, no luminescence was detected for the PLGA:ZnO 10:2 sample. This suggests a minimum threshold of ZnO concentration necessary to induce luminescence. The samples were washed 3 times with water under centrifugation at 10000 rpm, temperature of 4°C and time of 30 minutes for each wash. The solution was then diluted with water. The results are shown in **Figure III.12**.

Figure III.12. Pictures of PLGA:ZnO samples after washing and excitation with a 365 nm lamp: a) 10:2; b) 10:4; c) 10:6; and d) 10:8.

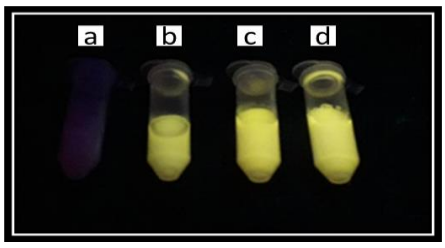

Source: by the author.

After washing (**Figure III.12**), the luminescence of the samples was maintained. Suitable dispersion in water was obtained. The samples were stored at ~4°C for 5 days. The size of the PLGA:ZnO particles was evaluated, and the results are shown in **Table III.5**.

Table III.5. Size of PLGA NPs containing ZnO in different proportions after 5 days of dispersion in water.

PLGA:ZnO (w:w, mg)	Size (nm)	PDI
10:2	267.0 ± 3.3	0.072 ± 0.016
10:4	254.2 ± 1.9	0.189 ± 0.023
10:6	359.6 ± 3.5	0.289 ± 0.021
10:8	434.1 ± 3.5	0.375 ± 0.037

Some conclusions can be drawn from **Table III.5**. Before the washing step, the samples obtained a reasonable size after synthesis (~220 nm). After a few days of storage at ~4 °C, under the conditions of synthesis, the size was maintained. After washing, the samples were diluted in 1 mL water and stored in a freezer, The size of the NPs increased with the increase in the nominal amount of ZnO used.

According to the results, the PLGA:ZnO NPs containing 2 mg of ZnO are not able to show any luminescent properties according to the emission and excitation spectra. In addition, by analysing the images of the excited solutions in the UV camera at 365 nm, the absence of luminescence can be verified. This PLGA:ZnO 10:2 (w:w, mg) NP preparation was not considered for further testing. For the PLGA:ZnO 10:4 (w:w, mg) NP preparation , luminescence was observed, but the luminescence intensity was lower than for PLGA:ZnO 10:6 (w:w, mg) and PLGA:ZnO 10:8 (w:w, mg) NP. Interestingly, luminescence intensity of the PLGA:ZnO 10:6 (w:w, mg) and PLGA:ZnO 10:8 (w:w, mg) NP preparation are close suggesting that a plateau may be reached. It has also been observed that the concentration of the ZnO is a critical factor for the stability of the system. The more ZnO incorporated into the PLGA particle, the larger the NP and the lower the NP stability in water. The minimum and maximum concentrations of ZnO and IO incorporated into the PLGA NPs were evaluated for the next tests.

III.2.3.3 ZnO & IO interaction

Preliminary results have shown that the luminescence intensity of the ZnO suspension in DCM is significantly reduced in the presence of IO. Therefore, the luminescence intensity behaviour of ZnO mixed and dispersed in DCM in the presence of IO was evaluated as a first step. Concentrations ranging from 1 mg to 4 mg of IO were observed in the presence of 4 mg of ZnO. The samples, initially at a concentration of 40 mg mL^{-1}, were diluted in a 2:1000 (v:v) ratio to a final theoretical concentration of 80 μg mL^{-1}. The results are shown in **Figure III.13**.

Figure III.13. Different ratios of ZnO and IO dispersed in DCM. a) Emission spectrum, excitation at 343 nm; b) Emission spectrum, normalized intensity; c) plot of intensity maximum of ZnO:IO in DCM at different ratios; and d) wavelength maximum of ZnO:IO in DCM at different ratios.

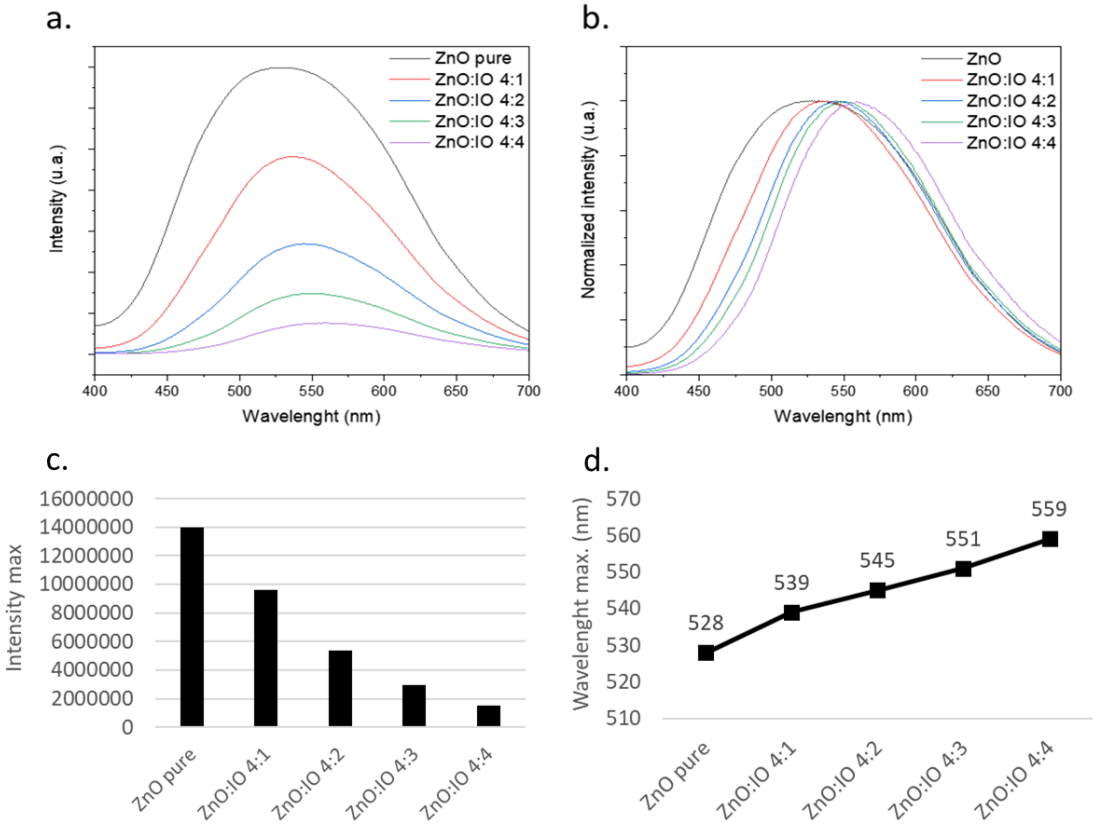

Source: by the author.

The luminescence of ZnO in the presence of IO dispersed in DCM was studied (**Figure III.13**). According to the results obtained, two important conclusions can be

drawn. First, with increasing IO concentration, the luminescence intensity of the dispersion decreases. Second, with increasing IO concentration, the maximum emission wavelength shifts to the right. There is a red shift of 30 nm. Thus, the luminescence properties of the material is affected by the presence of IO.

III.2.3.4 PLGA:ZnO:IO size and luminescence study

According to the impact of the IO on ZnO luminescence in DCM solution, the impact of the ratio IO/ZnO in PLGA was also evaluated. ZnO was fixed at the highest nominal mass tested in PLGA:ZnO study, i.e. 8mg of ZnO for 10 mg PLGA. IO were tested for quantities ranging between 1mg and 4mg. The assays tested are described in **Table III.6**.

Table III.6. IO ratio as a function of the PLGA particle size, with a constant amount of ZnO.

Sample	**Proportion**
PLGA:ZnO:IO 10:8:1 (w:w, mg)	10 mg of PLGA + 8 mg ZnO + 1 mg IO
PLGA:ZnO:IO 10:8:2 (w:w, mg)	10 mg of PLGA + 8 mg ZnO + 2 mg IO
PLGA:ZnO:IO 10:8:3 (w:w, mg)	10 mg of PLGA + 8 mg ZnO + 3 mg IO
PLGA:ZnO:IO 10:8:4 (w:w, mg)	10 mg of PLGA + 8 mg ZnO + 4 mg IO

The samples were analysed for their size on the day of synthesis and for their stability after 15 days of storage. The results of these tests are shown in **Table III.7**.

Table III.7. Size of PLGA NPs containing ZnO in different proportions after 15 days of dispersion in water and storage at approximately 4°C.

PLGA:ZnO:IO	Synthesis		15 days	
(w:w:w, mg)	Size (nm)	PDI	Size (nm)	PDI
10:8:1	247.0 ± 2.3	0.157 ± 0.020	236.0 ± 2.2	0.144 ± 0.019
10:8:2	280.3 ± 2.9	0.204 ± 0.042	270.1 ± 5.5	0.191 ± 0.022
10:8:3	236.1 ± 1.6	0.233 ± 0.006	277.1 ± 9.3	0.289 ± 0.109
10:8:4	264.6 ± 7.5	0.288 ± 0.034	318.6 ± 69.1	0.409 ± 0.113

According to the results in **Table III.7**, two important conclusions can be made regarding the size of the NPs: The size of the synthesized NPs remained in the range of 240 to 280 nm, which remains in the range of the PLGA:ZnO particles synthesized without IO. With time, after 15 days of storage at ~4 °C, the tested preparations showed that the particles with the highest IO content tend to grow. The solutions were evaluated by luminescence assay after 15 days storage. The change of luminescence between 0 and 15 days of the synthesis was not evaluated. The results are shown in **Figure III.14**.

Figure III.14. Spectra of samples of PLGA:ZnO:IO, ZnO = 8 mg, IO = 1, 2, 3, and 4 mg. a) Emission spectra with excitation wavelength at 350 nm, b) emission spectra with excitation wavelength at 343 nm, and c) excitation spectra with emission wavelength at 540 nm.

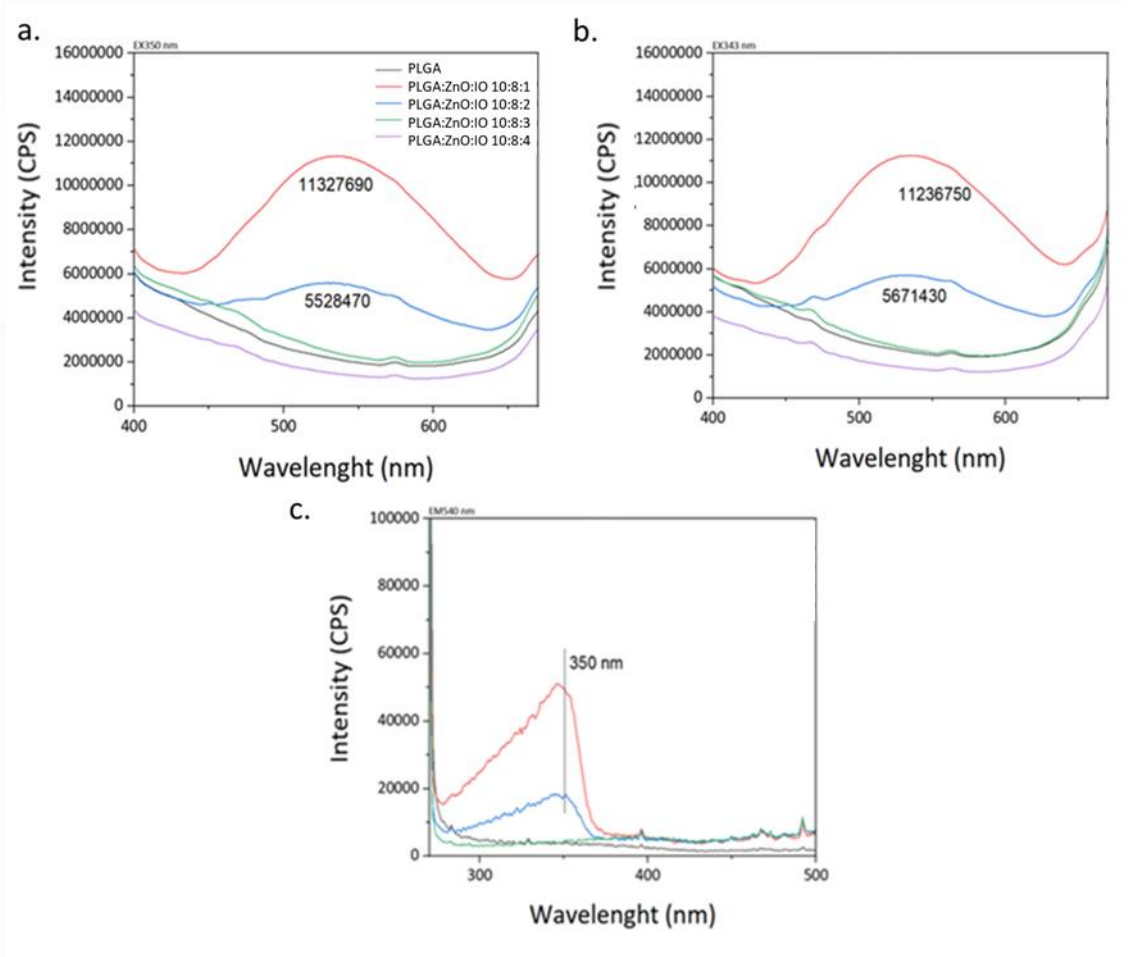

Source: by the author.

It can be observed that the luminescence intensity of the ZnO QDs is strongly affected by the increase in the amount of IO as shown in **Figure III.14**. When excited at 350 and 343 nm, the luminescence intensity of the PLGA:ZnO:IO 10:8:1 samples

shows the same luminescence intensity. Increasing the iron content to 2mg to produce the PLGA:ZnO:IO 10:8:2 samples, decreases luminescence intensity. At higher amounts of IO, the luminescence is null. Therefore, the best concentration of IO for testing the PLGA:ZnO:IO samples is 1 mg. This concentration will have to be investigated for MRI contrast.

Even though the PLGA:ZnO experiments reported in Section III.2.3.2 and the PLGA:ZnO:IO experiment reported above, we have explored the impact of the ZnO amount, keeping the iron amount at 1mg. The tested samples are described in **Table III.8**.

Table III.8. PLGA:ZnO:IO samples with different amounts of ZnO and IO

Sample	Proportion
PLGA:ZnO:IO 10:4:1 (w:w, mg)	10 mg of PLGA + 4 mg ZnO + 1 mg IO/AO
PLGA:ZnO:IO 10:6:1 (w:w, mg)	10 mg of PLGA + 6 mg ZnO + 1 mg IO/AO
PLGA:ZnO:IO 10:8:1 (w:w, mg)	10 mg of PLGA + 8 mg ZnO + 1 mg IO/AO

The size of the PLGA particles was analysed after synthesis and 15 days after formulation. The results are shown in **Table III.9**.

Table III.9. PLGA:ZnO:IO samples with different amounts of ZnO

PLGA:ZnO:IO	Synthesis		15 days	
(w:w:w, mg)	Size (nm)	PDI	Size (nm)	PDI
10:4:1	193.8 ± 0.3	0.061 ± 0.012	200.1 ± 0.4	0.091 ± 0.017
10:6:1	235.0 ± 0.8	0.066 ± 0.021	222.0 ± 1.8	0.096 ± 0.030
10:8:1	247.0 ± 2.3	0.157 ± 0.020	236.0 ± 2.2	0.144 ± 0.019

According to the results of the **Table III.9**, it can be seen that PLGA:ZnO:IO NPs with mass variations depending on the amount of ZnO did not show significant differences in PLGA particle size. And they were stable in PVA+T80 solution in the period of 15 days stored at low temperature. The 10:2:1 ratio was not tested because it has already been found that there is no significant presence of luminescence in this synthesis ratio. The PDI of the tested formulations also remained constant with low values. This means that the samples are presented in the form of a monodispersion. A

test of the luminescence properties after 15 days was carried out. Difference between intensity of luminescence after 15 days was not evaluated. Samples were diluted in 10:1000 (v:v) PLGA:water. The results are shown in **Figure III.15**.

Figure III.15. Luminescence results of PLGA:ZnO:IO, with differences proportion of ZnO: a) excitation spectra with emission in 540 nm, b) emission spectra with excitation in 343 nm, and c) emission spectra with excitation lamp in 350 nm.

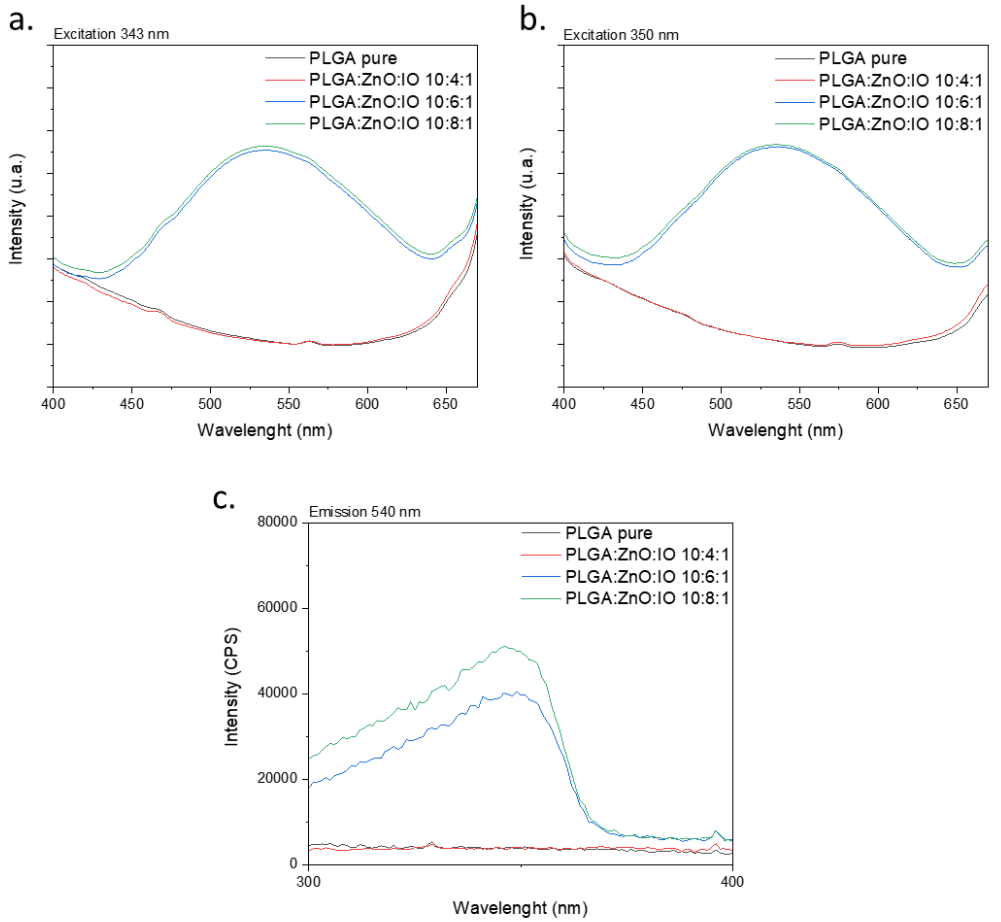

Source: by the author.

Based on the findings in **Figure III.15**, emission is noticeable in PLGA:ZnO:IO 10:6:1 and 10:8:1 samples but absent in the PLGA:ZnO:IO 10:4:1 sample. Hence, a minimum of 6 mg of ZnO is necessary to confer luminescent properties to this material in the presence of 1 mg of iron in the PLGA:ZnO:IO formulation.

The next step in the work was to evaluate the Mp. This was roughly evaluated using the capability of an external magnet to drag the particles. The result is shown in **Figure III.16**.

Figure III.16. PLGA:ZnO:IO suspensions in the ratios a) 10:6:1, and b) 10:8:1 with Mf application.

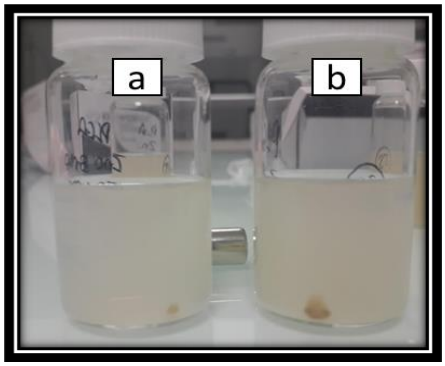

Source: by the author.

Figure III.16 shows that the NPs agglomerate when an external magnet is applied to the preparation. This indicates that the suspended PLGA:ZnO IO NPs possess Mp. With this, the following samples are tested in **Table III.10** for testing the NPs for the next steps.

Table III.10. PLGA:ZnO:IO samples analysed by MRI.

Sample	Proportion
PLGA	10 mg of PLGA
PLGA:IO 10:1	10 mg of PLGA + 1 mg IO
PLGA:ZnO 10:6	10 mg of PLGA + 6 mg ZnO
PLGA:ZnO 10:8	10 mg of PLGA + 8 mg ZnO
PLGA:ZnO:IO 10:6:1	10 mg of PLGA + 6 mg ZnO + 1 mg IO
PLGA:ZnO:IO 10:8:1	10 mg of PLGA + 8 mg ZnO + 1 mg IO

These samples were selected because QDs luminescence was evident in luminescence assays at 6 mg and 8 mg ZnO. MRI is then carried out on these samples. The samples were purified and lyophilized in accordance with the purification procedure in **Section II.2.5**.

III.2.4 Infrared analysis

Infrared analysis was performed on PLGA particles containing ZnO and IO in a synthesis ratio of PLGA:ZnO:IO 10:6:1. This ratio was chosen according to the best results obtained in luminescence analysis of these compounds. The results are shown in **Figure III.17**.

Figure III.17. Infrared spectra of PLGA:ZnO:IO 10:6:1 NP. a) infrared analysis between 400-4000 cm^{-1}, b) magnified between 400-600 cm^{-1}.

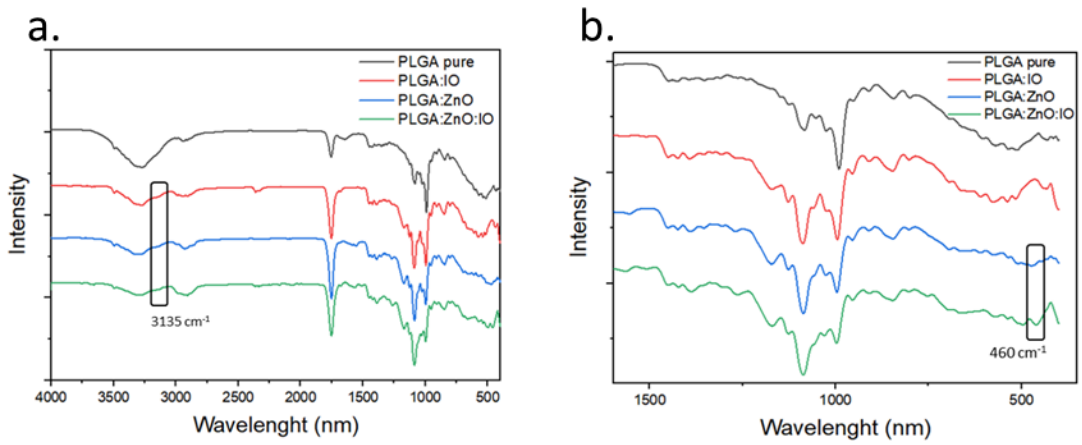

Source: by the author.

It can be observed that bands appear in the region of 3135 cm^{-1} and 460 cm^{-1}. They can be attributed to the presence of Zn-O bond (CHAKRABORTY et al., 2019). Another band appears nearby 425 cm^{-1}, it can be related to octahedral site of IO (GARG; PATI; CARLOS DE OLIVEIRA, 2015). It can be assumed that ZnO and IO are present in the structure of PLGA copolymer.

III.2.5 TEM Analysis

Samples were analysed by TEM. The samples were obtained from lyophilized samples. The results of the TEM analyses were performed with the polymer particles containing ZnO and IO NPs. The main results are shown in **Figure III.18**.

Figure III.18. TEM results of PLGA:ZnO:IO NPs at 10:0:0 (a,b,c), 10:6:0 (d,e,f), 10:8:0 (g,h,i), 10:0:1 (j,k,l), 10:6:1 (m,n,o), and 10:8:1 (p,q,r) at different scale bars (50, 100, and 200 nm).

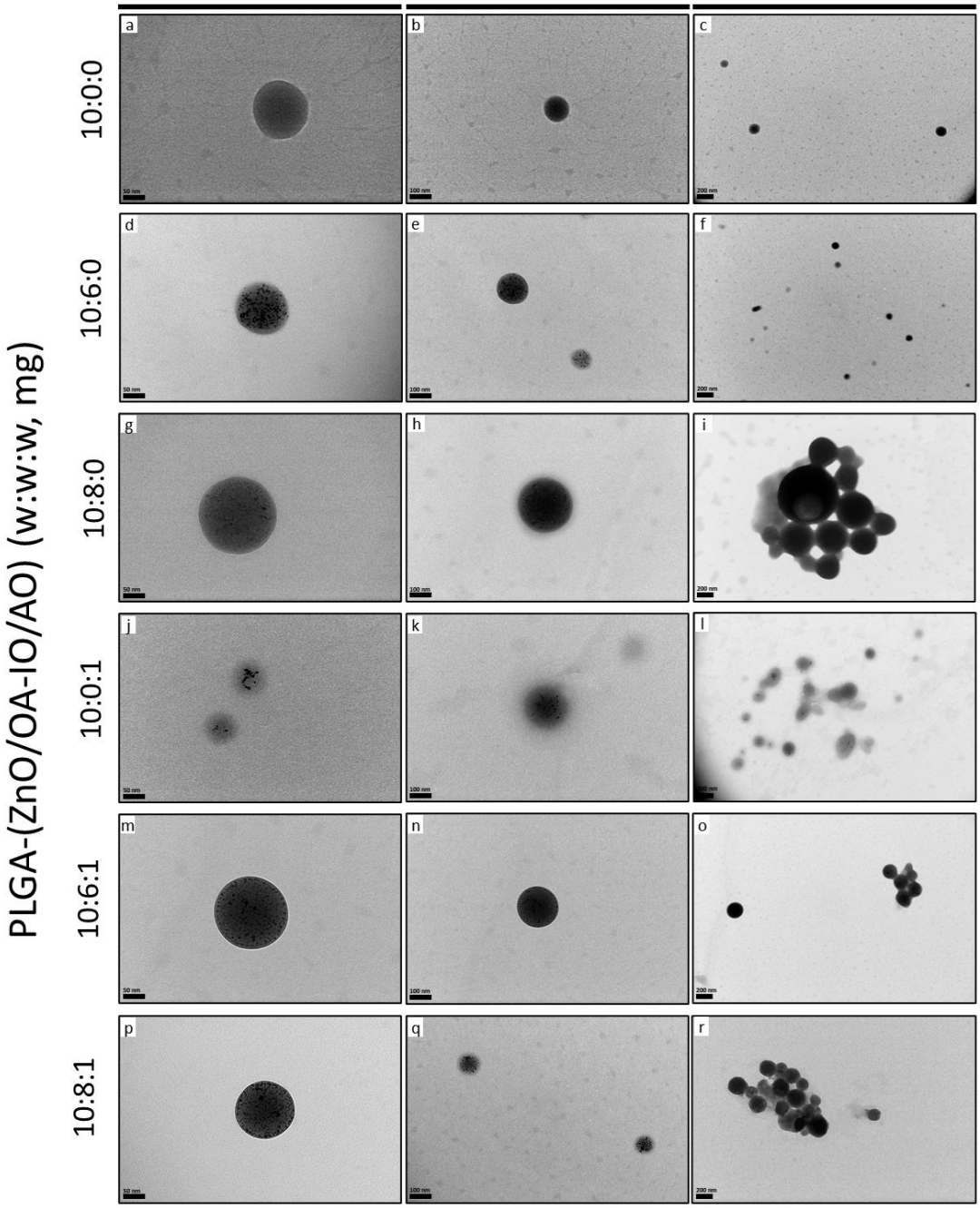

Source: by the author.

Based on the findings depicted in **Figure III.18**, all variations mentioned above yielded NPs with a spherical morphology. The NP sizes were determined using ImageJ software, with results presented in **Figure III.19** and **Table III.11**, comparing with previous DLS analysis results.

Figure III.19. Histogram spectra of PLGA:ZnO:IO NPs with different nominal ratio.

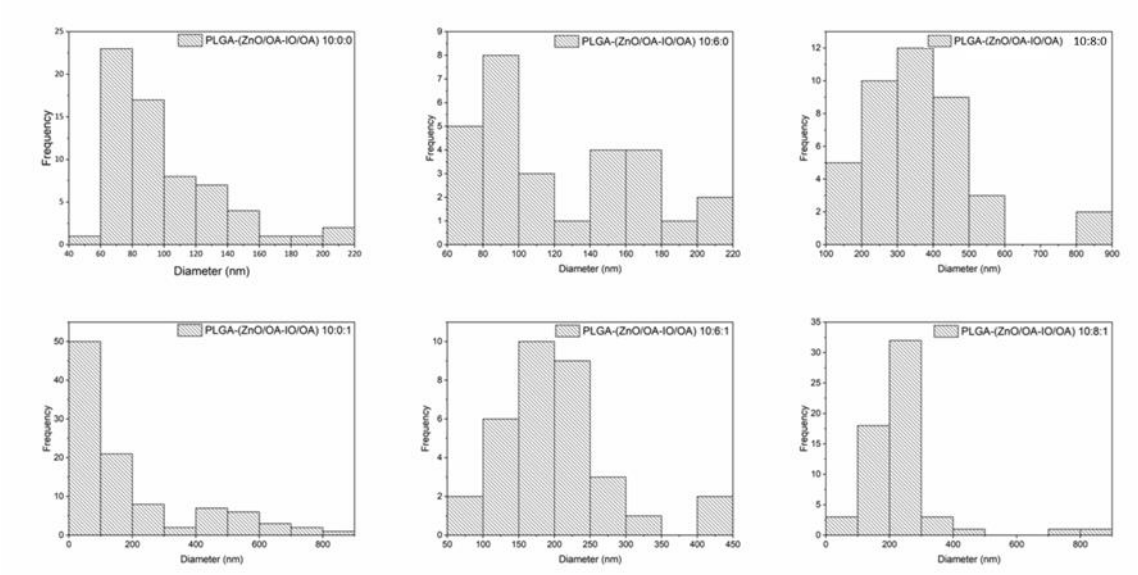

Source: by the author.

Table III.11. DLS and TEM analysis of the size of PLGA:ZnO:IO.

PLGA:ZnO:IO (w:w:w, mg)	TEM results (nm)	DLS results (nm)	PDI
10:0:0	78.78 ± 18.27	86.31 ± 0.86	0.18 ± 0.01
10:6:0	85.05 ± 10.83	272.0 ± 6.51	0.35 ± 0.02
10:8:0	333.72 ± 10.71	331.1 ± 8.65	0.34 ± 0.11
10:0:1	82.22 ± 1.20	152.1 ± 0.91	0.10 ± 0.03
10:6:1	187.59 ± 4.60	222.7 ± 1.78	0.10 ± 0.03
10:8:1	218.73 ± 2.92	235.9 ± 2.11	0.16 ± 0.02

The DLS results were obtained prior to the purification and lyophilisation process. The results DLS and TEM size are similar between the samples 10:0:0, 10:8:0, 10:6:1 and 10:8:1. This means that there is stability in size after lyophilisation. However, there is no similar size for samples 10:6:0 and 10:0:1 that can maybe be explained by the fact that the TEM measurement is performed on a limited number of particles. TEM provides detailed images of individual particles, but its analysis can be limited by sample selection and particle count, potentially leading to an unrepresentative overall size distribution (VERLEYSEN et al., 2019).

More interestingly, PLGA NPs containing only ZnO or IO NPs are observed to have black dots. No black dots were observed in the image of PLGA alone. **Figure III.20** shows the size of ZnO and IO NPs by SEM analysis.

Figure III.20. TEM of ZnO/OA and IO/OA NPs size. Scale bars: 20 nm (10:0:1, 10:6:0 and 10:8:1), and 50 nm (10:0:0).

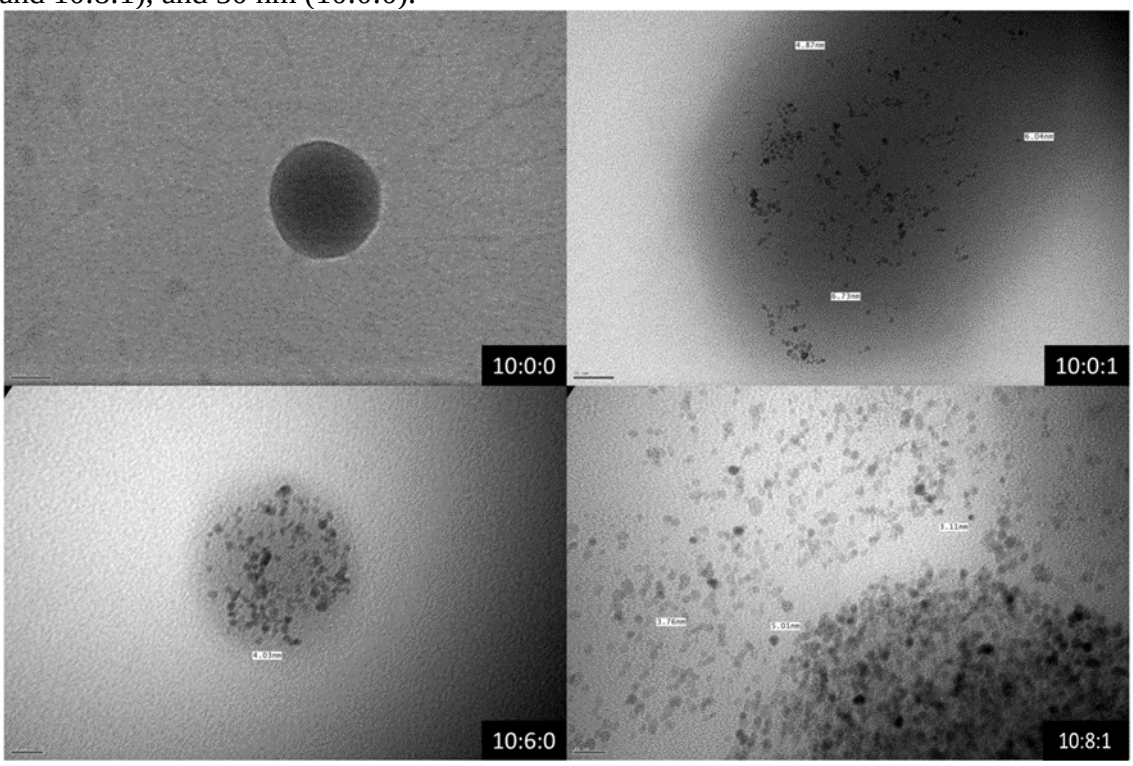

Source: by the author.

The size calculation of ZnO and IO NPs was conducted based on TEM analysis using a scale bar of 20 nm, and the results are presented in **Table III.12**. The PLGA:ZnO:IO 10:0:1 sample (containing only IO) exhibits dots with a diameter of 7.33 ± 0.28 nm, while the PLGA:ZnO:IO 10:6:0 sample (containing only ZnO) shows dots with a diameter of approximately 4.73 ± 0.16 nm. These sizes are consistent with those reported in previous studies by Lallo Da Silva et al. (2019) for ZnO NPs and Luque-Michel, Lemaire & Blanco-Prieto (2021) for IO NPs. **Figure III.21** shows the results for the PLGA NP loaded with ZnO and IO NPs.

Figure III.21. Size analysis of NPs encapsulated within PLGA was conducted for PLGA:ZnO:IO samples with nominal ratio of 10:6:1 and 10:8:1, using scale bars of 20 nm and 50 nm.

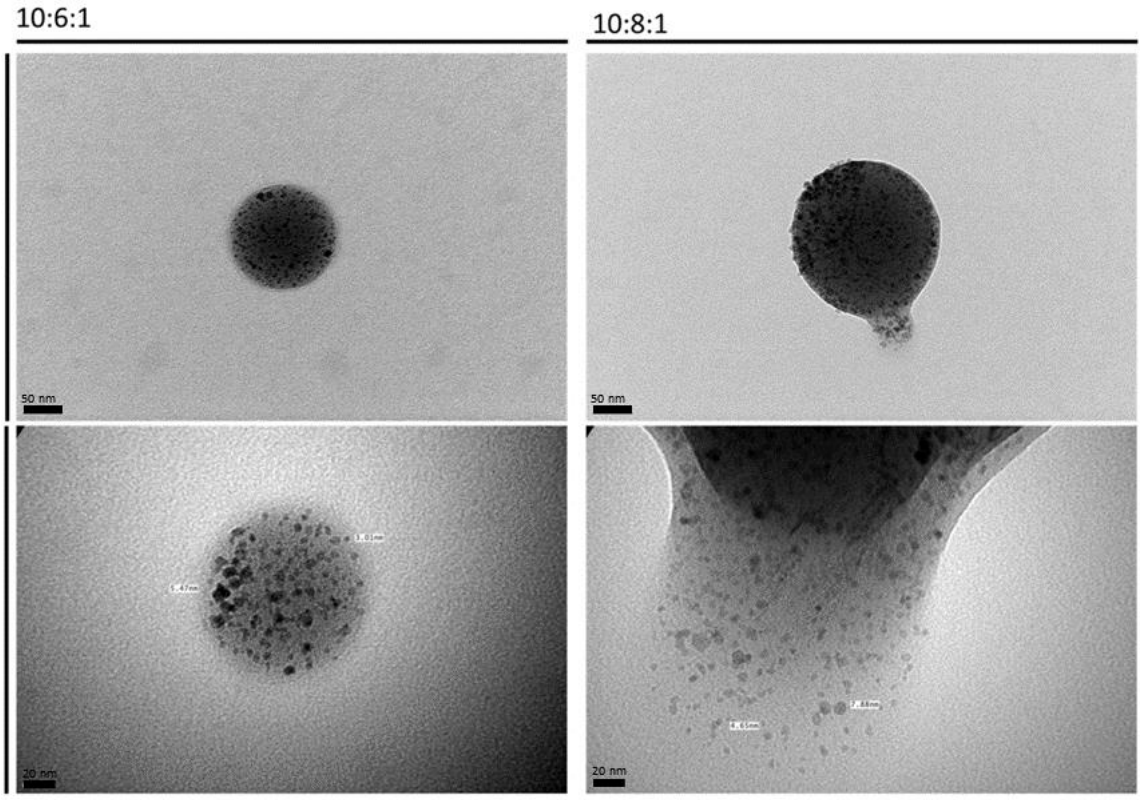

Source: by the author.

According to **Figure III.21**, the PLGA was successfully incorporated with the ZnO and IO NPs. Dense particles with sizes ranging from 3 to 8 nm are seen. Size measurements of the dense particles were performed using ImageJ and shown in histogram and average calculated by Gaussian curve to better analyse the size of NPs of ZnO and IO. The results are shown in **Figure III.22** and **Table III.12**.

Table III.12. Size of ZnO and IO analyzed by TEM and calculated by Gaussian curve.

PLGA:ZnO:IO	TEM results (nm)
10:6:0 (ZnO)	4.73 ± 0.16
10:8:0 (ZnO)	4.56 ± 0.16
10:0:1 (IO)	7.33 ± 0.28
10:6:1 (ZnO+IO)	4.03 ± 0.10
10:8:1 (ZnO+IO)	4.64 ± 0.14

Figure III.22. Size of IO and ZnO from PLGA:ZnO:IO NPs in the nominal ratio of 10:0:1 (a), 10:6:0 (b), 10:6:1 (c), 10:8:0 (d), and 10:8:1 (e).

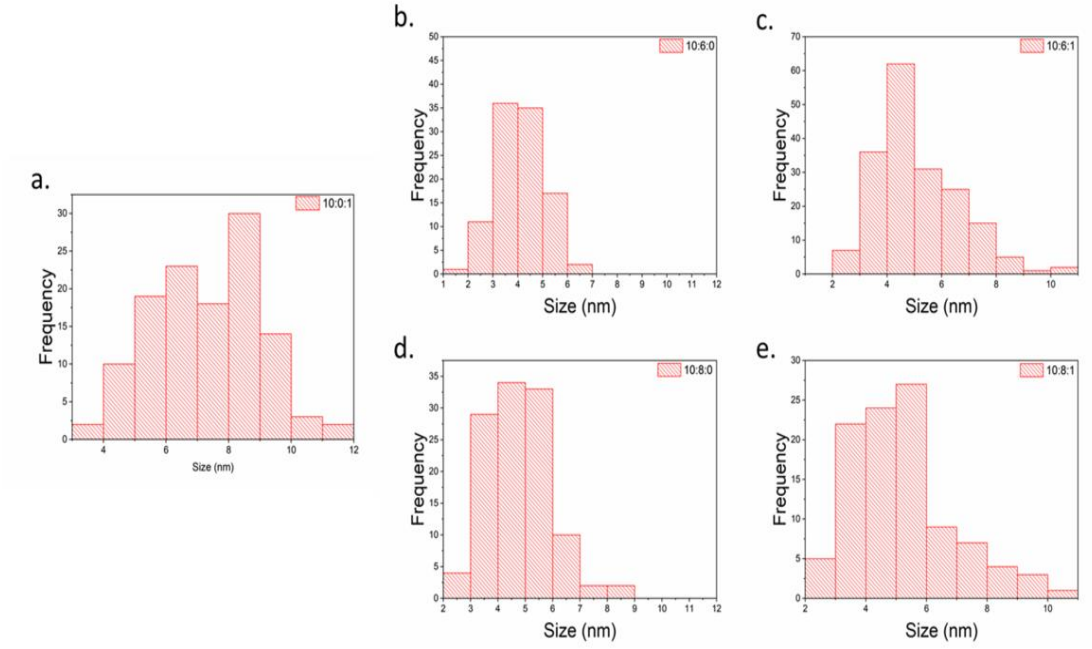

Source: by the author.

Although there is no significant difference in the average sizes of NPs observed in PLGA:ZnO:IO 10:8:1 or 10:6:1 (4.64 ± 0.14 nm & 4.03 ± 0.10 nm, respectively) compared to PLGA:ZnO:IO 10:8:0 or 10:6:0 (4.73 ± 0.16 nm & 4.56 ± 0.16 nm, respectively), it is evident that the former exhibits a wider distribution with particles larger than 6 nm, whereas the latter demonstrates a narrower distribution. Nonetheless, it can be inferred that both ZnO and IO can be simultaneously encapsulated within PLGA.

III.2.6 MRI analysis

MRI was used to evaluate the Mp of PLGA particles containing ZnO and IO. An initial concentration of 2.5 mg mL^{-1} of PLGA:ZnO:IO NP in water was considered. The weight of lyophilized samples was considered in the analysis. Analyses of PLGA and PLGA containing only ZnO were used to verify whether ZnO has a magnetic effect. PLGA:ZnO:IO 10:6:1 and 10:8:1 NPs were chosen because they exhibited the highest luminescence emission intensities. The scanning results for T2-weighted and T1-

weighted are shown in **Figure III.23** and the T2 and T1 values for each sample are shown in **Table III.13**.

Figure III.23. MRI results of PLGA:ZnO:IO samples: a) PLGA; b) PLGA:ZnO 10:8; c) PLGA:ZnO 10:6; d) PLGA:IO 10:1; e) PLGA:ZnO:IO 10:6:1; and f) PLGA:ZnO:IO 10:8:1. MRI results of T2 weighting left and T1 weighting right. The concentration of the samples is expressed in 2.5 mg mL^{-1}.

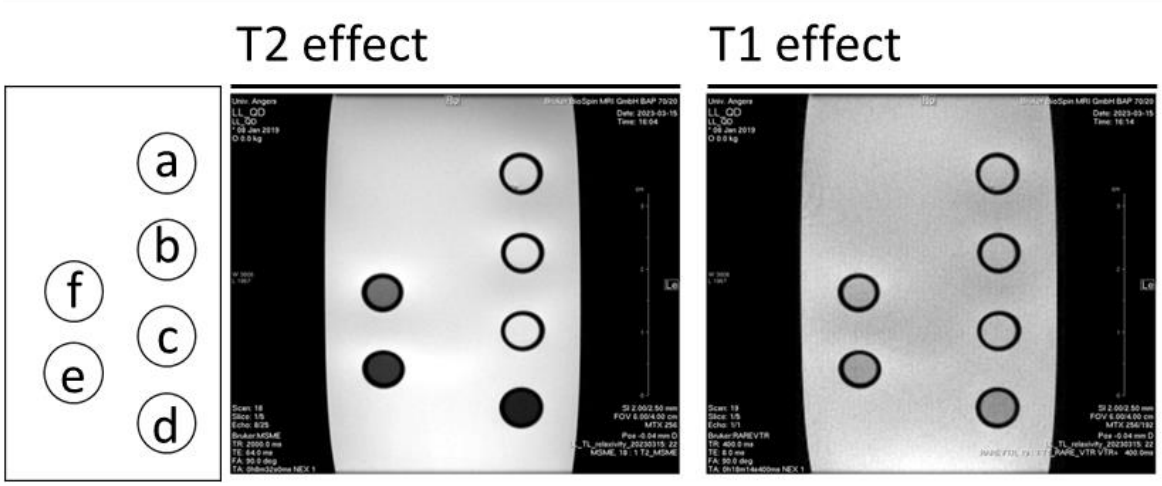

Source: by the author.

Table III.13. T1 and T2 values of PLGA:ZnO:IO samples

Sample	T2 (ms)	T1 (ms)
H2O	747 ± 32	2517 ± 16
PLGA:ZnO:IO 10:8:1	106 ± 1	2495 ± 24
PLGA:ZnO:IO 10:6:1	50 ± 1	2530 ± 23
PLGA:ZnO:IO 10:0:1	36 ± 1	2476 ± 41
PLGA:ZnO:IO 10:6:0	918 ± 49	2572 ± 11
PLGA:ZnO:IO 10:8:0	874 ± 41	2582 ± 54
PLGA:ZnO:IO 10:0:0	823 ± 32	2491 ± 19

According to **Figure III.23**, a notable effect on the contrast of T2-weighted images is observed in the presence of IO, as evident in samples of PLGA:IO 10:1 (d), PLGA:ZnO:IO 10:6:1 (e), and PLGA:ZnO:IO 10:8:1 (f), with the most significant effect observed for the PLGA NP containing only IO (resulting in a darker spot - **Figure III.23d**). The quantitative analysis of these images confirms a substantial reduction in

T2 for PLGA:ZnO:IO 10:0:1 (36 ± 1ms) compared to PLGA:ZnO:IO 10:6:1 & 10:8:1 (measuring 50 ± 1ms & 106 ± 1ms, respectively). Interestingly, in the absence of IO, the T2 is measured in the range typical for PLGA (approximately 800-900ms).

In the T1-weighted images, a slight effect is noticeable, but accurate quantification (via T1 calculation) was not feasible due to be not the most suitable acquisition parameters resulting in images that were not fully relaxed. Consequently, similar T1 values are reported in **Table III.13**. Therefore, no further interpretation of the T1 data, such as r1 relaxivity, will be conducted.

To calculate the relaxivity (r1 & r2) of NPs (expressed in mmol L^{-1} s^{-1} and presented in **Figure III.24**), iron quantitation and knowledge of T1 & T2 values are required. Iron quantitation was performed using ICP-MS, and the data are reported in **Table III.14**. T1 and T2 values were measured for various dilutions, and the data are reported in **Table III.15**.

Table III.14. Amount of iron measured in PLGA:ZnO:IO samples by ICP technique.

Sample	**[ ] mg Fe / g of sample**
PLGA:IO 10:1	1.71
PLGA:ZnO:IO 10:6:1	3.05
PLGA:ZnO:IO 10:8:1	2.56

Table III.15. Report of 1/T2 in relation to the concentration of iron

PLGA:IO 10:1 (w:w, mg)		**PLGA:ZnO:IO 10:6:1 (w:w:w, mg)**		**PLGA:ZnO:IO 10:8:1 (w:w:w, mg)**	
[ ] Fe mmol L^{-1}	**1/T2 s^{-1}**	**[ ] Fe mmol L^{-1}**	**1/T2 s^{-1}**	**[ ] Fe mmol L^{-1}**	**1/T2 s^{-1}**
0.075	27.78	0.137	24.39	0.115	11.24
0.037	14.93	0.068	12.50	0.057	5.81
0.019	8.33	0.034	6.90	0.029	3.28
0.009	4.50	0.017	3.80	0.014	2.17
0.005	2.72	0.009	2.35	0.007	1.47

To calculate the relaxivity (r2) for each sample, a plot of 1/T2 as a function of iron concentration was generated (Figure III.24), and the relaxivity values are summarized in **Table III.16**.

Figure III.24. Relaxivity calculation for PLGA samples containing IO and ZnO. Calculation made from the concentration of iron in each sample. Graph of samples a) PLGA:IO 10:1, b) PLGA:ZnO:IO 10:6:1 and PLGA:ZnO:IO 10:8:1.

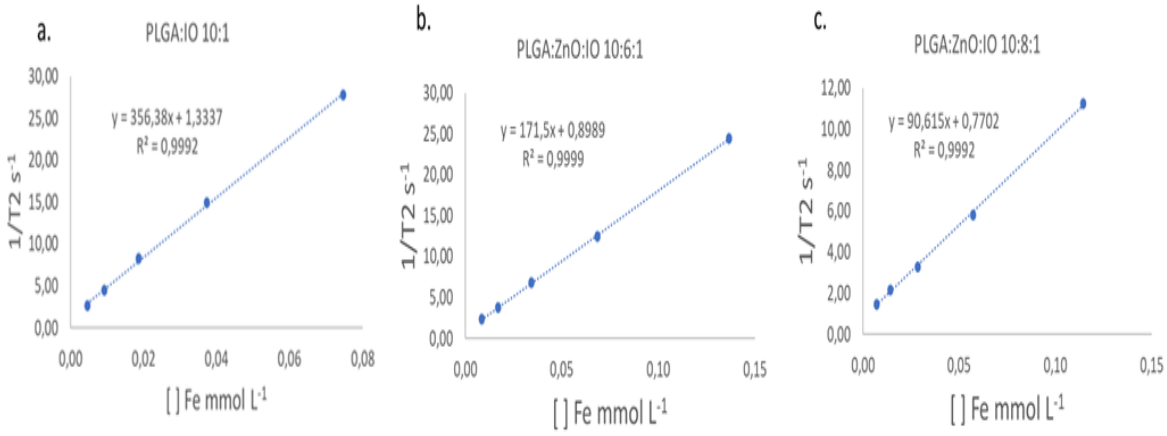

Source: by the author.

Table III.16. Relaxivity (r2) of PLGA:ZnO:IO samples.

Sample	Relaxivity (r2) (mmol L^{-1} s^{-1})
PLGA:IO 10:1	356.38
PLGA:ZnO:IO 10:6:1	171.50
PLGA:ZnO:IO 10:8:1	90.62

To conclude on the Mr analysis of the PLGA:ZnO:IO NPs, it is evident that the presence of IO is essential for an effect on Mr images, particularly on T2-weighted images. Additionally, the presence of Zn has a positive impact on the loading of iron in the PLGA NPs (**Table III.14**) but negatively affects the relaxivity of the PLGA NPs (**Table III.16**). This paradoxical observation may stem from the organization of iron within the NPs, with ZnO potentially limiting the aggregation of IO, as observed in the TEM images of the 10:0:1 sample presented in **Figure III.18** and **Figure III.20**.

III.2.7 Zeta Potential analysis

To complete the PLGA based NPs physico-chemical characterisation, zeta potential was measured. The results are shown in **Table III.17.**

Table III.17. Zeta potential of PLGA:ZnO:IO samples.

PLGA:ZnO:IO (w:w:w, mg)	Zeta Potential (mV)
10:0:0	-21.3 ± 1.0
10:0:1	-25.4 ± 0.2
10:6:0	-12.2 ± 1.6
10:6:1	-33.2 ± 1.4

The results of **Table III.17** show that the zeta potential of PLGA, at -21 mV, is consistent with previous literature results (CHIU et al., 2021b). Encapsulation of IO alone, ZnO alone or IO/ZnO concomitantly does not affect the zeta potential of the particles and then will not impact the stability/dispersibility of the NP. The maintenance of the zeta potential at -21 mV suggests that the electrostatic stability of the nanoparticles is not compromised, preventing aggregation and keeping the particles well dispersed. The dispersibility of the nanoparticles also remains unchanged, which is crucial for drug delivery systems, ensuring therapeutic efficacy (PHAN; HAES, 2019).

III.3 Conclusion

A PLGA particle system containing ZnO and IO NPs was developed for use in diagnostic imaging. The ZnO NPs were successfully modified by OA, where it was found that a concentration of 21 mmol L^{-1} of oleic acid was sufficient to coat the ZnO without altering its physicochemical properties and possible dispersion in DCM for subsequent incorporation into the PLGA aqueous system.

The synthesis of IO NPs was also optimized for the possible determination of the IO mass concentration by an ethanol washing process. The IO was successfully dispersed in DCM for subsequent incorporation into PLGA systems.

It has been noted that varying proportions of ZnO and IO embedded in PLGA NPs can influence their physicochemical properties, including luminescence, Mp, and size. The size of the PLGA particles falls within the range of 200 nm, with ZnO and IO NPs measuring approximately 4 nm and 8 nm, respectively.

There is an interaction between the ZnO NPs and the IO. When the concentration of IO is increased, the luminescence of the system decreases. Increasing the concentration of ZnO can affect the Mp of the material.

It was found that an initial mass ratio of PLGA:ZnO:IO of 10:6:1 was sufficient to ensure suitable luminescence and Mp. Luminescence intensity was observed with emission at 540 nm when excited at 343 nm. For Mp, a relaxivity value of 171 mmol L^{-1} s^{-1} was found.

The development of this PLGA:ZnO:IO NP system was successful, but for use in diagnostic imaging, it would be interesting to work with a system containing both Zn and Fe in the same nanoparticle to verify its luminescence and Mp.

With this in mind, in the next chapter, FeZnO systems with both elements in the same system were prepared and investigated for their possible use in aqueous media with GPTMS coating or coated with oleic acid for incorporation into PLGA systems.

REFERENCES

BABES, L. et al. Synthesis of Iron Oxide Nanoparticles Used as MRI Contrast Agents: A Parametric Study. **Journal of Colloid and Interface Science**, v. 212, n. 2, p. 474–482, 15 abr. 1999.

CHAKRABORTY, T. et al. ZnO–Bentonite nanocomposite: an efficient catalyst for discharge of dyes, phenol and Cr(VI) from water. **Journal of Coordination Chemistry**, v. 72, n. 1, p. 53–68, 2019.

CHIU, H. I. et al. Cytotoxicity of targeted PLGA nanoparticles: a systematic review. **RSC Advances**, v. 11, n. 16, p. 9433, 2021.

GARG, V. K.; PATI, S.; CARLOS DE OLIVEIRA, A. **International Journal of Chemical, Molecular, Nuclear, Materials and Metallurgical Engineering**, v.9, n.6, 2015.

LUQUE-MICHEL, E.; LEMAIRE, L.; BLANCO-PRIETO, M. J. SPION and doxorubicin-loaded polymeric nanocarriers for glioblastoma theranostics. **Drug Delivery and Translational Research**, v. 11, n. 2, p. 515–523, 2021.

MANAIA, E. B. et al. Surface modified Mg-doped ZnO QDs for biological imaging. **European Journal of Nanomedicine**, v. 7, n. 2, p. 109–120, 2015.

RAJAN, C. P. et al. Local structural studies through EXAFS and effect of Fe2+ or Fe3+ existence in ZnO Nanoparticles. **Journal of Physical Chemistry C**, v. 25, n. 24, p. 13523–13533, 2021.

PHAN, H. T.; HAES, A. J. What Does Nanoparticle Stability Mean? The journal of physical chemistry. C, **Nanomaterials and interfaces**, v. 123, n. 27, p. 16495, 7 jul. 2019.

SPANHEL, L.; ANDERSON, M. A. Semiconductor Clusters in the Sol-Gel Process: Quantized Aggregation, Gelation, and Crystal Growth in Concentrated ZnO Colloids. **Journal of the American Chemical Society**, v. 113, n. 8, p. 2826–2833, 1991.

VERLEYSEN, E. et al. Evaluation of a TEM based Approach for Size Measurement of Particulate (Nano)materials**. Materials**, v. 12, n. 14, 2019.

YANG, G. et al. Tribological properties of oleic acid-modified zinc oxide nanoparticles as the lubricant additive in poly-alpha olefin and diisooctyl sebacate base oils. **RSC Advances**, v. 6, p. 69836-69844, 2016.

CHAPTER IV

Study of Nanoparticles of Fe-doped ZnO as bimodal agent for bioimaging.

CHAPTER IV. Study of Nanoparticles of Fe-doped ZnO as bimodal agent for bioimaging.

IV.1 INTRODUCTION

The synthesis of FeZnO NPs was carried out to obtain NPs with potential for diagnostic use by doping technique. The FeZnO has potential in the literature as it is well studied.

In this chapter, FeZnO NP exhibiting both visible luminescence and Mp are synthesized for use in diagnostic imaging. Specifically, the synthesis of (i) FeZnO prepared by the sol-gel method exhibiting visible luminescence, (ii) FeZnO modified with GPTMS forming a stable colloidal suspension in water, and (iii) PLGA NPs embedded with FeZnO coated are presented.

FeZnO NPs were synthesized, and their luminescence and Mp were studied. The synthesis of ZnO NPs was carried out by the sol-gel method proposed by Spanhel and Anderson (1991). The method used to obtain the material was doping with iron ions, as described by Manaia (2015). Due to its high quantum yield, ZnO has luminescent properties. Iron, in turn, can give the material Mp. Thus, the aim is to create a bimodal material for the complementary use of luminescent and Mp for use in diagnostics by fluorescence imaging and MRI. Iron and zinc were chosen as elements with low cytotoxicity. The choice of dopant is critical to the formation of the doped compound. In this paper we will discuss the use of three iron precursors for this purpose. These are iron nitrate, iron chloride and iron acetate.

FeZnO NPs were prepared by the condensation hydrolysis reactions described in Chapter II (Sections II.2.1 and II.2.4). Different times for the introduction of the dopant into the reaction have been studied. In all the tests, ZnO was used as a standard to compare the results of the main fluorescence and Mp.

The results obtained from the FeZnO composite under standard conditions are described as follows: the addition of iron precursor is carried out after 30 min of reaction, the reaction time was 60 min, the reaction temperature was 60°C, the amount of zinc acetate precursor was 10 mL, the ratio between the molar concentration of [Fe]/[Fe+Zn] was kept constant within the range of 1 to 20 mol%.

IV.2 RESULTS AND DISCUSSION

IV.2.1 Iron precursor Analyse

For the preparation of FeZnO NPs, the choice of iron source is crucial. The three available iron precursors are FeCl3, $Fe(NO_2)_3$ and $Fe(ace)_2$. $FeCl_3$ and $Fe(NO_2)_3$ can provide Fe^{3+}. Ferric acetate provides Fe^{2+} but is a less soluble compound in ethanol. The solution of iron chloride and iron nitrate were not heated before use. Iron acetate was heated and under 2 hours in 98°C, under argonium atmosphere and under reflux. When the solution is heated, $Fe(ace)_2$ can be observed in **Figure IV.1**.

Figure IV.1. Pictures of (top) Iron chloride solution before (a) and after (b) heating for 2 hours. (bottom) Iron acetate solution, a) before heating, b) after heating, c) after heating with addition of acidic solution, d) after heating with addition of basic solution.

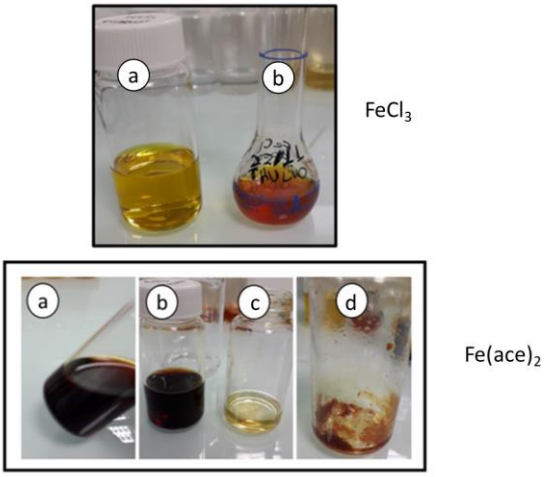

Source: by the author.

According to the results, after 2 hours, the iron acetate solution changes color from yellow to reddish, likely due to the formation of iron hydroxides, as $Fe(OH)_3$. When working with ferric acetate, the solution is initially reddish and remains so after heating. To determine if the iron has oxidized, the ferric acetate solution was tested with acidic and basic solutions. When drops of 0.1 mol L^{-1} hydrochloric acid are added, the solution turns yellow, indicating the presence of Fe^{3+} ions. When drops of sodium hydroxide are added, a brownish precipitate forms, which is also consistent with Fe^{3+} ions. For comparison, a solution containing Fe^{2+} ions would turn green in an acidic solution and form a white precipitate in a basic solution (VOGEL, 1981). These

observations confirm that Fe^{2+} is oxidized to Fe^{3+} when iron acetate is heated at 98°C for two hours under an argon atmosphere. The resulting solution was then used to form FeZnO.

IV.2.2 Fe-doped ZnO quantum dots synthesis

All the results for the selection of suitable formulations are based on their luminescence results. The concentration of the dopant is studied between the lowest concentration that gives suitable luminescence and magnetism results. In addition, the highest percentage of iron that can be incorporated into the zinc NP is checked. According to the literature, the highest amount of iron that can be used as a dopant in the ZnO is 20% in terms of moles of iron.

The conditions tested for the preparation of FeZnO NPs were carried out according to 1) choosing the doping iron source; 2) choosing the appropriate concentration of iron used; 3) choosing the doping time.

IV.2.2.1 Determination of the parameters of syntheses - iron concentration

First, attempts were made to dope ZnO NPs with amounts of iron dopant ranging from 1 to 20% iron dopant. The photoluminescence results in the UV chamber are shown in **Figure IV.2**.

Figure IV.2. Results of FeZnO with iron nitrate precursor (% = [Fe]/[Fe+Zn] * 100%): a) pictures of photoluminescence of ZnO NPs doped with iron in proportions of 1, 5, 10, 15 and 20%; b) Diffractogram of FeZnO samples in proportions of 1, 5, 10, 15 and 20%. c) Absorption spectra of FeZnO samples in proportions of X = 1, 5, 10, 15 and 20%.

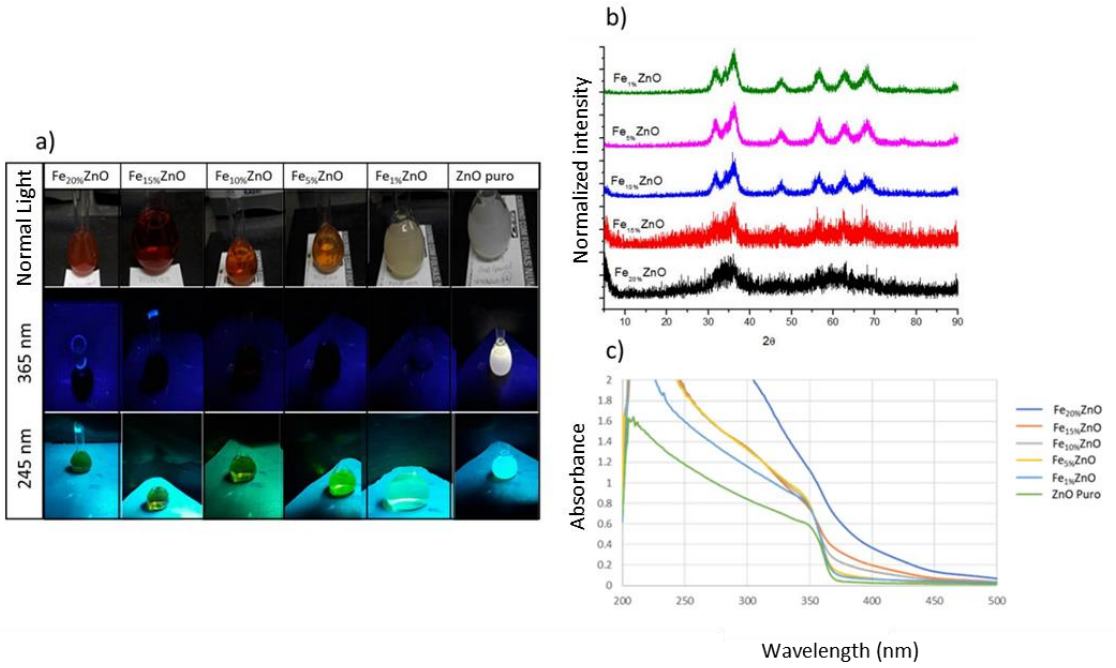

Source: by the author.

According to the **Figure IV.2a**, the samples showed no photoluminescence when excited at 365 nm in the UV development chamber compared to the pristine ZnO standard. However, when developed in the UV chamber with excitation in the 245 nm lamp, the samples showed decreasing luminescence intensity in the green region according to the increase of Fe in the sample. It can be assumed that ZnO loses its ability to excite in the wavelength of 365 nm when doped with iron.

According to the results shown in **Figure IV.2c**, it has been possible to analyse that there is an increase in the absorbance between 350 to 400 nm as the doping of the ZnO with the iron precursor is increased. This has been confirmed by others studying the optical properties of materials such as FeZnO, which shows greater absorption at longer wavelengths than a standard ZnO spectrum (BA-ABBAD et al., 2013). Literature data on the photoluminescence, emission, and excitation spectra of FeZnO are neglected, probably due to this loss of luminescence behaviour.

According to the results shown in the XRD spectrum in **Figure IV.2b**, it can be concluded that the higher the amount of Fe doped, the lower the intensity and resolution

of the diffraction peaks of the samples, indicating that the doping of ZnO NPs with iron interferes with the crystallinity and size of the NPs. The Bragg peaks found were 2θ = 31.81°, 34.09°, 36.30°, 47.80°, 56.83°, 62.83°, 68.29°, which can be attributed to the (100), (002), (101), (102), (110), (103) and (112) planes of ZnO crystal. A consequence of this higher Fe^{3+} doping concentration is the formation of smaller NP (BA-ABBAD et al., 2013; SEKAR et al., 2018). X-ray diffraction pattern of the synthesized compound shows a predominance of Bragg peaks with the hexagonal phase of ZnO (JCPDS 01-076-0704), but with a slight shift to higher angles, confirming the entry of Fe into the ZnO matrix (GHALAJKHANI, HAGHIGHI, SHABANI, 2018). Therefore, it is seen that the higher the concentration of the iron doping solution in the reaction with ZnO, the lower the intensity of the peaks and apparently the broader their width. This behavior can be explained by the presence of the doping agent, which is able to modify the structure of ZnO and make the particle size smaller (BA-ABBAD et al., 2013; GHALAJKHANI, HAGHIGHI, SHABANI, 2018). So far, the presence of impurity peaks related to the formation of other products has not been observed.

The next tests were carried out with a smaller amount of dopant, between 0.1 and 0.5% Fe. For this, iron nitrate was used as the precursor of Fe. It was also found that the luminescence properties of the material can be affected by the doping time, that means, the time in which the amount of Fe is added after the hydrolysis reaction has started. **Figure IV.3** shows the luminescence results of FeZnO samples with doping amounts ranging from 0.1 to 0.4% added 0 and 30 minutes after the start of the sol-gel hydrolysis reaction with LiOH.

Figure IV.3. Pictures of photoluminescence of FeZnO NPs in proportions of 0.1, 0.2, 0.3 and 0.4 % added 0 and 30 minutes after the start of the reaction. Images are shown in UV chamber with excitation in 365 nm and 254 nm.

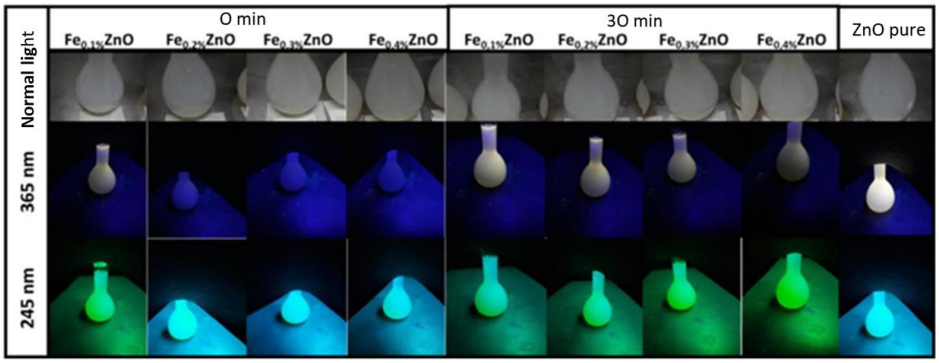

Source: by the author.

From the **Figure IV.3**, it can be said that the samples with the dopant added after 30 minutes showed luminescence in the yellow region when excited at 365 nm. They were also able to emit luminescence in the green region when excited at 245 nm. **Figure IV.4** shows the emission spectra of the doping tests with dopant addition times at 30 minutes.

Figure IV.4 Emission spectra (a) of FeZnO with iron concentration between 0.1 and 0.5 %, and a doping time of 30 min, and emission spectra with the normalized intensity (b). Samples excited at the wavelength of 365 nm.

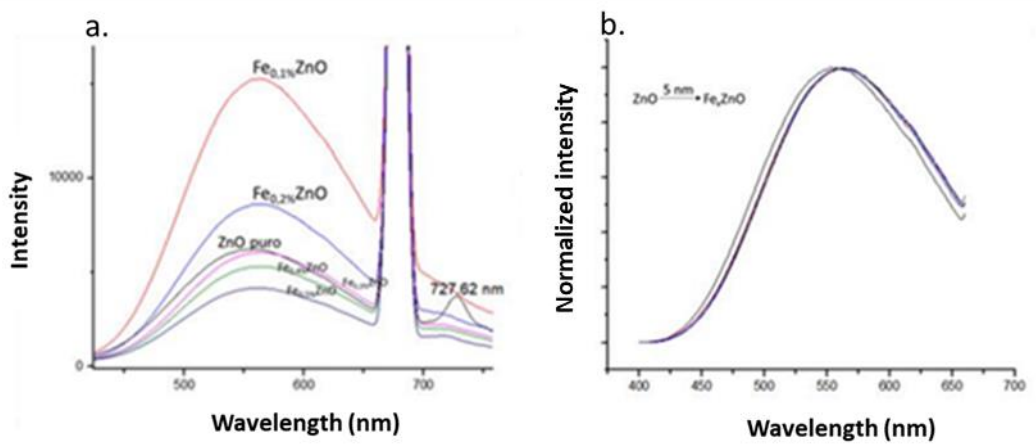

Source: by the author.

According to **Figure IV.4**, when the results were normalized, it could be seen that there was no significant shift in the emission maximum of the samples analysed. However, when the photoluminescence intensities of samples stored at 4°C for two weeks were considered, the Fe0.1%ZnO samples gave higher emission intensity than standard samples, such as ZnO, in all the tests performed. The intensity of luminescence was not measured in the first day of the synthesis. Therefore, it can be seen luminescence stability of samples doped with 0.1% iron, which is promising for use in diagnostic imaging.

Therefore, initial tests have shown that a lower percentage of iron doping may be important for the synthesis of this compound. In addition, different doping times can influence the luminescence intensity.

IV.2.2.2 Determination of the Doping time by luminescence tests

As described in the previous item, a higher doping time, the higher the luminescence intensity is. The samples were evaluated with different doping times. This means that the amount of iron solution was added after X minutes in the ZnO hydrolysis reaction (ultrasonic step at 60 °C and 60 min). For this, iron acetate was chosen as iron source, as described in item IV.2.1. The time used is shown in **Table IV.1**.

Table IV.1. FeZnO synthesis with different doping times

Reaction	**Condition**
0 min	Addition of the iron precursor at the beginning of the reaction;
15 min	Addition of the iron precursor after 15 minutes of the beginning of the reaction between the Zn acetate precursor and LiOH.
30 min	Addition of the iron precursor 30 minutes after the start of the reaction between the Zn acetate precursor and LiOH.

The samples were analysed initially with a concentration of Fe between 0.1 to 20 %. The results of the samples are shown in **Figure IV.5**.

Figure IV.5. Pictures of FeZnO with different times of addition of the iron precursor and emission analysed in a UV chamber with excitation at 254 nm. The samples are shown from the left to the right: Fe doped ZnO ([Fe]/[Fe+Zn]*100 % in mol L^{-1}) = 0, 0.1, 0.5, 1, 3, 5, 10, 15 and 20%.

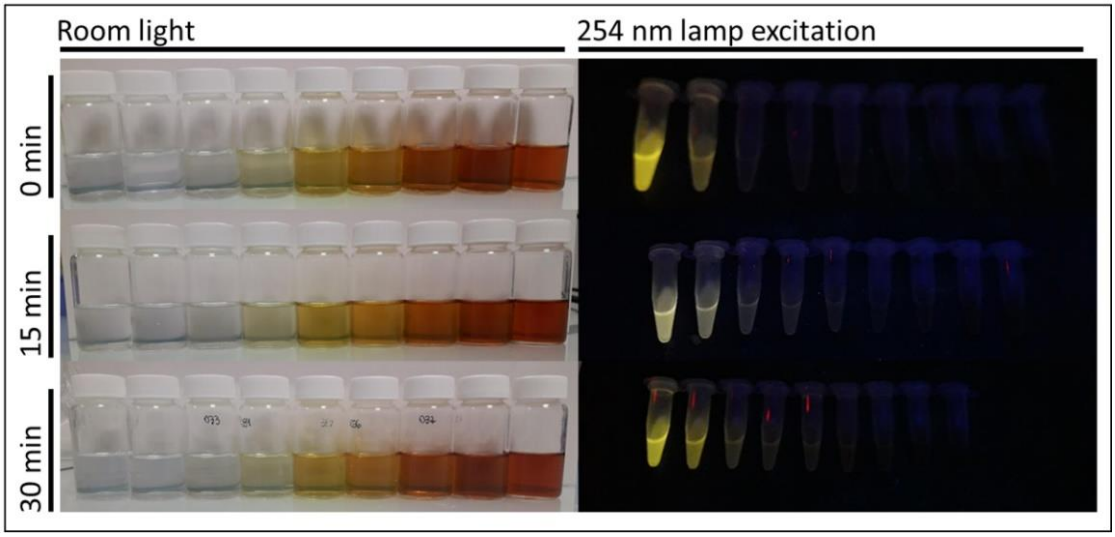

Source: by the author.

As shown in **Figure IV.5**, the luminescence intensity of the samples decreases with increasing amount of dopant. The samples analysed are in ethanol. Another factor to analyse is that the luminescent properties of ZnO are maintained with increasing doping time. After 30 minutes, the intensity of the luminescence is observed for the samples with up to 5% of iron, which is not observed for the other solutions.

The samples were modified by GPTMS, and the luminescence spectra of the samples were analysed. The initial concentration is 40 mg mL^{-1}. All samples were taken at the same dilution of 2 μL for 1000 μL water. The spectra result of absorbance, excitation, emission, and normalized emission for FeZnO samples synthesized with iron acetate are shown in **Figure IV.6**.

Figure IV.6. Luminescence and absorbance spectra of FeZnO samples synthesized from iron acetate. The samples are divided by doping time: Time 0 with a) spectra of absorbance, b) excitation using emission at 540 nm, c) emission using excitation at 343 nm, and d) emission with normalized intensity; Time 15 with e) spectra of absorbance, f) excitation using emission at 540 nm, g) emission using emission at 343 nm, and h) emission with normalized intensity; and time 30 with i) spectra of absorbance, j) excitation using emission at 540 nm, k) emission using emission at 343 nm, and l) emission with normalized intensity.

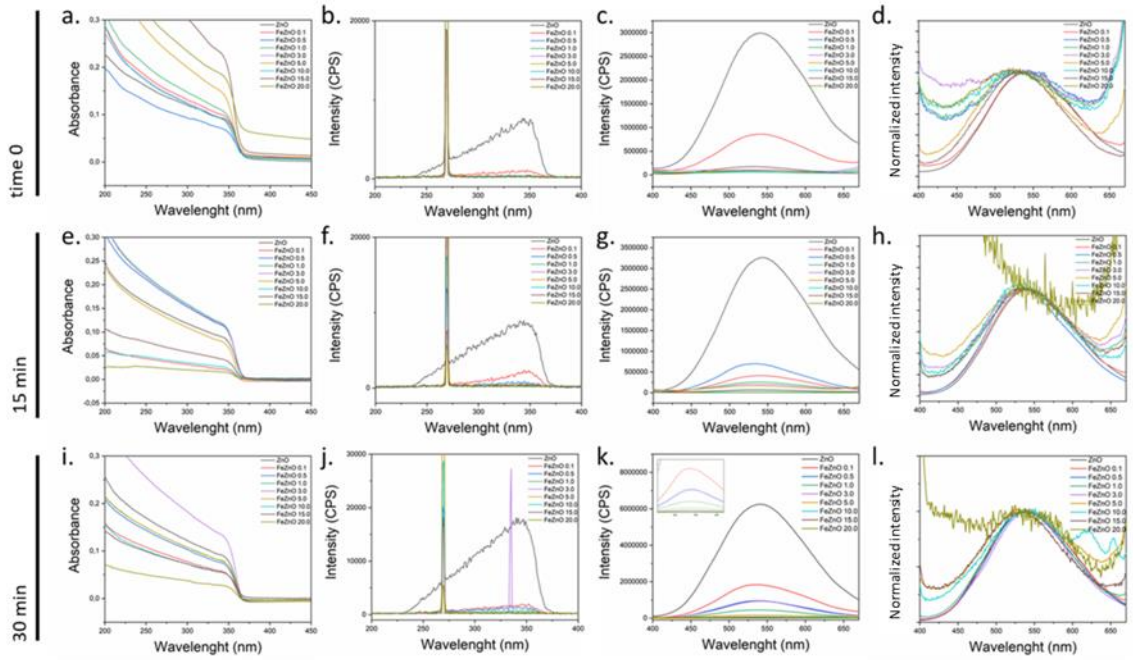

Source: by the author.

According to **Figure IV.6**, all samples, regardless of the doping time, showed the formation of the absorbance band of Zn-O, characterized by the shoulder at about 350 nm. Thus, it can be assumed that even with the presence of iron in the structure and the coating of GPTMS for dispersion in water, all samples present the formation of stable ZnO.

With the absorption band (excitation band) of ZnO at 350 nm, it can be assumed that the absorption band is in the same wavelength range analysed in **Figures IV.6b, f and j**. The absorption spectra of pristine ZnO show the formation of an excitation band between 250 and 350 nm. This is expected from the absorption test. There is a decay in the excitation band at about 355 nm. It is not possible to excite the sample above this wavelength. There are no emission bands for these samples above 350 nm excitation. However, between 340 and 350 nm there is a plateau in the excitation band. To excite the sample and visualize the emission band, the wavelength of 343 nm was chosen.

As expected, the emission band of pristine ZnO shows higher intensity compared to the other FeZnO samples in the emission graphs shown in **Figures IV.6c, g and k**. Pristine ZnO shows an emission peak at 540 nm. This is the same wavelength used to determine the excitation spectrum of the samples. Among the samples with normalized intensity of emission, **Figure IV.6 d, h** and **i** show that there is no significant emission peak shift when excited at this wavelength. An emission plateau around 540 nm is still present in the samples. However, the peak intensity of each sample must be analysed. These are shown in **Table IV.2**.

Table IV.2. Maximum emission intensity at 540 nm, excitation at 343 nm, with different dopant addition times.

	Time 0	**15 min**	**30 min**
pristine ZnO	2995850	-	-
FeZnO 0.1	861200	413550	1832490
FeZnO 0.5	79980	696260	954360
FeZnO 1	78110	256470	453370
FeZnO 3	107650	203590	931390
FeZnO 5	89200	169010	164260
FeZnO 10	54970	34860	72360
FeZnO 15	17630	71810	49130
FeZnO 20	87520	1530	5460

For better comparison, results are presented in the bar graphic in **Figure IV.7**.

Figure IV.7. Intensities of the samples according to doping time. Emission intensity at 540 nm when excited at 343 nm.

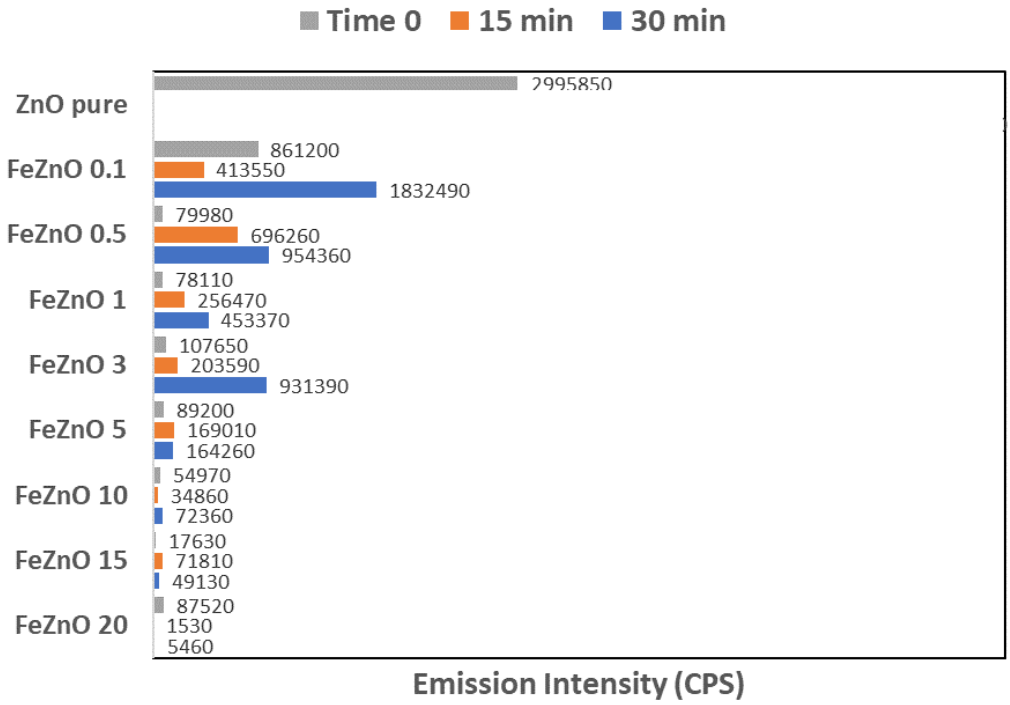

Source: by the author.

According to **Figure IV.7**, it can be observed that the pristine ZnO samples have a high luminescence intensity. However, the iron doped synthesis method shows the highest luminescence intensity after 30 minutes compared to other doped samples. This means the ZnO structure is better developed and luminescence increases. For samples containing iron doping over to 5% no more significant luminescence was observed.

IV.2.2.3 Luminescence tests with different iron source

As mentioned before, the samples with the lowest concentration of iron showed the best results of luminescence, with high intensity of emission in 540 nm, characteristic of pristine ZnO, and the time doping of 30 min show the highest intensity of emission.

Considering this, the luminescence of each sample was studied in different concentrations of iron between 0.1, 0.5 and 1.0 % of iron with 30 min of doping time for different iron sources. The results are shown in **Figure IV.8**. The same mass

concentration of 20 mg mL^{-1} was used for all samples in water. The samples were diluted in water at a ratio of 2:1000.

Figure IV.8. Luminescence study of FeZnO samples disperse in EtOH prepared with iron acetate (a, d, g, j), iron chloride (b, e, h and k) and iron nitrate (c, f, i, l) for absorbance spectra (a, b, c), excitation spectra (absorption spectra) (d, e, f), emission spectra (g, h, i) and normalized intensity emission (j, k l).

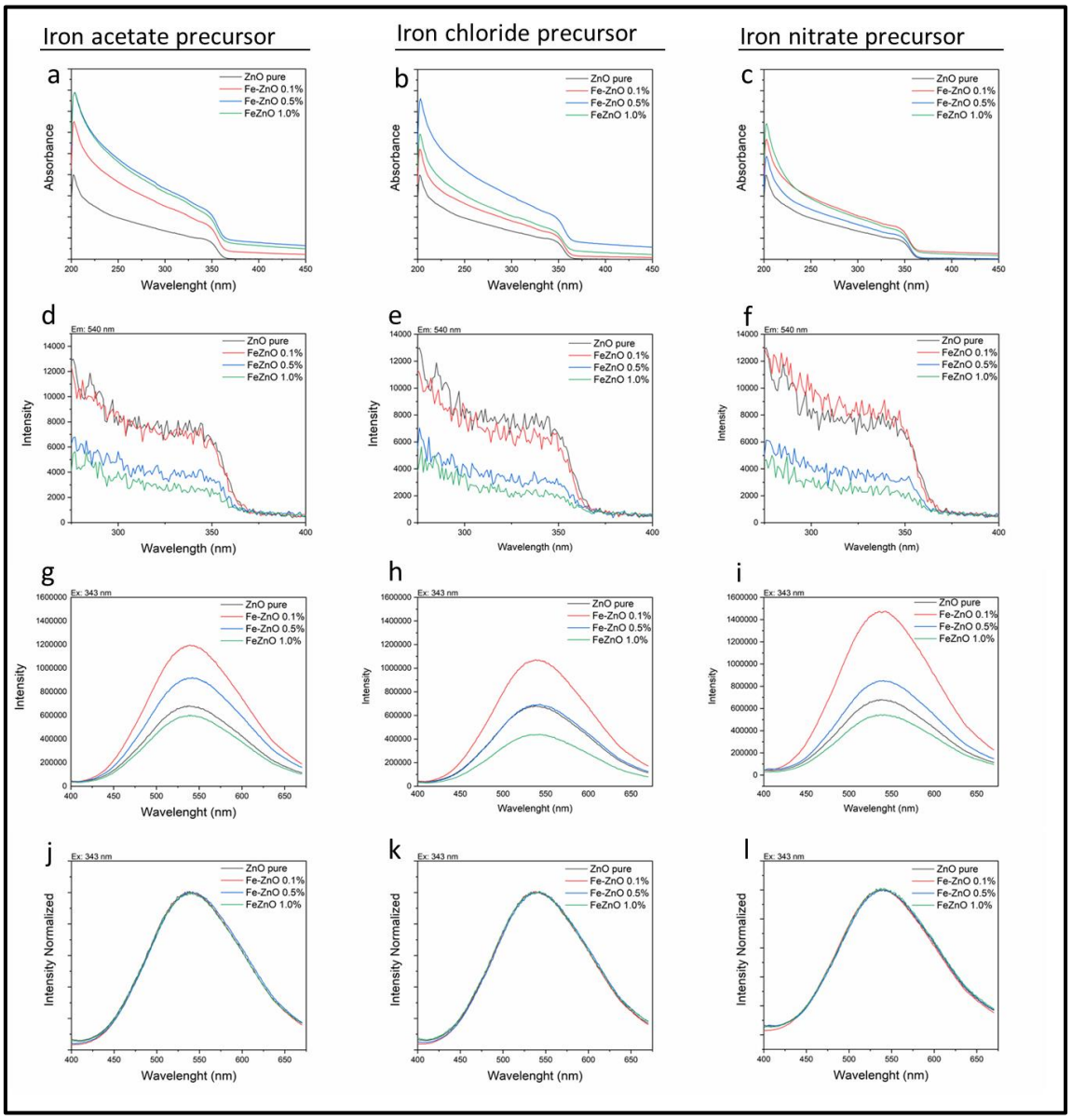

Source: by the author.

According to **Figure IV.8**, it can be observed that the absorbance spectra show the formation of the ZnO absorbance band at 350 nm. All the samples were synthesized under the same conditions in terms of temperature, reaction time, doping time, similar concentrations of Fe and different source of iron that were used. The excited bands

show a band in a similar region to the absorbance band. For the three types of dopants used, the intensity of the excitation band decreases as the percentage of dopant increases. The intensity of the excitation spectrum for the different dopants is similar for the different iron precursors and for the different amounts of the dopants. For different sources, the excitation spectrum of ZnO and FeZnO 0.1% samples is similar. However, for the same iron content, the emission of the samples synthesized with the iron acetate shows a higher intensity when we evaluate the emission spectra. To visualize the lower levels, the maximum intensity of luminescence in 540 nm with different amounts of iron has been plotted in **Figure IV.9**.

Figure IV.9. Graphic intensity of Fe doped ZnO at Fe concentration between 0 and 1% (% = [Fe]/[Fe+Zn]x100, mol L^{-1}) prepared with different iron sources (iron nitrate, iron chloride and iron acetate). Maximum luminescence intensity in 540 nm.

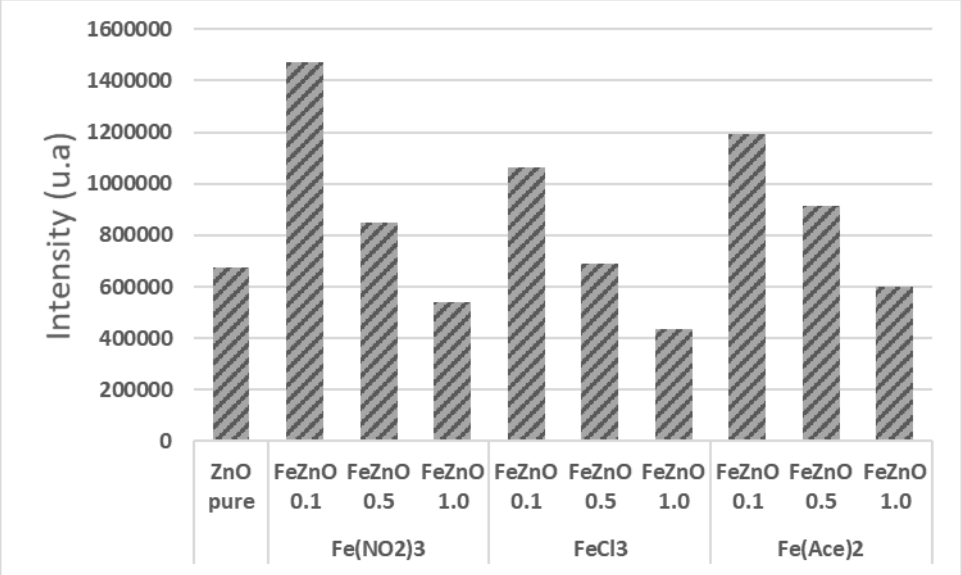

Source: by the author.

According to Figure IV.9, the addition of 0.1% iron as a dopant in the reaction increased the luminescence intensity of the composite relative to the luminescence of pristine ZnO for all iron sources used. Although the use of the nitrate iron precursor showed the highest luminescence intensity of 0.1% Fe doped ZnO, the iron acetate precursor was shown to produce 3 different concentrations of Fe doped ZnO with the highest luminescence intensity for 0.5% and 1% Fe doped ZnO. The iron acetate was chosen as the mainly iron precursor for the next steps.

IV.2.3 MRI study of FeZnO /GPTMS

The Mp of Fe doped ZnO have been investigated.

IV.2.3.1 MRI study of FeZnO /GPTMS with different source of iron

The concentration of FeZnO samples coated with GPTMS is 40 mg mL^{-1}. The samples studied were 0.1 %, 1 %, 5 % and 20 % Fe doped ZnO using iron sources with $FeCl_3$ as source of Fe^{3+} and $Fe(ace)_2$ as source of Fe^{2+}. First, iron acetate was used to test the samples of FeZnO. The results are shown in **Figure IV.10**.

Figure IV.10. MRI analysis of GPTMS coated FeZnO samples using iron acetate with 0.1% (a), 1.0% (b), 5.0% (c) and 20% (d) of iron. The T2-weighted (left) and T1-weighted (right) Mr images are shown.

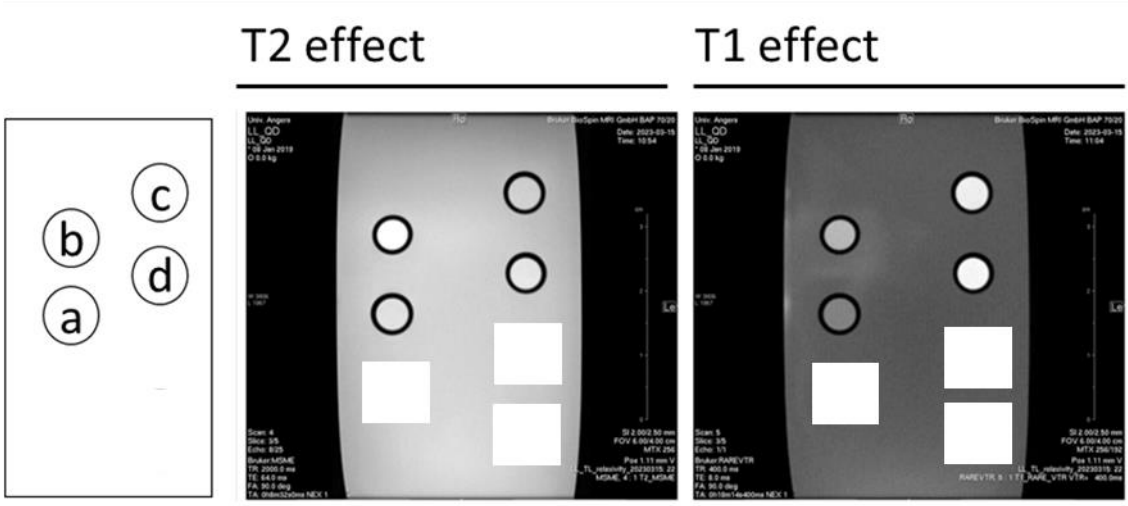

Source: by the author.

The images were acquired with TR/TE = 2000/64 ms (T2-weighted) and with TR/TE = 400/8ms (T1-weighted). Both on T1-weighted and T2-weighted images, an evident effect of increasing the amount of iron is observed. To characterise the samples, the T2 and T1 values were measured and are shown in **Table IV.3**.

Table IV.3. T2 and T1 values for solution prepared with different amounts of FeZnO synthesised from iron acetate.

Sample	T2 (ms)	T1 (ms)
H2O	947 ± 35	2337 ± 57
ZnO	731 ± 28	2468 ± 51
FeZnO 0.1	264 ± 5	1774 ± 12

Continuation Table IV.3…

Sample	T2 (ms)	T1 (ms)
FeZnO 1.0	216 ± 3	1243 ± 16
FeZnO 5.0	100 ± 1	823 ± 13
FeZnO 20.0	117 ± 1	785 ± 8

According to **Table IV.3**, all samples exhibit a notable T2 effect and a T1 effect. Regarding the T2 effect, the relaxation time decreases with the increase in the iron dopant concentration from 0.1% iron to 5% iron, with no significant difference observed between concentrations from 5% to 20%. The same trend is observed for T1. Undoped ZnO demonstrates no T1 or T2 effect compared to pure water. This suggests that the magnetic effect observed in this sample is attributed to the iron doping of ZnO.

In the next step, iron chloride was used as an iron source in the synthesis of FeZnO to study the Mp of FeZnO. For this purpose, the same concentrations of iron (0.1, 1.0, 5.0 and 20% of iron) were used. The results are shown in **Figure IV.11.**

Figure IV.11. MRI analysis of GPTMS coated FeZnO samples using iron chloride with 0.1% (a), 1.0% (b), 5.0% (c) and 20% (d) iron. The T2-weighted (left) and T1-weighted (right) Mr images are shown.

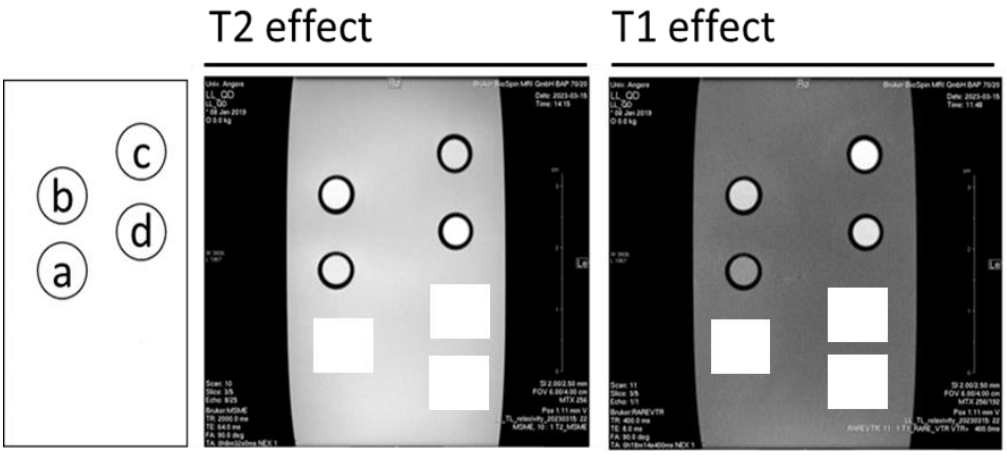

Source: by the author.

The images were acquired with TR/TE = 2000/64 ms (T2-weighted) and with TR/TE = 400/8ms (T1-weighted). Both on T1-weighted and T2-weighted images, an evident effect of increasing the amount of iron is observed. To characterise the samples, the T2 and T1 values were measured and are shown in **Table IV.4**.

Table IV.4. T2 and T1 values for solution prepared with different amounts of FeZnO synthesised from iron chloride.

Sample	T2 (ms)	T1 (ms)
H2O	666 ± 16	2417 ± 34
ZnO	734 ± 20	2496 ± 23
FeZnO 0.1	308 ± 4	1921 ± 22
FeZnO 1.0	194 ± 2	1198 ± 51
FeZnO 5.0	132 ± 1	939 ± 13
FeZnO 20.0	185 ± 1	1088 ± 47

A strong effect is observed on T2 values as the doping percentage increases in FeZnO. The T1 effect, despite existing, is limited. To determine whether there is a difference in doping with ferric acetate or ferric chloride (at equivalent percentage), the T2 and T1 values are compared in **Table IV.5**.

Table IV.5. Magnetic Effect Comparison between Iron Chloride and Iron Acetate used as iron source.

Samples	T2 (ms)		T1(ms)	
	Iron ACE	Iron CL	Iron ACE	Iron CL
ZnO	731	734	2468	2496
FeZnO 0.1	264	308	1774	1921
FeZnO 1	216	194	1243	1198
FeZnO 5	100	132	823	939
FeZnO 20	117	185	785	1088

The samples produced with different iron sources do not show such significant differences between the value of T2 and T1. Both show similar T2 and T1 effects.

IV.2.3.2 MRI study of FeZnO/GPTMS with different doping time

As it has shown that using FeCl3 or Fe(Ac)2 led to the same MRI effect, the next step was to study the Mp of FeZnO with different doping time. For this, iron acetate was used as a source of iron, and concentration of iron between 0.1 to 20 % and doping was carried out by adding the iron source at the beginning of the experiment (time 0), 15 min after the beginning of ZnO QD synthesis process (time 15 min), and 30

min after the beginning of ZnO QD synthesis process (time 30 min). The studied samples and the positions in the MRI analyses are shown in **Figure IV.12**.

Figure IV.12. Position of the samples in the MRI analyses.

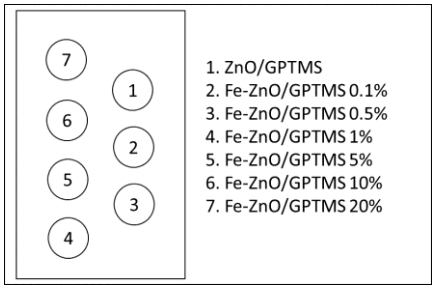

Source: by the author.

The initial concentration of the doped samples coated with GPTMS is 20 mg mL^{-1}. The samples tested were FeZnO where the iron concentrations are: 0, 0.1, 0.5, 1, 5, 10 and 20% [Fe]/[Fe+Zn], mol/mol. The results are shown in **Figure IV.13** and described in **Table IV.6** and **Table IV.7**. Each sample was measured in triplicate.

Figure IV.13. T2-weighted and T1-weighted images of particles coated with FeZnO with varying iron proportions. The samples were synthesized using iron acetate as the iron precursor, and the doping time was tested (0, 15, and 30 minutes).

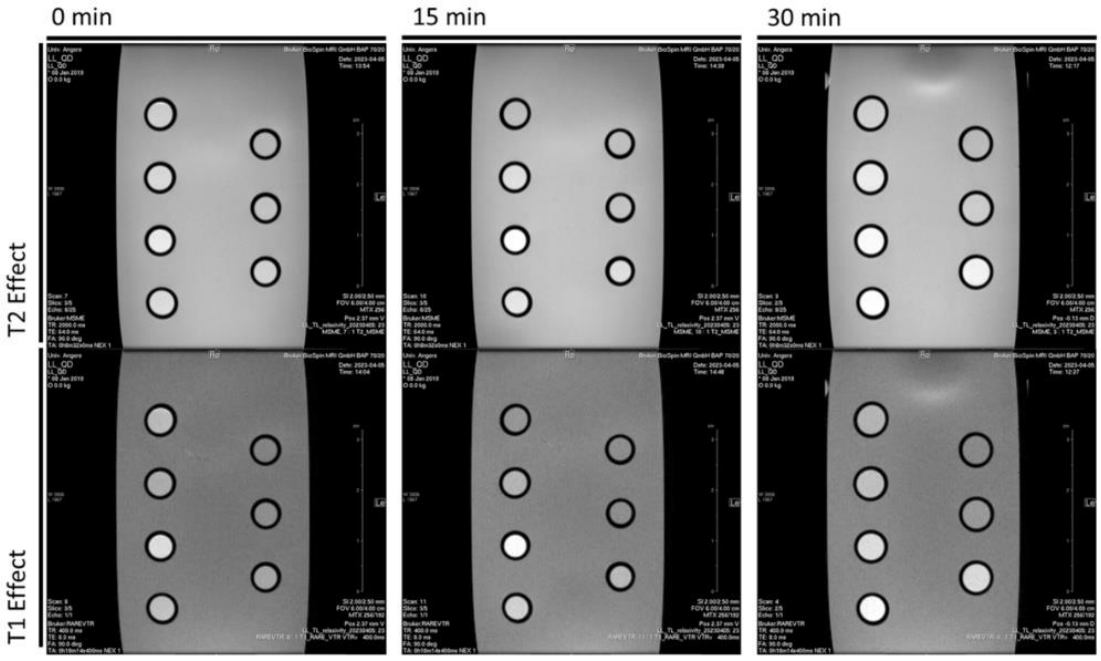

Source: by the author.

Table IV.6. T2 values of GPTMS coated FeZnO with different proportion of Fe in mol %, samples concentration in 20 mg mL^{-1}.

	T2 values		
	0 min	**15 min**	**30 min**
ZnO	1036 ± 50	1020 ± 46	970 ± 48
FeZnO 0.1	742 ± 29	826 ± 35	815 ± 34
FeZnO 0.5	573 ± 14	583 ± 13	456 ± 9
FeZnO 1	566 ± 12	531 ± 9	453 ± 7
FeZnO 5	344 ± 6	403 ± 7	512 ± 12
FeZnO 10	560 ± 17	614 ± 19	651 ± 23
FeZnO 20	410 ± 68	848 ± 29	532 ± 12

Table IV.7. T1-weighted values of FeZnO with different proportions of Fe in mol%, sample concentration in 20 mg mL^{-1}.

	T1 values		
	0 min	**15 min**	**30 min**
ZnO	2468 ± 34	2507 ± 30	2420 ± 25
FeZnO 0.1	2237 ± 16	2414 ± 20	2197 ± 37
FeZnO 0.5	1914 ± 13	1852 ± 18	1549 ± 17
FeZnO 1	1701 ± 19	1743 ± 32	1383 ± 20
FeZnO 5	1416 ± 9	1367 ± 10	1573 ± 20
FeZnO 10	1868 ± 15	1982 ± 17	1797 ± 20
FeZnO 20	1638 ± 16	2300 ± 25	1841 ± 27

It can be observed that the samples containing iron present T1 and T2 effects. The results were plotted in a distribution graph for better comparison. The results are presented in **Figure IV.14**.

Figure IV.14. Graphs of relaxation effects induced by GPMTS-coated FeZnO samples with different proportions of [Fe]/[Fe+Zn], mol/mol %, with different doping time. T2 effect (a) and T1 effect (b).

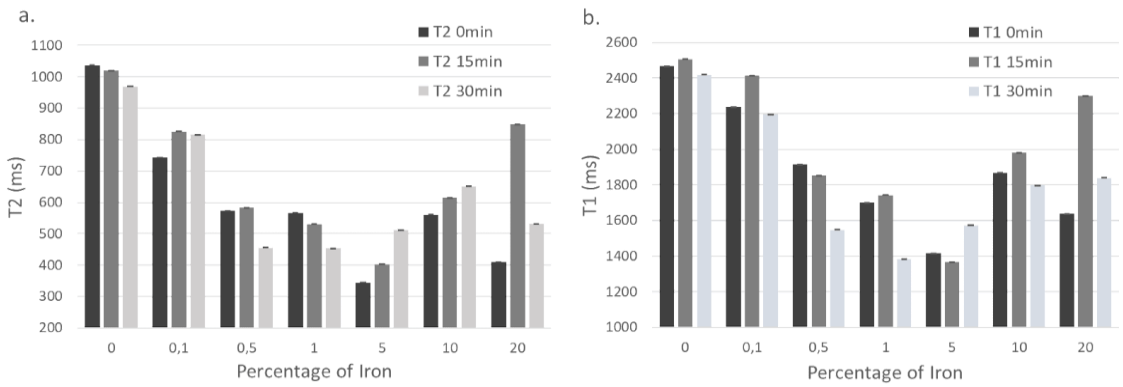

Source: by the author.

Based on **Figure IV.14**, it is evident that iron doping within the ZnO structure induces relaxation effects. Even small quantities of iron in the compounds were capable of imparting Mp. Concerning the doping time, it is noticeable that the 30-minute doping time resulted in shorter T1 and T2 values within the 0.1 to 1.0 % iron range compared to other doping times. Specifically, the T1 values for FeZnO 1.0% at 30 minutes matched those of FeZnO 5.0% at time 0 and 15 minutes of doping time. Consequently, lower iron concentrations with a 30-minute doping time yield superior outcomes, as they also enhance the material's luminescence properties.

To calculate the relaxivity of the synthesized CA, the iron content must be determinate. Samples at different doping time, at a concentration of 0.5% relative to the amount of Fe, were tested. The samples employed for the MRI analyses followed the sequence shown in **Figure IV.15**. The concentration of FeZnO 0.5 tested ranged from 0.625 to 20 mg mL^{-1}. The findings are shown in **Figure IV.16**.

Figure IV.15. Sample distribution in the MRI analyses.

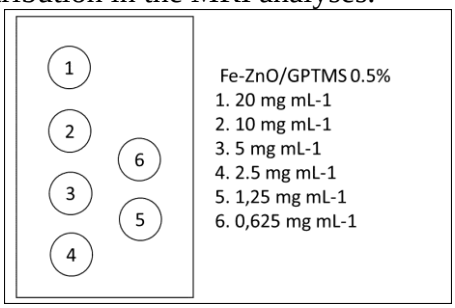

Source: by the author.

Figure IV.16. T2-weighted and T1-weighted outcomes of FeZnO samples containing 0.5% iron. The concentration ranges from 0.625 to 20 mg mL^{-1}.

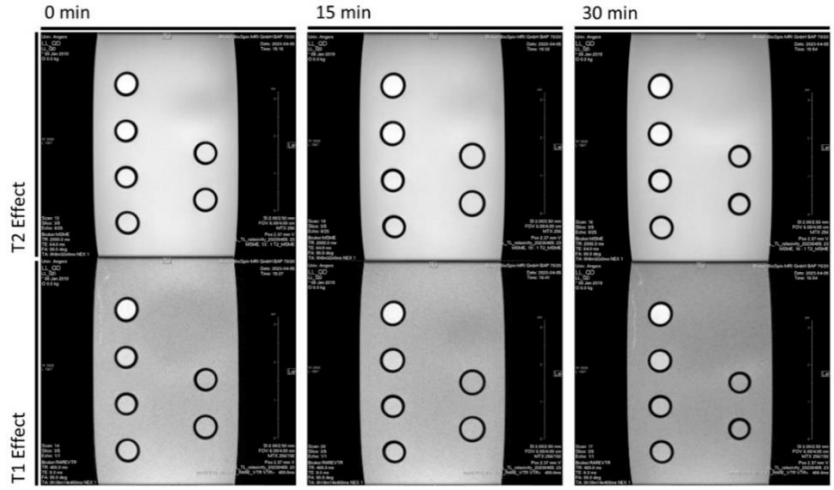

Source: by the author.

The T2 and T1 values are shown in **Table IV.8** and **Table IV.9**, respectively.

Table IV.8. T2 values for different concentration of FeZnO 0.5% and relaxation time calculation.

FeZnO 0.5	**0 min**		**15 min**		**30 min**	
[ ] mg mL^{-1}	**T2 (ms)**	**1/T2 (1/s^{-1})**	**T2 (ms)**	**1/T2 (1/s^{-1})**	**T2 (ms)**	**1/T2 (1/s^{-1})**
20	569	1.76	586	1.71	456	2.19
10	780	1.28	807	1.24	678	1.47
5	959	1.04	964	1.04	872	1.15
2.5	1060	0.94	1051	0.95	1003	1.00
1.25	1082	0.92	1056	0.95	1049	0.95
0.625	1126	0.89	1149	0.87	1146	0.87

Table IV.9. T1 values for different concentration of FeZnO 0.5 % and the calculation of relaxation time.

FeZnO 0.5	**0 min**		**15 min**		**30 min**	
[ ] mg mL^{-1}	**T1 (ms)**	**1/T1 (1/s^{-1})**	**T1 (ms)**	**1/T1 (1/s^{-1})**	**T1 (ms)**	**1/T1 (1/s^{-1})**
20	1899	0.53	1841	0.54	1554	0.64
10	2172	0.46	2174	0.46	1956	0.51
5	2342	0.43	2304	0.43	2173	0.46
2.5	2343	0.43	2333	0.43	2276	0.44
1.25	2509	0.40	2505	0.40	2417	0.41
0.625	2561	0.39	2563	0.39	2479	0.40

The calculation of molar concentration of Fe in each sample was determinate by ICP assay. The results are shown in **Table IV.10**.

Table IV.10. ICP calculation of Fe in FeZnO0.5 samples with different doping time.

Sample	**[ ] mmol L^{-1} of iron**
FeZnO0.5 0 min	0.39
FeZnO0.5 15min	0.24
FeZnO0.5 30min	0.26

The values were plotted in a graph dispersion for the calculation of the relaxivity of FeZnO 0.5 at various doping times. The outcomes are shown in **Figure IV.17** and Relaxivity values are shown in **Table IV.11**.

Table IV.11. Relaxivity values of FeZnO0.5 samples with different doping time.

Sample	r2 (mmol L^{-1} s^{-1})	r1 (mmol L^{-1} s^{-1})	r2/r1
FeZnO0.5 0 min	2.36	0.35	6.74
FeZnO0.5 15min	3.43	0.59	5.81
FeZnO0.5 30min	5.13	0.92	5.57

Figure IV.17. Relaxivity plots of FeZnO0.5 samples in different doping time. Relaxivity for r2 (a) and r1 (b).

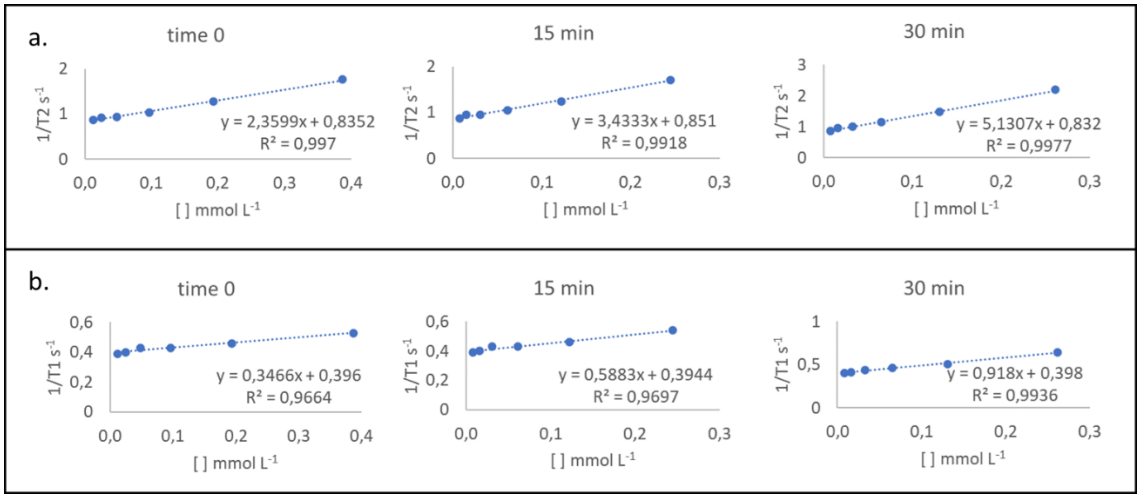

Source: by the author.

According to **Figure IV.17**, it is evident that the samples of FeZnO0.5 synthesized with a doping time of 30 minutes exhibit the highest slope value, indicating enhanced relaxivity. Therefore, the doping duration of 30 minutes appears to be optimal for synthesizing the CA with the most pronounced Mr effect.

Many CAs pose cytotoxic risks and various side effects (KALLER; AN, 2023). Enhanced relaxivity in MRI allows for reduced CA dosage in clinical investigations (LOEVNER et al., 2022). It is plausible that a higher concentration of FeZnO does not exhibit the same cytotoxicity as Gd at higher concentrations in terms of r1 relaxivity. Utilizing a larger quantity of FeZnO in GPTMS may therefore be feasible with reduced cytotoxicity.

IV.2.3.3 MRI study of FeZnO adopting iron concentration between 0.1 to 1 %

As it has shown that the condition “30 min” (addition of iron source 30 min after the start of the ZnO formation) allows the synthesis of the best Mr CA, the next step is to evaluate the impact of the percentage of iron added to prepare the FeZnO. The tested percentages were 0.1, 0.5 and 1.0 % using iron acetate as source of iron. The T1 and T2 values are described in **Table IV.12** and plotted in the form of a graph in **Figure IV.18**.

Table IV.12. T1 and T2 values for the FeZnO-GPTMS samples with different concentration of iron (0.1, 0.5 and 1.0 %).

Samples	T1 (ms)	T2 (ms)
Water	2674 ± 28	1110 ± 73
ZnO-GPTMS	2531 ± 24	870 ± 34
FeZnO0.1-GPTMS	1867 ± 10	377 ± 9
FeZnO0.5-GPTMS	1271 ± 5	213 ± 3
FeZnO1.0-GPTMS	1125 ± 4	188 ± 1

Figure IV.18. T1 and T2 values of FeZnO-GPTMS in the range of 0 to 1.0%.

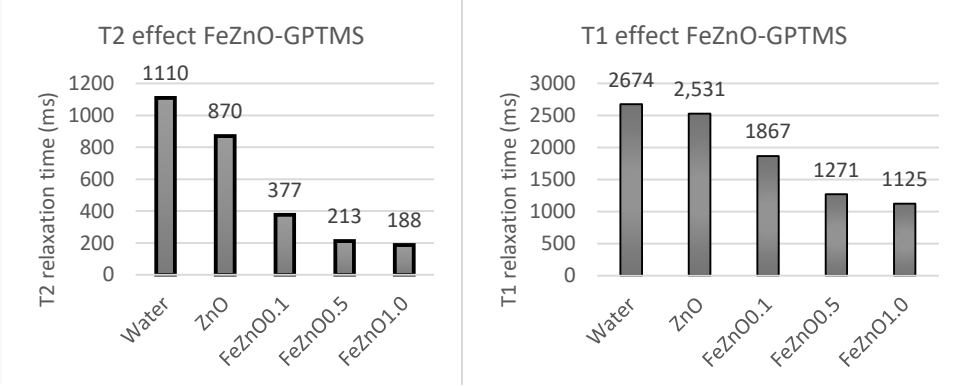

Source: by the author.

According to **Figure IV.18**, the FeZnO-GPTMS samples exhibit notable T2 relaxation effects along with favourable T1 effects. The analysis was conducted using samples at a concentration of 20 mg mL^{-1}. To ascertain the relaxivity values relative to iron concentration, sample concentration among 0.1, 0.5, and 1.0% of iron were assessed, and the iron content was quantified via ICP analysis. The resulting T2 and T1 values obtained from MRI analysis are summarized in **Table IV.13** and **Table IV.14**,

respectively, while **Table IV.15** outlines the iron concentrations determined by ICP analysis. The relaxivity calculations were performed by plotting the data, as shown in **Figure IV.19**.

Table IV.13. T2 values for Fe-ZnO samples between 0.1, 0.5 and 1.0%.

Fe-ZnO	**Fe-ZnO 0.1**		**Fe-ZnO 0.5**		**Fe-ZnO 1.0**	
[ ] mg mL^{-1}	**T2 (ms)**	**1/T2 (1/s^{-1})**	**T2 (ms)**	**1/T2 (1/s^{-1})**	**T2 (ms)**	**1/T2 (1/s^{-1})**
20	390	2.56	232	4.31	223	4.48
10	639	1.56	423	2.36	404	2.48
5	827	1.21	648	1.54	620	1.61
2.5	931	1.07	824	1.21	810	1.23
1.25	1122	0.89	992	1.01	1038	0.96
0.625	1139	0.88	1078	0.93	1099	0.91
water	1060	0.94	1029	0.97	1041	0.96

Table IV.14. T1 values for Fe-ZnO samples between 0.1, 0.5 and 1.0%.

Fe-ZnO	**Fe-ZnO 0.1**		**Fe-ZnO 0.5**		**Fe-ZnO 1.0**	
[ ] mg mL^{-1}	**T1 (ms)**	**1/T1 (1/s^{-1})**	**T1 (ms)**	**1/T1 (1/s^{-1})**	**T1 (ms)**	**1/T1 (1/s^{-1})**
20	1889	0.53	1326	0.75	1201	0.83
10	2252	0.44	1789	0.56	1661	0.60
5	2473	0.40	2133	0.47	2020	0.50
2.5	2546	0.39	2310	0.43	2214	0.45
1.25	2646	0.38	2594	0.39	2466	0.41
0.625	2754	0.36	2664	0.38	2624	0.38
water	2857	0.35	2872	0.35	2723	0.37

Table IV.15. ICP calculation of Fe in FeZnO samples with different iron concentration: 0.1, 0.5, and 1.0%.

Sample	**[ ] mmol L^{-1} of iron**
FeZnO0.1	0.09
FeZnO0.5	0.36
FeZnO1.0	0.65

Figure IV.19. Scatter plot showing relaxivity as a function of iron concentration for FeZnO samples. Relaxivity for r2 (a), and r1 (b).

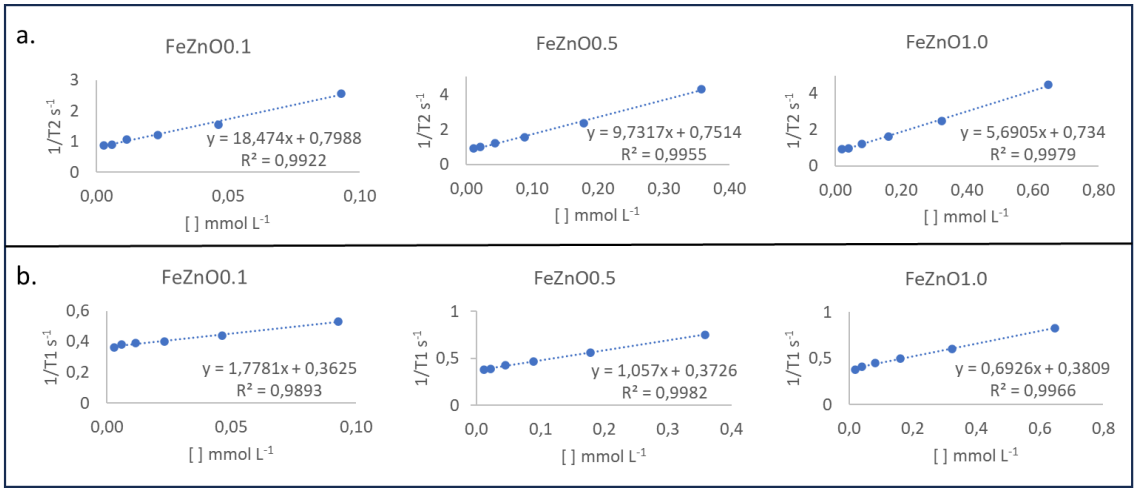

Source: by the author.

The relaxivity values of FeZnO as a function of iron concentration are shown in **Table IV.16**.

Table IV.16. Relaxivity value of Fe-ZnO at concentration of 0.1%, 0.5%, and 1.0% Fe.

Samples	FeZnO 0.1	FeZnO 0.5	FeZnO 1.0
r2	18.47	9.73	5.69
r1	1.78	1.06	0.69
r1/r2	0.10	0.11	0.12

According to the results shown in **Table IV.16**, the r1 & r2 values increase as iron theoretical content increases. The ratio r1/r2 increases with iron content showing that the CA is mainly a T2 CA.

IV.2.4 Characterization

After defining the best test conditions, characterization tests were conducted to confirm the doped structure of Fe-ZnO. For this purpose, two tests were added: XRD and EXAFs. Samples of Fe-ZnO with different doping times (0, 15, and 30 minutes) and with different iron concentrations (0.1%, 0.5%, and 1.0%) were analysed.

IV.2.4.1 X-ray diffraction

The diffractograms are shown in **Figure IV.20**.

Figure IV.20. Diffractogram of Fe-ZnO samples with varying concentrations and consistent doping time for 0 min (a), 15 min (b), and 30 min (c); and with differing doping times and consistent concentration for FeZnO 0.1 (d), FeZnO 0.5 (e), and FeZnO 1.0 (f).

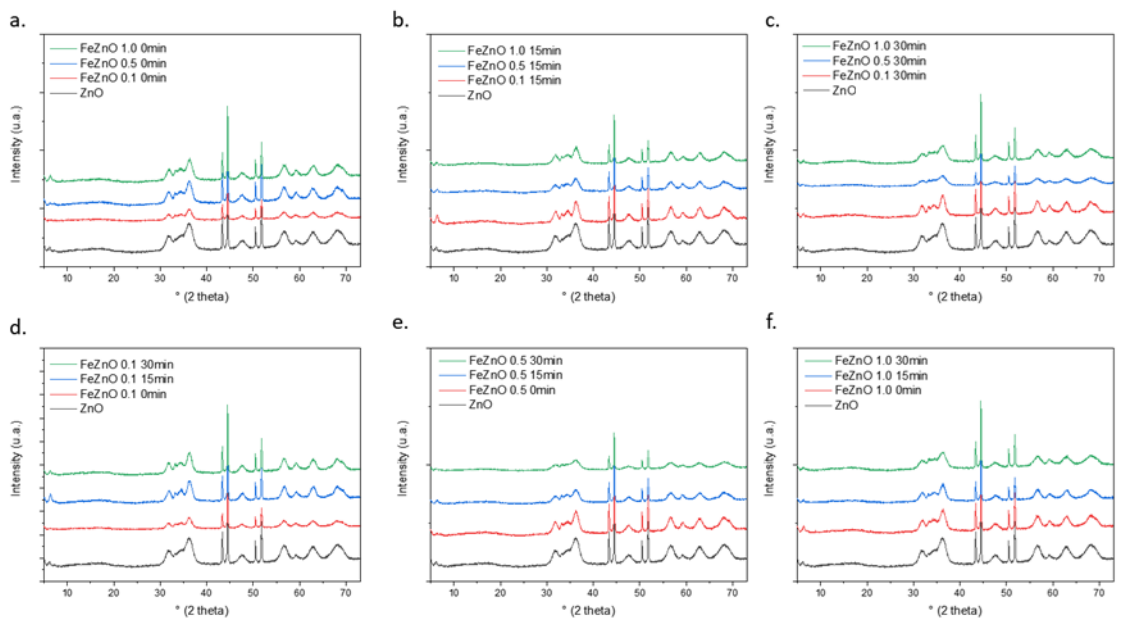

Source: by the author.

Some additional peaks appeared in the X-ray diffractogram of the samples; however, these peaks located at 43.32°, 44.46°, 50.43°, and 51.77° 2θ angles result from the metallic apparatus used for conducting the experiments. All X-ray diffraction patterns showed the presence of the ZnO phase. The Bragg peaks found were 2θ = 31.81°, 34.09°, 36.30°, 47.80°, 56.83°, 62.83°, and 68.29°, which correspond to the (100), (002), (101), (102), (110), (103), and (112) planes of ZnO crystal identified in all doped ZnO samples (BA-ABBAD et al., 2013; SEKAR et al., 2018). The crystallite size can be calculated using the Scherrer equation (CHÉRIF et al., 2023; SALEM et al., 2023) described in the following equation (2):

$$D = \frac{K\lambda}{\beta \cos\theta} \qquad (2),$$

where D represents the crystallite size (nm), K is the Scherrer constant (0.9), λ is the wavelength of the X-ray source (0.15406), β is the Full Width at Half Maximum (FWHM) (in radians), and θ is the peak position (in radians). The size was calculated from the mean ± SD of the major peaks in the X-ray diffractogram presented in **Figure**

IV.20. The particle sizes for different concentrations and different doping times are described in **Table IV.17.**

Table IV.17. Particle Size of Fe-ZnO samples calculated using the Scherrer equation (mean ± sd).

	Doping time		
Samples	**0 min**	**15 min**	**30 min**
FeZnO0.1	6.69 ± 2.11 nm	6.98 ± 2.16 nm	6.91 ± 2.26 nm
FeZnO0.5	6.29 ± 1.91 nm	6.19 ± 1.71 nm	4.90 ± 1.11 nm
FeZnO1.0	6.18 ± 1.82 nm	6.33 ± 1.85 nm	5.23 ± 1.30 nm
pristine ZnO	5.00 ± 1.23 nm	-	-

According to **Table IV.17**, the doping time shows a greater influence on the final particle size of the samples than the different concentrations of iron used to form the ZnO particle. Although there was no statistical difference ($p > 0.05$) between the average particle sizes for both cases of different doping times and different concentrations. When considering the luminescent and Mp of the studied materials, it can say that there is no correlation between particle size and the studied properties. Therefore, the presence of iron in the doped structure is responsible for altering the luminescent and Mp.

IV.2.4.2 XAS analysis

The XAS technique was performed to study the absorption edge behavior in the X-ray region of Fe and Zn elements in the doped Fe-ZnO structure. XAS yields results from both XANES, which investigates electronic properties, geometry, and the oxidation state of the material under study, and EXAFs, which provide information such as the type and number of neighboring elements to the studied element, their distance, and disorder. This will give an idea of the distribution of iron and zinc elements in the doped material.

The EXAFs spectra for Fe-doped ZnO samples, focusing on the energy of the iron atom's K-edge (K ~7112 eV), are shown in **Figure IV.21** for the same concentration of iron and different doping times, as well as for the same doping time but different iron concentrations.

Figure IV.21. XAS spectra (XANES + EXAFs) at the iron atom's K-edge energy for different Fe-ZnO samples. (a) Different doping times at the same iron ratio, and (b) Different iron ratios at the same doping time.

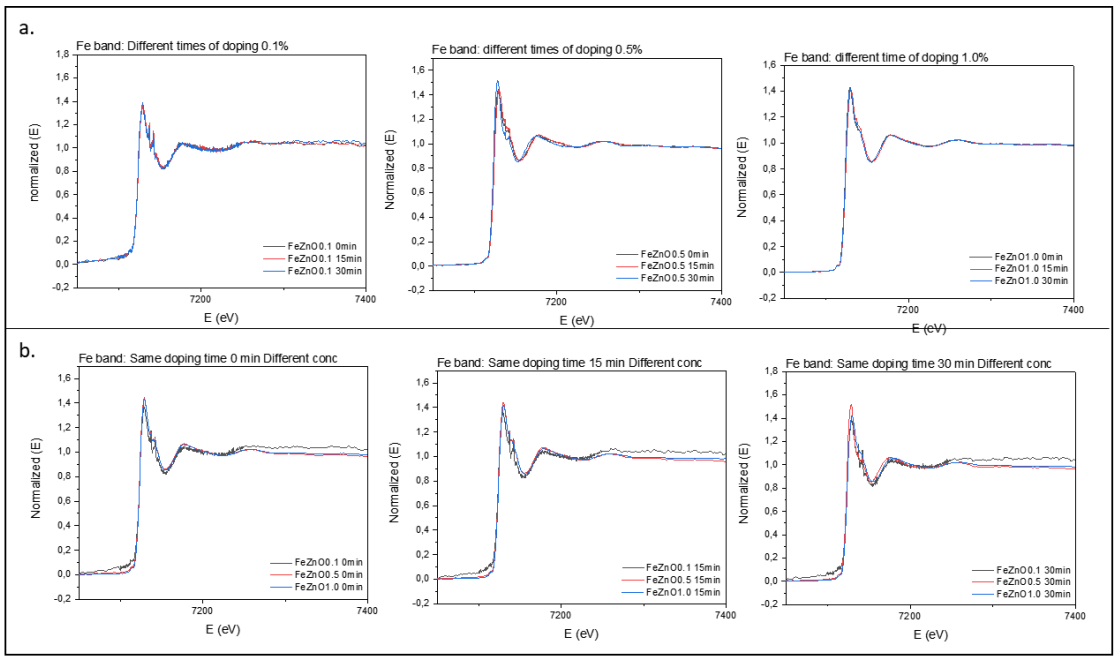

Source: by the author.

Based on the obtained results (**Figure IV.21**), the assessment of the iron absorption edge and XANES spectra can be conducted by comparing them with standard oxidation-reduction patterns of this element with Fe^{3+} and Fe^{2+}. The results are shown in **Table IV.18.**

Table IV.18. Oxidation-reduction patterns of Fe-ZnO samples based on XANES spectra for the Fe band.

	0 min	**15 min**	**30 min**
FeZnO 0.1	100% « Fe^{2+}»	100 % « Fe^{2+}»	100% « Fe^{2+}»
FeZnO 0.5	59% « Fe^{3+}» + 41% « Fe^{2+}»	100 % « Fe^{3+}»	100% « Fe^{2+}»
FeZnO 1.0	68% « Fe^{3+}» + 32% « Fe^{2+}»	100 % « Fe^{3+}»	79% « Fe^{3+}» + 21% « Fe^{2+}»

* Percentage of oxidation related to Fe^{3+} and Percentage of Reduction related to Fe^{2+}.

According to the XANES results shown in **Table IV.18**, it can be concluded that there is a predominance of Fe(II) in FeZnO 0.1 samples, with no percentage of oxidation characteristic of Fe(II) regardless of the doping time. Concerning higher amounts of Fe, there is a greater difference in oxidation-reduction percentage, which

analyzes the Fe-O distance in terms of oxidation and reduction. There is a significant change in the local order around Fe, particularly in the first coordination layer (Fe-O). The distance (Fe-O) for "red" is smaller than the distance for "ox" by 0.1 Å.

The proportion of Fe^{2+} to Fe^{3+} can help explain differences in the magnetic and luminescent properties of the material, as they depend on the presence of iron in the ZnO crystal structure and the deformation that occurs when zinc atoms are replaced by iron atoms. According to Rajan et al. (2021), the crystal structure is more stable when zinc atoms are replaced by Fe^{2+}, while deformation is more pronounced when the substitution is by Fe^{3+} atoms. Looking at Figure IV.14, which presents results for T2 (in milliseconds), it can see that values for Fe-ZnO samples with 0.5% doping decrease as doping time increases. This can be attributed to a higher presence of Fe^{2+} ions, as indicated in **Table IV.18**. This observation also explains why the Fe-ZnO samples with 0.1% doping exhibit higher r2 relaxivity values, indicating a predominance of Fe^{2+} ions.

The XAS spectra for the energy of the Zn atom's K-edge (K ~9660 eV) were also studied, and the results are shown in **Figure IV.22**.

Figure IV.22. XAS spectra (XANES + EXAFs) at the zinc atom's K-edge energy for different Fe-ZnO samples. (a) Different doping times at the same iron ratio, and (b) Different iron ratios at the same doping time.

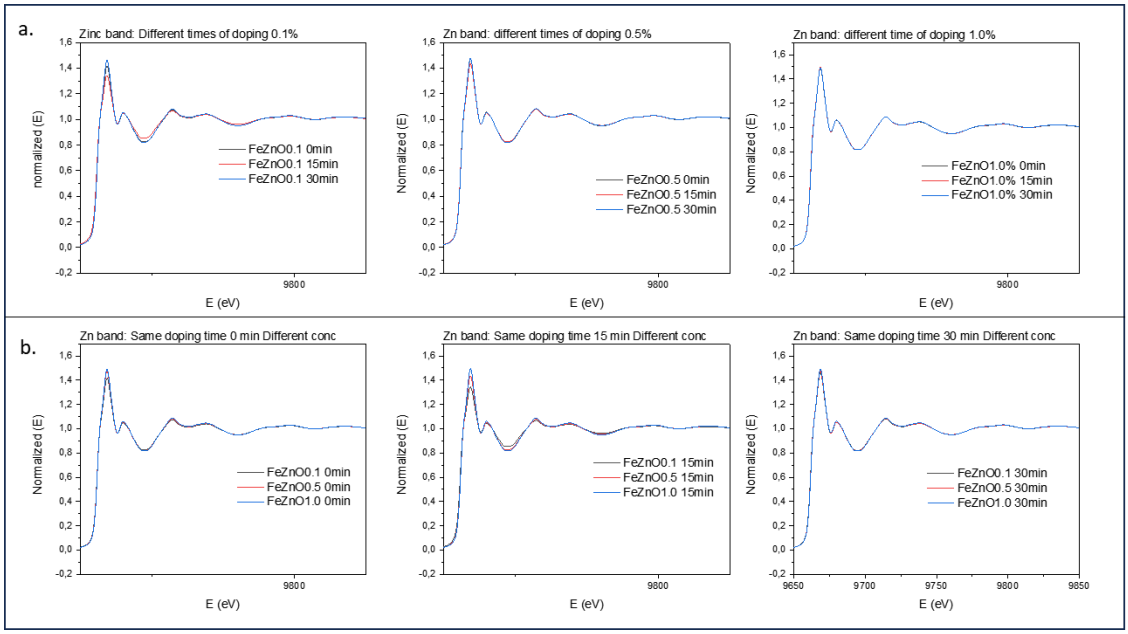

Source: by the author.

The XAS spectra at the zinc atom's K-edge energy were demonstrated in **Figure IV.22**. The resolution of these spectra aimed to determine if the coordination spheres in

the EXAFs spectra could provide an indication that iron atoms may be interconnected with zinc atoms, thereby proving a doped structure. Additionally, it sought to ascertain whether this crystalline structure presents iron atoms internally bonded to the zinc atom or if it is interconnected as a core@shell structure. This study is being conducted in collaboration with the Synchrotron Light Laboratory Soleil, France, and so far, the results have not been fitted to confirm this theory. The data will need to be processed using mathematical equations and Fourier transformation. Once the data is processed, these results will be incorporated into the article titled "Fe-Doped ZnO Structures: A Study on Doping Iron Concentration and Doping Times to Enhance Luminescent and Magnetic Properties", which is currently in progress.

IV.2.4 Fe-doped ZnO into PLGA particles

After the FeZnO/GPTMS analysis, a study was performed with the Fe-ZnO NPs inside the PLGA particles. The experimental conditions were based on the results obtained for the synthesis of PLGA:ZnO particles described in **Chapter III**.

The best results of PLGA:ZnO were obtained in the nominal ratio of 10:6 (w:w, mg), and the choice of components to be tested in FeZnO NPs were PLGA:FeZnO 10:6 (w:w, mg). The best iron percentages chosen were 0.1, 0.5 and 1.0% Fe in terms of the molar concentration of [Fe]/[Fe+Zn], which were based on the results obtained for FeZnO NPs coated with GPTMS.

IV.2.4.1 FeZnO coated by OA

FeZnO is coated by OA to embed in PLGA particles. Yield results in mass are described in **Table IV.19**.

Table IV.19. Mass yield of FeZnO NPs

Sample	Yield (mg)
ZnO/OA	75.7
FeZnO 0.1% / OA	68.9
FeZnO 0.5% / OA	74.2
FeZnO 1.0% / OA	77.6

According to the results described in **Table IV.19**, the mass proportions of the synthesised components were similar. All samples were dispersed in DCM at a concentration of 40 mg mL^{-1} for further synthesis of PLGA NPs. The luminescence properties were analysed at a concentration of 0.08 mg mL^{-1}. The results are shown in **Figure IV.23**.

Figure IV.23. Luminescence of Fe-ZnO/OA compounds dispersed in DCM: a) emission spectra, excitation in 343 nm; b) emission spectra, normalized intensity; and c) maximum intensity of emission.

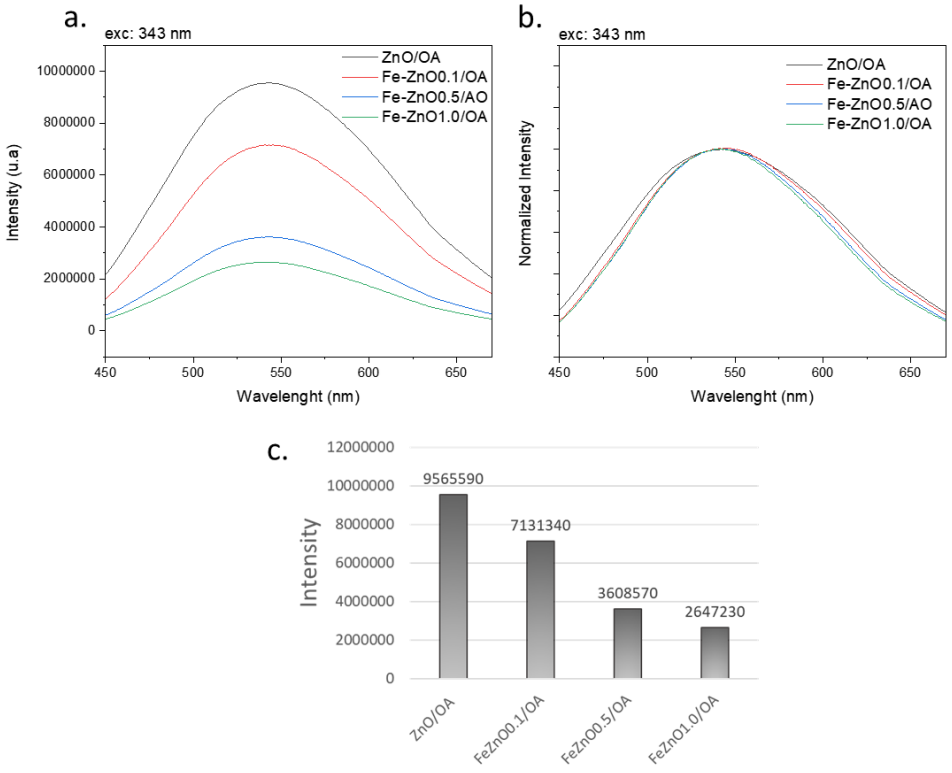

Source: by the author.

Figure IV.23 shows that the maximum emission intensity decreases with the amount of dopant used. The samples were analysed 15 days after synthesis. All samples have the same concentration in mg mL^{-1}. There is no maximum intensity shift in the presence of iron. However, the luminescence response can be considered larger than that of the Fe-ZnO NPs modified with GPTMS. The stability of the luminescence of the samples has been maintained over the period of analysis.

IV.2.4.2 PLGA:FeZnO Luminescence assays and size analyse

After synthesis, the FeZnO components were incorporated into PLGA NPs. The synthesis was performed as described in **Table IV.20**.

Table IV.20. Synthesis conditions of PLGA:FeZnO

Samples	Composition
PLGA:ZnO 10:6	10 mg of PLGA + 6 mg of ZnO
PLGA:FeZnO0.1 10:6	10 mg of PLGA + 6 mg of Fe-ZnO 0.1 %
PLGA:FeZnO0.5 10:6	10 mg of PLGA + 6 mg of Fe-ZnO 0.5 %
PLGA:FeZnO1.0 10:6	10 mg of PLGA + 6 mg of Fe-ZnO 1.0 %

All three PLGA:FeZnO samples were tested at Fe concentrations between 0.1 and 1.0% in terms of luminescence and Mp. PLGA:ZnO samples were used as parameters to compare. The results of size are shown in **Table IV.21**.

Table IV.21. Results of DLS size analysis of PLGA:Fe-ZnO samples

Sample	Size (nm)	PDI
PLGA	131.6 ± 4.0	0.152 ± 0.038
PLGA:ZnO	141.2 ± 2.8	0.149 ± 0.009
PLGA:Fe-ZnO0.1 10:6	182.0 ± 3.0	0.098 ± 0.022
PLGA:Fe-ZnO0.5 10:6	228.9 ± 2.3	0.161 ± 0.016
PLGA:Fe-ZnO1.0 10:6	233.8 ± 1.1	0.195 ± 0.012

According to the results shown in **Table IV.21**, the size of the NPs is close to 200 nm. The PDI of the samples was less than 0.2, indicating a uniform population size of the NPs. The size of 200 nm is in accordance with the expected results for PLGA NPs. The samples were evaluated for stability in PVA and T80% suspension 7 days after preparation. The results are presented in **Table IV.22**.

Table IV.22. Size and zeta potential of PLGA:Fe-ZnO samples after 7 days of preparation

Sample	Size (nm)	PDI	ZP (mV)
PLGA	147.2 ± 4.8	0.213 ± 0.017	-23.40 ± 0.46
PLGA:ZnO	157.4 ± 3.1	0.237 ± 0.007	-13.50 ± 2.31
PLGA:Fe-ZnO0.1 10:6	213.2 ± 1.8	0.221 ± 0.005	-14.10 ± 1.14
PLGA:Fe-ZnO0.5 10:6	295.3 ± 6.2	0.299 ± 0.012	-10.80 ± 0.25
PLGA:Fe-ZnO1.0 10:6	224.5 ± 6.4	0.256 ± 0.009	-8.43 ± 0.70

According to the stability results in **Table IV.22** and considering the results described in **Table IV.21**, it can be observed that the particle size of PLGA:FeZnO and PLGA:ZnO particles increased after the period of 7 days. In addition, the PDI values also increased, indicating that there was an aggregation process of the PLGA particles. The presented PDI values are below 0.3 and can still be used for further testing. Considering that the size does not exceed 300 nm, the NPs can be studied. The zeta potential values were also observed. It can be observed that the PLGA particles did not significantly change their size after 7 days, although their PDI increased, considering that the zeta potential value was the same as that found in the literature, which is common for this particle. The other PLGA particles presented a zeta potential value close to -10 mV, which could explain the stability of the compounds dispersed in PVA over the 7-day period, with an increase in size and PDI value.

The samples were analysed in Luminescence assay, the results are shown in **Figure IV.24**.

Figure IV.24. Analysis of the luminescence results of the Fe-ZnO samples with iron concentrations of 0, 0.1, 0.5 and 1.0 %.

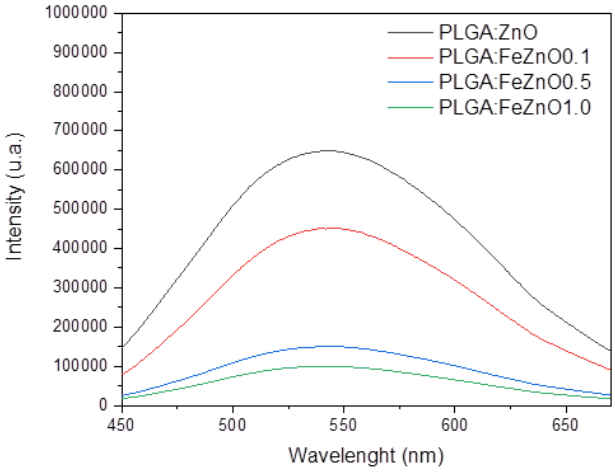

Source: by the author.

According to results shown in **Figure IV.24**, when excited in 343 nm wavelength, the samples shown luminescence emission in 540 nm. The samples shown decrease of intensity with the increase of iron content as expected results.

IV.2.4.3 TEM analyses.

The samples were analysed by TEM at Fe-ZnO ratios of 0.1, 0.5 and 1.0%. Unlike the PLGA:ZnO:IO samples, the PLGA:FeZnO samples were not lyophilised and were analysed by drying the samples dispersed in PVA/T80. The PLGA particles are sensitive to heating steps. The average size of the particles could not be calculated. The results for PLGA:FeZnO0.1 are shown in **Figure IV.25**.

Figure IV.25. TEM analysis of PLGA:FeZnO0.1. Different scale bars are shown in a) 100 nm, b) 100 nm; c) 50 nm and d) 20 nm.

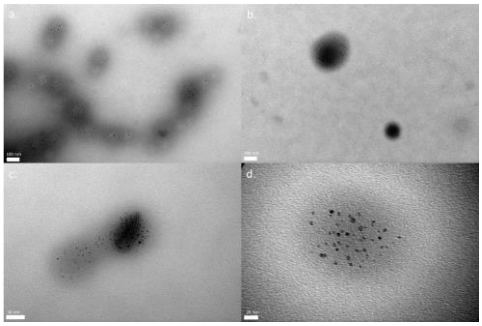

Source: by the author.

According to results shown in **Figure IV.25**, it can see the PLGA particles containing FeZnO are able to form. A spherical shape is obtained. It can be seen NP of Fe-ZnO0.1 inside of the PLGA structure in all the pictures. The **Figure IV.25a** shows that the particles are close one of other, but o aggregation process is not observed. The **Figure IV.25b** shows that different sizes are obtained for this particle, and this can be explained for the PDI value obtained for this sample according to **Table IV.22**. The results of TEM for PLGA:FeZnO0.5 samples are shown in **Figure IV.26**.

Figure IV.26. TEM analysis of PLGA:FeZnO0.5. Different scale bars are shown in a) 100 nm, b) 100 nm; c) 50 nm and d) 20 nm.

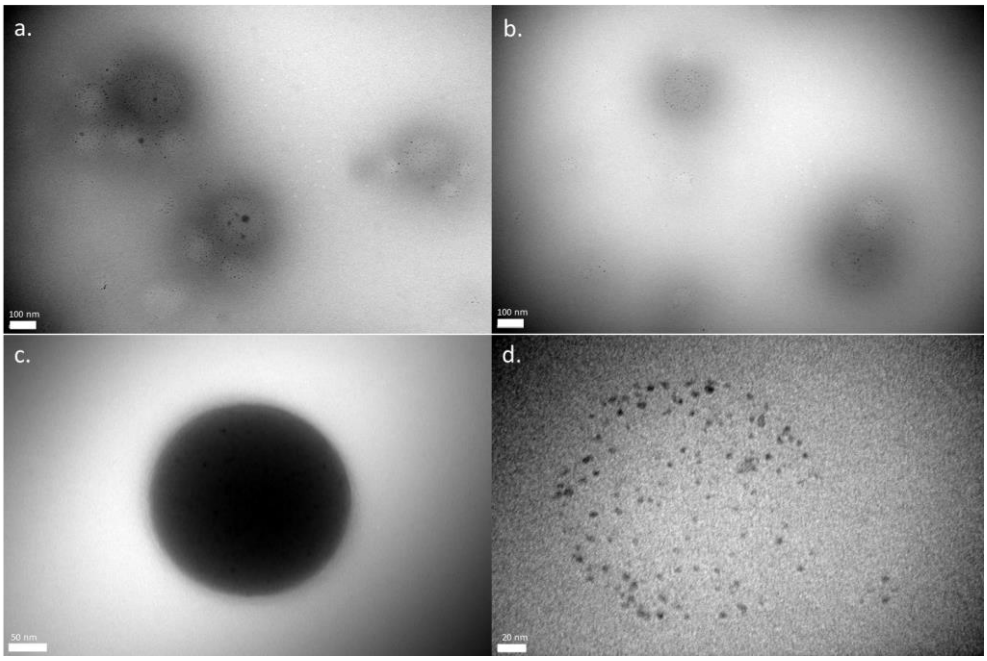

Source: by the author.

According to the results shown in **Figure IV.26**, it can be observed that the PLGA particles containing 0.5% Fe doped ZnO NPs are formed. The PLGA particles in **Figure IV.26a** and **IV.26b** can show that PLGA particles with spherical shape are formed, the boundary of the NPs is not fully observed due to the spreading of PLGA after the drying process, so the average calculation of the particle size is not possible. The FeZnO0.5 NPs are not found outside the PLGA in **Figures IV.26a and IV.26b**, which can confirm that the NPs are fully embedded. In **Figure IV.26c**, it can be observed that a regular spherical shape of PLGA:FeZnO0.5 is formed in which FeZnO0.5 is completely inside the PLGA structure. In **Figure IV.26d**, FeZnO0.5 NPs can be observed and their size can be calculated (**Table IV.23**). The results for PLGA:FeZnO1.0 are shown in **Figure IV.27**.

Figure IV.27. TEM analysis of PLGA:FeZnO1.0. Different scale bars are shown in a) 100 nm, b) 100 nm; c) 50 nm and d) 20 nm.

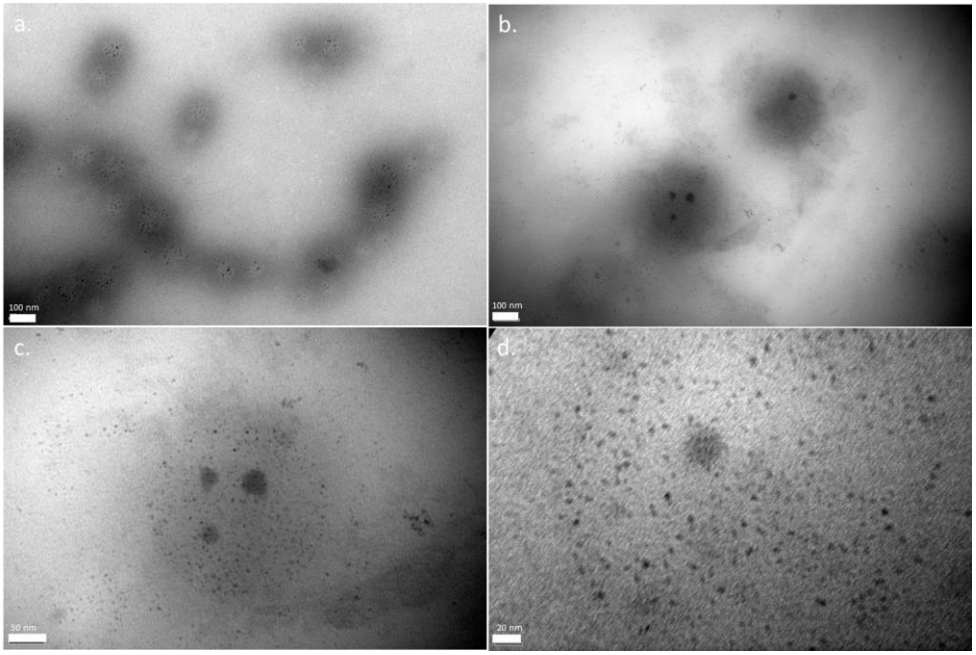

Source: by the author.

According to the result of **Figure IV.27**, in relation to PLGA:FeZnO1.0 particles, there was the presence of structures outside the PLGA particles (**Figure IV.27b**), without the presence of FeZnO particles inside, in addition, large particles appeared inside the PLGA besides FeZnO, which seemed to form a core inside the PLGA. In **Figure IV.27d**, an aggregate of FeZnO particles can be seen within these darker regions. Iron may have promoted the aggregation of FeZnO NPs. In addition, FeZnO NPs were observed outside the PLGA structure, which is not observed in the PLGA:FeZnO0.1 and PLGA:FeZnO0.5 samples. The size of the PLGA particles cannot be calculated for MET analysis due to the dispersion effect after the drying process. The size of FeZnO1.0 NPs was measured and the results are given in **Table IV.23**. To compare the results, PLGA:ZnO NPs prepared under the same conditions as PLGA:FeZnO particles were analysed by TEM, the results are shown in **Figure IV.28**.

Figure IV.28. TEM analysis of PLGA:ZnO. Different scale bars are shown at a) 50 nm and b) 20 nm.

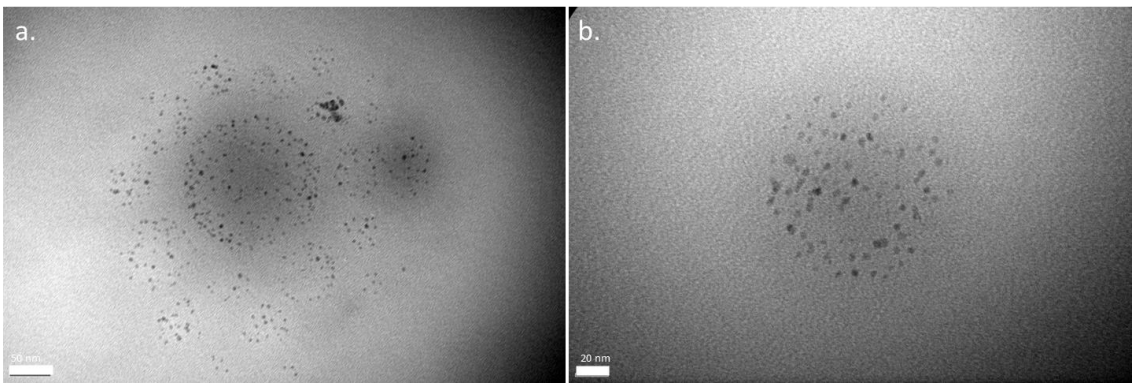

Source: by the author.

As shown in **Figure IV.28**, PLGA:ZnO particles were successfully prepared. The size of the PLGA particles cannot be calculated due to the dispersion of the PLGA after the drying process. In **Figure IV.28a**, it can be observed that smaller particles are very close due to a possible aggregation process, which is evident from the size results measured in DLS and can also be explained by the lower stability according to the zeta potential calculations (**Table IV.23**).

The size of ZnO and Fe-ZnO NPs was calculated from the data collected using ImageJ software. Histograms of the NPs were constructed, and the mean was calculated from the Gaussian curve. The results are presented in **Figure IV.29** and **Table IV.23**.

Figure IV.29. Histogram of NPs size inside of PLGA of a) ZnO, b) FeZnO0.1, c) FeZnO0.5, and FeZnO1.0.

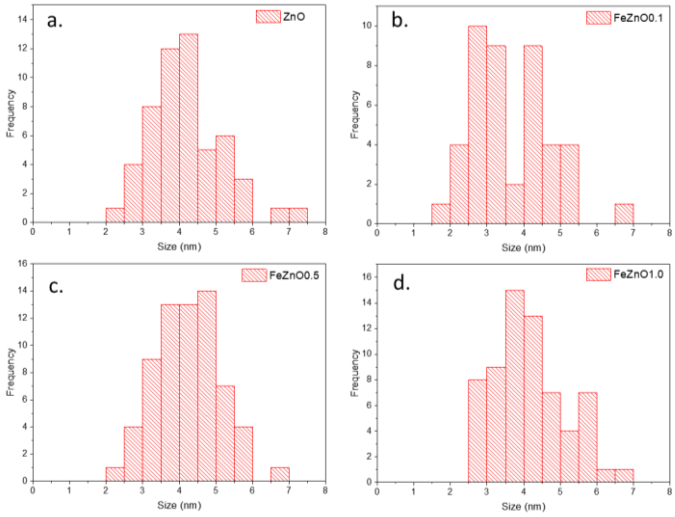

Source: by the author.

Table IV.23. Size of FeZnO NP by Gaussian curve built from Histogram.

Sample	Size (nm)
ZnO	3.97 ± 0.32
FeZnO0.1	3.43 ± 0.05
FeZnO0.5	4.21 ± 0.14
FeZnO1.0	3.84 ± 0.09

According to the results in **Table IV.23**, there is no significant difference in size between the synthesised FeZnO NPs and the ZnO NP. The calculated particle sizes are around 4 nm. Therefore, there is evidence that, in this case, it is not the size of the NPs that is the dominant factor affecting the luminescence and magnetism of the compounds, but the presence of the iron dopant.

IV.2.4.4 MRI results

The samples were lyophilized to perform the MRI studies at the appropriate concentration. The concentration used for the evaluation of the MRI analyses was 20 mg mL^{-1}. This is the same concentration in mass as was used for the verification of the Mp of the Fe-ZnO:GPTMS samples. In the case of the lyophilized samples, it was found that the samples were not able to disperse completely in water.

Since the samples showed strong indications of precipitation, the samples were evaluated by magnetic effect using T2 map and T1 map (**Figure IV.30)**.

Figure IV.30. Mr results of PLGA:FeZnO: a) T2 map (TR = 2000 ms; TE = 8 ms); and b) T1 map of PLGA:FeZnO (TR = 400 ms; TE = 8 ms).

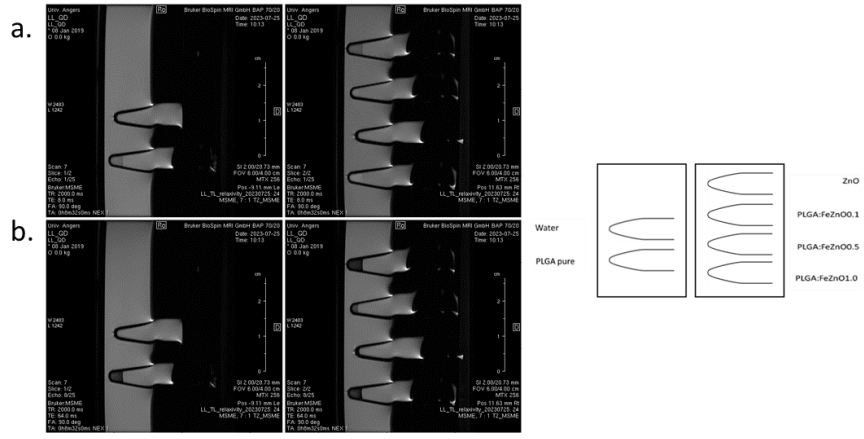

Source: by the author.

According to the results shown in **Figure IV.30**, they are represented in the value of T2 in two different regions of the precipitate. The top part with the NPs dispersed in the water and the bottom part with the precipitate. The values are shown in **Table IV.24.**

Table IV.24. T2 map values for PLGA:FeZnO samples.

Samples	**T2-map (ms)**	
	Top	**Bottom**
Water	1125 ± 68	1138 ± 51
PLGA	650 ± 20	78 ± 1
PLGA:ZnO	593 ± 16	63 ± 1
PLGA:FeZnO0.1	714 ± 30	112 ± 2
PLGA:FeZnO0.5	561 ± 16	462 ± 9
PLGA:FeZnO1.0	653 ± 15	60 ± 2

The analyses of **Table IV.24** show that the samples present a T2 effect in the region of the precipitate. This effect is also present in the PLGA:ZnO. However, this can be attributed to the precipitated formed. The PLGA:FeZnO0.5 samples showed uniform dispersion. The value of the T2 effect was more similar between the bottom and top regions.

In comparison with PLGA:FeZnO samples, it can be observed that the samples of PLGA and PLGA:ZnO show no different effect T1 when observing the precipitate. For better comparison, the value has been included in **Table IV.25**.

Table IV.25. T1 map values for PLGA:FeZnO samples.

Samples	**T1 map (ms)**	
	Top	**Bottom**
Water	2414 ± 83	2591 ± 51
PLGA	2327 ± 80	2124 ± 44
PLGA:ZnO	2393 ± 89	2223 ± 20
PLGA:FeZnO0.1	2336 ± 84	1544 ± 18
PLGA:FeZnO0.5	2136 ± 72	2071 ± 60
PLGA:FeZnO1.0	2321 ± 85	975 ± 5

According to the results presented in **Table IV.25**, in terms of the T1 effect, no effect is observed for PLGA or PLGA:ZnO. For the doped particles, a decrease in T1 effect of 1544 ms is observed for PLGA:FeZnO0.1 and 975 ms for PLGA:FeZnO1.0. There is a slight reduction of 2071 for the PLGA:FeZnO0.5 pellet. However, this solution was more uniform with less pellet formation.

IV.3 Conclusion

In this chapter, a system of Fe-doped ZnO NPs has been synthesized. The FeZnO NPs were studied using three main parameters: the concentration of doping iron, the doping time, and the choice of iron source.

From the Fe doping concentration studies, it was found that the luminescence properties of the material were maintained at lower iron concentrations. At a concentration of Fe between 0.1 and 1%, based on the percentage of [Fe]/[Fe+Zn] in mol, the luminescence properties were maintained with an emission peak at 540 nm when excited at 343 nm. The concentration of 0.1% in FeZnO showed a higher emission intensity than the emission intensity of pristine ZnO.

When the doping time was studied, it was found that the longer the doping time, i.e., the time the iron source was added to the synthesis, the more the properties such as luminescence intensity changed. It was observed that a doping time of 30 minutes was sufficient to produce particles with higher luminescence intensity.

About the iron source, tests were mainly carried out with ferric chloride and ferric acetate, and it was found that ferric acetate as an iron ion donor gave the best luminescence results.

The luminescence properties were interesting from the point of view of this study because FeZnO has MRI properties with T2 and T1 effects, with the relaxation effect values decreasing as the amount of iron increases. The FeZnO 0.5 sample at a concentration of 20 mg mL^{-1} showed values of T2 = 213 ms and T1 = 1271 ms. Changing the iron source did not significantly change the relaxation values. However, the doping time of 30 min increased the relaxivity value in r2 and r1 calculated as a function of iron concentration. Furthermore, the Mp exhibited higher values of relaxivity r2 and r1 for samples containing lower concentrations of doped Fe (0.1%).

PLGA NPs containing FeZnO (PLGA:FeZnO) were also investigated in this chapter. Although the samples showed luminescence after being coated with oleic acid and embedded in PLGA particles, their Mp were not promising. This requires further investigation in the future.

FeZnO NPs have been successfully obtained, but they are particles that show emission when excited at a wavelength in the UV region, which is not very interesting for diagnostic imaging. With this in mind, the next chapter develops a system based on CIS/ZnS NPs, since this NP can be excited at a longer wavelength, 525 nm, more suitable for biological applications.

REFERENCES

BA-ABBAD, M. M. et al. Visible light photocatalytic activity of Fe3+-doped ZnO nanoparticle prepared via sol-gel technique. **Chemosphere**, v. 91, n. 11, p. 1604–1611, 2013.

CHÉRIF, I. et al. X-Ray Diffraction Analysis by Modified Scherrer, Williamson–Hall and Size–Strain Plot Methods of ZnO Nanocrystals Synthesized by Oxalate Route: A Potential Antimicrobial Candidate Against Foodborne Pathogens. **J. Cluster Sci.**, v. 34, n. 1, p. 623–638, 1 jan. 2023.

GHALAJKHANI, A.; HAGHIGHI, M.; SHABANI, M. Efficient photocatalytic degradation of methylene blue in aqueous solution over flowerlike nanostructured MoS2-FeZnO staggered heterojunction under simulated solar-light irradiation. **Journal of Photochemistry and Photobiology A: Chemistry**, v. 359, p. 145–156, 15 maio 2018.

KALLER, M. O.; AN, J. Contrast Agent Toxicity. **StatPearls**, 1 maio 2023.

LOEVNER, L. A. et al. Efficacy and Safety of Gadopiclenol for Contrast-Enhanced MRI of the Central Nervous System The PICTURE Randomized Clinical Trial. 2022.

LUQUE-MICHEL, E., SEBASTIAN, V., LARREA, A., MARQUINA, C., BLANCO-PIETRO, M.J. Co-encapsulation of superparamagnetic NPs and doxorubicin in PLGA nanocarriers: Development, characterization and in vitro antitumor efficacy in glioma cells. **Eur. J. Pharm. Biopharm.**, 145, 65–75, 2019

MANAIA, E.B., KAMINSKI, R.C.K., CAETANO, B.L., BRIOIS V., CHIAVACCI, L.A., BOURGAUX C. Surface modified Mg-doped ZnO QDs for biological imaging. **Eur. J. Nanomed.** 7(2), 109–120, 2015.

SALEM, M. et al. Optical and passivation properties of ZnO:fe on silicon substrates. **J. Mater. Sci. Mater. Electron.**, v. 34, n. 4, p. 1–6, 1 fev. 2023.

SEKAR, A. D. et al. Photocatalytic degradation of naphthalene using calcined Fe–ZnO/ PVA nanofibers. **Chemosphere**, v. 205, p. 610–617, 1 ago. 2018.

SPANHEL L., ANDERSON M.A. Semiconductor Clusters in the Sol-Gel Process: Quantized Aggregation, Gelation, and Crystal Growth in Concentrated ZnO Colloids. **J. Am. Chem. SOC.** 113, 2826-2833, 1991.

VOGEL, A. I. **Química analítica qualitativa**. São Paulo: Mestre Jou, 1981

CHAPTER V

CIS/ZnS e Fe3O4 as bimodal contrast agent for biological imaging

CHAPTER V. CIS/ZnS and Fe_3O_4 as bimodal contrast agent for biological imaging

V.1 INTRODUCTION

All the QD used at the moment to confer luminescent properties to our dual CAs are based on ZnO and present one major limitation for in vivo applications due to the excitation wavelength required, i.e. ~343 nm. Such excitation can indeed be harmful for tissues and with very limited penetration (MORDON et al., 2010). The aim of this chapter is to evaluate the feasibility of producing QD with excitation shifted from the UV region and to use this new QD to prepare dual CAs.

In 2021, the CMAF research group in collaboration with Mint Lab prepared dual CAs based on core/shell conjugated systems consisting of copper, indium, sulfur as the core and zinc sulfide as the shell layer (CIS/ZnS) and ZnO doped with gadolinium (Gd-ZnO). This dual CA was indeed an MRI CA and a luminescent CA characterized by an emission at 600 nm when excited at 365nm but also at 500 nm (DA SILVA et al., 2021). However, the presence of Gadolinium, may limit the biological application of this new dual CA, due to the high toxicity of this ion ("FDA warns that gadolinium-based CAs (GBCAs) are retained in the body; requires new class warnings", 2017).

On this basis and according to the knowledge acquired during the currently presented work, three types of dual CAs were evaluated in this thesis: i) a PLGA:CIS/ZnS:IO dual CA, ii) Fe-CIS/ZnS by coupling synthesis, and iii) CIS/ZnS:Fe-ZnO.

V.2 RESULTS AND DISCUSSION

V.2.1 CIS/ZnS synthesis

V.2.1.1 CIS/ZnS luminescent analyses

Preparation of IO follows the protocol described in **Chapter II.2.4.** Preparation of CIS/ZnS is described in **Chapter II.2.7** according to the study of YI et al. (2015), with a few modifications.

The resulting synthesised CIS/ZnS was dispersed in DCM at a concentration of 40 mg mL^{-1} in order to work with the PLGA particles. The luminescence properties of the CIS/ZnS were evaluated. The results are shown in **Figure V.1**.

Figure V.1. Luminescence spectra of a) excitation (emission at 600 nm); b) emission (excitation at 400 nm); and c) emission (excitation at 500 nm), and picture of d) diluted to 0.4 mg mL^{-1} (10 uL in 1000 uL DCM) and excited at 254 nm.

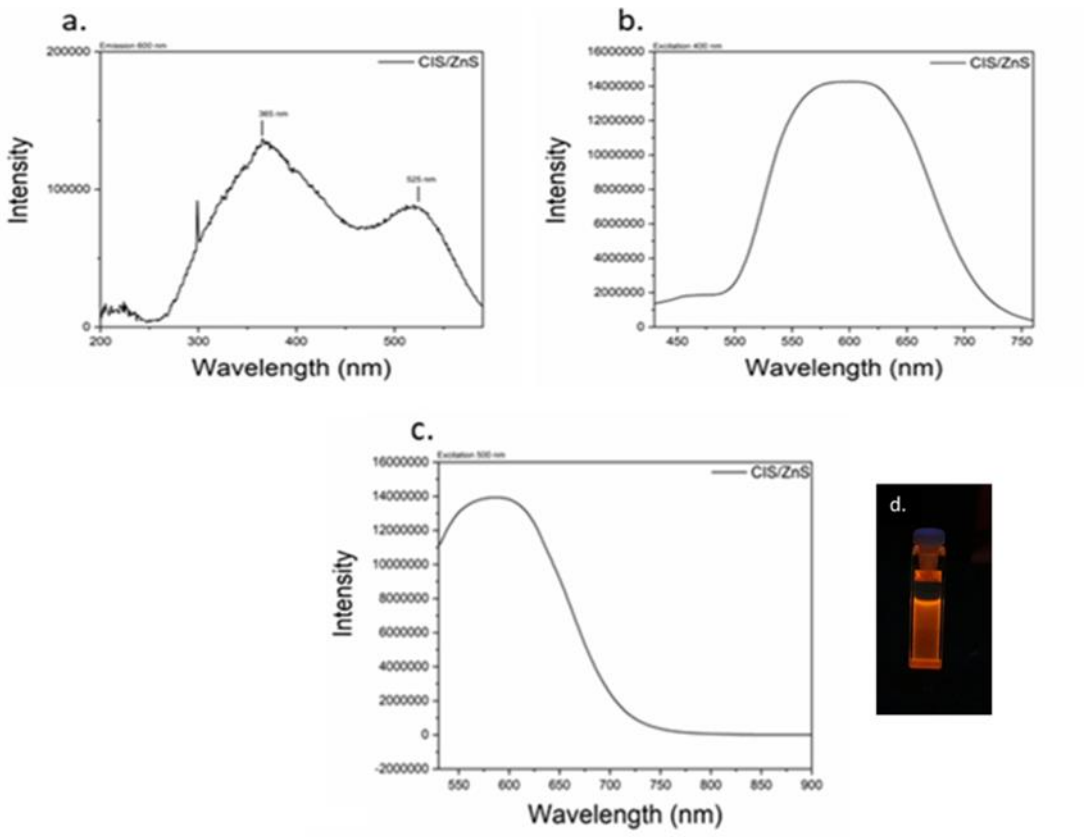

Source: by the author.

It can be observed that the CIS/ZnS has a suitable dispersion in DCM. The dispersion also shows suitable luminescence with an orange appearance when excited at a concentration of 0.4 mg mL^{-1} (**Figure V.1d**).

As can be seen in **Figure V.1a**, it was observed that CIS/ZnS has 2 excitation peaks with a maximum at 365 nm and a maximum at 525 nm responsible for the emission around 600 nm. The CIS/ZnS compound was then excited at two wavelengths.

In relation to emission spectra, the compound was excited in 400 and 500 nm because they are wavelengths close to excitation peaks. These assays were made before to analyse the spectra of excitation. When the compound is excited at 400 nm, it shows

an emission between 589 and 614 nm, and when the compound is excited at 500 nm, it shows an emission maximum between 576 and 598 nm. Therefore, the compound has a broad excitation range and a broad emission range that does not shift significantly in terms of both the wavelength and the intensity of the emission.

The CIS/ZnS was evaluated by characterization techniques of infrared and thermogravimetric assays.

V.2.1.2 Infrared Analysis

Infrared spectroscopy was used to characterize CIS/ZnS QDs. The results are shown in **Figure V.2**.

Figure V.2. Infrared spectra of CIS/ZnS.

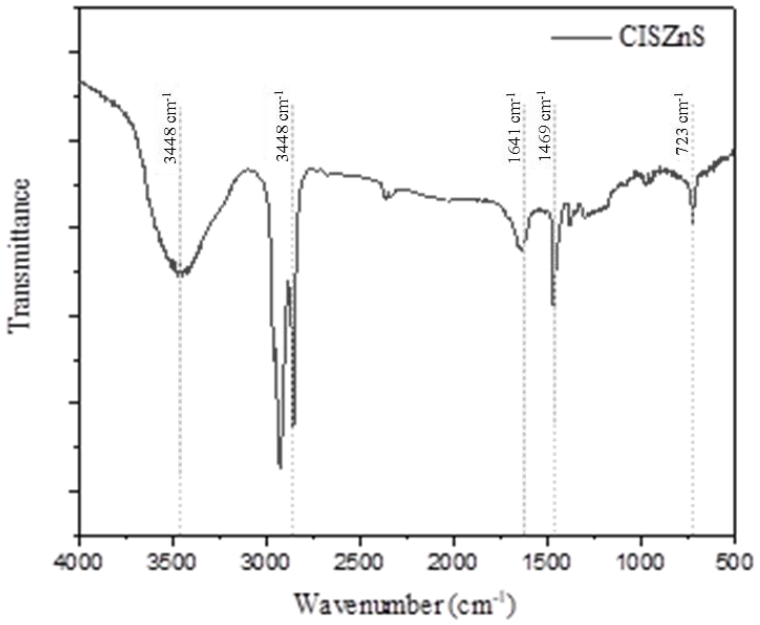

Source: by the author.

According to the results shown in **Figure V.2**, the presence of -OH stretching band at 3448 cm^{-1} was observed, and it is normal to observe this type of behaviour in samples functionalized with 1-DDT. The spectra showed characteristic behaviour of the infrared spectrum of 1-dodecanethiol (1-DDT), with the presence of characteristic bands at 2853 cm^{-1} and 1469 cm^{-1}, indicating successful adsorption of DDT on the surface of QD (WADA et al., 2017).

V.2.1.3 Thermogravimetric analysis

The samples were characterized using thermogravimetric analysis and the results are shown in **Figure V.3**.

Figure V.3. TG and DTA spectra for CIS/ZnS sample

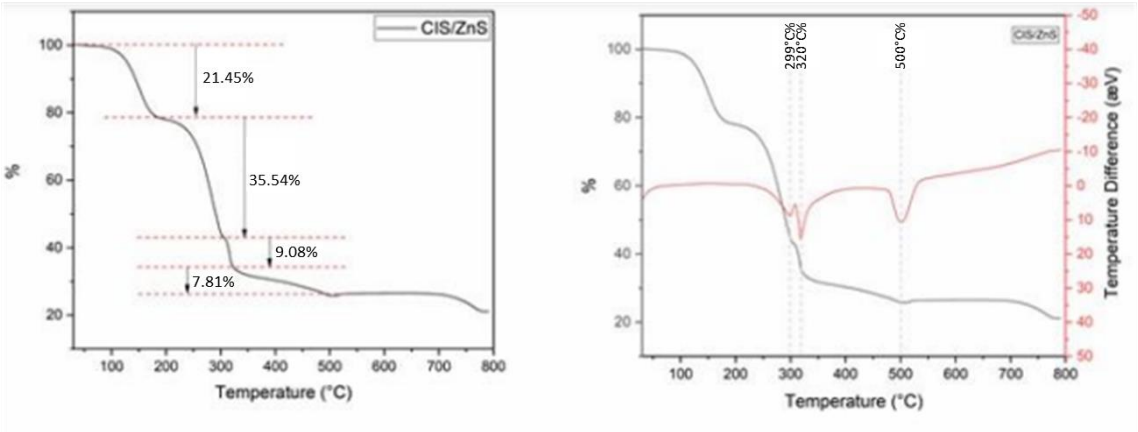

Source: by the author.

According to these results, it can be observed that the data found on the mass loss events of the standard CIS/ZnS composite are consistent with those reported in the literature (LEE; HAN, 2015), where three main mass loss events at 21,45%, followed by two consecutive mass loss events at 35.54% and 9.08%, and one mass loss at 7.81%, which were found in the ranges of 74.59°C to 189.93°C, 189.93°C to 304.74°C, 304.74°C to 320.90, and 32.90 to 507.34°C, respectively. The mass loss at 21.45°C was not a correlated event with the TGA curve. This may be due to desorption of components such as N2 or residual solvent used to solubilize the sample.

Under these synthesis conditions, reagents such as 1-DDT, oleic acid and oleylamine were used. The decomposition of oleic acid and oleylamine is observed between 200 and 450°C (CHANDUNIKA; RAJAGOPALAN; SAHU, 2020). The addition of the "thiol" group in the synthesis of the compounds causes the thermogravimetric analysis of the compounds to show a better-defined decomposition loss near 300°C. This can be characterized as successful NP functionalizing by 1-DDT (JAYABHARATHI et al., 2017).

V.2.2 PLGA:CIS/ZnS:IO particles

V.2.3.1 Interaction of CIS/ZnS and IO

Before forming PLGA NPs containing CIS/ZnS and IO NPs, it is first necessary to observe the impact of IO on the luminescence properties of CIS/ZnS. As with the compound PLGA:ZnO:IO that was studied in **Chapter III**, the IO reduces the luminescence intensity of the ZnO. Therefore, in this first test, the presence of both compounds in the same solution has been analysed. CIS/ZnS and IO were analysed at different concentrations and dispersed in DCM. The results are shown in **Figure V.4**. for the fluorescence spectra and the value of emission is presented in **Table V.1**.

Table V.1. Intensities of luminescence peak of samples containing CIS/ZnS and IO dispersed in DCM.

Samples	λ exc = 365 nm		λ exc = 525 nm	
	λ max	**Intensity**	**λ max**	**Intensity**
CIS/ZnS 6 mg	597	1880660	594	721580
CIS/ZnS 5 mg + IO 1 mg	603	1758900	582	648200
CIS/ZnS 6 mg + IO 1 mg	603	2000240	597	725160
CIS/ZnS 7 mg + IO 1 mg	603	2282080	597	906080
CIS/ZnS 8 mg + IO 1 mg	603	2541330	597	962420

Figure V.4. Different concentrations of CIS/ZnS with different concentrations of IO and their interference on luminescence. Excitation spectra with emission at 600 nm (a), Emission spectra with excitation at 365 nm (b), and Emission spectra with excitation at 525 nm (c).

a.

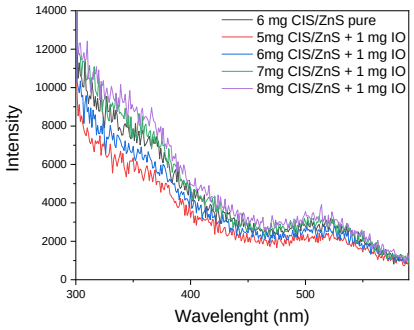

b. c.

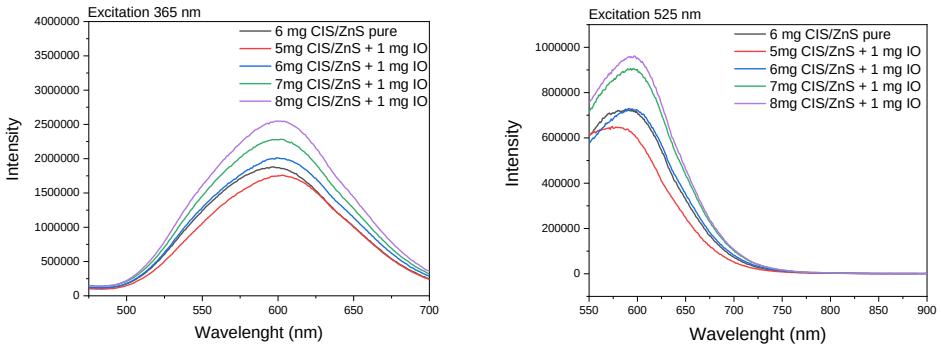

According to **Figure V.4a**, it can be observed that the excitation peaks (365 nm and 525 nm as previously measured) do not shift with the addition of IO at the tested concentrations. CIS/ZnS luminescence intensity (after excitation at 525 nm) is not affected by the presence of IO as a value of 721580 is measured for the sample containing 6mg CIS/ZnS compared to and 725160 for the sample where 1mg IO is added to the 6mg CIS/ZnS (**Table V.1**). However, a slight shift in the maximum wavelength is observed (respectively, 597nm to 603nm).

When compared with the emission intensity of the CIS/ZnS sample at both wavelengths, the intensity of the samples did not decrease with the presence of iron. Therefore, the luminescence properties of CIS/ZnS were not affected by the presence of

IO. This can be explained by the stability of CIS/ZnS, which presents a DTT solvent surface that provides stability to the molecule.

V.2.3.2 Luminescence properties and Size measurements of the PLGA based particle

V.2.3.2.1 PLGA:CIS/ZnS NPs

CIS/ZnS QDs were used to load PLGA particles. The steps used to prepare the PLGA particles were performed as described in Section II.2.5. The samples that were prepared are described in **Table V.2**.

Table V.2. Code of PLGA:CIS/ZnS samples.

Samples	Content
PLGA:CIS/ZnS 10:1	10 mg of PLGA + 1 mg of CIS/ZnS
PLGA:CIS/ZnS 10:2	10 mg of PLGA + 2 mg of CIS/ZnS
PLGA:CIS/ZnS 10:3	10 mg of PLGA + 3 mg of CIS/ZnS
PLGA:CIS/ZnS 10:4	10 mg of PLGA + 4 mg of CIS/ZnS

The PLGA:CIS/ZnS samples in PVA and T80 suspension were evaluated for size and zeta potential by DLS, the results are shown in **Table V.3**.

Table V.3. Size and zeta potential of PLGA:CIS/ZnS particles in PVA/T80 suspension (n=3)

Sample	Size (nm)	PDI	ZP (mV)
PLGA:CIS/ZnS 10:1	197.3 ± 6.619	0.224 ± 0.007	-25.10 ± 2.33
PLGA:CIS/ZnS 10:2	167.3 ± 5.277	0.217 ± 0.019	-24.60 ± 1.35
PLGA:CIS/ZnS 10:3	168.0 ± 2.173	0.182 ± 0.029	-23.20 ± 3.12
PLGA:CIS/ZnS 10:4	173.2 ± 3.387	0.248 ± 0.034	-20.90 ± 0.40

Table V.3 shows that the size of the NPs is in the same range around 200nm. This means that incorporation of CIS/ZnS in PLGA has limited impact on the final size of PLGA. The PDI results were also similar between the samples with values around 0.2. The zeta potential was also measured, the results show a ZP between -25 and -20 mV, in accordance with the PLGA value previously shown. The stability of the samples

after 7 days in PVA solution and T80% at room temperature was evaluated and the results are shown in **Table V.4**.

Table V.4. Stability assay of PLGA:CIS/ZnS analysed after 7 days of synthesis (n=3)

Sample	Size (nm)	PDI
PLGA:CIS/ZnS 10:1	174.0 ± 3.270	0.158 ± 0.035
PLGA:CIS/ZnS 10:2	158.9 ± 4.204	0.185 ± 0.019
PLGA:CIS/ZnS 10:3	232.9 ± 1.274	0.188 ± 0.033
PLGA:CIS/ZnS 10:4	239.5 ± 4.900	0.243 ± 0.011

According to the results presented in **Table V.4**, and despite a slight increase of the PLGA particle size for the highest CIS/ZnS loading, the average particle size for PLGA:CIS/ZnS remains around 200nm. The dispersions were evaluated for their luminescence properties. Samples were diluted in a 2:1000 (v:v) ratio. The results are shown in **Figure V.5**.

Figure V.5. Luminescence properties of PLGA:CIS/ZnS samples in mass ratios of 10:1, 10:2, 10:3, and 10:4. a) Absorbance spectra; b) Comparison of maximum emission when excited at 365 nm and 525 nm; c) Emission spectra, for excitation at 365 nm; d) Emission spectra, for excitation at 525 nm.

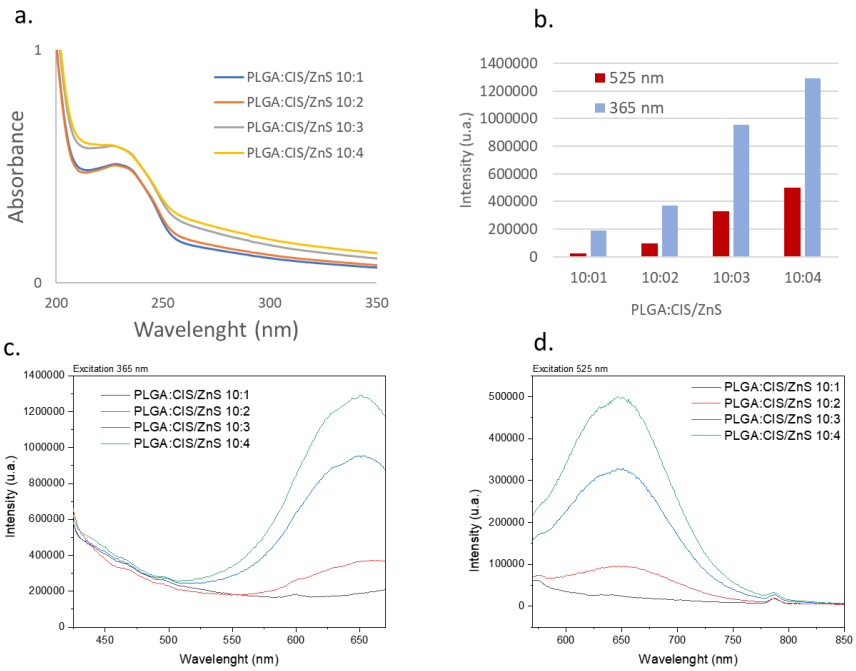

Source: by the author.

A shoulder at 245 nm was observed in the CIS/ZnS samples. This shoulder is characteristic to PLGA in formulation (BASU, PAL, SINGH, 2016). Absorbance bands of CIS/ZnS is not possible to be verified. When excited at 365 nm and 525 nm, the PLGA:CIS/ZnS 10:4 and 10:3 showed an emission peak at 650 nm whereas PLGA:CIS/ZnS 10:2 and 10:1 were poorly luminescent. Comparing the two excitation wavelengths, the emission intensity is higher when excited at 365 nm, but for diagnostic use, the excitation wavelength at 525 nm is better.

V.2.3.3 PLGA:CIS/ZnS:IO particles

After showing that the encapsulation of CIS/ZnS was possible without interfering on the size and stability of PLGA based particles, and that in solution the presence of IO does not impact the fluorescence of CIS/ZnS, a dual CA in which IO and CIS/ZnS was produced. For the PLGA:ZnO:IO tests, the iron nominal mass was kept constant at 1 mg, a value chosen based on **Chapter III** where it has shown that this amount encapsulated in PLGA is sufficient to induce a strong magnetic effect. The nominal mass of PLGA was also fixed at 10 mg. The nominal mass of CIS/ZnS varied between 1 and 4 mg of sample. The samples analysed are listed in **Table V.5**.

Table V.5. Code of PLGA:CIS/ZnS:IO samples.

Samples	Content
PLGA:CIS/ZnS:IO 10:2:1	10 mg of PLGA + 2 mg of CIS/ZnS + 1 mg IO
PLGA:CIS/ZnS:IO 10:3:1	10 mg of PLGA + 3 mg of CIS/ZnS + 1 mg IO
PLGA:CIS/ZnS:IO 10:4:1	10 mg of PLGA + 4 mg of CIS/ZnS + 1 mg IO

The PLGA:CIS/ZnS:IO samples in PVA and T80 suspension were evaluated for size and zeta potential by DLS. The results are shown in **Table V.6**.

Table V.6. Size and zeta potential of PLGA:CIS/ZnS:IO NPs in PVA/T80 suspension (n=3).

Sample	Size (nm)	PDI	ZP (mV)
PLGA:CIS/ZnS:IO 10:2:1	196.9 ± 1.1	0.202 ± 0.017	-17.6 ± 0.7
PLGA:CIS/ZnS:IO 10:3:1	181.4 ± 0.6	0.225 ± 0.017	-15.7 ± 0.9
PLGA:CIS/ZnS:IO 10:4:1	170.7 ± 0.6	0.198 ± 0.016	-20.1 ± 0.5

According to the results of **Table V.6**, the size was similar for all samples, with a PDI less than 0.3. The zeta potential values are close to -20 mV, corresponding to the PLGA NPs. The stability of the suspensions was evaluated after 7 days. The results are presented in **Table V.7**.

Table V.7. Stability of PLGA:CIS/ZnS analysed after 7 days of synthesis (n=3)

Sample	Size (nm)	PDI
PLGA:CIS/ZnS:IO 10:2:1	184.5 ± 1.060	0.119 ± 0.012
PLGA:CIS/ZnS:IO 10:3:1	176.8 ± 6.251	0.197 ± 0.022
PLGA:CIS/ZnS:IO 10:4:1	182.6 ± 4.917	0.232 ± 0.013

According to **Table V.7**, no significant change in size and PDI after 7 days. The luminescence of the samples was studied. The results are shown in **Figure V.6**.

Figure V.6. Luminescence properties of PLGA:CIS/ZnS:IO samples in mass ratios of 10:2:1, 10:3:1, and 10:4:1. a) Absorbance spectra; b) Comparison of maximum emission when excited at 525 nm and 365 nm; c) Emission spectra, excited at 365 nm; d) Emission spectra, excited at 525 nm.

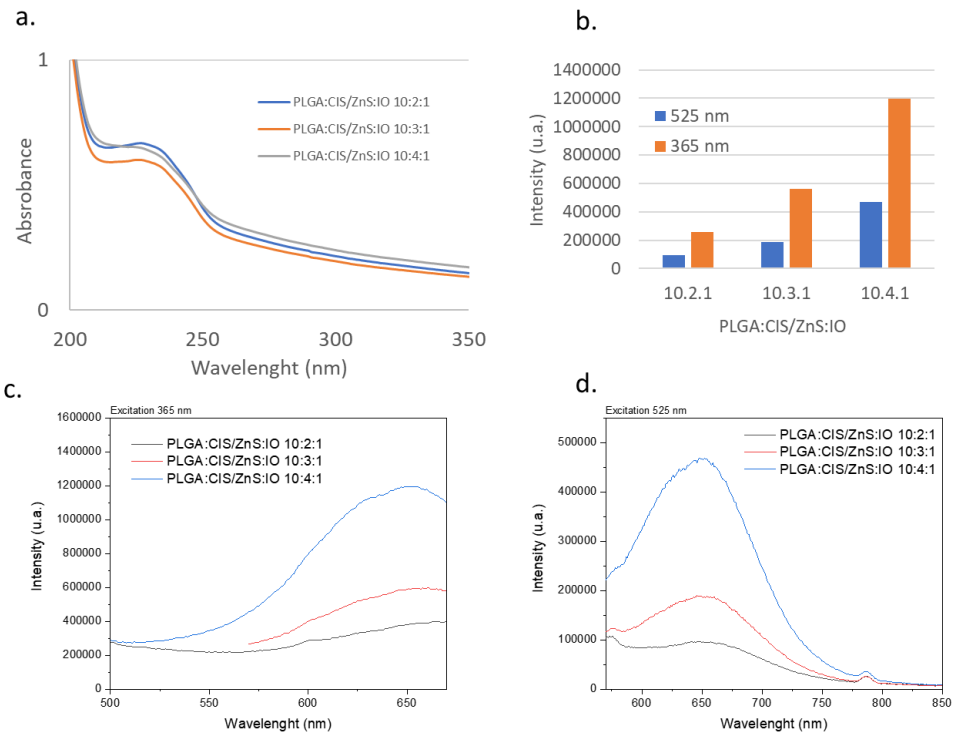

Source: by the author.

According to the results shown in **Figure V.6a**, the same absorbance shoulder appears at 245 nm in the PLGA:CIS/ZnS:IO samples, and no second band is formed, which may indicate that the IO and the CIS/ZnS are completely embedded in the PLGA. Luminescence was tested at two different wavelengths, 365nm (**Figure V.6c**) and 525nm (**Figure V.6d**). The luminescence intensity of PLGA:CIS/ZnS:IO at 525 nm remains like the results of PLGA:CIS/ZnS samples, whereas the luminescence intensity of PLGA:CIS/ZnS:IO at 365 nm decreased compared to PLGA:CIS/ZnS samples. This means that the behaviour of CIS/ZnS at 525 nm is not changed by the presence of IO embedded in PLGA particles. However, there is a change when the emission at 365 nm is considered. The sample's maximum peak remains at 650 nm. There is a peak at 785 nm, but it does not change with the concentration of the sample. This peak is not associated with CIS/ZnS or IO emission compounds.

V.2.3.3 TEM analysis

The morphology of PLGA:CIS/ZnS was performed by TEM, the results are shown in **Figure V.7**.

Figure V.7. Morphology of PLGA:CIS/ZnS 10:4 by TEM analysis. Different scale bars are used in a) 50 nm, and b) 20 nm.

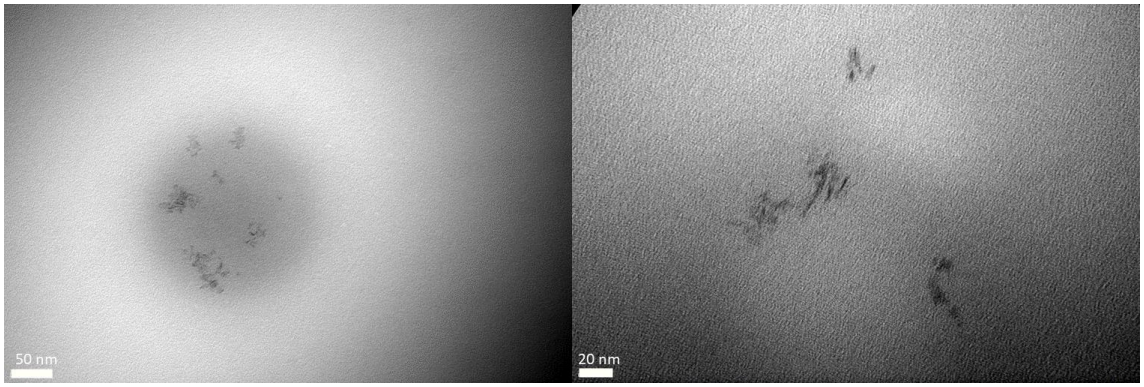

Source: by the author.

According to **Figure V.7**, it can be observed that the morphology of PLGA:CIS/ZnS is formed by spherical particles and the CIS/ZnS are presented embedded in PLGA particles. The CIS/ZnS appear as aggregated groups of NPs. The shape of the CIS/ZnS is not well defined (**Figure V.7b**) and therefore the size of the CIS/ZnS NPs cannot be calculated.

The PLGA:CIS/ZnS:IO were also analyzed by TEM. The results are shown in **Figure V.8**.

Figure V.8. Morphology analysis of PLGA:CIS/ZnS:IO 10:4:1 by TEM. Scale bar in 50 nm.

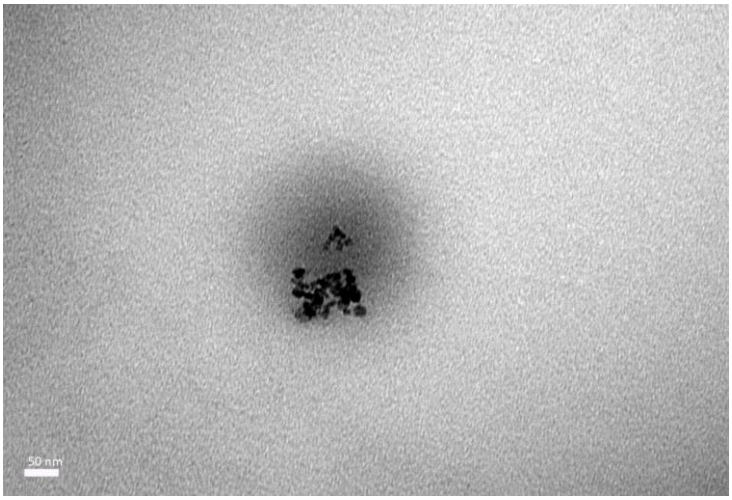

Source: by the author.

From **Figure V.8**, it can be seen that PLGA:CIS/ZnS:IO NPs have been formed. As shown above, CIS/ZnS NPs are very small and the size cannot be measured directly from the image. There are two groups of NPs present inside of PLGA particles. The group of NPs at the top can be considered as the CIS/ZnS NP group, since this group of NPs is small compared to the larger NPs and has an undefined shape, while the NP group at the bottom can be considered as IO NPs due to their larger size.

V.2.3.4 MRI analysis

MRI analysis was performed. The samples were lyophilized and Trehalose was used as a cryoprotectant at a theoretical concentration of 37% (w/w) relative to the initial mass of PLGA in the syntheses.

Samples were dispersed at 2.5 mg mL^{-1} concentration, the same concentration used for PLGA:ZnO:IO evaluation reported in **Chapter III**. The results are shown in **Figure V.9**.

Figure V.9. MRI analysis on PLGA:CIS/ZnS:IO samples. a) Sample position; b) T2 weighted image (TR = 2000 ms, TE = 104 ms); c) T1 weighted image (TR = 2000 ms; TE = 104 ms).

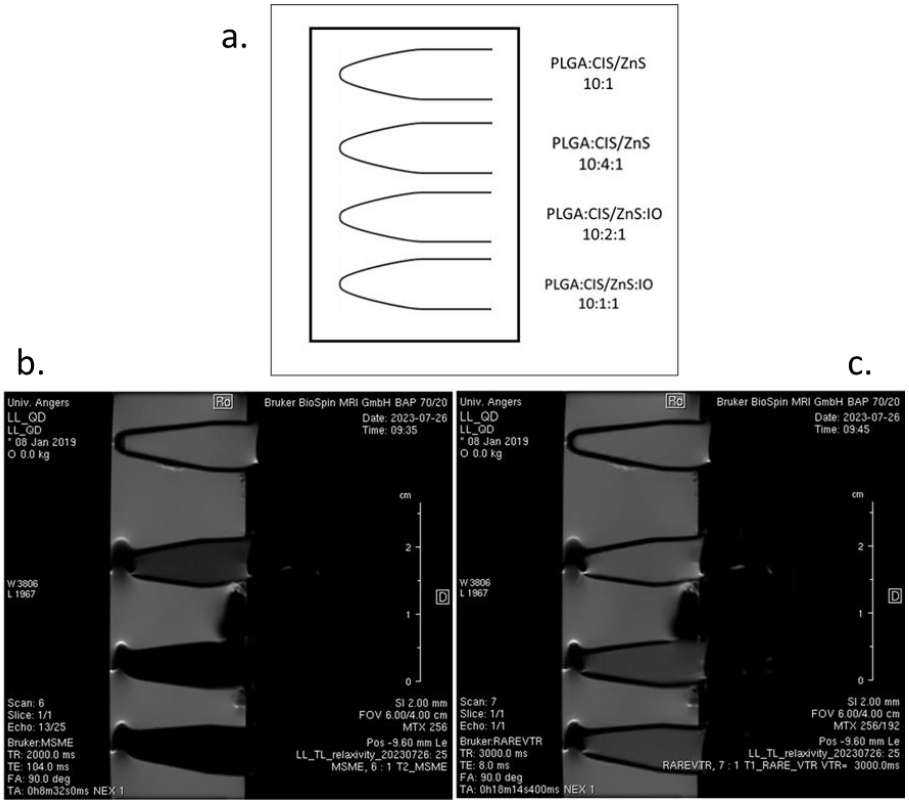

Source: by the author.

According to **Figure V.9**, the dispersion of PLGA:CIS/ZnS:IO in water was incomplete, resulting in visible sedimentation. This poor dispersion hinders quantitative analysis of the Mp of these NPs, as it is challenging to accurately determine the dispersed quantity of PLGA:CIS/ZnS:IO. However, qualitative analysis remains feasible. A significant T2 effect is evident in the PLGA:CIS/ZnS:IO samples (**Figure V.9**, bottom left). At the sedimentation zone of the PLGA:CIS/ZnS:IO samples, observed outside the tube, a hyperintense region indicates a susceptibility artifact caused by the high iron concentration. Notably, although the exact dispersed quantity of PLGA:CIS/ZnS:IO is unknown, it can be assumed to be consistent across tubes. The darker appearance of PLGA:CIS/ZnS:IO 10:1:1 compared to other samples suggests a higher iron content in these NPs. In contrast, PLGA:CIS/ZnS particles did not exhibit any T2 or T1 contrast effects. Specifically regarding T1 contrast, no discernible effects were observed in all analyzed samples.

V.2.2 Development of FeCIS / ZnS quantum dots

Next step of this work was tried to create a system that can include the iron in the structure of CIS/ZnS from doping process, as made of FeZnO in **Chapter IV**.

The FeCIS/ZnS QDs were prepared according to the method described by Yang et al. (2015), with a Cu/In/Fe nominal molar ratio of 2.0/2.0/1.0. The composition of the elements in the sample has a direct effect on the behaviour of the optical properties of the compounds under study. It has been observed that in FeCIS/ZnS QDs show a dark green colour after purification. The analyses of infrared spectroscopy, thermogravimetry analyses and luminescence analyses were made to characterize the compound synthetized.

V.2.2.1 Infrared Analysis

Infrared spectroscopy was used to characterize CISZnS and FeCISZnS QDs for different nucleation times. The results are shown in **Figure V.10**.

Figure V.10. Infrared spectra of CISZnS, FeCISZnS 30 min, FeCISZnS 60 min, FeCISZnS 90 min samples.

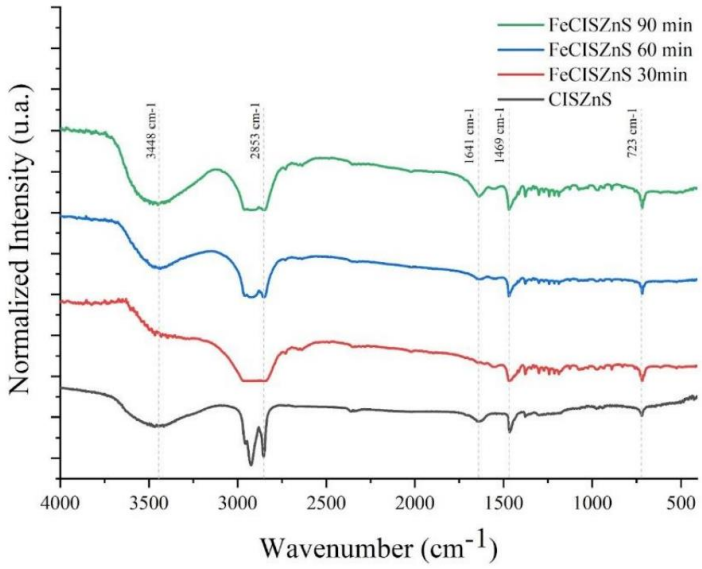

Source: by the author.

According to the results shown in **Figure V.10**, the presence of an -OH stretching band at 3448 cm^{-1} was observed, and it is normal to observe this type of

behaviour in samples functionalized with 1-DDT (Jayabharathi et al., 2017). The spectra showed characteristic behaviour of the infrared spectrum of 1-dodecanethiol (1-DDT), with the presence of characteristic bands at 2853 cm-1 and 1469 cm^{-1}, indicating successful adsorption of DDT on the surface of QD (WADA et al., 2017). Differences in the band at 2950 cm^{-1} are observed when comparing pristine CIS/ZnS and FeCIS/ZnS. This shows that there is an interaction between the structure formed and the presence of iron, in particular this interaction is related to the characteristic bands of 1-DDT. There is no evidence of a difference in infrared spectra when comparing different nucleation times.

V.2.2.2 Thermogravimetric analysis

The samples were characterized using thermogravimetric analysis and the results are shown in **Figure V.11**. Under these synthesis conditions, reagents such as 1-DDT, oleic acid and oleylamine were used. The decomposition of oleic acid and oleylamine is observed between 200 and 450°C (Chandunika, Vijayaghavan & Sahu, 2020). The addition of the "thiol" group in the synthesis of the compounds causes the thermogravimetric analysis of the compounds to show a better-defined decomposition loss near 300°C. This can be observed in the FeCIS/ZnS samples of synthesis times 30, 60 and 90 minutes. This can be characterized as successful NP functionalizing by 1-DDT (Jayabharathi et al., 2017). In addition, it can be mentioned that there was an increased proportion of 1-DDT decomposition events for the times ranging from 30 to 90 minutes.

The percentage mass loss increases with increasing nucleation time in the presence of iron. The same DTG events were observed in the presence of iron compared to pristine CIS/ZnS. This could mean that the same decomposition mass loss events were observed regardless of the presence of iron, which is related to the successful formation of the CIS composite in the presence of iron.

Figure V.11. TG and DTA spectra for CIS/ZnS samples in comparison to FeCIS/ZnS samples.

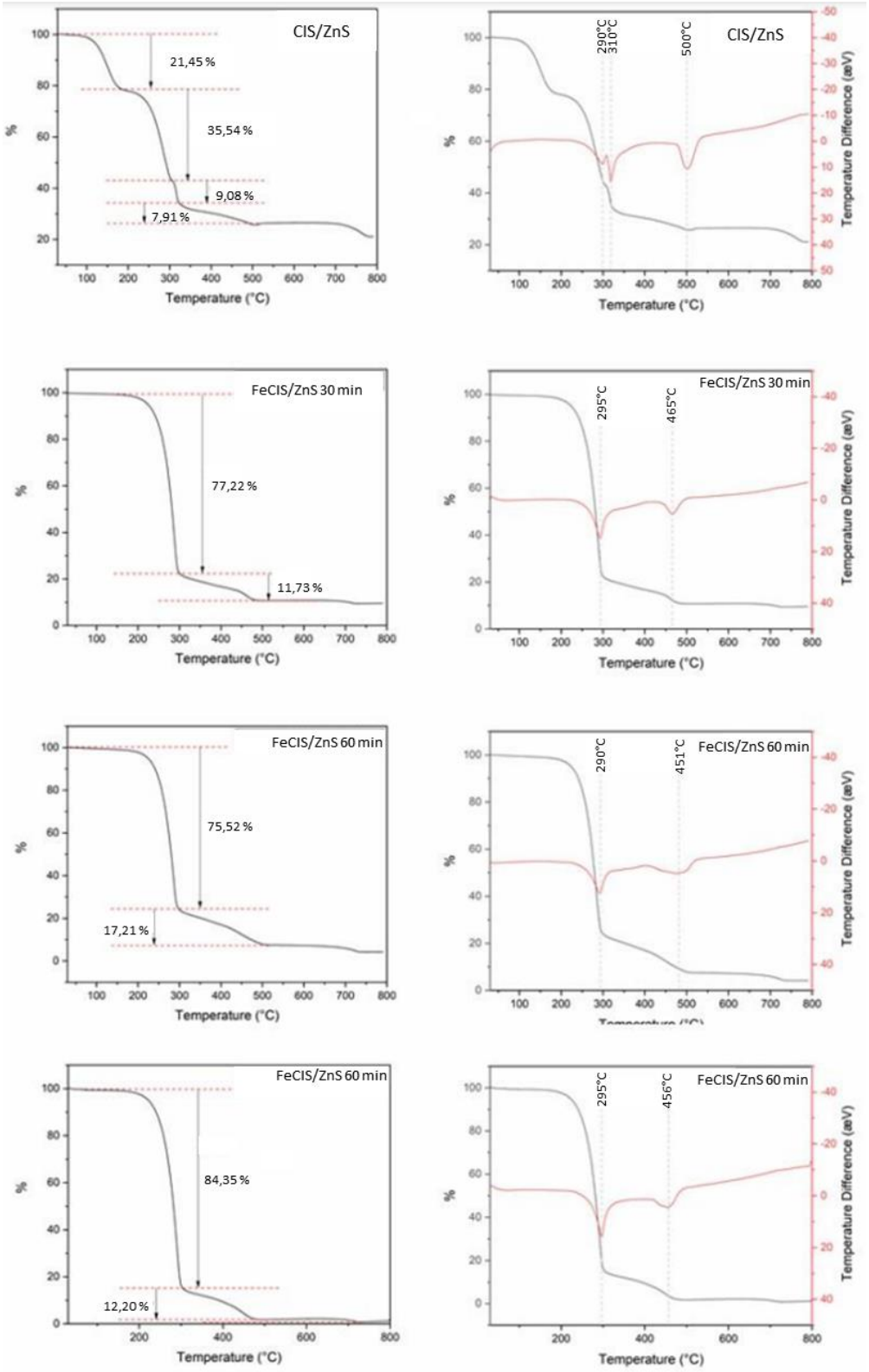

Source: by the author.

V.2.2.3 Absorbance and Luminescence assay

Figure V.12 shows the absorbance and fluorescence (FL) spectra of the investigated QDs.

Figure V.12. Optical properties of colloidal FeCIS Fluorescence spectra of CISZnS and FeCIS/ZnS QDs excited at 365 nm (a) and 516 nm (b). Absorption spectrum (c) of CIS/ZnS compared to FeCIS/ZnS.

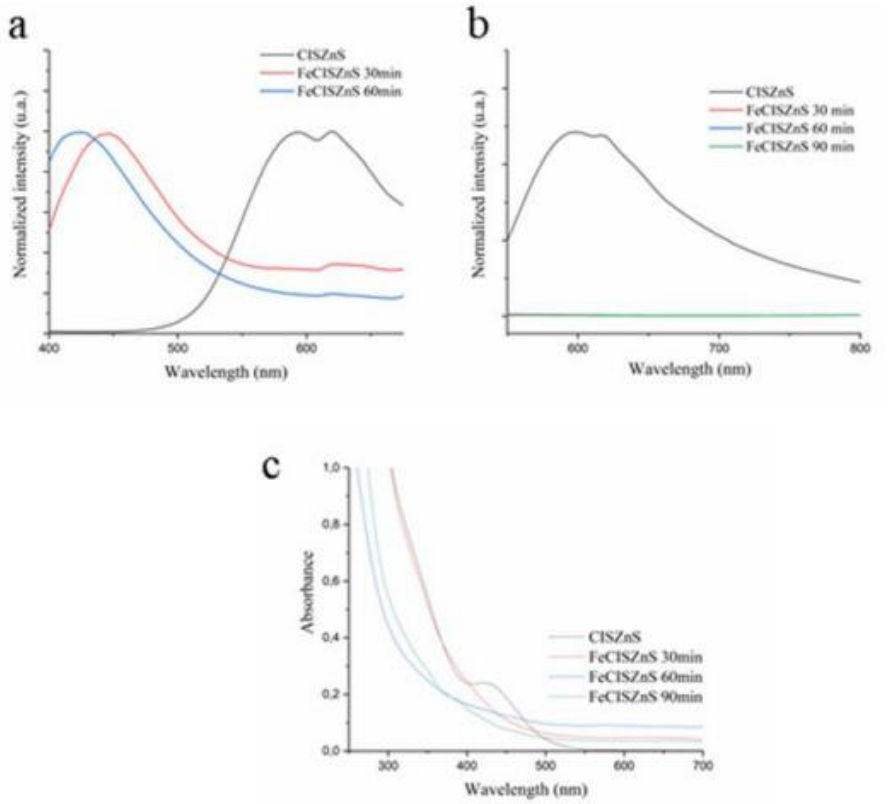

Source: by the author.

As shown in **Figure V.12**, a shoulder with maximum at 425 nm is observed in the absorbance spectrum of CIS/ZnS sample. This band was previously observed in the literature (WANG et al., 2015), attributed to intraband states of CIS QDs. This compound shows a blue shift, which can be attributed to the addition of the Zn shell, which can increase the luminescence intensity. However, the luminescence is shifted to the blue region. The presence of iron in the crystal structure of the synthesized compounds can explain the disappearance of this shoulder in the absorbance spectrum of the FeCIS/ZnS QDs and, consequently, the loss of emission when the FeCIS/ZnS samples are excited at the wavelength of 516 nm (**Figure V.12b**).

The analyses of the emission bands were normalized for a better discussion between the FL maxima (**Figure V.12a and V.12b**). The fluorescence band of CIS/ZnS showed a characteristic emission band maximized between 594 and 619 nm, when excited at both 365 and 519 nm wavelengths. The CIS/ZnS band is consistent with the emission shown in recent literature (MIR et al., 2018). The emission band of each sample synthesized with different times of ZnS shell formation was studied, and it can be observed that the introduction of iron into the structure causes the disappearance of the luminescence when excited at 516 nm (**Figure V.12b**). Upon excitation at 365 nm (**Figure V.12a**), emission bands were formed with a maximum at 440 nm for the FeCIS/ZnS 30 min sample and a maximum at 424 nm for the FeCIS/ZnS 60 min sample. Thus, with increasing FeCIS core synthesis time, there was a shift to lower wavelengths. This can be explained by the increase of defects in the structure with the increase of reaction time, which has a stated blue shift (WANG et al., 2018).

V.2.3 FeZnO@CIS/ZnS Coupling

A system was proposed with the formation of a core-shell system between the CIS/ZnS structures detailed at the beginning of Chapter V and FeZnO, based on the results found in Chapter IV. Recently, a study carried out by the CMAF laboratory (Unesp - Brazil) in partnership with the MINT laboratory (University of Angers - France), addressed the issue of producing a CIS/ZnS-ZnO compound using an overheating process (DA SILVA et al., 2021). Despite the suitable luminescent properties of the material with the introduction of ZnO, no MRI results were analysed, as ZnO itself does not show obvious contrast T1 or T2 effects.

The samples were placed in calculated amounts according to the proportions listed in **Table II.2** (**Chapter II**). The coupling reaction was carried out in porcelain crucibles. Subsequently, the samples were dispersed in chloroform and analysed using fluorescence spectrophotometry. Fluorescence assays were conducted at 365 nm due to the available lamp in the laboratory, at 343 nm because of the ZnO excitation wavelength, and excitation spectra with emission at 570 nm, revealing increased fluorescence for samples with a higher proportion of ZnO and FeZnO. The spectra are shown in **Figure V.13**.

Figure V.13. Fluorescence spectra for ZnO@CIS/ZnS samples (a, b, c), FeZnO0.1@CIS/ZnS (d, e, f), FeZnO0.5@CIS/ZnS (g, h, i), and FeZnO1.0@CIS/ZnS (j, k, l). Emission spectra with excitation at 343 nm (a, d, g, j), at 365 nm (b, e, h, k), and absorption spectra with emission at 570 nm (c, f, i, l).

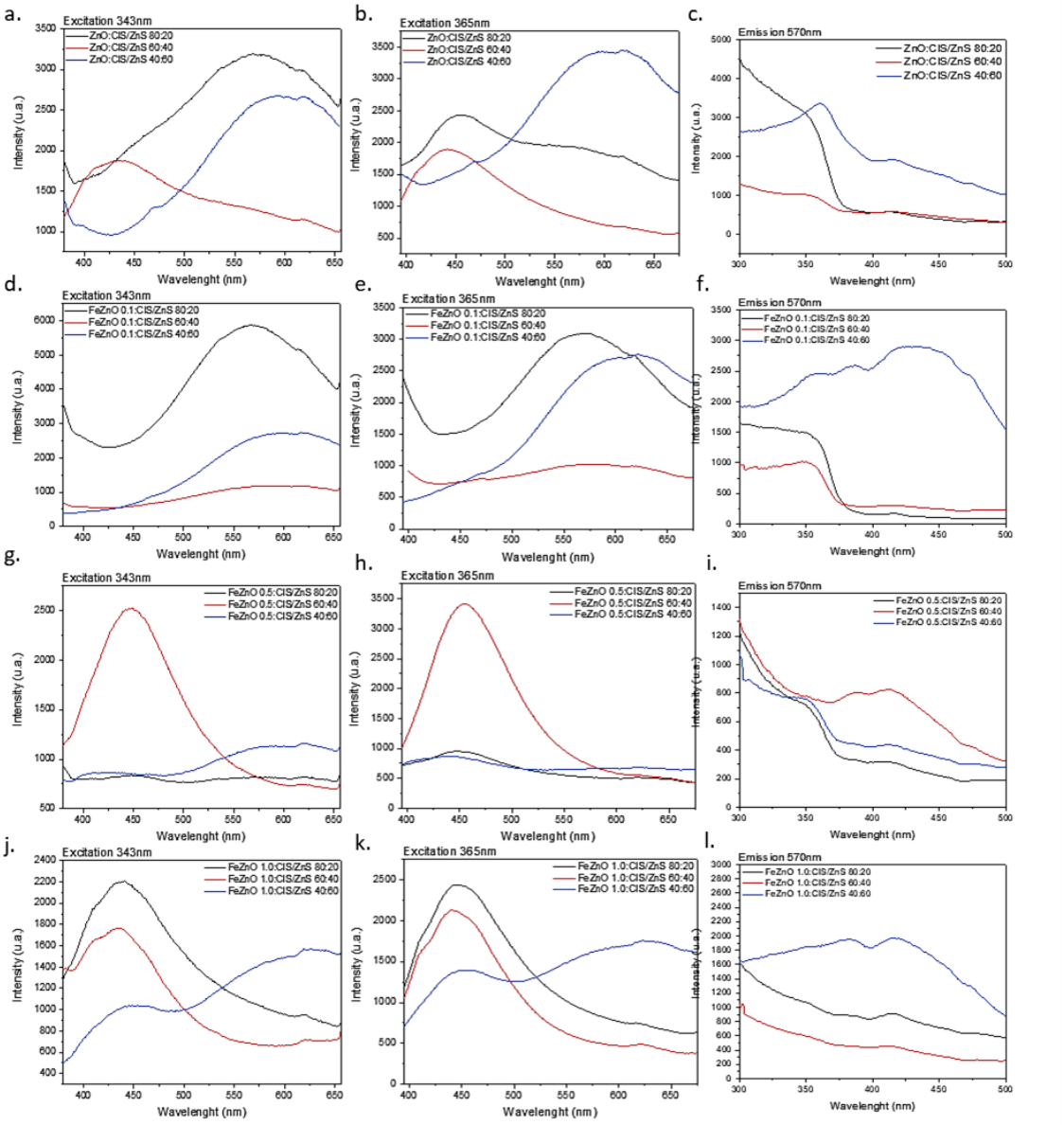

Source: by the author.

According to the results in **Figure V.13**, the concentrations used were not standardized. Samples with higher Fe content (0.5 and 1.0%) showed a loss of emission in the orange region when treated thermally, with an emission peak at 450 nm when excited at a wavelength of 365 nm. Samples with higher CIS/ZnS content (60%) for 0.5 and 1.0% of iron showed emission in the range of 650 nm. However, as demonstrated

earlier, the pasty consistency and yellowish colour of the FeZnO@CIS/ZnS 40:60 samples indicate an excess of CIS/ZnS that did not undergo the coupling process. The samples with highest intensity in orange region were evaluated (**Figure V.14**).

Figure V.14. Emission spectrum with excitation at 343 nm of ZnO@CIS/ZnS 80:20 and FeZnO0.1@CIS/ZnS 80:20 samples compared to pristine ZnO.

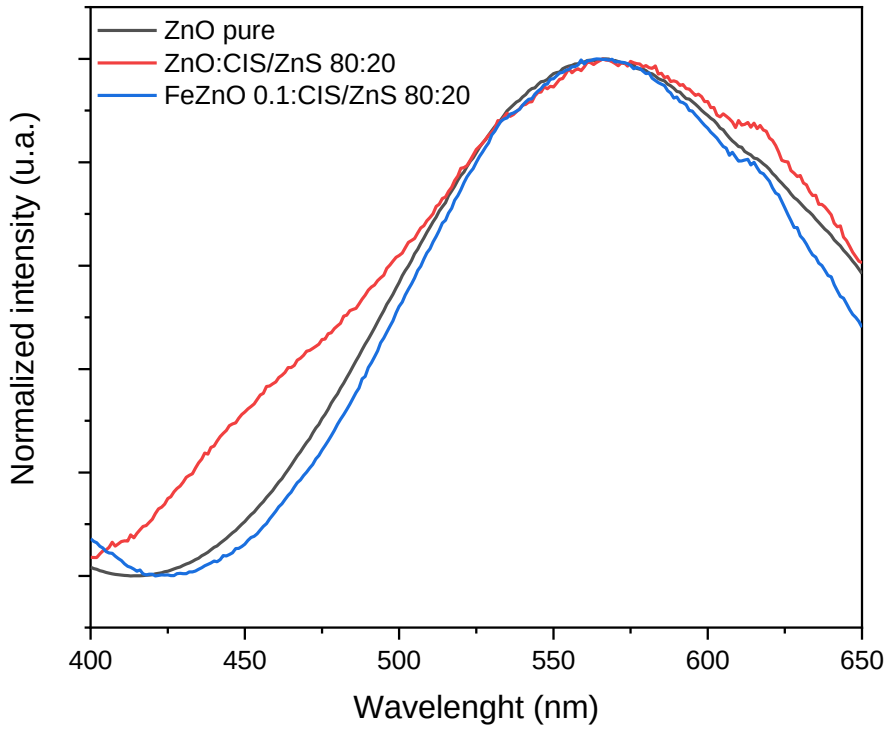

Source: by the author.

The FeZnO0.1@CIS/ZnS samples exhibited significant results in the luminescence of the formed compound. When compared with pristine ZnO, as depicted in **Figure V.14**, both FeZnO0.1@CIS/ZnS and ZnO@CIS/ZnS in an 80:20 ratio displayed the same emission range as pristine ZnO. Moreover, the samples exhibited uniform appearance. The absorption bands of these two compounds mirrored those of pristine ZnO, featuring a shoulder at 365 nm, with absorption bands at 425 nm observed in both samples. The shift in the emission peak is better observed in the FeZnO0.1@CIS/ZnS 60:40 sample (**Figure V.13e**), with an emission peak between 600

and 650 nm, where the absorption spectrum also differs from pristine ZnO and pristine CIS/ZnS, showing a peak between 425 and 475 nm.

V.3 Conclusion

A CIS/ZnS particle system has been studied for its luminescence properties and the introduction of iron has allowed the integration of Mp to form a bimodal component for use in fluorescence bioimaging and MRI.

Firstly, a system of PLGA polymer particles was adopted with the incorporation of CIS/ZnS NP and IO NP. It was found that the stability of CIS/ZnS in terms of its luminescence was maintained in the presence of IO when dispersed in DCM. This is a fundamental step in the formation of PLGA particles. This was observed in contrast to the PLGA:ZnO:IO system studied in Chapter III. A system with an initial mass ratio of PLGA:CIS/ZnS:IO of 10:4:1 was adopted as the best result for fluorescence and MRI.

The fluorescence of PLGA NPs containing CIS/ZnS showed an emission at 650 nm when excited at 525 nm, even in the presence of IO. This excitation wavelength is a better choice compared to ZnO alone. The PLGA NPs were freeze-dried and after this process the PLGA NPs did not disperse well in water. However, when MRI analyses were carried out, there is a strong T2 contrast effect.

Fe doped CIS/ZnS particles were prepared by the method described by Yang 2015, but characterisation and luminescence tests showed that the presence of iron can alter the structure of CIS and the luminescence. The excitation peak at 525 nm disappears and the emission peak is shifted to the region between 400 and 500 nm, which is not interesting from a diagnostic imaging point of view. The same was observed when core@shell system of FeZnO@CIS/ZnS was tested. The highest concentration of iron shift the peak of luminescence to smaller wavelength (blue shift).

REFERENCES

DONAT, F.; CORBEL, S.; ALEM, H.; PONTVIANNE, S.; BALAN, L.; MEDJAHDI, G.; SCHNEIDER, R. ZnO nanoparticles sensitized by CuInZnxS2+x quantum dots as highly efficient solar light driven photocatalysts. **Beilstein J. Nanotechnol.** 2017, 8, 1080–1093.

CHANDUNIKA, R. K., VIJAYARAGHAVAN, R., & SAHU, N. K. Magnetic hyperthermia application of MnFe2O4 nanostructures processed through solvents with the varying boiling point. Materials Research Express, v. 7, e. 6, p. 064002, 2020. doi:10.1088/2053-1591/ab955e

HEMMER, E., BENAYAS, A., LÉGARÉ, F., & VETRONE, F. Exploiting the biological windows: current perspectives on fluorescent bioprobes emitting above 1000 nm. Nanoscale Horizons, v. 1, e. 3, p. 168–184, 2016. doi:10.1039/c5nh00073d

JAYABHARATHI, J., SUNDARI, G. A., THANIKACHALAM, V., JEEVA, P., & PANIMOZHI, S. A dodecanethiol-functionalized Ag nanoparticle-modified ITO anode for efficient performance of organic light-emitting devices. RSC Advances, v. 7, e. 62, p. 38923–38934, 2017. doi:10.1039/c7ra07080b

LEE, J., & HAN, C.-S. Bright, stable, and water-soluble CuInS2/ZnS nanocrystals passivated by cetyltrimethylammonium bromide. Nanoscale Research Letters, v. 10, e. 1, p. 1-9, 2015. doi:10.1186/s11671-015-0836-0

MIR, I. A., DAS, K., AKHTER, T., RANJAN, R., PATEL, R., & BOHIDAR, H. B. Ecofriendly synthesis of CuInS2 and CuInS2@ZnS quantum dots and their effect on enzyme activity of lysozyme. RSC Advances, v. 8, e. 53, p. 30589–30599, 2018. doi:10.1039/c8ra04866e

SADEGHIMAKKI, B., ZHENG, Y., JAHED, N. M. S., & SIVOTHTHAMAN, S. Synthesis of CIS Quantum Dots in Low-Temperature Regime: Effects of Precursor Composition and Temperature Ramps. IEEE Transactions on Nanotechnology, v. 16, e. 4, p. 659–666, 2017. doi:10.1109/tnano.2017.2703162

SENTHILKUMAR, M., MARY, C. I., PANDIYARAJAN, M., MANOBALAJI, G., & BABU, S. M. Copper indium sulphide:zinc sulphide (CIS:ZnS)-alloyed quantum dots as an eco-friendly absorber in solar cells. Bulletin of Materials Science, v. 42, e. 6, p. 1-6, 2019. doi:10.1007/s12034-019-1957-3 WADA, C., ISO, Y., ISOBE, T., & SASAKI, H. Preparation and photoluminescence properties of yellow-emitting CuInS2/ZnS quantum

dots embedded in TMASderived silica. RSC Advances, v. 7, e. 13, p. 7936–7943, 2017. doi:10.1039/c7ra00081b

WANG, Z. et al. Facile Synthesis of Cu-In-S/ZnS Core/Shell Quantum Dots in 1-Dodecanethiol for Efficient Light-Emitting Diodes with an External Quantum Efficiency of 7.8%. Chemistry of Materials. v. 30, p. 8939-8947, 2019. doi:10.1021/acs.chemmater.8b0428

YANG, W. et al. (2015). Facile Synthesis of Gd–Cu–In–S/ZnS Bimodal Quantum Dots with Optimized Properties for Tumor Targeted Fluorescence/Mr In Vivo Imaging. ACS Applied Materials & Interfaces, v. 7, e. 33, p. 18759–18768, 2015.

CHAPTER VI

Preliminary evaluation of cytotoxicity and cellular uptake

CHAPTER VI – Preliminary evaluation of cytotoxicity and cellular uptake

VI 1 Introduction

After the physic-chemical characterization of the different types of dual CA, and according to the final objective of the aforementioned agents, i.e. in bioimaging, preliminary experiments looking at their toxicity and cellular uptake were performed. Even though all the systems synthesized during this thesis will be evaluated, to date, only the PLGA:ZnO:IO particles and FeZnO-GPTMS NPs were carried out. The cytotoxicity test was made by Resazurin test described according to (PINHO et al., 2020).

VI.2 Results and Discussion

VI.2.1 Cytotoxicity assay for PLGA containing ZnO and IO NPs

The cytotoxicity assay of the dual CAs under investigation was performed using the assay described in **Figure VI.1** where both the amount of agent and the time of exposure were evaluated. THP1 cells, a human monocytic cell line that can be differentiated into highly phagocytic macrophage-like were used.

Figure VI.1. Cytotoxicity Test Methodology

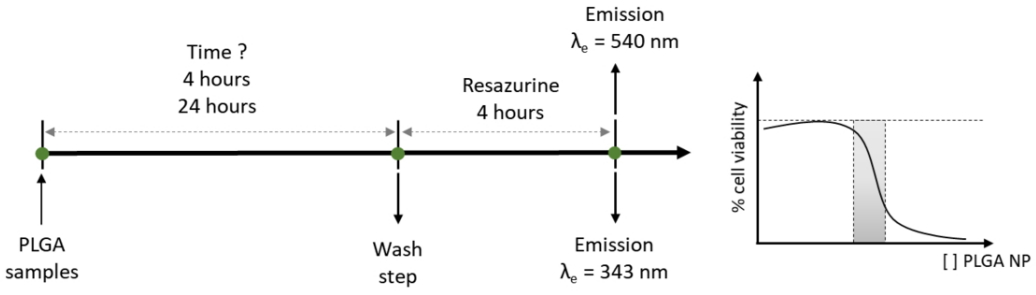

Source: by the author.

PLGA, IO-loaded PLGA (PLGA:IO 10:1), ZnO-loaded PLGA (PLGA:ZnO 10:6) and IO-ZnO co-loaded PLGA (PLGA:ZnO:IO 10:6:1) particles were evaluated for cytotoxicity. The doses evaluated ranged from 7.8 ng mL^{-1} to 128 µg mL^{-1} knowing that unloaded PLGA particles can be supported by Hela cells for example at

concentrations larger than 100 µg mL^{-1} (HASAN et al., 2012). The results are shown in **Table VI.1** for 4 hours of incubation and **Table VI.2** for 24 hours of incubation.

Table VI.1 Cell viability after 4 hours exposure to PLGA NPs (n=3, mean ± SD).

[ ] µg mL^{-1}	**PLGA**	**PLGA:ZnO**	**PLGA:IO**	**PLGA:ZnO:IO**
128	93.54 ± 7.67	80.93 ± 1.67	87.22 ± 5.35	82.98 ± 15.71
32	106.34 ± 16.17	107.55 ± 19.47	88.73 ± 2.75	92.02 ± 19.81
16	93.31 ± 11.43	100.78 ± 10.62	97.54 ± 9.67	105.58 ± 10.33
8	92.28 ± 2.81	81.83 ± 3.36	74.70 ± 5.94	101.63 ± 2.07
4	88.23 ± 3.77	84.57 ± 11.77	79.99 ± 4.75	89.30 ± 8.71
2	91.69 ± 19.38	103.74 ± 19.30	87.59 ± 7.13	110.98 ± 15.38
0.5	102.99 ± 14.67	90.46 ± 19.12	96.86 ± 5.15	111.24 ± 1.95
0.0625	111.75 ± 7.09	86.20 ± 2.35	94.98 ± 2.25	100.18 ± 3.99
0.0078	96.36 ± 1.20	80.93 ± 4.70	87.55 ± 8.10	97.89 ± 6.55

TableVI.2. Cell viability after 24 hours exposure to PLGA NPs (n=3, mean ± SD).

[ ] µg mL^{-1}	**PLGA**	**PLGA:ZnO**	**PLGA:IO**	**PLGA:ZnO:IO**
128	91.02 ± 6.70	64.30 ± 14.48	73.07 ± 8.83	85.99 ± 18.51
32	93.88 ± 12.10	90.09 ± 11.91	69.34 ± 3.41	130.56 ± 21.35
16	87.89 ± 2.93	101.54 ± 9.97	99.76 ± 1.71	99.65 ± 0.84
8	89.90 ± 5.29	97.90 ± 5.62	76.87 ± 4.18	84.97 ± 11.09
4	88.35 ± 4.91	92.44 ± 9.78	72.52 ± 4.21	93.80 ± 5.66
2	90.44 ± 10.38	85.24 ± 3.66	69.42 ± 9.75	89.19 ± 3.25
0.5	105.22 ± 7.74	107.83 ± 6.53	90.63 ± 16.07	120.56 ± 9.97
0.0625	91.86 ± 6.48	107.15 ± 12.96	92.22 ± 16.53	105.63 ± 4.38
0.0078	83.71 ± 14.27	90.63 ± 1.17	89.21 ± 7.51	98.69 ± 14.45

The results have been plotted to help to compare. The results are shown for 4 hours incubation for **Figure VI.2** and 24 hours for **Figures VI.3**.

Figure VI.2. Plot of cell viability after 4 h incubation at PLGA particle concentrations between 0.0078 and 128 µg mL^{-1} (n=3, mean ± SD).

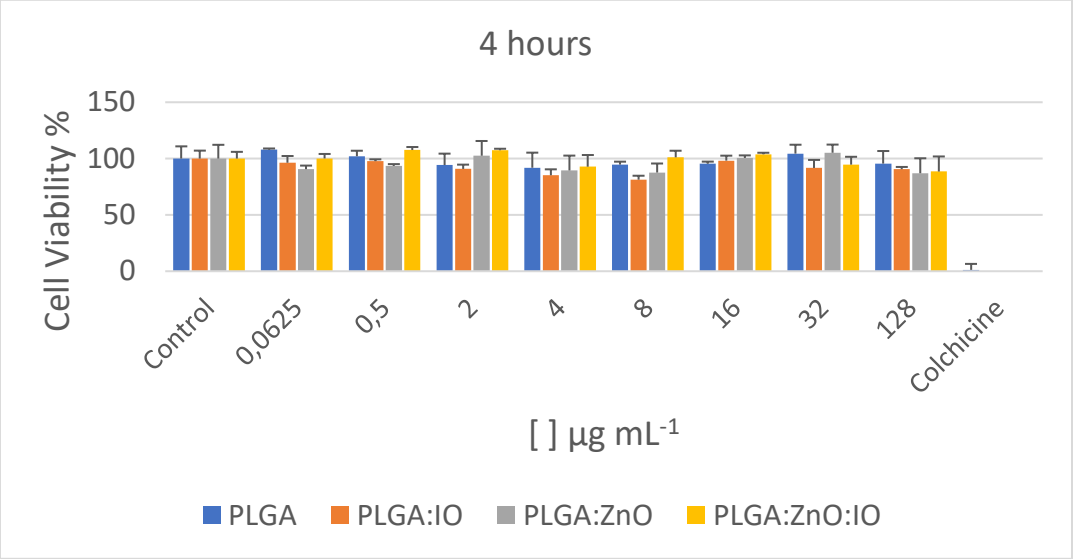

Source: by the author.

Figure VI.3. Plot of cell viability after 24 h incubation at PLGA particle concentrations between 0.0078 and 128 µg mL^{-1} (n=3, mean ± SD).

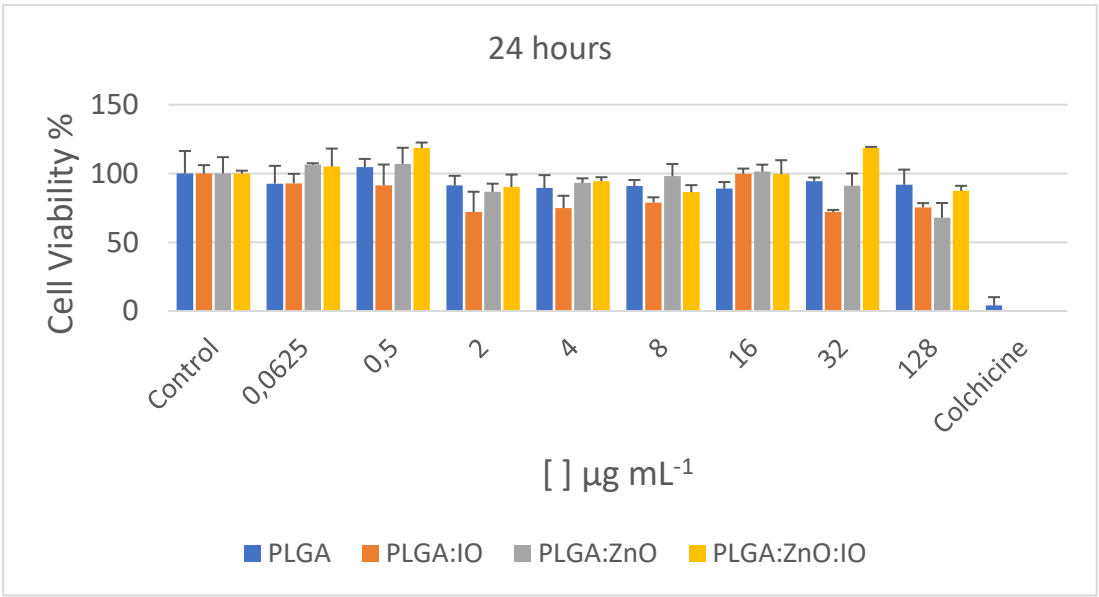

Source: by the author.

As reported in viability assay, no toxicity was observed in the concentrations range assessed even after 24h incubation. PLGA particles containing only IO NPs exhibited lower cellular viability, reaching 74% when the concentration of 8 µg mL^{-1} was tested. However, this value did not show a statistically significant difference when

compared to the control group ($p > 0.05$). When observed at the 24-hour incubation time, the cell viability of PLGA particles and PLGA particles containing ZnO and IO NPs showed similarity to the 4-hour incubation time. The cell viability of PLGA NPs containing only ZnO exhibited higher values than the 4-hour incubation time. The cell viability of PLGA particles containing only IO showed lower values compared to the 4-hour time. There was a statistically significant difference for concentrations of 32 µg mL-1 at different incubation times ($p<0.05$). Thus, there was a decrease in cell viability at this concentration for PLGA:IO. However, factors such as particle size increase as indicated by DLS results and the presence of ZnO NPs in the PLGA system led to increased cell viability.

VI.2.2 Uptake assay for PLGA containing ZnO and IO NPs

Complementary to the cytotoxicity assay, an uptake assay was performed to evaluate the capacity of the PLGA NPs to label THP1 cells. Labelling was assessed after 4 hours or 24 hours using luminescence, the excitation being performed at 343 nm and reading at 540 nm. The results are shown in **Figure VI.4** and **Table VI.3**.

Figure VI.4. Uptake cells by luminescence assay for PLGA particles containing ZnO and IO NP. Time of incubation of 4 hours (a) and 24 hours (b). Excitation wavelength in 343 nm, and emission wavelength 540 nm. (n=3, mean ± SD).

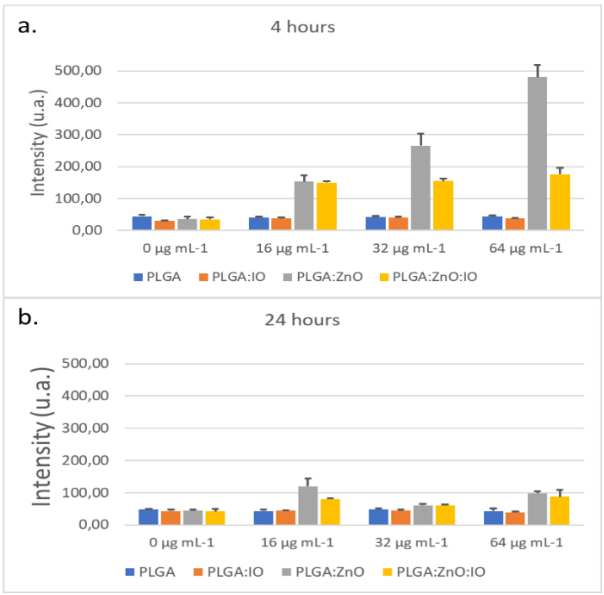

Source: by the author.

Table VI.3. Uptake by THP1 cells assessed by luminescence for the PLGA particles. Time of incubation of 4 hours (a) and 24 hours (b). Excitation wavelength in 343 nm, and emission wavelength 540 nm. (n=3, mean ± SD).

[ ]	PLGA		PLGA:IO		PLGA:ZnO		PLGA:ZnO:IO	
µg mL^{-1}	PL 4h	PL 24h	PL 4h	PL 24h	PL 4h	PL 24h	PL 4h	PL 24h
0	44.71 ± 4.08	47.53 ± 2.23	29.95 ± 1.99	42.82 ± 4.96	35.72 ± 7.59	44.00 ± 3.29	35.37 ± 5.85	42.23 ± 7.83
16	40.76 ± 1.79	43.28 ± 5.16	37.81 ± 4.22	44.84 ± 0.31	152.91 ± 20.24	119.69 ± 23.55	150.57 ± 3.99	80.51 ± 2.62
32	42.77 ± 2.12	48.77 ± 4.96	40.29 ± 4.08	44.34 ± 2.64	265.11 ± 38.25	60.25 ± 4.72	155.04 ± 7.92	60.36 ± 3.48
64	44.64 ± 1.93	43.45 ± 4.49	38.25 ± 1.73	38.83 ± 1.79	480.82 ± 38.08	98.12 ± 6.39	175.87 ± 20.87	87.28 ± 21.14

From **Figure VI.4a**, it appears that only the ZnO-loaded PLGA particles uptake can be detected using luminescence, but one can assume that the same uptake occurs for IO loaded PLGA or PLGA particles, this will be assessed using MRI for the IO containing PLGA particles. Interestingly, the luminescence of the particles uptaked appears to increase as particle concentration in the incubation medium increases. This can be observed in other studies (DA SILVA et al., 2021; KANEHIRA et al., 2019), , corroborating the data presented in **Figure VI.4a**.

However, increasing the incubation time up to 24 hours changes the luminescence profile (Figure VI.4b). One hypothesis for this observation could be that as time increases, the particles are ‘processed’ by the cells, entering the lysosomes whose acid pH dissolves the luminescent ZnO explaining the loss of labelling (MUDUNKOTUWA et al., 2012).

The pictures of the cells after uptake were analysed. The results are shown in the following figures. Remember that different plates were used in the assays for different incubation times.

Figure VI.5. Pictures of morphological analysis of THP-1 cells in plate after uptake assay treated with PLGA particles. a) untreated cells after 4 hours; b) untreated cells after 24 hours; c) cells treated with PLGA 16 μg mL^{-1}, uptake after 4 hours; d) cells treated with PLGA 16 μg mL^{-1}, uptake after 24 hours; e) cells treated with PLGA 32 μg mL^{-1}, uptake after 4 hours; f) cells treated with PLGA 32 μg mL^{-1}, uptake after 24 hours; g) cells treated with PLGA 64 μg mL^{-1}, uptake after 4 hours; h) cells treated with PLGA 64 μg mL^{-1}, uptake after 24 hours.

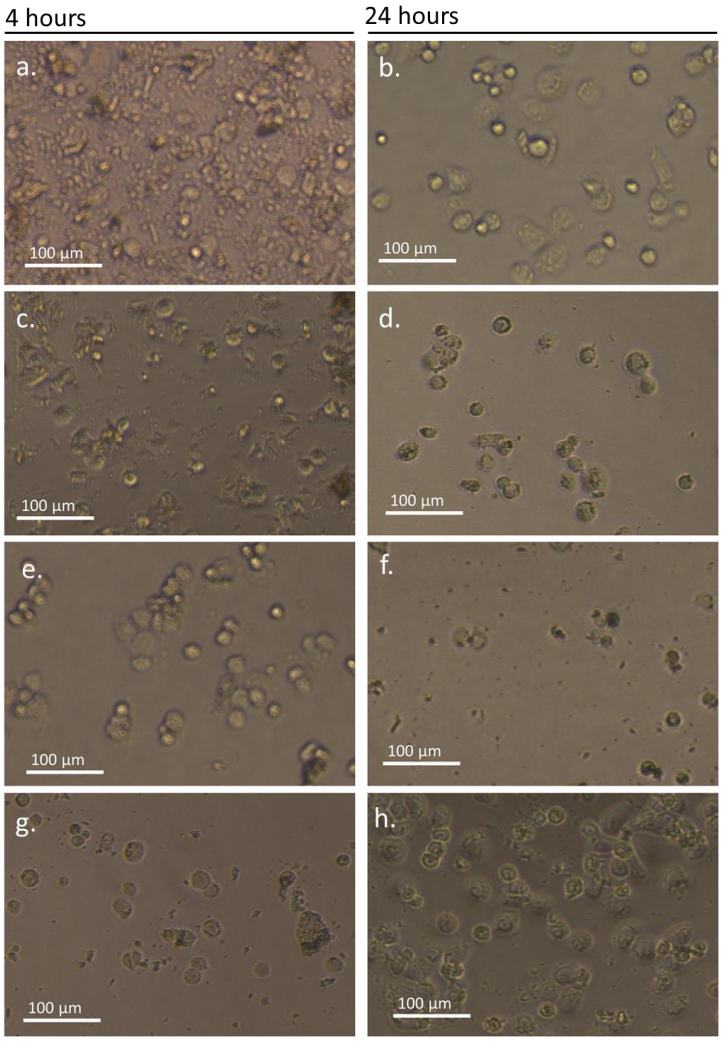

Source: by the author.

According to the results shown in **Figure VI.5**, the shape and size characteristics of THP-1 cells were maintained at all PLGA concentrations used after 4 and 24 hours of incubation. This means that according to the cytotoxicity results, PLGA particles at different concentrations between 16 and 64 μg mL^{-1} did not show significant cytotoxicity to THP-1 cells. The amount of extracellular material is not taken into account because of the result of the 4 h incubation sample without the presence of

PLGA particles, which showed a large number of extracellular components. The results for cells treated with PLGA:IO are shown in **Figure VI.6**.

Figure VI.6. Morphological analysis of THP-1 cells in plate after uptake assay treated with PLGA:IO particles. a) untreated cells after 4 hours; b) untreated cells after 24 hours; c) cells treated with PLGA:IO 16 μg mL^{-1}, uptake after 4 hours; d) cells treated with PLGA:IO 16 μg mL^{-1}, uptake after 24 hours; e) cells treated with PLGA:IO 32 μg mL^{-1}, uptake after 4 hours; f) cells treated with PLGA:IO 32 μg mL^{-1}, uptake after 24 hours; g) cells treated with PLGA:IO 64 μg mL^{-1}, uptake after 4 hours; h) cells treated with PLGA:IO 64 μg mL^{-1}, uptake after 24 hours.

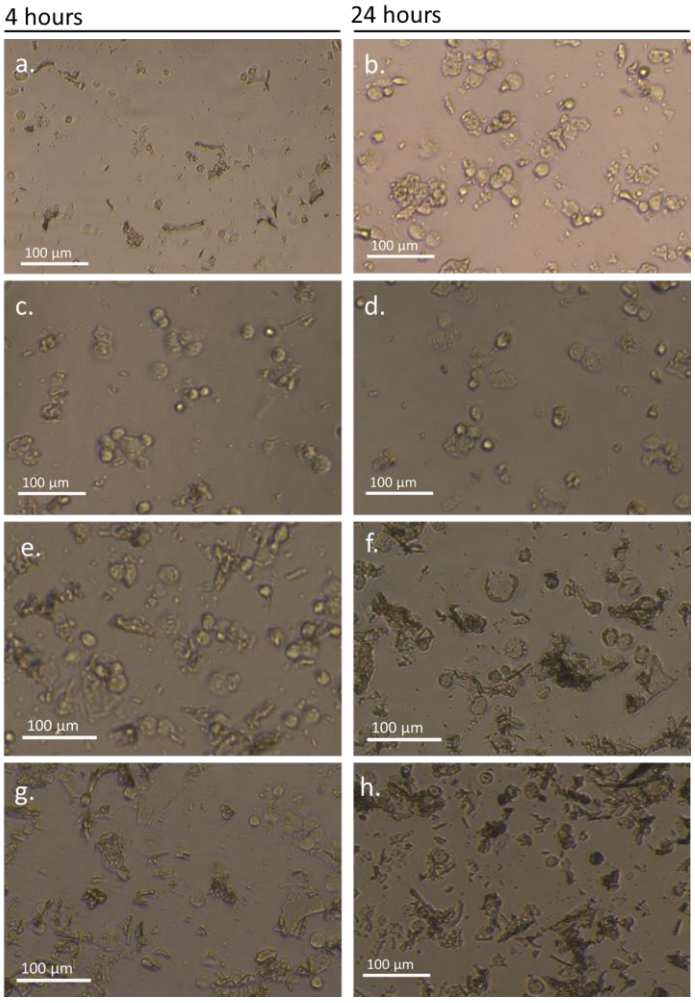

Source: by the author.

According to the results in **Figure VI.6**, the presence of extracellular material is seen in treated cells but also in untreated cells. At a concentration of 32 μg mL^{-1}, cell death is evident after 24 hours. Cell morphology is preserved at all concentrations after 4 hours of incubation, but increased cell volume is observed at the concentration of 32 μg mL^{-1} after 24 hours. At the concentration of 64 μg mL^{-1} there is little evidence as there are many extracellular components that make it difficult to visualise the cells. For

cells treated at the concentration of 16 μg mL^{-1}, cell characteristics were preserved after 24 hours of incubation. The visual analysis of PLGA:ZnO treated cells is shown in **Figure VI.7**.

Figure VI.7. Morphological analysis of THP-1 cells in plate after uptake assay treated with PLGA:ZnO particles. a) untreated cells after 4 hours; b) untreated cells after 24 hours; c) cells treated with PLGA:ZnO 16 μg mL^{-1}, uptake after 4 hours; d) cells treated with PLGA:ZnO 16 μg mL^{-1}, uptake after 24 hours; e) cells treated with PLGA: ZnO 32 μg mL^{-1}, uptake after 4 hours; f) cells treated with PLGA:ZnO 32 μg mL^{-1}, uptake after 24 hours; g) cells treated with PLGA:ZnO 64 μg mL^{-1}, uptake after 4 hours; h) cells treated with PLGA:ZnO 64 μg mL^{-1}, uptake after 24 hours.

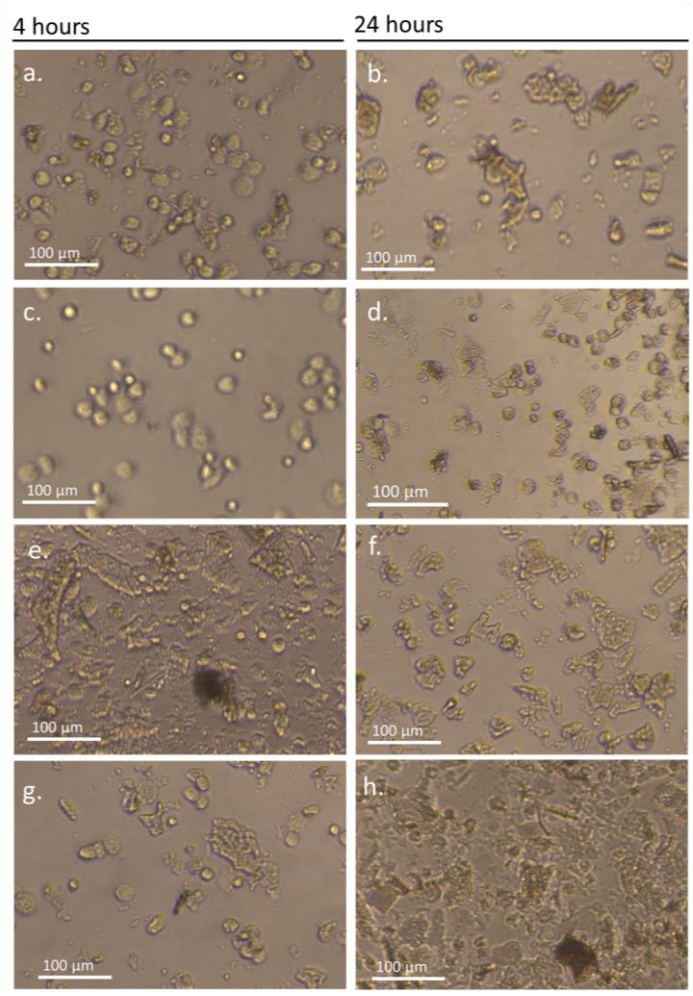

Source: by the author.

According to the results shown in **Figure VI.7**, cell integrity is preserved at both incubation times when analysing the 16 μg mL^{-1} concentration of PLGA:ZnO NPs. At the concentration of 32 μg mL^{-1}, cell integrity is preserved after 4 hours of incubation, but after 24 hours an increase in cell volume of some cells can be observed and the intracellular content changes, indicating possible uptake of the NPs. No cell death was

observed at the concentration analysed. At the concentration of 64 μg mL^{-1}, cell integrity is maintained after 4 hours. After 24 hours, it is not possible to distinguish the cells from the extracellular content at the concentration of 64 ug mL^{-1}, so no definitive conclusions can be drawn. The analysis of THP-1 cells after treatment with PLGa:ZnO:IO NPs is shown in **Figure VI.8**.

Figure VI.8. Morphological analysis of THP-1 cells in plate after uptake assay treated with PLGA:ZnO:IO particles. a) untreated cells after 4 hours; b) untreated cells after 24 hours; c) cells treated with PLGA:ZnO:IO 16 μg mL^{-1}, uptake after 4 hours; d) cells treated with PLGA:ZnO:IO 16 μg mL^{-1}, uptake after 24 hours; e) cells treated with PLGA:ZnO:IO 32 μg mL^{-1}, uptake after 4 hours; f) cells treated with PLGA:ZnO:IO 32 μg mL^{-1}, uptake after 24 hours; g) cells treated with PLGA:ZnO:IO 64 μg mL^{-1}, uptake after 4 hours; h) cells treated with PLGA:ZnO:IO 64 μg mL^{-1}, uptake after 24 hours.

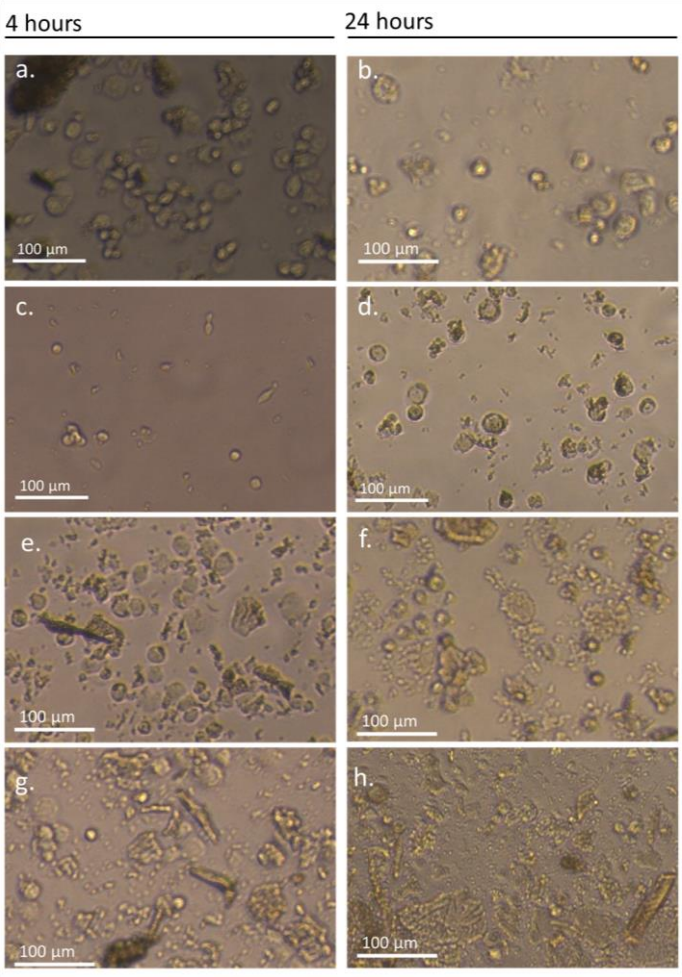

Source: by the author.

According to the results in **Figure VI.8**, cell integrity was maintained after 4 h for cells treated with 16 and 64 μg mL^{-1}, but at the 32 μg mL^{-1} concentration, cell morphology changed with increasing cell volume. The same result is not observed after

24 hours of incubation for the 32 μg mL^{-1} concentration, where the cells maintain their cellular integrity. The amount of extracellular components increases with increasing concentration of PLGA:ZnO:IO in the medium and after 24 hours of incubation for the concentration of 64 μg mL^{-1}, it is not possible to accurately identify the cell morphology due to the large number of extracellular components.

VI.2.3 Luminescence Stability of Fe-ZnO Quantum Dots Prior to Cellular Assays

The luminescence stability of GPTMS-coated Fe-doped ZnO components dispersed in cellular medium was assessed (Figure VI.9). Thus far, the behaviour of Fe-doped ZnO following synthesis in ethanol and dispersion in water has been examined. However, the behaviour of Fe-ZnO after surface modification and dispersion in cellular medium for cell testing over time remains unknown, as the luminescent properties of ZnO are also influenced by the pH of the medium. Different samples were tested at a theoretical concentration of 20 mg mL^{-1}, and stability was measured after 1, 3, 6, and 24 hours. The results are shown in **Figure VI.9**.

Figure VI.9. Intensity and behaviour of Fe-ZnO samples when dispersed in cellular medium and luminescence stability study over a 24-hour period (n=3).

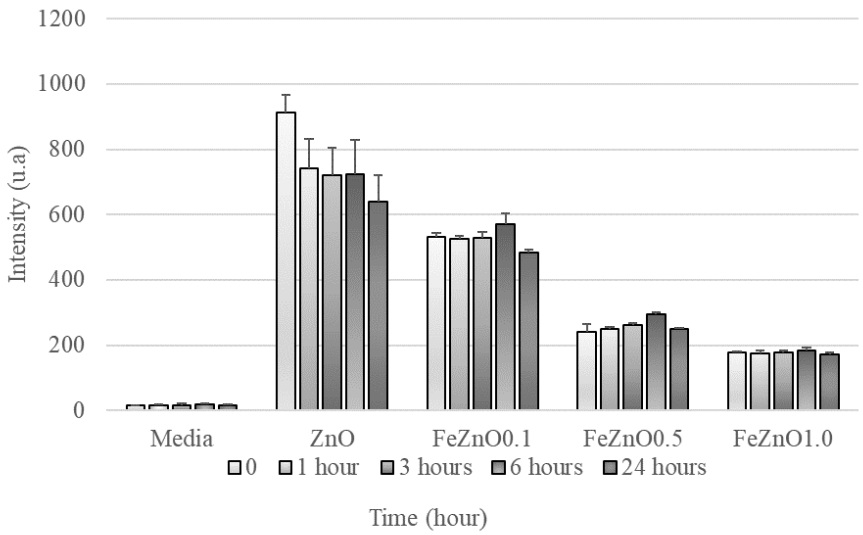

Source: by the author.

According to Figure VI.9, it is evident that the luminescence stability of FeZnO samples in cellular medium remained consistent after 24 hours. There was no statistically significant difference between the adopted time points for the same sample ($p>0.05$). Furthermore, all samples exhibited higher luminescence intensity compared to

the medium alone. Subsequently, cellular uptake assays of the samples were conducted in cellular medium containing THP-1 cells, the same cells used for the cytotoxicity assay of PLGA samples containing ZnO and IO NPs. The initial particle concentration tested was set at 10%, at a theoretical concentration of 0.2 mg mL^{-1}. Assays with medium without cells were also analysed. The results are shown in Figure VI.10.

Figure VI.10. Cellular uptake assay with FeZnO samples after 6 and 24 hours of incubation (n=3). Samples excited at 343 nm and emitting at 540 nm.

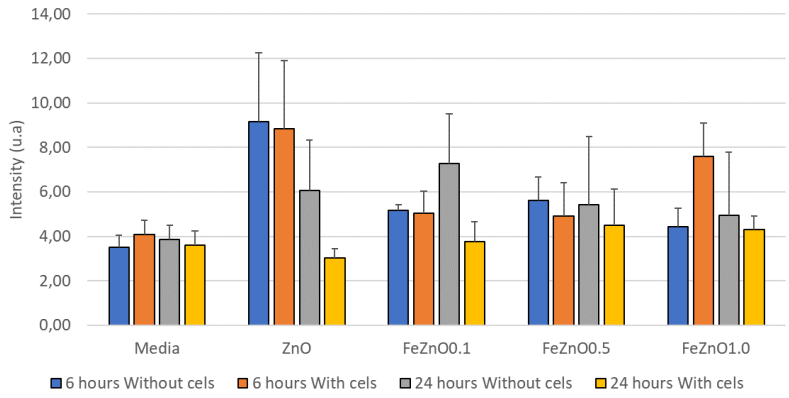

Source: by the author.

Based on the results, it was found that the concentration of FeZnO NPs used was not sufficient to demonstrate a statistically significant difference compared to samples containing only the cell medium with or without cells. A higher concentration, exceeding 10% by proportion, is needed to assess if there is adequate luminescence for cell analysis. Consequently, cytotoxicity assays for this NP concentration have not been conducted thus far. The GPTMS-coated ZnO sample showed higher luminescence intensity, and it was observed that there was a decrease in luminescence intensity after 6 hours of incubation, which further decreased after 24 hours of incubation, with a p-value <0.05. Future assays will be necessary to assess the cytotoxicity of FeZnO NPs at higher concentrations.

VI.3 Conclusion

The cytotoxicity of PLGA:ZnO:IO NPs was evaluated against THP-1 cells. The uptake of the NPs was monitored by luminescence.

It was found that the PLGA particles containing IO and ZnO showed no significant cytotoxicity after 4 and 24 hours of incubation. Regarding the uptake test, it

was found that cells showed luminescence after uptake with PLGA particles containing ZnO and co-loading with ZnO and IO after 4 hours of incubation. After 24 hours of incubation, the luminescence disappeared, but this can be explained by the stability of the PLGA system after uptake and the action of the liposomes and the acidic pH that degrades the ZnO NP.

REFERENCES

DA SILVA, B. L. et al. Magnetic and Highly Luminescent Heterostructures of Gd3+/ZnO Conjugated to GCIS/ZnS Quantum Dots for Multimodal Imaging. **Nanomaterials** 2021, v. 11, n. 7, p. 1817, 2021.

HASAN, W. et al. Delivery of multiple siRNAs using lipid-coated PLGA nanoparticles for treatment of prostate cancer. **Nano letters**, v. 12, n. 1, p. 287–292, 2012.

KANEHIRA, K. et al. Fluorescence Enhancement Effect of TiO2 Nanoparticles and Application for Photodynamic Diagnosis. **International Journal of Molecular Sciences**, v. 20, n. 15, 2019.

MUDUNKOTUWA, I. A. et al. Dissolution of ZnO nanoparticles at circumneutral pH: A study of size effects in the presence and absence of citric acid. **Langmuir**, v. 28, n. 1, p. 396–403, 2012.

PINHO, A. R. et al. In Vitro Cytotoxicity Effects of Zinc Oxide Nanoparticles on Spermatogonia Cells. **Cells**, v. 9, n. 5, 2020.

CHAPTER VII

Final conclusions

CHAPTER VII – Final conclusions

The aim of this work was the development of iron- and zinc-based nanosystems as agents for diagnostic imaging, due to the suitable luminescence properties of the Zn-based compounds and the suitable Mp of the iron-based compounds. The nanometric particles have special properties at the level of the atom. In addition to the use of components with low toxicity in comparison to the QDs that are currently used, such as Cd and Gd.

A system based on ZnO and IO was developed as a first step. For this purpose, a particle system based on polylactide coglycolide acid (PLGA) copolymer was chosen. This copolymer is biocompatible, widely used as a drug carrier, and shows suitable selectivity for cancer cells. A study to modify the NP surface with oleic acid was performed.

The NPs were suitably modified with oleic acid. PLGA particles were prepared. The PLGA particles were prepared using a simple emulsion and solvent evaporation method that involves easily accessible, inexpensive components and simple synthesis without using temperature. The particles showed a circular shape with adequate size from the TEM and DLS results, which can be used as drug carriers.

From the results, it has been observed that there is an interaction between the IO NPs and the ZnO NPs. The luminescence properties of ZnO are lost with the increased presence of iron. However, a study of the ratio of ZnO to IO was performed and it was found that the nominal ratio of PLGA:ZnO:IO 10:6:1 (w:w:w, mg) is important to get luminescence intensity in the PLGA particles. The luminescence intensity of the ZnO is affected below this nominal ratio in relation to ZnO. However, at this amount, ZnO luminescence is preserved and with the results presented in MRI measurements, this ratio was sufficient to show a suitable T2 effect.

The polymeric system was tested on TPH1 cells for uptake and cytotoxicity. The uptake was efficient as after 4 hours incubation, the cells were luminescent and the loading did not induce toxicity.

The doping of ZnO with iron was studied as the production of PLGA particles loaded with IO and ZnO might not be satisfactory as with time, both imaging tags can be released and then label different cells or cells compartment. An attempt was made to

observe how the iron interact with the ZnO through a doping process. The sol-gel process and ultrasound were used for the doping process. The molar concentration of the iron was observed in relation to the molar concentration of the zinc. It was observed that as the concentration of the doped iron increases, the ZnO loses its luminescence. A minimum amount of iron was observed to be sufficient for ZnO to keep its luminescence. In addition, it has been observed that the doping time can influence the properties of this material. It has been observed that the time of addition of the dopant to the medium after the start of the reaction can influence the luminescence properties of this material. To maintain the luminescent properties of the material, it is believed that the formation of the ZnO core is essential. The luminescence intensity is increased with the addition of 0.1% iron ions in the solution. It has been shown that the particle size of the ZnO does not change when the iron content is between 0 and 1 %.

In addition, the Mp of the material were also observed by means of MRI. The FeZnO NPs with GPTMS surface modification were able to produce T2 and T1 effects. These effects are not observed with pristine ZnO NPs. The effect increases with increasing iron concentration. However, 0.1% is sufficient to produce these effects.

About CIS/ZnS NPs. Attempts have been made to dope the CIS/ZnS composite with iron. However, it has been observed that the material properties are lost with the Fe:In:Cu ratio used. In addition, the crystalline structure is modified. Different mass losses were observed in the thermogravimetry spectra. In the processing of CIS/ZnS and IO NPs. These particles have been incorporated into the polymer system of PLGA. The luminescence properties of CIS/ZnS in the presence of IO were not affected. The luminescence maximum was observed at 650 nm. The Mp showed suitable T2 contrast due to the presence of IO.

The results of this study demonstrate the successful development of iron- and zinc-based nanosystems, which combine luminescent and magnetic properties for diagnostic imaging applications. The cost-effective synthesis ensured the formation of biocompatible nanometric particles that are efficient in cellular uptake without toxicity. The optimization of ZnO and IO ratios in PLGA particles resulted in preserved luminescence and suitable T2 effect, highlighting the potential of these systems as multimodal imaging agents. The modification with oleic acid and the iron doping study further reinforces the versatility and efficacy of these materials, offering a promising and less toxic alternative to conventional imaging agents.